1-1-2012

An Improved Model For Precise Point Positioning With Modernized Glogbal Positioning System

Mohamed E. Elsobeiey
Ryerson University

AN IMPROVED MODEL FOR PRECISE POINT POSITIONING WITH MODERNIZED GLOBAL POSITIONING SYSTEM

by

Mohamed Elsayed Elsobeiey

B.Sc. (Hons) in Civil Engineering, Zagazig University, Egypt, 2000
M.Sc. in Civil Engineering, Zagazig University, Egypt, 2005

A dissertation

presented to Ryerson University

in partial fulfillment of the

requirements for the degree of

Doctor of Philosophy

in the Program of

Civil Engineering

Toronto, Ontario, Canada, 2012

AUTHOR'S DECLARATION FOR ELECTRONIC SUBMISSION OF A DISSERTATION

I hereby declare that I am the sole author of this dissertation. This is a true copy of the dissertation, including any required final revisions, as accepted by my examiners.

I authorize Ryerson University to lend this dissertation to other institutions or individuals for the purpose of scholarly research.

I further authorize Ryerson University to reproduce this dissertation by photocopying or by other means, in total or in part, at the request of other institutions or individuals for the purpose of scholarly research.

I understand that my dissertation may be made electronically available to the public.

Mohamed Elsobeiey

ABSTRACT

Mohamed Elsayed Elsobeiey

AN IMPROVED MODEL FOR PRECISE POINT POSITIONING WITH MODERNIZED GLOBAL POSITIONING SYSTEM

PhD. of Civil Engineering, Ryerson University

2012

Recent developments in GPS positioning show that a user with a standalone GPS receiver can obtain positioning accuracy comparable to that of carrier-phase-based differential positioning. Such a technique is commonly known as precise point positioning (PPP). A significant challenge of PPP, however, is that it typically requires a minimum of 30 minutes to achieve centimeter- to decimeter-level accuracy. This relatively long convergence time is the result of un-modeled GPS residual errors. This thesis addresses error mitigation techniques to achieve near real-time PPP.

To explore the full advantage of the modernized GPS L2C signal, it is essential to determine its stochastic characteristics and code bias. GPS measurements were collected in order to study the stochastic characteristics of the modernized GPS L2C signal. As a byproduct, the stochastic characteristics of the legacy GPS signals, namely C/A and P2 codes, were also determined and then used to verify the developed stochastic model of the modernized signal. The differential code biases between P2 and C2, DCB_{P2-C2}, were also estimated using the Bernese GPS software.

A major residual error component, which affects the convergence of PPP solution, is the higher-order ionospheric delay. We rigorously modeled the second-order ionospheric delay, which represents the bulk of higher-order ionospheric delay, for our PPP model. First, we investigated the effect of second-order ionospheric delay on GPS satellite orbit and clock corrections. Second, we used the estimated satellite orbit and clock corrections to process the GPS data from several IGS stations after correcting the data for the effect of second-order ionospheric delay. The results demonstrated an improvement of up to 25% in the precision of the estimated coordinates with the second-order ionospheric delay, as well as reduction of the convergence time of the estimated parameters by about 15%, depending on the geographic location and ionospheric and geomagnetic conditions.

Between-satellite single-difference PPP algorithms were developed to cancel out the receiver clock error, receiver initial phase bias, and receiver hardware delay. The decoupled clock corrections, provided by NRCan, were also applied to account for the satellite hardware delay and satellite initial phase bias. GPS data collected from several IGS stations were processed using the un-differenced model, un-differenced decoupled clock model, between-satellite single-difference (BSSD) model, and between-satellite single-difference using the decoupled clock (BSSD-DC) model. The results showed that the proposed BSSD model significantly improved the PPP convergence time by 50% and improved the solution precision by more than 60% over the traditional un-differenced PPP model.

ACKNOWLEDGEMENTS

Above all, I am in debt to ALLAH who has given me the health, strength and patience, and granted me the opportunity to complete my graduate studies at Ryerson University.

First, I would like to express my special thanks and gratitude to my distinguished supervisor, Professor Dr. Ahmed El-Rabbany, for his professional supervision, encouragement, valuable suggestions, guidance, and proposed ideas throughout my study and this research. His abundant cooperation and understanding deserve unbounded appreciation. It was my great pleasure working under his supervision.

In addition, I wish to extend my appreciation and thanks to the committee members, Dr. Claus Rinner, Dr. Peter Dare, Dr. Sri Krishnan, Dr. Ahmed Shaker, and Dr. Arnold Yuan for dedicating their valuable times to review my thesis.

Appreciations are given to the Geodetic survey division of Natural Resources Canada (NRCan) for providing the source code of the traditional un-differenced GPSPace PPP software. The author is also grateful to Mr. Paul Collins from NRCan for the fruitful discussion about his method for estimating the decoupled clocks.

Finally, many thanks go to all my colleagues in the Department of Civil Engineering for the unforgettable moments, friendship, and support I received throughout the entire course of my research: Abdulla Al-Naqbi, Hamad Yousif, Hassan Ibrahim, Akram Afifi, and Mahmoud Farag. I must express a special thanks to Dr. Mahmoud Taha, Dr. Mahmoud AbdelGalil, Dr. Mohamed El-Diasty and Wai Yeung Yan for their valuable support and precious ideas through my graduate studies.

DEDICATION

To the people who praise nothing but noble values and deserve vast respect -

My parents, my uncle, my sister, my brothers, my wife, and my child AbdAllah

TABLE OF CONTENTS

LIST OF FIGURES

LIST OF TABLES

ABBREVIATIONS

AFS	Atomic Frequency Standards
ARP	Antenna Reference Point
BCE	Broadcast Ephemerides
BRSD	between-receiver single-difference
BSSD	Between-satellite single-difference
BSSD-DC	Decoupled clock BSSD
C/A code	Coarse/ Acquisition
CODE	Centre for Orbit Determination in Europe
CONUS	Continental United States
DCB	Differential Code Biases
DD	Double Difference
DGPS	Differential Global Positioning System
DoD	Department of Defence
DOP	Dilution of Precision
ECMWF	European Center for Medium-range Weather Forecast
ECEF	Earth Centered Earth Fixed
ECI	Earth-Centered Inertial System
EUV	Extreme Ultraviolet
FSL	Forecast Systems Lab
GIM	Global Ionosphere Maps
GLONASS	Global Navigation Satellite System

GNSS	Global Navigation Satellite Systems
GPS	Global Positioning System
HDOP	Horizontal Dilution of Precision
IGS	International GNSS Service
IONEX	IONosphere Exchange format
IPP	Ionospheric Pierce Point
JPL	Jet Propulsion Laboratory
LC	Linear Combination
LOS	Line-of-Sight
MCS	Master Control Station
MEDLL	Multipath Elimination Delay Lock loop
NAVSTAR	NAVigational System using Timing and Ranging
NMF	Niell Mapping Function
NOAA	National Oceanic and Atmospheric Administration
NOAATrop	NOAA Tropospheric Model
NRCan	Natural Resources Canada
NWP	Numerical Weather Prediction
PCO	Phase Center Offset
P-code	Precise
PCV	Phase Center Variation
PDOP	Position Dilution of Precision
PPP	Precise Point Positioning
PRN	Pseudorandom Noise

RCP	Right Circularly Polarized
RINEX	Receiver-Independent Exchange Format
SA	Selective Availability
SNR	Signal to Noise ratio
STEC	Slant Total Electron Content
TEC	Total Electron Content
VDOP	Vertical Dilution of Precision
VMF1	Vienna Mapping Function 1
VTEC	Vertical Total Electron Content
US-TEC	United States Total Electron Content
UV	Ultraviolet
ZHD	Zenith Hydrostatic Delay
ZWD	Zenith Wet Delay

1. INTRODUCTION

This chapter introduces the comprehensive work included in this thesis. Section 1.1 summarizes the necessary background for this research. Section 1.2 explains the previous studies in precise point positioning with emphasis on the limitations of previous work. Section 1.3 describes the objectives of this research. Section 1.4 briefly outlines the contents of Chapters 2 to 6, and Section 1.5 highlights the areas in which this thesis makes a significant contribution to research.

1.1 Background

Differential carrier-phase-based GPS techniques have traditionally been used in positioning applications requiring great accuracy. These techniques inherit their high accuracy from the fact that GPS receivers in close proximity share many of the same errors and biases. The shorter the receiver separation, the more similar are the errors and biases. As such, a major part of the GPS error budget can be removed by differencing between the GPS observables from these receivers. Unfortunately, as the baseline length increases, the errors at the reference and the rover receivers become less correlated; i.e., they would not cancel out sufficiently through differencing. This leads to unsuccessful fixing for the ambiguity parameters, which in turn deteriorates the positioning accuracy. In addition, a major disadvantage of differential techniques is their dependency on the measurements or corrections from a reference receiver or network. This, however, may not be a practical solution in many cases, as a result of, for example, high cost or lack of infrastructure.

With the termination of selective availability (SA) in May 2000, and the production of satellite precise orbit and clock corrections such as those provided by the International GNSS Service (IGS), it became evident that centimetre to decimetre positioning accuracy is possible with standalone geodetic-grade GPS receivers. Such a technique is commonly known as precise point positioning (PPP). Unlike classical GPS point positioning, PPP attempts to account for all the GPS errors and biases. In addition to being cost-effective, the PPP method provides an accuracy level comparable to that of differential carrier-phase-based positioning (i.e., centimetre- to decimetre-level accuracy).

1.2 Previous Studies and Limitations

PPP was first introduced by researchers at the Jet Propulsion Laboratory (Zumberge et al., 1997). Kouba and Heroux (2001) introduced a PPP model, which employs an un-differenced dual-frequency pseudorange and carrier-phase measurements to form first-order ionosphere free linear combinations. They showed that decimetre-level positioning accuracy can be achieved in post-processing mode.

Gao and Shen (2001, 2002) proposed a PPP model which takes the average of pseudorange and carrier phase measurements on both GPS frequencies to remove the first-order ionospheric delay. According to Gao and Shen (2002), both multipath effect and measurement noise can be reduced through a smoothing process. However, this leads to mathematical correlation between observations. Unless accounted for, this correlation

results in longer convergence time for the estimated parameters and overestimation of the resulting covariance matrix.

Colombo et al. (2004) developed a PPP method based on between-satellite single-difference of ionosphere-free code and carrier-phase measurements, which eliminates the receiver clock error, receiver initial phase bias, and receiver hardware delay. They were able to obtain a positioning accuracy of a few centimetres in static mode and less than 10 cm in the kinematic mode.

A major drawback of the above mentioned traditional PPP models is that a minimum of 30 minutes are required to achieve centimetre- to decimetre-level accuracy. This relatively long convergence time results from improper modeling of GPS errors and biases, including receiver and satellite hardware delays, initial phase biases, higher-order ionospheric delay, and stochastic characteristics of modernized GPS signals.

More recently, Ge et al. (2008) used a network of reference stations to solve for the carrier-phase ambiguities. The average values of the fractional cycle part of the real-valued wide-lane and narrow-lane ambiguities are used as corrections for wide-lane and narrow-lane real ambiguities from a single receiver. Collins et al. (2010) developed a method known as the decoupled clock model. This method allows for the satellite hardware delays and satellite carrier-phase initial phase bias to be lumped to the GPS satellite clock corrections. The major drawback of these two methods is that they do not

account for the time variation of receiver hardware delay which deteriorates the convergence time of the estimated parameters.

1.3 Objectives

The main objective of this research is to develop rigorous precise point positioning models that meet the accuracy requirements of near real-time precise point positioning. This will be fulfilled through a number of tasks to improve the PPP solution convergence time and the accuracy of the estimated parameters. These tasks can be summarized as follows:

1. to develop a stochastic model for the modernized GPS L2C signals.
2. to estimate the L2C code bias (DCB_{P2C2}) and to assess the performance of the combined solution of both the modernized L2C and legacy GPS signals.
3. to develop a model for the second-order ionospheric delay, which represents the bulk of higher-order terms. This includes an assessment of the impact of second-order ionospheric delay on the determination of GPS satellite orbit and clock corrections.
4. to develop an un-differenced decoupled clock model and to study the decoupled receiver clock behaviour to get inference about the time-dependent receiver hardware delays.
5. to develop between-satellite single-difference (BSSD) model to cancel out the receiver clock error, receiver hardware delay and receiver initial phase bias.
6. to apply the decoupled satellite clock corrections to the BSSD model (BSSD-DC) to account for the satellite hardware delay and satellite initial phase bias.

1.4 Thesis Outline

Chapter 1 presents an introduction, previous studies and limitations, thesis objectives, thesis outline, and research contribution.

Chapter 2 provides the GPS background necessary to support the research. It addresses the GPS signal structure, modernization program, observables, and positioning techniques.

Chapter 3 introduces the various GPS measurements errors and the ways to account for them.

Chapter 4 deals with PPP functional and stochastic models. It presents the traditional un-differenced, un-differenced decoupled clock, BSSD, and BSSD-DC PPP models. This chapter covers also the least-squares technique to solve the different PPP models.

Chapter 5 is devoted to show the different results obtained through different model conditions. PPP accuracy and convergence time are extensively studied in all cases.

Chapter 6 presents the summary and conclusions of this research, and suggests some recommendations for future research.

Appendix A presents the results obtained from the developed observations' stochastic models.

Appendix B presents the effect of modernized L2C signal on the PPP solution.

Appendix C illustrates the steps followed in the estimation of the GPS satellite orbit using the Bernese GPS software.

Appendix D illustrates the steps followed in the estimation of the GPS satellite clock corrections using the Bernese GPS software.

Appendix E presents the effect of second-order ionospheric delay on the PPP solution.

Appendix F presents the results obtained using the developed PPP models.

1.5 Research Contributions

The contributions made in this research can be summarized as follows:

- To develop a stochastic model for the modernized GPS L2C signal.
- To estimate the L2C code bias (DCB_{P2-C2}) and assess the PPP performance using the combined modernized GPS L2C signal and legacy GPS signals in terms of the positioning accuracy and convergence time.
- To study the impact of second-order ionospheric delay on GPS satellite orbit and satellite clock corrections.
- To develop a second-order ionospheric delay model for PPP and to study the effect of second-order ionospheric delay on the PPP solution accuracy and convergence time of the estimated parameters.
- To develop an un-differenced decoupled clock model and to study the behaviour of the receiver decoupled clock errors.
- To develop functional and stochastic models for between-satellite single-difference (BSSD) PPP model.
- To assess the performance of the un-differenced and BSSD decoupled clock models.

2. GPS OVERVIEW

2.1 Introduction

Global Positioning System (GPS) is a satellite-based navigation system developed by the United States Department of Defence (DoD) in the early 1970s to fulfill the military requirements but later made available for civilian users (El-Rabbany, 2006). The system provides the user with a great deal of valuable information, including position, velocity, and time in a common reference system, anywhere on or near the surface of the Earth under all weather conditions. Since GPS serves an unlimited number of users, both civilian and military, it has been designed as a one-way passive system where the users can only receive satellite signals (El-Rabbany, 2006). This chapter describes the GPS system, signal structure, including the modernized signals, GPS observables, and GPS positioning techniques.

2.2 GPS System

The GPS nominal constellation consists of 24 satellites arranged on six orbital planes with 55° inclination to the equator. The satellites are orbiting the earth at an altitude of about 20,200 km with orbital periods of approximately 11 hours 58 minutes (half a sidereal day). The full constellation provides global coverage with four or more simultaneously observable satellites above 15° elevation everywhere on the Earth at all times (Hofmann-Wellenhof *et al.*, 2008). Each GPS satellite transmits a microwave radio signal centred on the L-band carrier frequency of the electromagnetic spectrum. The carrier frequencies are identified as the L1 signal with a frequency of 1575.42 MHz, and

the L2 signal at a frequency of 1227.60 MHz. The satellite signal consists of the two L-band carrier frequencies, the ranging codes modulated on these carrier waves, and the navigation message.

2.3 GPS Signal Structures

All signals transmitted by the GPS satellites are derived from the fundamental frequency $f_0 = 10.23\,\text{MHz}$, generated by the atomic clocks aboard the satellites. Atomic clocks are based on atomic frequency standards (AFS) which produce the reference frequency by stimulated radiation. Atomic clocks are the key to the accuracy of satellite navigation (Hofmann-Wellenhof *et al.*, 2008). The L1 and L2 carrier frequencies are generated by multiplying the fundamental frequency by 154 and 120, respectively. Their corresponding wavelengths are approximately 19 cm and 24 cm, respectively. The signals contain codes that identify each satellite, time of the emitted signal, satellite position, satellite clock corrections, and other data related to the ionosphere and the satellite. The L1 signals carry a Coarse/Acquisition (C/A) code, which is available for civilian users, and a more precise P(Y) code, which is available for authorized users only. The L2 signals, on the other hand, carry the precise P(Y) code, which is available for authorized users only. The C/A-code has a unique sequence of 1,023 binary chips (zeros and ones) with a width of 300 m and repeating every millisecond (Teunissen and Kleusberg, 1998). The P-code is extremely long (~10^{14} chips) but with 10 times smaller chip width, 30 m, and repeats itself every one week. High quality receivers use several techniques such as squaring and cross correlation to acquire the P code on L1 and L2, but

with noisier characteristics compared with the original codes (Hofmann-Wellenhof *et al.*, 2008).

2.4 GPS Modernization

To meet future requirements, and to be competitive with other satellite navigation systems (e.g. Galileo and GLNASS), the USA initiated an ambitious plan for GPS modernization. The first step towards GPS modernization took place in May 2000, when the GPS Selective Availability (SA) feature was turned off. The first satellite of the modernized Block IIR-M was launched on September 25, 2005. Block IIR-M transmits a new civil L2C code on the L2 frequency in addition to the new military M-code on L1 and L2. The next generation of satellites after Block IIR-M is Block IIF ("F" denotes follow on). The main feature of Block IIF generation is the additions of a third civil signal denoted as L5C as well as two military M-code signals on a new frequency of 1176.45 Mhz (L5) (Hofmann-Wellenhof *et al.*, 2008). At present, August 15, 2011, the GPS constellation consists of 32 satellites, including 7 Block IIR-M satellites and two Block IIF satellites. The GPS modernization program includes the launch of Block III satellites that transmit the modernized fourth civil L1C signal, which will not replace the C/A-code (Hofmann-Wellenhof *et al.*, 2008).

2.5 GPS Observables

Civil GPS receivers can acquire three types of observables from the GPS satellite signals, code pseudoranges, phase measurements, and Doppler shifts. Pseudorange and carrier phase are based on measured time or phase differences between the transmitted satellite signals and the receiver-generated signals (Hofmann-Wellenhof *et al.*, 2008). Since these observations are based on two different unsynchronized clocks (the satellite clock, and the receiver clock), they are denoted as pseudoranges.

2.5.1 Code Pseudoranges

The pseudorange is the biased distance between the GPS satellite at signal transmission time and the receiver at signal reception time. The signal travel time is computed by alignment of the transmitted satellite signal with a receiver-generated replica signal by the code tracking loop. The pseudorange is then computed by multiplying the signal travel time by the speed of light (299,729,458 m/s). This measured pseudorange, however, is biased by different error sources. A detailed description of these error sources and the corresponding mitigation techniques is given in Chapter 3. The code observation equation can be given as follows (Teunissen and Kleusberg, 1998):

$$P_i = \rho + c(dt^r - dt^s) + T + I_i + \varepsilon_{Pi} \tag{2.1}$$

where,

P_i pseudorange measurements on L_i frequency

ρ	the true geometric range from receiver antenna phase-centre at reception time to satellite antenna phase-centre at transmission time
c	the speed of light in a vacuum
dt^r, dt^s	receiver and satellite clock errors, respectively
T	tropospheric delay
I_i	the ionospheric delay
ε_{Pi}	the unmodelled error sources including orbital error, hardware delays, multipath, and others

2.5.2 Carrier Phase Measurements

The second type of observable is the carrier phase measurement. The carrier phase measurements are inherently more precise than the code measurements. The carrier phase has a precision of 1% of the chip length, i.e., millimetre level (1-3 mm). Therefore, carrier phase is the key for precise GPS positioning applications. Unlike the pseudorange measurements, the carrier phase is ambiguous by an unknown integer number of cycles denoted as the ambiguity number. The receiver can measure a fraction of a cycle but cannot differentiate between one full cycle and another. Fortunately, the initial number of complete cycles remains constant overtime as long as no loss of lock or cycle slip occur. If, however, a cycle slip occurs, a new integer ambiguity constant is introduced for the new carrier phase observations. Equation 2.2 defines the carrier phase observations scaled to metres (Teunissen and Kleusberg, 1998).

$$\Phi_i = \rho + c(dt^r - dt^s) + T - I_i + \lambda_i N_i + \varepsilon_{\Phi i} \tag{2.2}$$

where,

Φ_i	carrier-phase measurements on Li scaled to distance (m)
ρ	the true geometric range from receiver antenna phase-centre at reception time to satellite antenna phase-centre at transmission time
c	the speed of light in a vacuum
dt^r, dt^s	receiver and satellite clock errors, respectively
T	tropospheric delay
I_i	the ionospheric delay
λ_i	carrier-phase wavelength
N_i	integer ambiguity parameter
$\varepsilon_{\Phi i}$	the unmodelled error sources including orbital error, hardware delays, multipath error, and others

The difference between Equations 2.1 and 2.2 is that carrier phase measurements are biased by the integer ambiguity number. In addition, initial phase bias, different hardware delay and multipath effects. Furthermore, the negative ionospheric error means that the ionospheric delay advances the carrier measurement while the ionospheric error delays the code measurement (El-Rabbany, 2006).

2.6 GPS Positioning Techniques

In general, there are two methods to obtain positioning solution from GPS observations: point positioning and relative or differential positioning.

2.6.1 Point Positioning

GPS point positioning, or autonomous positioning, represents the use of GPS measurements from a single GPS receiver to compute the location of a point on the surface of the Earth. In point positioning, however, four or more satellites are required to determine the user position.

2.6.1.1 Classical Point Positioning

In classical point positioning, pseudoranges from at least four satellites are used to compute the user position. The broadcast ephemeris is used to compute the corresponding satellite coordinates, satellite clock corrections, and ionospheric delay. The expected accuracy of the classical point positioning is about 13 m at the 95% probability level (Hofmann-Wellenhof *et al.*, 2008).

2.6.1.2 Precise Point Positioning

With the termination of selective availability (SA) in May 2000 and the production of precise ephemeris and clock data through, e.g., IGS, it became evident that centimetre to decimetre positioning accuracy is possible with standalone geodetic-grade GPS receivers.

Such technique is commonly known as precise point positioning (PPP). Unlike classical GPS point positioning, PPP attempts to account for all the GPS errors and biases. In addition to being cost effective, the PPP method provides an accuracy level comparable to that of differential carrier-phase-based positioning (i.e., centimetre- to decimetre-level accuracy).

2.6.2 Relative Positioning

Relative or differential GPS (DGPS) techniques have been used for positioning applications that require high accuracy. These techniques inherit their high accuracy from the fact that GPS receivers in close proximity share, to a high degree of similarity, the same errors and biases. The shorter the receiver separation is, the more similar the errors and biases. As such, for those receivers, a major part of the GPS error budget can simply be removed by combining their GPS observables. Unfortunately, as the baseline length increases, the errors at the reference and the rover receivers become less correlated; i.e., they would not cancel out sufficiently through differencing. This leads to unsuccessful fixing of the ambiguity parameters, which in turn deteriorates the positioning accuracy. In addition, a major disadvantage of differential techniques is their dependency on the measurements or corrections from a reference receiver or network. This, however, may not be a practical solution in many cases, as a result of, for example, high cost or lack of infrastructure.

3. GPS ERROR SOURCES AND BIASES

GPS observations are contaminated with random and systematic errors which should be accounted for to obtain accurate positioning. In differential techniques, most of the GPS errors are cancelled out by differencing. Precise point positioning accuracy, on the other hand, depends on the ability to mitigate all kinds of errors. These errors can be classified into three categories; satellite related errors, signal propagation related errors, and receiver/antenna configuration errors (El-Rabbany, 2006).

GPS errors attributed to the satellites, include satellite clock errors, orbital errors, satellite hardware delay, satellite antenna phase centre variation, and satellite initial phase bias. Errors attributed to signal propagation, include the delays of the GPS signal as it passes through the ionospheric and tropospheric layers. Errors attributed to receiver/antenna configuration include the receiver clock errors, multipath, receiver noise, receiver hardware delay, receiver initial phase bias, and receiver antenna phase center variations.

In addition to the effect of these errors, the accuracy of the computed GPS position is also affected by site specific error sources such as satellite geometry as seen by the receiver, Earth tide, and ocean tide loading. This chapter addresses the PPP related errors and their mitigation models.

3.1 Satellite Clock Errors

GPS Satellites carry highly accurate atomic clocks (cesium and/or rubidium) that are carefully monitored by the master control station (MCS), however, these clocks are not perfect. Satellite clocks have stability that is about 1 to two parts in 10^{13} over a period of one day. This stability range means that the satellite clock error is in the range of 8.64 to 17.28 ns per day (El-Rabbany, 2006). Satellite clock errors are reflected as an error in the measured GPS observations. That means the satellite clock error contribution in the GPS measurements ranges from 2.59 m to 5.18 m. Cesium clocks behave better than rubidium clocks over a longer period of time. The amount of the satellite clock drift is calculated and transmitted as a part of the navigation message in the form of three coefficients of a second-order polynomial.

Satellite clock errors can be modeled and corrected using the coefficients transmitted in the navigation message: satellite clock bias $(a_\circ)$, satellite clock drift (a_1), and drift rate (a_2). The equation for the satellite clock error is:

$$dt^s = a_\circ + a_1(t - t_c) + a_2(t - t_c)^2$$

where,

t	the time of the observation epoch
t_c	the time of the satellite clock reference epoch

As the satellite clock error is common to all receivers observing the same satellite, the errors can be removed using between-receivers single-difference (BRSD) (El-Rabbany,

2006). In PPP, however, satellite clock error should be accounted for using the IGS precise satellite clock corrections rather than using the corrections derived from the navigation message (see Table 3.1 for the corresponding accuracy of both satellite clock corrections).

3.2 Satellite Orbital Errors

Ephemeris errors are caused by the imperfect modeling of the forces that act on GPS satellites. A satellite ephemeris is determined by the MCS overlapping four hours of GPS data spans to predict fresh satellite orbital elements for each one hour period, and broadcast to users via the navigation message. Broadcast ephemeris (BCE) errors are reported to be in the order of 1.0 m (IGS, 2011). The error can be eliminated by differencing observations between receivers for short baselines. When the baseline increases, differencing observations will not completely remove the error because each satellite is viewed at different angles by the various ground receivers.

In PPP, precise ephemeris data must be used in the data processing rather than using the broadcast ephemeris. A precise ephemeris is produced by organizations such as the IGS, Jet Propulsion Laboratory (JPL), and Natural Resources Canada (NRCan). At present, precise ephemeris is made available online at no cost, and deliver accuracies that range from less than 2.5 cm when final precise orbits are used to about 5 cm when ultra-rapid orbits are used. Table 3.1 summarizes the present (August 15, 2011) accuracy of the broadcast ephemeris and availability and accuracy of the IGS precise satellite orbit and clock corrections (IGS, 2011).

Table 3.1: Broadcast Ephemerides Accuracy, Availability and Accuracy of the IGS Precise Orbit and Clock Corrections (IGS, 2011)

Product		Accuracy	Latency	Sample Interval
Broadcast	orbits	~100 cm	real-time	daily
	Sat. clocks	~5 ns RMS, ~2.5 ns SDev		
Ultra-Rapid (predicted half)	orbits	~5 cm	real-time	15 min
	Sat. clocks	~3 ns RMS, ~1.5 ns SDev		
Ultra-Rapid (observed half)	orbits	~3 cm	3-9 hours	15 min
	Sat. clocks	~150 ps RMS, ~50 ps SDev		
Rapid	orbits	~2.5 cm	17-41 hours	15 min
	Sat. clocks	~75 ps RMS, ~25 ps SDev		5 min
Final	orbits	~2.5 cm	12-18 days	15 min
	Sat. clocks	~75 ps RMS, ~20 ps SDev		30 seconds

3.3 Receiver Clock Errors

Unlike the GPS satellites, GPS receivers use inexpensive crystal clocks causing an error more than that of the satellites clock error. These clocks are sensitive to temperature changes, shocks and vibrations, and are not as stable as atomic satellite clocks. Receiver clocks are not synchronized with satellite clocks or with GPS time. Receiver clock error can be eliminated by differencing observations between satellites (BSSD). It can also be mitigated as an additional unknown parameter during the estimation process.

3.4 Receiver Noise

GPS receiver noise error is caused by the limitations of the individual receiver's electronics. Therefore, receiver noise is unique to each receiver. The noise comes essentially from the thermal noise, which is caused by the electrons movement within the receiver's parts (Teunissen and Kleusberg, 1998).

The effect of receiver noise error can be dramatically reduced by selecting a good quality GPS receiver. The receiver noise error of modern receivers is, however, less than 1 millimetre for carrier-phase and a few centimetres for code observations (El-Rabbany, 2006).

3.5 Ionospheric Delay

The ionosphere is the uppermost part of the Earth's atmosphere, extending in various layers from about 50 kms up to about 1,000 km or more above the Earth (Hofmann-Wellenhof *et al.*, 2008). The ionosphere contains ionized particles created by the Sun's

ultraviolet radiation. The density of the ionized particles is not constant along the ionospheric region. It differs with altitude and can be illustrated as four layers named D, E, F1, and F2 (El-Rabbany, 2006). Generally, different layers are characterized by the maximum density at a certain altitude and the density decreases with altitude on both sides of the maximum (Schunk and Nagy, 2009). Table 3.2 summarizes the main characteristics of the main ionospheric layers (Komjathy, 1997; Kelley, 2009; Schunk and Nagy, 2009). From table 3.2, it is seen that layer F2 is the most significant layer showing the largest electron density peak in the ionosphere.

Table 3.2: Characteristics of the Main Ionospheric Layers (Komjathy, 1997), (Kelley, 2009) and (Schunk and Nagy, 2009)

Layer	Altitude (km)	Electron Density (electron/m^3)	Characteristics
D	50-90	1.3E8-13.1E8	Solar x-ray UV radiation
E	90-140	1.3E11-1.7E11	Solar x-ray EUV radiation
F1	140-210	2.3E11-3.3E11	EUV radiation Auroral precipitation
F2	210-1000	2.8E11-5.2E11	EUV radiation

The ionosphere is a dispersive medium that affects the speed, frequency, direction, and polarization of GPS signals, and introduces phase and amplitude scintillation (Klobuchar, 1996). The ionosphere causes GPS signal delays proportional to the total electron content (TEC) along the path from the GPS satellite antenna to the receiver antenna. It speeds up the carrier phase beyond the speed of light while it delays the code. In general, the ionosphere can introduce a ranging error of the order of 5 m to 15 m, and up to 150 m under extreme solar activities (El-Rabbany, 2006).

3.5.1 Ionospheric Variability

As a result of solar activities, the ionospheric delay is changing significantly in space and time. Therefore, the ionospheric delay is highly unpredictable in extreme conditions. This section summarizes the factors affecting ionospheric delay variation.

Altitude

As indicated before, the ionosphere consists of different layers. The total electron density is increasing as the altitude increases until a specific height (h_{ion}) where the maximum electron density is reached. Above the height h_{ion} the electron density decreases because of the decrease of the ionized molecules.

Time of the day

Because the Sun plays a significant role in forming the free electrons, there is strong correlation with the free electron density and the Earth's diurnal period. The solar activity

is at its daily maximum around the local noon and at its minimum around the night time. So, the greatest ionospheric delay is observed at midday, and the smallest delay is observed between midnight and early morning.

User latitude

The Earth's magnetic field affects the ionized part of the atmosphere. In general, the world is divided into three regions depending on the magnetic field (Komjathy, 1997); equatorial, mid-latitude, and auroral or polar regions. The electron density size and variability are usually the highest at the equatorial zone and auroral/polar zones. At mid-latitude, the size and variability of the electron density are relatively small.

Season

Seasons are formed because of the inclination of the Earth's equator with respect to the ecliptic. Solar activities and therefore electron density are variant from season to season. Lower electron density levels are observed in the summer than in the winter (El-Rabbany, 2006).

Solar cycle

The UV radiation from the Sun is influenced by the number of sunspots on the Sun's surface, photosphere, which can last from several hours to several months as a result of stormy localized magnetic fields (Schunk and Nagy, 2009). They appear dark because they are cooler than the surrounding photosphere (Komjathy, 1997). The sunspots themselves do not affect the ionosphere, but the strength of the solar emissions that

influence the ionosphere are linked to the sunspot number, a standard index of solar activity that changes with the 11-year solar cycle (Barclay, 2002).

3.5.2 Ionospheric Delay Mitigation

The ionospheric effect can be considered one of the major GPS error sources. It must be accounted for to derive accurate positioning results from GPS measurements. In relative mode, accurate positioning can be achieved if the baselines are relatively short (less than 10 km) because the ionospheric error is highly correlated at both ends. In PPP, dual frequency users can cancel out the first–order ionospheric delay using the first-order ionosphere-free linear combination. Single frequency users, however, have to account for ionospheric error using specific models such as Klobuchar model, regional ionospheric models (e.g. United States Total Electron Content (US-TEC) maps), or global ionospheric models (e.g. IGS ionospheric maps (IONEX)).

3.6 Tropospheric Delay

The tropospheric delay can be defined as the delay that the signal experiences during its path through the lower layer of the atmosphere. This layer extends up to about 50 kms above the surface of the earth (El-Rabbany, 2006). Unlike the ionosphere, the effect of the tropospheric delay is equal on both codes and carrier phases. This is why the tropospheric delay cannot be eliminated using the linear combination while maintaining the geometry. Tropospheric delay is a function of temperature, pressure, and humidity along the signal propagation path. The effect is also governed by the satellite elevation

angle, and by the altitude of the observer. The delay reaches its maximum value when the satellite is near the user's horizon, and at its minimum value when the satellite is at the user's zenith.

The tropospheric delay can be divided into two components namely, wet and dry component. The wet component represents 10% of the total troposphere delay (Misra and Enge, 2006). The wet component is caused by the water vapour in the lower part of the tropospheric layer, up to 11 kms from sea level, as it contains most of the water vapour. Because of the variation of water vapour density with position and time, the modeling of the wet component is difficult. The average total troposphere delay at the zenith varies between 2.3 and 2.6 m (Teunissen and Kleusberg, 1998), and it does not experience large variation over time. The dry and wet components of the tropospheric delay are usually modeled at zenith and then mapped to any elevation angle using a mapping function as follows (IERS, 2010):

$$T = T_{Z,d} M_d + T_{z,w} M_w + \left[G_N \cos(\alpha) + G_E \sin(\alpha) \right] M_g$$

$$M_g = \frac{1}{\sin(E)\tan(E) + 0.0032}$$

Where,

T the total zenith tropospheric delay

$T_{z,d}$ the zenith dry component of total zenith tropospheric delay

$T_{z,w}$ the zenith wet component of total zenith tropospheric delay

M_d the dry mapping function

M_w the wet mapping function

G_N, G_E are the northern and eastern horizontal delay gradients, respectively

M_g the tropospheric gradient mapping function

α, E the satellite azimuth and elevation angle, respectively

Different models are available to compute the zenith tropospheric delay (dry and wet components). Tropospheric models include Saastamoinen model, Davis et al. model, Baby et al. model, Hopfield model, NOAA tropospheric model (NOAATrop). Mapping functions, on the other hand, include Chao mapping function, Davis mapping function, Herring mapping function (MTT), Niell mapping function (NMF), and Vienna mapping function (VMF1). The following provides the description of the tropospheric models used in the thesis (Hopfield and NOAATrop) along with the applied mapping functions (Niell and VMF1). For more details about other tropospheric models and mapping functions, refer to (Hofmann-Wellenhof *et al.*, 2008) and (Leick, 2004).

3.6.1 Tropospheric Models

3.6.1.1 Hopfield Model

Hopfield developed a tropospheric model using real global data (Hopfield, 1969). The Hopfield model applies a single layer polytropic model atmosphere extending from the Earth's surface to altitudes of about 11 kms for the wet layer and to an altitude of about 40 km for the dry layer (Witchayangkoon, 2000). Hopfield model depends on

temperature, pressure, and humidity. The models for zenith wet and dry troposphere components can be summarized as follows (Hofmann-Wellenhof *et al.*, 2008):

$$N_d^{Trop} = N_{d,0}^{Trop}\left[\frac{H_d - h}{H_d}\right]^{\mu} \tag{2.3}$$

$$N_w^{Trop} = N_{w,0}^{Trop}\left[\frac{H_w - h}{H_w}\right]^{\mu} \tag{2.4}$$

where,

$\mu = 4$	empirically determined power of the height ratio,
$H_d = 40136 + 148.72(T - 273.16)$	a polytropic thickness for the dry part (m) as a function of temperature (T) in kelvin,
$H_w = 11000$	a polytropic thickness for the wet part (m),
$N_{d,0}^{Trop} = K_1 \frac{P_0}{T_0}$	dry tropospheric refractivity for the station at the Earth's surface as a function of pressure (millibars) and temperature (Kelvin),
$N_{w,0}^{Trop} = K_2 \frac{e_0}{T_0} + K_3 \frac{e_0}{T_0^2}$	wet tropospheric refractivity for the station at the Earth's surface as a function of water vapour, pressure, and temperature

The tropospheric zenith delay can then be computed as:

$$T^z = \frac{10^{-6}}{5}\left[N_{d,0}^{Trop} H_d + N_{w,0}^{Trop} H_w\right] \tag{2.5}$$

Typically, the values of the dry and wet polytropic thickness, H_d and H_w, are in the range from 40-45 km and 10-13 km, respectively (Hofmann-Wellenhof *et al.*, 2008). The computed tropospheric zenith delay computed using Equation 3.3 can be employed along with the tropospheric mapping function to obtain the tropospheric delay at a specific satellite elevation angle.

3.6.1.2 NOAA Tropospheric Model

The US National Oceanic and Atmospheric Administration (NOAA) tropospheric corrections model has been developed by the NOAA Forecast Systems Lab (FSL). This model is superior to other models because it is based on numerical weather prediction (NWP) models, where surface- and space-based meteorological measurements and others are combined into the model (Ahn *et al.*, 2006). The NOAA model estimates both the zenith hydrostatic (dry) tropospheric delay (ZHD) and the zenith tropospheric wet delay (ZWD) every hour.

The NOAA model covers parts of North America. The FSL of NOAA produces 20 km grids that include the ZWD and the altimeter setting. Hourly grid files are generated and stored in an FTP server and available for public use free of charge. The FSL of NOAA has also developed a software package that computes and predicts values of hydrostatic, wet, and total zenith tropospheric delay. The software inputs are the station's position (latitude, longitude, and ellipsoidal height) and the time. The software uses the station's latitude and longitude to interpolate between the NOAA tropospheric grids to compute

the ZWD and the altimeter setting. A built in geoid model is used to compute the orthometric height which is used along with the altimeter setting to compute the total pressure. The total pressure is then used to compute the ZHD. The total tropospheric delay is the summation of both ZWD and ZHD. For more details about NOATrop mathematical models, refer to (Ibrahim and El-Rabbany, 2008).

3.6.2 Tropospheric Mapping Functions

3.6.2.1 Niell Mapping Function (NMF)

Niell (1996) introduced his mapping function (NMF) based on temporal changes and geographic location rather than on surface meteorological parameters. NMF was derived from temperature and relative humidity profiles, which are, in some sense, averages over broadly varying geographical regions. NMF is different for wet and dry tropospheric components. The wet mapping function is shown in Equation 3.4 (Leick, 2004).

$$M_w = \frac{1+\dfrac{a}{1+\dfrac{b}{1+c}}}{\sin(E)+\dfrac{a}{\sin(E)+\dfrac{b}{\sin(E)+c}}} \tag{2.6}$$

where,

E	elevation angle,
$a, b,$ and c	coefficients depend on station latitude

The dry mapping function, on the other hand, is more complex compared to the wet mapping function (Leick, 2004). It includes a height correction as shown in Equation 3.5. Table 3.3 shows the wet and dry mapping functions' coefficients (Leick, 2004).

$$M_h = \frac{1+\dfrac{a}{1+\dfrac{b}{1+c}}}{\sin(E)+\dfrac{a}{\sin(E)+\dfrac{b}{\sin(E)+c}}} + h \times \left[\frac{1}{\sin(E)} - \frac{1+\dfrac{a_h}{1+\dfrac{b_h}{1+c_h}}}{\sin(E)+\dfrac{a_h}{\sin(E)+\dfrac{a_h}{\sin(E)+\dfrac{b_h}{\sin(E)+c_h}}}} \right] \tag{2.7}$$

where,

$$a_h(\phi, DOY) = \tilde{a}(\phi) - a_p(\phi)\cos\left(2\pi \frac{DOY - DOY_0}{365.25}\right)$$

$$b_h(\phi, DOY) = \tilde{b}(\phi) - b_p(\phi)\cos\left(2\pi \frac{DOY - DOY_0}{365.25}\right)$$

$$c_h(\phi, DOY) = \tilde{c}(\phi) - c_p(\phi)\cos\left(2\pi \frac{DOY - DOY_0}{365.25}\right)$$

$a, b,$ and c	coefficients dependent on station latitude
$\tilde{a}, \tilde{b},$ and $\tilde{c}$	coefficients dependent on station latitude
$a_h, b_h,$ and c_h	coefficients dependent on station latitude

DOY	day of the year
DOY_0	Constant, equal to 28 or 211 for stations at the north and south of the equator, respectively
h	Station height

Table 3.3: Wet and Dry Mapping Functions Coefficients (Leick, 2004)

Coefficient	Latitude				
	15°	30°	45°	60°	75°
$\tilde{a} \times 10^3$	1.2769934	1.2683230	1.2465397	1.2196049	1.2045996
$\tilde{b} \times 10^3$	2.9153695	2.9152299	2.9288445	2.9022565	2.9024912
$\tilde{c} \times 10^3$	62.610505	62.837393	63.721774	63.824265	64.258455
$a_p \times 10^3$	0	1.2709626	2.6523662	3.4000452	4.1202191
$b_p \times 10^5$	0	2.1414979	3.0160779	7.2562722	11.723375
$c_p \times 10^5$	0	9.0128400	4.3497037	84.795348	170.37206
$a \times 10^4$	5.8021897	5.6794847	5.8118019	5.9727542	6.1641693
$b \times 10^3$	1.4275268	1.5138625	1.4572752	1.5007428	1.7599082
$c \times 10^2$	4.3472961	4.6729510	4.3908931	4.4626982	5.4736038

3.6.2.2 Vienna Mapping Function (VMF)

The hydrostatic and wet Vienna mapping functions are given as (Boehm and Schuh, 2004):

$$M_h = \frac{1 + \dfrac{a_h}{1 + \dfrac{b_h}{1 + c_h}}}{\sin(E) + \dfrac{a_h}{\sin(E) + \dfrac{b_h}{\sin(E) + c_h}}} \tag{2.8}$$

$$M_w = \frac{1 + \dfrac{a_w}{1 + \dfrac{b_w}{1 + c_w}}}{\sin(E) + \dfrac{a_w}{\sin(E) + \dfrac{b_w}{\sin(E) + c_w}}} \tag{2.9}$$

Where,

$a_h, b_h,$ and c_h	hydrostatic mapping function coefficients
$a_w, b_w,$ and c_w	wet mapping function coefficients

The more significant improvement in VMF over NMF is that the coefficients a_h and a_w are fitted to raytracing with the Numerical Weather Model (NWM) of the European Centre for Medium-Range Weather Forecast (ECMWF) in six-hour intervals. The coefficients $b_h, b_w, c_h,$ and c_w, on the other hand, are obtained through empirical

representations (Kouba, 2007). An updated version of the VMF, with improved empirical representation of the coefficients b_h, b_w, c_h, and c_w is known as VMF1. The hydrostatic and wet coefficients b and c are given as:

$$b_h = 0.002905$$
$$c_h = 0.0634 + 0.0014\cos(2\phi)$$
$$b_w = 0.00146$$
$$c_w = 0.04391$$

VMF1 data are generated and available from the ECMWF NWM with (2.0° × 2.5°) grid. VMF1 grids include hydrostatic and wet mapping functions coefficients as well as the hydrostatic and wet Zenith Path Delay (ZPD). Four files are produced per day at 0, 6, 12, and 18h UT. ECMWF has produced hydrostatic and wet mapping functions coefficients for most IGS stations since 2004 (Kouba, 2007). Each file contains a time series of records, containing the following information: station name, modified Julian date, hydrostatic coefficient (a_h), wet coefficient (a_w), hydrostatic zenith delay in metre, wet zenith delay in metre, mean temperature in Kelvin, pressure at the station in hPa, temperature at the station in degree Celsius, water vapor pressure at the station in hPa, and the approximate orthometric height in metre.

3.7 Satellite Geometry

Satellite geometry represents the geometric locations of GPS satellites as seen by the user. Good satellite geometry is obtained when the tracked satellites are spread out in the sky (El-Rabbany, 2006).

A dilution of Precision (DOP) factor can be used to measure satellite geometry instantaneously (Hofmann-Wellenhof *et al.*, 2008). Lower DOP values result in more precise positioning, and vice versa. The effect of satellite geometry on the three-dimensional user's position (latitude, longitude, and height) is known as Position Dilution of Precision (PDOP). PDOP can be broken into two components: HDOP which represents the geometry effect on the horizontal component of the computed position, and VDOP which represents the effect on the vertical component. Most GPS software packages have a mission planning tool by which the geometry of satellites can be predicted using the user's approximate location and a recent almanac file. Generally, DOP can be computed from the inverse of the normal equation matrix as follows (Hofmann-Wellenhof *et al.*, 2008):

$$C_X = \left(A^T P_\ell A\right)^{-1} = \begin{bmatrix} c_{xx} & c_{xy} & c_{xz} & c_{xt} \\ c_{yx} & c_{yy} & c_{yz} & c_{yt} \\ c_{zx} & c_{zy} & c_{zz} & c_{zt} \\ c_{tx} & c_{ty} & c_{tz} & c_{tt} \end{bmatrix} \tag{2.10}$$

$$GDOP = \sqrt{c_{xx} + c_{yy} + c_{zz} + c_{tt}} \tag{2.11}$$

$$PDOP = \sqrt{c_{xx} + c_{yy} + c_{zz}} \tag{2.12}$$

where A is the design matrix which contains the partial derivatives of the observation equations with respect to the unknown parameters, and P_ℓ is the observations weight matrix. To calculate the HDOP and VDOP, the cofactor matrix C_X must be transformed to the local cofactor matrix C_x using the law of covariance propagation. Disregarding the time component of C_X and considering only the geometrical components, the local cofactor matrix will be as follows:

$$C_x = RC_X R^T = \begin{bmatrix} c_{nn} & c_{ne} & c_{nu} \\ c_{en} & c_{ee} & c_{eu} \\ c_{un} & c_{ue} & c_{uu} \end{bmatrix} \tag{2.13}$$

where the rotation matrix R^T = [n e u] contains the axes of the local coordinate system. The PDOP value computed from the local system is identical to the value computed from the global system because of the matrix trace is invariant with respect to rotation. HDOP and VDOP can be computed as follows:

$$HDOP = \sqrt{c_{nn} + c_{ee}} \tag{2.14}$$

$$VDOP = \sqrt{c_{uu}} \tag{2.15}$$

3.8 Sagnac Effect

Because of the rotation of the Earth during the GPS signal propagation, a relativistic error is introduced, known as the sagnac effect, when the satellite coordinates are computed in the ECEF coordinate system (Kaplan and Christopher, 2006). During the GPS signal propagation time, the GPS receiver clock on the Earth's surface experiences a finite rotation with respect to an Earth-Centered Inertial system (ECI) coordinate system. In general, if the user experiences rotation away from the GPS satellite, the propagation time will increase, and vice versa. The correction for the sagnac effect can be computed as follows:

$$\Delta t_{Sagnac} = -\frac{\vec{r}_r^{\,s} \bullet \vec{v}_r^{\,s}}{c^2} \tag{2.16}$$

where,

$\vec{r}_r^{\,s}$	the instantaneous position vector from receiver to satellite
$\vec{v}_r^{\,s}$	the instantaneous velocity vector from receiver to satellite
c	speed of light
$\bullet$	dot product

3.9 Relativity Effect

GPS positioning is based on measuring the time difference between transmission and reception times. However, the measured time is affected by two factors; satellite motion and the Earth's gravity field. The satellite motion forces the satellite's clock to run slower. Because of the near circular orbit of the GPS satellite, however, the effect of satellite motion is periodic and can be modeled using Equation 3.17 (ARINC Engineering Services, 2010). The Earth's gravity field, on the other hand, causes curvature of the satellite signal and a speeding of the satellite clock. Therefore, a propagation correction should be applied to the measured ranges. The range correction can be expressed in Equation 3.18 (Hofmann-Wellenhof *et al.*, 2008).

$$\Delta t_{relativity} = -\frac{2\vec{r}^{s} \bullet \vec{v}^{s}}{c^{2}} \tag{2.17}$$

$$\Delta t_{gravity} = \frac{2GM_{E}}{c^{2}} \ln\left(\frac{r^{s} + r^{r} + r_{r}^{s}}{r^{s} + r^{r} - r_{r}^{s}}\right) \tag{2.18}$$

where,

$\vec{r}^{s}$	the instantaneous position vector of the satellite
$\vec{v}^{s}$	the instantaneous velocity vector of the receiver
c	speed of light
G	gravitational constant
M_{E}	mass of the Earth

r^s	distance between the Earth center and the satellite
r^r	distance between the Earth center and the receiver
r_r^s	distance between the receiver and the satellite

3.10 Phase Wind up

GPS satellites transmit right circularly polarized (RCP) signals. Therefore, the measured carrier-phase depends on the orientation of the satellite and receiver antennas. Any rotation of either the satellite or the receiver antennas will be interpreted as a change in the line of sight distance. Therefore, the relative rotation of the two antennas must be accounted for using phase wind up corrections when using GPS carrier-phase observations. The phase wind up error can reach one phase cycle (Kouba, 2009). Phase wind up usually exists even if the receiver antenna is fixed in a specific direction. The satellite antenna experiences slow rotation due to the continuous reorientation of its solar panels toward the Sun. Satellite antenna also experiences up to one revolution within half an hour during eclipsing seasons (Kouba, 2009). The phase wind up correction can be modelled as follows (Leick, 2004; Wu *et al.*, 1993):

$$d = x - k\left(k \bullet x\right) - k \times y \tag{2.19}$$

$$\bar{d} = \bar{x} - k\left(k \bullet \bar{x}\right) + k \times \bar{y} \tag{2.20}$$

$$\delta\phi = \sin\left(k \bullet \left(\bar{d} \times d\right)\right)\cos^{-1}\left(\frac{d \bullet \bar{d}}{\|d\|\|\bar{d}\|}\right) \tag{2.21}$$

where,

k	the instantaneous satellite to receiver unit vector
x, y, z	the instantaneous satellite body unit vector
$\bar{x}, \bar{y}, \bar{z}$	the receiver local unit vector
$\lVert \bar{d} \rVert$	the magnitude of the vector
$\delta\phi$	the phase wind up correction
$\bullet$	the dot product

3.11 Initial Phase Bias

Carrier-phase measurements can be expressed as the sum of the total number of full carrier cycles, plus fractional cycles at the receiver and the satellite (El-Rabbany, 2006). Because the carrier waves are just pure sinusoidal waves, the GPS receiver has no way to differentiate between one cycle from another. Therefore, the total number of cycles remains unknown but constant under the condition that no cycle-slip occurs. However, the receiver can measure a fraction of a cycle with accuracy less than 2 mm (El-Rabbany, 2006)

Initial phase bias is a fraction of a cycle that is introduced by the receiver and the satellite. It varies from satellite to satellite and from receiver to receiver, i.e., it is hardware dependent. The receiver initial phase bias is constant since the receiver is turned on. Satellite rise/fall does not affect the initial phase bias stability. Receiver restarts, and full loss of lock, on the other hand, changes the receiver initial phase bias

(Wang and Gao, 2007). The receiver initial phase bias can be cancelled out by differencing the observations between satellites. Satellite initial phase bias can be cancelled out by differencing observations between receivers. Both receiver and satellite initial phase biases can be cancelled out in double-difference technique.

3.12 Antenna Phase Centre Offsets

3.12.1 GPS Receiver Antenna Phase Center Offsets

The GPS antenna receives the incoming satellite signal and then converts its energy into an electric current, which can be handled by the GPS receiver (El-Rabbany, 2006). The point at which the GPS signal is received is called the antenna phase center. Antenna phase center cannot be accessed by the GPS user, i.e., direct measurements by a tape. Therefore, a geometrical point is defined as the intersection of the vertical antenna axis of symmetry with the bottom of antenna. This point is known as the antenna reference point (ARP).

The electrical antenna phase center, however, varies according to satellite elevation angle, azimuth, signal frequency, and intensity of the satellite signal. That means each satellite signal has its own electrical antenna phase center. Therefore, antenna calibration should be performed to determine the mean position of the electrical antenna phase center. The difference between the mean electrical antenna phase center and the ARP is known as the antenna phase center offset (PCO).

The antenna PCO is frequency-dependent and its three-dimensional value in is usually given for each frequency. The difference between the antenna phase center of each measurement and the mean electrical antenna phase center is known as the antenna phase center variation (PCV). The total antenna phase center correction for an individual phase measurement is the summation of the PCO and the azimuth- and elevation-dependent PCV (Hofmann-Wellenhof *et al.*, 2008).

3.12.2 GPS Satellite Antenna Phase Center Offsets

Typically, GPS measurements are measured from the satellite antenna phase center to the receiver antenna phase center. Unlike the broadcast ephemerides, the force models used for satellite orbit modelling refer to the satellite center of mass. That means that antenna phase center correction should be considered when using the IGS precise orbit and clock corrections. In general, neglecting the satellite antenna phase center affects the station height (Zhu *et al.*, 2002). The phase centers for most satellites are offset in the body *Z*-coordinate direction (which is the direction of a vector passing through the satellite center of mass and the center of the Earth) and for some satellites also in the body *X*- coordinate direction, which is the direction of the vector joining the Sun and the satellite center of mass (Kouba, 2009). Table (3.4) shows the satellites antenna phase center offsets taken into account by the IGS during the precise orbit and clock correction estimation process in GPSW 1648 (August 8, 2011) (IGS, 2011).

Table 3.4: Satellite antenna phase center offset (GPSW 1648) (IGS, 2011)

PRN	Block	Δ X (m)	Δ Y (m)	Δ Z (m)	Valid From		
					yy	mm	dd
G01*	IIF	0.394	0.00	1.650	2011	07	16
G02	IIR-B	0.00	0.00	0.7786	2004	11	06
G03	IIA	0.279	0.00	2.7926	1996	03	28
G04	IIA	0.279	0.00	2.420	1993	10	26
G05	IIR-M	0.00	0.00	0.8226	2009	08	17
G06	IIA	0.279	0.00	2.8786	1994	03	10
G07	IIR-M	0.00	0.00	0.8529	2008	03	15
G08	IIA	0.279	0.00	2.5781	1997	11	06
G09	IIA	0.279	0.00	2.4614	1993	06	26
G10	IIA	0.279	0.00	2.5465	1996	07	16
G11	IIR-A	0.00	0.00	1.1413	1999	10	07
G12	IIR-M	0.00	0.00	0.8408	2006	11	17
G13	IIR-A	0.00	0.00	1.3895	1997	07	23
G14	IIR-A	0.00	0.00	1.3454	2000	11	10
G15	IIR-M	0.00	0.00	0.6811	2007	10	17
G16	IIR-A	0.00	0.00	1.5064	2003	01	29
G17	IIR-M	0.00	0.00	0.8271	2005	09	26
G18	IIR-A	0.00	0.00	1.2909	2001	01	30
G19	IIR-B	0.00	0.00	0.8496	2004	03	20
G20	IIR-A	0.00	0.00	1.3436	2000	05	11
G21	IIR-A	0.00	0.00	1.4054	2003	03	31
G22	IIR-B	0.00	0.00	0.9058	2003	12	21
G23	IIR-B	0.00	0.00	0.8082	2004	06	23
G24	IIA	0.279	0.00	2.6038	1991	07	04
G25	IIF	0.394	0.00	1.6632	2010	05	28
G26	IIA	0.279	0.00	2.4594	1992	07	07
G27	IIA	0.279	0.00	2.6334	1992	09	09
G28	IIR-A	0.00	0.00	1.0428	2000	07	16
G29	IIR-M	0.00	0.00	0.8571	2007	12	20
G30	IIA	0.279	0.00	2.622	2011	08	05
G31	IIR-M	0.00	0.00	0.9714	2006	09	25
G32	IIA	0.279	0.00	2.7772	2006	12	02

*Preliminary values

The correction for the satellite antenna phase center can be computed as follows (Leick, 2004):

$$X_{phase\,center} = X_{center\,of\;mass} + \begin{bmatrix} x & y & z \end{bmatrix}^{-1} X \tag{2.22}$$

where,

x, y, z	the instantaneous satellite body unit vector
X	$\begin{bmatrix} x_{offset} & y_{offset} & z_{offset} \end{bmatrix}^T$ is the offset in the satellite fixed coordinate system

3.13 Solid Earth Tides

The Earth is not a totally solid body; it is affected by the gravitational forces imposed by the Sun and the Moon. Solid Earth tides cause deformation of the Earth's body of several decimeters in height (Seeber, 2003). The periodic vertical and horizontal site displacement caused by tides are represented by spherical harmonics of degree and order (n, m) characterized by the Love number h_{nm} and the Shida number l_{nm}. Solid Earth tide effect can reach 30 cm in station height, whereas it can reach only 5 cm in the horizontal direction (Kouba, 2009). The displacement caused by the solid Earth tide has a permanent component, which can reach 12 cm in mid-latitudes, and a periodic component, which is characterized with diurnal and semi diurnal trends (Kouba, 2009). The solid Earth tide effect $\Delta\vec{r}^T = \begin{bmatrix} \Delta x & \Delta y & \Delta z \end{bmatrix}$ can be modeled as:

$$\Delta\vec{r} = \sum_{j=2}^{3} \frac{GM_j}{GM} \frac{r^4}{R_j^3} \left\{ \left[3l_2 \left(\hat{R}_j \bullet \hat{r} \right) \right] \hat{R}_j + \left[3\left(\frac{h_2}{2} - l_2 \right) \left(\hat{R}_j \bullet \hat{r} \right)^2 - \frac{h_2}{2} \right] \hat{r} \right\} +$$

$$\left[-0.025 \sin\phi \cos\phi \sin\left(\theta_g + \lambda \right) \right] \bullet \hat{r} \qquad (2.23)$$

where,

GM	the gravitational parameter of the Earth
GM_j	the Gravitational parameter of the Moon $(j = 2)$ and the Sun $(j = 3)$
R	geocentric state vector of the station
R_j	geocentric state vectors of the Moon $(j = 2)$ and the Sun $(j = 3)$
$\hat{r}$	geocentric state unit vectors of the station
$\hat{R}_j$	geocentric state unit vectors of the Moon $(j = 2)$ and the Sun $(j = 3)$
l_2	nominal second degree Love number (0.609)
h_2	nominal Shida dimensionless number (0.085)
ϕ	Site latitude
λ	Site longitude
θ_g	Greenwich mean sidereal time

3.14 Ocean Tide loading

The ocean tide loading effect is similar to the solid Earth tide effect. The Moon and the Sun cause diurnal and semi diurnal changes in the sea level causing a load of the ocean tides on the underlying crust. The effect of the ocean tide loading is almost an order of magnitude smaller than that due to the solid Earth tide (it can reach 5 cm in the vertical and 2 cm in the horizontal directions, respectively). However, ocean tide loading does not have a permanent part. Unless the ocean loading effect is accounted for, it will be mapped into tropospheric ZWD and the station clock solutions. The ocean loading effect can be modelled as follows (IERS, 2010):

$$\Delta c = \sum_{k=1}^{11} f_k A_{ck} \cos\left(\chi_k(t) + u_k - \phi_{ck}\right) \tag{2.24}$$

where,

Δc	displacement due to ocean tide loading
k	represents the 11 tidal waves known as M_2, S_2, N_2, K_2, K_1, O_1, P_1, Q_1, M_f, M_m, and S_{sa}
f_k	depends on the longitude of lunar node ($f_k = 1$ for precision 1-3 mm)
u_k	depends on the longitude of lunar node ($u_k = 0$ for precision 1-3 mm)
$\chi_k(t)$	astronomical arguments at time t
A_{ck}	site-dependent amplitude
ϕ_{ck}	site-dependent phases

3.15 Multipath

Multipath is the phenomenon by which the signal reaches the receiver via more than one path after being reflected or diffracted from various objects near the receiver. Multipath is a major source of error in GPS positioning (Leick, 2004) and it affects code severely compared to carrier phase observations.

Multipath is mainly caused by reflecting surfaces near the receiver, but a secondary cause for multipath can be attributed to reflections at the satellite, which is called satellite multipath (Hofmann-Wellenhof *et al.*, 2008). Receiver multipath is more severe and defined as the signal entering the antenna from different paths. These paths can be the direct line-of-sight signal and the reflected signals from objects surrounding the receiver antenna (El-Rabbany, 2006). As multipath is localized and environmentally dependent, modeling multipath is a complicated task, and the effect of multipath cannot be removed by differential positioning. The path traveled by the reflected signal is always longer than the direct path.

Various techniques and methodologies have been implemented to mitigate the effect of multipath, including careful site selection, using special antenna types (such as choke-ring), and using modern GPS receivers that employ mitigation algorithms at the receiver signal processing level. The Multipath Elimination Delay Lock Loop (MEDLL) is an example of a mitigation algorithm. However, antenna and receiver mitigation techniques are less efficient for short delay multipath signals introduced by nearby reflectors, located within 30 metres of the GPS antenna (Zhong et al., 2007).

3.16 Hardware Delays

Hardware delay refers to time delays that occur during transmission of the GPS signal by the satellite, and during reception of the signal by the receiver. Hardware delay errors are classified as either satellite hardware delay or as receiver hardware delay.

Satellite hardware delay is defined as the time delay that occurs between the signal generation inside the satellite signal generator and the signal transmission by the satellite antenna (El-Rabbany, 2006). Receiver hardware delay is defined as the delay that occurs in the GPS receiver as the signal passes through the receiver-antenna, the analog hardware, and the digital processing to the point where pseudorange and carrier phase measurements are physically made within the digital receiver channel (Kaplan and Christopher, 2006).

Hardware delays are different from observable to observable. P1 and P2 satellite differential hardware delays can be cancelled out by forming the ionospheric-free linear combination observable using measurements on both frequencies and using the IGS satellite clock corrections. The errors can also be eliminated by differencing the observations between two stations and two satellites (double-difference modes). Single-frequency users of C/A code observations can, however, only mitigate hardware delay errors by applying differential code bias corrections (C1-P1) produced by IGS (El-Rabbany, 2006).

4. PPP MATHEMATICAL AND STOCHASTIC MODELS

This chapter presents the functional (mathematical) and stochastic models used in precise point positioning. It starts with a detailed description of GPS observation equations. A comprehensive study of modelling of second-order ionospheric delay is also introduced. Un-differenced and between-satellite single-difference mathematical and stochastic models are also covered. Finally, a brief description of the least-square adjustment procedure used in this thesis is outlined.

4.1 GPS Observation Equations

The mathematical models of un-differenced GPS pseudorange and carrier-phase measurements can be found in Hofmann-Wellenhof et. al. (2008) and Leick (2004). Considering the second-order ionospheric delay (Bassiri and Hajj, 1993) and satellite and receiver hardware delays, the mathematical models of un-differenced GPS pseudorange and carrier-phase measurements can be written as:

$$P_1 = \rho + c(dt^r - dt^s) + T + \frac{q}{f_1^2} + \frac{s}{f_1^3} + c(d_{P1}^r - d_{P1}^s) + \varepsilon_{P1} \tag{4.1}$$

$$P_2 = \rho + c(dt^r - dt^s) + T + \frac{q}{f_2^2} + \frac{s}{f_2^3} + c(d_{P2}^r - d_{P2}^s) + \varepsilon_{P2} \tag{4.2}$$

$$\Phi_1 = \rho + c(dt^r - dt^s) + T - \frac{q}{f_1^2} - \frac{s}{2f_1^3} + c(\delta_{\Phi1}^r - \delta_{\Phi1}^s) + \lambda_1\left[N_1 + \phi_{\Phi1}^r(t_0) - \phi_{\Phi1}^s(t_0)\right] + \varepsilon_{\Phi1} \tag{4.3}$$

$$\Phi_2 = \rho + c(dt^r - dt^s) + T - \frac{q}{f_2^2} - \frac{s}{2f_2^3} + c(\delta_{\Phi 2}^r - \delta_{\Phi 2}^s) +$$

$$\lambda_2 \left[N_2 + \phi_{\Phi 2}^r(t_0) - \phi_{\Phi 2}^s(t_0) \right] + \varepsilon_{\Phi 2} \tag{4.4}$$

where,

P_1, P_2	pseudorange measurements on L1 and L2, respectively
Φ_1, Φ_2	carrier-phase measurements on L1 and L2, respectively, scaled to distance (m)
f_1, f_2	L1 and L2 frequencies, respectively, ($L_1 : f_1 = 1.57542\ GHz\ ; L_2 : f_2 = 1.22760\ GHz$)
dt^r, dt^s	receiver and satellite clock errors, respectively
$\varepsilon_{P1}, \varepsilon_{P2}, \varepsilon_{\Phi 1}, \varepsilon_{\Phi 2}$	the un-modeled error sources including multipath effect
λ_1, λ_2	the wavelengths for L1 and L2 carrier frequencies, respectively
N_1, N_2	integer ambiguity parameters for L1 and L2, respectively
δ_*^r, δ_*^s	frequency-dependent carrier-phase hardware delay for receiver and satellite, respectively
d_*^r, d_*^s	code hardware delay for receiver and satellite, respectively
c	the speed of light in vacuum
T	tropospheric delay
ρ	the true geometric range from receiver antenna phase-centre at reception time to satellite antenna phase-centre at transmission time

q the integrated total electron content along the line of sight

s the second-order ionospheric effect

Defining $\xi_1 = \left(\frac{f_1^{\,2}}{f_1^{\,2} - f_2^{\,2}} \right)$ and $\xi_2 = \left(\frac{f_2^{\,2}}{f_1^{\,2} - f_2^{\,2}} \right)$, the well-known first-order ionosphere free linear combination can be formed to eliminate the first-order ionospheric delay as,

$$P_3 = \xi_1 P_1 - \xi_2 P_2, \;\; \Phi_3 = \xi_1 \Phi_1 - \xi_2 \Phi_2$$

$$P_3 = \rho + c(dt^r - dt^s) + T + \frac{s}{f_1 f_2 (f_1 + f_2)} + b_{P3}^r - b_{P3}^s + \varepsilon_{P3} \tag{4.5}$$

$$\Phi_3 = \rho + c(dt^r - dt^s) + T - \frac{s}{2 f_1 f_2 (f_1 + f_2)} + b_{\Phi 3}^r - b_{\Phi 3}^s + \lambda_3 N_3 + \varepsilon_{\Phi 3} \tag{4.6}$$

where;

$$b_{P3}^r = c\left(\xi_1 d_{P1}^r - \xi_2 d_{P2}^r \right)$$

$$b_{P3}^s = c\left(\xi_1 d_{P1}^s - \xi_2 d_{P2}^s \right)$$

$$b_{\Phi 3}^r = \left[c\left(\xi_1 \delta_{\Phi 1}^r - \xi_2 \delta_{\Phi 2}^r \right) + \left(\xi_1 \lambda_1 \phi_{\Phi 1}^r(t_0) - \xi_2 \lambda_2 \phi_{\Phi 2}^r(t_0) \right) \right]$$

$$b_{\Phi 3}^s = \left[c\left(\xi_1 \delta_{\Phi 1}^s - \xi_2 \delta_{\Phi 2}^s \right) + \left(\xi_1 \lambda_1 \phi_{\Phi 1}^s(t_0) - \xi_2 \lambda_2 \phi_{\Phi 2}^s(t_0) \right) \right]$$

$$\lambda_3 = \frac{c}{\left(f_1^{\,2} - f_2^{\,2} \right)}, N_3 = \left(f_1 N_1 - f_2 N_2 \right)$$

P_3, Φ_3 the first-order ionosphere-free code and carrier-phase combinations, respectively

$\varepsilon_{P3}, \varepsilon_{\Phi 3}$ the first-order ionosphere-free combination of $\varepsilon_{P1}, \varepsilon_{P2}$ and $\varepsilon_{\Phi 1}, \varepsilon_{\Phi 2}$, respectively

4.2 Modelling of Second-Order Ionospheric Delay

As indicated earlier, the first-order ionospheric delay can be cancelled out using the first-order ionosphere free linear combination. However, this linear combination leaves a few centimetres residual errors pertaining to the higher-order ionospheric delay terms. In this thesis, we restrict ourselves to the second-order ionospheric delay term, which represents the bulk of higher-order ionospheric delay. The second-order ionospheric delay can be expressed as (Hernández-Pajares *et al.*, 2007):

$$s = \frac{eA}{2\pi m_e} B_0 \cos(\theta) \int N_e dl = 7527 * c * B_0 * \cos(\theta) * STEC \tag{4.7}$$

where,

e the electron charge $\left(e = 1.60218 \times 10^{-19} \text{ Coulomb}\right)$

A $A = \dfrac{e^2}{4\pi^2 m_e \varepsilon_0} \approx 80.6\,\text{m}^3/\text{s}^2$

m_e The electron mass $\left(m_e = 9.10939 \times 10^{-31} kg\right)$

ε_0 permittivity of free space $\left(\varepsilon_0 = 8.85419 \times 10^{-12} Farad / m\right)$

B_0 the magnetic field at the ionospheric piece point, Figure 4.1, (Tesla)

N_e the free electron density (m^{-3})

θ	The angle between the magnetic field and the propagation direction
$STEC$	The slant total electron content
c	the speed of light in vacuum

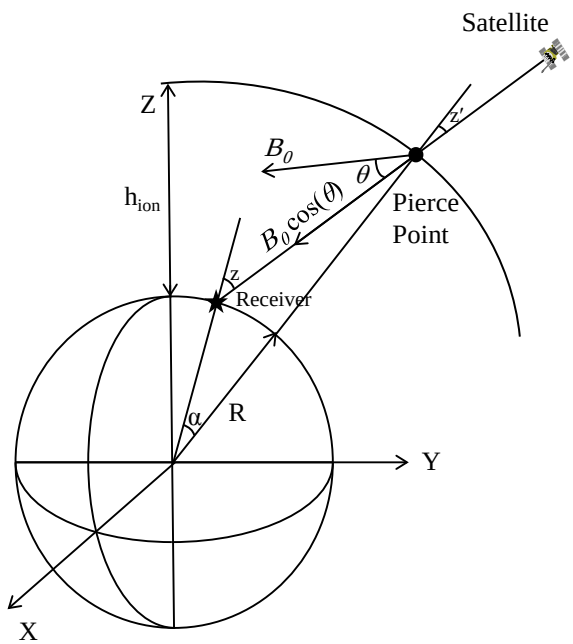

Figure 4.1 Magnetic Field and Propagation Direction

4.2.1 Computation of STEC

Equation 4.7 shows that the second-order ionospheric delay depends on the STEC along the line of sight and the magnetic-field parameters at the ionospheric pierce point (IPP). STEC values may be obtained from global ionospheric models such as the IGS GIM or regional ionospheric models such as the United States total electron content (US-TEC) produced by NOAA.

The IGS GIMs provide the vertical total electron content (VTEC) that has to be converted to STEC using a mapping function. However, STEC computed using the GIMs can introduce up to 50% error at low latitude and low elevations (Hernández-Pajares *et al.*, 2007). The US-TEC grids, on the other hand, include both STEC and VTEC for different locations and directions. Because of the US-TEC accuracy (1 to 3 TEC units), spatial resolution (1°×1°), and temporal resolution (15 minutes), it represents an accurate source of the STEC. For using US-TEC to compute STEC for second-order ionospheric delay computations, please refer to (Elsobeiey and El-Rabbany, 2009).

Alternatively, STEC can be estimated by forming the geometry-free linear combination of GPS pseudorange observables (Equation 4.8). However, this method requires apriori information about satellite and receiver differential code biases (DCB^{S}_{P1-P2} and DCB^{r}_{P1-P2}, respectively). Values of satellite and receiver differential code biases may be obtained from the IGS or estimated by processing the GPS data from a well-distributed

global network of GPS stations. Satellite and receiver differential code biases are stable over time and previous values may be used (Hernández-Pajares *et al.*, 2007).

$$STEC = \left[(P_2 - P_1) + c(DCB^{r}_{P1-P2} + DCB^{S}_{P1-P2}) \right] \left(\frac{f_2^{\,2}}{f_1^{\,2} - f_2^{\,2}} \right) \left(\frac{f_1^{\,2}}{40.3} \right) \tag{4.8}$$

where,

DCB^{r}_{P1-P2}	the receiver differential hardware delay between P1 and P2 pseudoranges
DCB^{S}_{P1-P2}	the satellite differential hardware delay between P1 and P2 pseudoranges

4.2.2 Geomagnetic Field Model

The geomagnetic field of the Earth can be approximated by a magnetic dipole placed at the Earth's centre and tilted 11.5° with respect to the axis of rotation. The magnetic-field inclination is downwards throughout most of the northern hemisphere and upwards throughout most of the southern hemisphere. A line that passes through the centre of the Earth along the dipole axis intersects the surface of the Earth at two points, referred to as the geomagnetic poles. Unfortunately, a dipole model only accounts for about 90% of the Earth's magnetic field at the surface (Merrill and McElhinny, 1983). After the best-fitting geocentric dipole is removed from the magnetic field at the Earth's surface, the remaining part of the field, about 10%, is referred to as non-dipole field. Both dipole and non-dipole

parts of the Earth's magnetic-field change with time (Merrill and McElhinny, 1983). The dipole approximation is more or less valid up to a few Earth radii; beyond this distance limit, the Earth's magnetic field significantly deviates from the dipole field because of the interaction with the magnetized solar wind (Houghton *et al.*, 1998).

A more realistic model for the Earth's geomagnetic field, which is used in this thesis, is the international geomagnetic reference field (IGRF). The IGRF model is a standard spherical harmonic representation of the Earth's main field. The IGRF is generally revised and updated every five years by the international association of geomagnetism and astronomy (IAGA). The IAGA released the 11th generation of the IGRF in December 2009. The 11th generation of the IGRF represents the latest version of a standard mathematical description of the Earth's main magnetic field that is used widely in studies of the Earth's interior, its crust and its ionosphere and magnetosphere. The IGRF is the product of a collaborative work between magnetic field modellers and the organizations involved in collecting and disseminating magnetic field data from different sources, including geomagnetic measurements from observatories, ships, aircrafts, and satellites (NOAA, 2010).

The relative difference between the dipole and IGRF models ranges from -20% in the east of Asia up to +60% in the so-called south Atlantic anomaly (Hernández-Pajares *et al.*, 2007).

4.3 Un-Differenced PPP Model

Because only the difference between receiver and satellite clock parameters $c(dt^r - dt^s)$ appears in the GPS observation equations, it is only possible to solve for the clock parameters in the relative sense. All clock parameters but one can be estimated, i.e., either a receiver or a satellite clock correction has to be fixed or selected as a reference. The only requirement is that the reference clock must be available for each epoch where the clock values are estimated (Dach *et al.*, 2007). A reference clock should be easily modelled by an offset and a drift. A polynomial is fitted to the combined values of the clock corrections. In this way, the time scale presented by the reference clock is the same for the entire solution.

Hardware delays, on the other hand, are not uniquely separable because of the identical functional behaviour with the associated clock parameters (Collins *et al.*, 2010). So it is usually carried over on to the carrier-phase ambiguity, leading to non-integer ambiguities. Assuming that the second-order ionospheric delay is accounted for, from the previous section, the un-differenced PPP model can be written as:

$$P_3 = \rho + c(dt^r_{P3} - dt^s_{P3}) + T + \varepsilon_{P3} \tag{4.9}$$

$$\Phi_3 = \rho + c(dt^r_{P3} - dt^s_{P3}) + T + \lambda_3 N'_3 + \varepsilon_{\Phi 3} \tag{4.10}$$

where,

$$dt^r_{P3} = dt^r + b^r_{P3}/c = dt^r + \xi_1 d^r_{P1} - \xi_2 d^r_{P2}$$

$$dt^s_{P3} = dt^s + b^s_{P3}/c = dt^s + \xi_1 d^s_{P1} - \xi_2 d^s_{P2}$$

$$N'_3 = (-b^r_{P3} + b^s_{P3} + b^r_{\Phi 3} - b^s_{\Phi 3}) / \lambda_3 + N_3$$

The main problem in Equations (4.9) and (4.10) is that the un-calibrated hardware delays, especially receiver hardware delays, are not constant overtime. As seen in Equation 4.10, the hardware delays are lumped to the carrier-phase ambiguities causing less possibility to apply ambiguity resolution techniques in PPP.

4.4 Between-Satellite Single-Difference (BSSD) Model

Differencing observations between satellites is an efficient method to cancel out the receiver clock error, receiver hardware delays, and non-zero initial phase of the receiver's oscillator. Starting from Equations (4.9) and (4.10), we can get the BSSD combination of two satellites *k* and *l* as:

$$P_3^{kl} = \rho^k - \rho^l + c(dt^l_{P3} - dt^k_{P3}) + T^k - T^l + \Delta\varepsilon_{P3} \tag{4.11}$$

$$L_3^{kl} = \rho^k - \rho^l + c(dt^l_{P3} - dt^k_{P3}) + T^k - T^l + \lambda_3\left(N''^k_3 - N''^l_3\right) + \Delta\varepsilon_{\Phi 3} \tag{4.12}$$

where,

$N''_3 = (b^s_{P3} - b^s_{\Phi 3}) / \lambda_3 + N_3$, in which receiver hardware delay and non-zero initial phase are cancelled out. $\Delta\varepsilon_{P3} = \varepsilon^k_{P3} - \varepsilon^l_{P3}$, and $\Delta\varepsilon_{\Phi 3} = \varepsilon^k_{\Phi 3} - \varepsilon^l_{\Phi 3}$

4.5 Decoupled Clock Model

As shown in Section 4.4, the un-modelled satellite hardware delays and non-zero initial phase are lumped with the carrier-phase ambiguities which destroy its integer properties. The use of the decoupled clock model allows for satellite carrier-phase hardware delay and non-zero initial phase bias to be lumped with the corresponding satellite carrier-phase clock corrections. Starting from Equations (4.5) and (4.6) the un-differenced decoupled clock model can be written as:

$$P_3 = \rho + c(dt^r_{P3} - dt^s_{P3}) + T + \varepsilon_{P3} \tag{4.13}$$

$$\Phi_3 = \rho + c(dt^r_{\Phi 3} - dt^s_{\Phi 3}) + T + \lambda_3 N_3 + \varepsilon_{L3} \tag{4.14}$$

where,

$$dt^r_{\Phi 3} = dt^r + b^r_{\Phi 3}/c = dt^r + \xi_1 \delta^r_{\Phi 1} - \xi_2 \delta^r_{\Phi 2} + \left(\xi_1 \lambda_1 \phi^r_{\Phi 1}(t_0) - \xi_2 \lambda_2 \phi^r_{\Phi 2}(t_0)\right)/c$$

$$dt^s_{\Phi 3} = dt^s + b^s_{\Phi 3}/c = dt^s + \xi_1 \delta^s_{\Phi 1} - \xi_2 \delta^s_{\Phi 2} + \left(\xi_1 \lambda_1 \phi^s_{\Phi 1}(t_0) - \xi_2 \lambda_2 \phi^s_{\Phi 2}(t_0)\right)/c$$

4.5.1 Satellite Decoupled Clock Corrections

Typically, the first-order ionosphere free linear combination of code and carrier-phase (Equations 4.9 and 4.10) is used to estimate the GPS satellite clock corrections. In this case the code will represent the datum for the estimated clock corrections (Collins *et al.*, 2010). According to Collins et al., 2010, using the code as a datum for estimation of the

precise satellite clock corrections is the reason for day boundary clock jumps. The estimated satellite clock corrections, on the other hand, will be affected with the code hardware delay and specific corrections for the differential code bias will be required when using C1 instead of P1 for instance to form the first-order ionosphere free code combination (Dach *et al.*, 2007).

Equations 4.13 and 4.14 can be used separately to estimate two types of satellite clock corrections, namely code and carrier-phase clock corrections. This method is known as the decoupled clock model. In this case, the code clock correction is estimated using the same known method in which one of the receiver clock should be fixed. However, the main issue here is the estimation of the satellite clock corrections from the carrier-phase, Equation 4.14, because of the system singularity. To solve this problem, the minimum constrained least-squares solution should be used by arbitrarily fixing one ambiguity associated with each phase clock, less one, and fix one of the phase clocks as a network datum (Collins *et al.*, 2010).

4.6 BSSD Decoupled Clock (BSSD-DC) Model

Forming BSSD from the un-differenced decoupled clock model will cancel out receiver clock error, receiver hardware delay, and receiver initial phase bias. At the same time, the clock corrections applied already include the satellite hardware delay and satellite non-zero initial phase. Differencing the un-differenced decoupled clock model (Equation 4.13 and 4.14) between satellites leads to the BSSD-DC model as follows:

$$P_3^{kl} = \rho^k - \rho^l + c(dt_{P3}^l - dt_{P3}^k) + T^k - T^l \tag{4.15}$$

$$\Phi_3^{kl} = \rho^k - \rho^l + c(dt_{\Phi 3}^l - dt_{\Phi 3}^k) + T^k - T^l + \lambda_3 \left(N_3^k - N_3^l \right) \tag{4.16}$$

4.7 Stochastic Modelling

The least squares solution of the PPP models is not only based on the functional model, but also based on the stochastic model. The stochastic properties of the observations are reflected in the observations' weight matrix which includes their absolute and relative accuracies with respect to each other. The power of the GPS signal is often used as a measure of its quality. The most common signal power measures that can be used for weighting are the signal-to-noise ratio and carrier-to-noise power density ratio (Ozludemir, 2004).

Satellite elevation angle, on the other hand, is also used to express the precision of the data from each satellite. The relationship between satellite elevation angle and the observations' precision can be modelled by a general sine or cosine functions as seen in Equation (4.17) (Ozludemir, 2004; Dach *et al.*, 2007).

$$\sigma = \frac{1}{\sin(Elevation)} \tag{4.17}$$

A GPS receiver can be calibrated to determine the stochastic properties of the received signals. Classical zero baseline tests are typically used to examine the receiver noise (Nolan *et al.*, 1992). However, the full GPS system noise can be tested using a short

baseline (a few metres apart) test over two consecutive days. In this case, the double-difference residuals of one day would contain the system noise and the multipath effect, if it exists. All other errors would cancel sufficiently. As the multipath effect repeats every sidereal day, differencing the double-difference observables over two consecutive days cancels out the multipath effect and leaves the system noise only (El-Rabbany, 2006). By differencing the double-difference observables over two consecutive days, however, the system noise is doubled and the standard deviation of the system noise should be divided by $\sqrt{2}$ to obtain the standard deviation of the double difference system noise.

Alternatively, the GPS system noise can be examined by differencing the code and the carrier-phase measurements (Elsobeiey and El-Rabbany, 2010). A new observable can be formed by differencing the code and carrier-phase measurements. As the noise level on carrier-phase measurements is approximately 1% of that of the code measurements, the carrier-phase noise and multipath are negligible in comparison with those of code measurements. For example, the P1-code noise level can be determined as follows:

$$P_1 - \Phi_1 = \frac{2q}{f_1^{\,2}} + \frac{3s}{2f_1^{\,3}} c\left(d_{p1}^{r} - \delta_{\Phi 1}^{r} - d_{P1}^{s} + \delta_{\Phi 1}^{s}\right) - \lambda_1\left[N_1 + \phi_{\phi 1}^{r}(t_0) - \phi_{\phi 1}^{s}(t_0)\right] + dm_{C1} + e_{C1} \quad (4.18)$$

Between-receiver single-difference (BRSD) can be formed using Equation (4.18), which cancels out the ionospheric delay sufficiently. The remaining terms include the hardware delay, the ambiguity parameter, the initial phase bias, multipath and the system noise.

The multipath effect is repeatable over two consecutive days and can be cancelled sufficiently by differencing over the two days. The hardware delay is stable over several days, while the ambiguity parameter and initial phase bias are constants for a continuous session of measurements. As such, they can be removed from the model by differencing with respect to the first value of the series. With these operations, only the differenced system noise remains in the model. The differenced measurements are divided into bins depending on the satellite elevation angle, and the best fitting mathematical model for the observation standard deviation is determined (Elsobeiey and El-Rabbany, 2010).

The above mentioned methods are used to determine the observables precision; however, in PPP models, the GPS observations are not used directly. Therefore, error propagation should be applied to determine the precision of the used combined observable. The mathematical correlation in both cases (Un-differenced and BSSD models) are illustrated below:

4.7.1 Traditional (Un-Differenced) Model

Assuming that the measured (or raw) phases are independent or uncorrelated, we can introduce a vector Φ_3 containing the ionosphere-free carrier-phase linear combination. If we assume equal accuracy, the covariance matrix of the ionosphere-free carrier-phase can be written as (Hofmann-Wellenhof *et al.*, 2008):

$$\Sigma_{\Phi 3} = \sigma^2 (\xi_1^2 + \xi_2^2) I$$

$$\Sigma_{\Phi 3} = \left(\frac{f_1^{\,2} + f_2^{\,2}}{f_1^{\,2} - f_2^{\,2}} \right) \sigma^2 I \tag{4.19}$$

Equation (4.19) shows that the ionosphere-free linear combination is not mathematically correlated under the assumption that the raw observations are independent, i.e., not physically correlated.

4.7.2 BSSD Model

Between-satellite single-difference of the ionosphere-free linear combination is mathematically correlated. Considering six satellites $j, k, l, m, n,$ and o at a specific time (t), and taking satellite j as a reference, five between-satellite single-differences can be formed from the ionosphere-free linear combinations as follows:

$$\begin{aligned}
\Phi_3^{jk} &= \Phi_3^{j} - \Phi_3^{k} \\
\Phi_3^{jl} &= \Phi_3^{j} - \Phi_3^{l} \\
\Phi_3^{jm} &= \Phi_3^{j} - L_3^{m} \\
\Phi_3^{jn} &= \Phi_3^{j} - \Phi_3^{n} \\
\Phi_{I\,3}^{jo} &= \Phi_3^{j} - \Phi_3^{o}
\end{aligned}$$

$$\begin{bmatrix} \Phi_3^{jk} \\ \Phi_3^{jl} \\ \Phi_3^{jm} \\ \Phi_3^{jn} \\ \Phi_3^{jo} \end{bmatrix} = \begin{bmatrix} 1 & -1 & 0 & 0 & 0 & 0 \\ 1 & 0 & -1 & 0 & 0 & 0 \\ 1 & 0 & 0 & -1 & 0 & 0 \\ 1 & 0 & 0 & 0 & -1 & 0 \\ 1 & 0 & 0 & 0 & 0 & -1 \end{bmatrix} \begin{bmatrix} \Phi_3^{j} \\ \Phi_3^{k} \\ \Phi_3^{l} \\ \Phi_3^{m} \\ \Phi_3^{n} \\ \Phi_3^{o} \end{bmatrix} \tag{4.20}$$

$$BSSD = \qquad C \qquad IF$$

Applying the covariance propagation law to Equation (4.20) gives

$$\Sigma_{BSSD} = C\,\Sigma_{\Phi 3} C^T = C\left(\frac{f_1^{\,2}+f_2^{\,2}}{f_1^{\,2}-f_2^{\,2}}\right)\sigma^2 I C^T = \left(\frac{f_1^{\,2}+f_2^{\,2}}{f_1^{\,2}-f_2^{\,2}}\right)\sigma^2 \begin{bmatrix} 2 & 1 & 1 & 1 & 1 \\ 1 & 2 & 1 & 1 & 1 \\ 1 & 1 & 2 & 1 & 1 \\ 1 & 1 & 1 & 2 & 1 \\ 1 & 1 & 1 & 1 & 2 \end{bmatrix} \qquad (4.21)$$

This means that BSSD of the ionosphere-free linear combinations are mathematically correlated. Generalizing Equation (4.21) for number of satellites n_s, the relative weight matrix $P(t)$ is obtained from the inverse of the covariance matrix as:

$$P(t) = \Sigma_{BSSD}^{-1} = \left(\frac{f_1^{\,2}-f_2^{\,2}}{f_1^{\,2}+f_2^{\,2}}\right)\frac{1}{n_s\sigma^2} \begin{bmatrix} (n_s-1) & -1 & -1 & -1 & -1 \\ -1 & (n_s-1) & -1 & -1 & -1 \\ -1 & -1 & (n_s-1) & -1 & -1 \\ -1 & -1 & -1 & (n_s-1) & -1 \\ -1 & -1 & -1 & -1 & (n_s-1) \end{bmatrix} \qquad (4.22)$$

We have shown in this section that the observations relative weight matrix in the BSSD mathematical model is not a diagonal matrix. It will be fully populated because of the correlation between the observables. It should be noted that Equation 4.22 is used for one epoch only. For multi-epoch PPP, the observation weight matrix will be a block diagonal matrix. The structure of each sub matrix along the diagonal line will be similar to 4.22, assuming that the same satellites are tracked.

4.8 Least-Squares Estimation Method

The method of least squares is a standard approach widely used to solve overdetermined systems (see e.g. Ghilani, 2011). Least squares method allows for appropriate weighting of all measurements and produces the adjusted quantities precisions from the resultant covariance matrix. The linearization of the GPS observation equations around the a-priori parameter values and observations $\left(X^{0}, \ell\right)$ in matrix format can be written as:

$$A\delta + W - V = 0 \tag{4.23}$$

where,

A	the design matrix which includes the partial derivatives of the observation equations with respect to the unknown parameters X
δ	the vector of corrections to the unknown parameters
W	the misclosure vector $W = f\left(X^{0}, \ell\right)$
V	vector of residuals

The design matrix A is formed by taking the partial derivatives of the observation equations with respect to the unknown parameters. The design matrix will be different based on the PPP model used. The design matrix and the vector of unknowns for different PPP models can be summarized as follows:

Un-Differenced PPP Model

The vector of the unknown parameters of the un-differenced PPP model includes the station coordinates (x, y, z), receiver clock error dt^r, wet component of the tropospheric zenith path delay (zpd_w), and non-integer ambiguities $(N^i, i = 1, n_s)$.

$$X = \left[x, y, z, dt^r_{P3}, zpd_w, N^1, N^2, \ldots N^{n_s} \right]^T_{1\times(n_s+5)}$$

$$A = \begin{bmatrix} \frac{x_0 - X^1}{\rho_0^1} & \frac{y_0 - Y^1}{\rho_0^1} & \frac{z_0 - Z^1}{\rho_0^1} & c\times 1e^{-9} & M_w^1 & 0 & 0 & \cdots & 0 \\ \frac{x_0 - X^1}{\rho_0^1} & \frac{y_0 - Y^1}{\rho_0^1} & \frac{z_0 - Z^1}{\rho_0^1} & c\times 1e^{-9} & M_w^1 & 1 & 0 & \cdots & 0 \\ \frac{x_0 - X^2}{\rho_0^2} & \frac{y_0 - Y^2}{\rho_0^2} & \frac{z_0 - Z^2}{\rho_0^2} & c\times 1e^{-9} & M_w^2 & 0 & 0 & \cdots & 0 \\ \frac{x_0 - X^2}{\rho_0^2} & \frac{y_0 - Y^2}{\rho_0^2} & \frac{z_0 - Z^2}{\rho_0^2} & c\times 1e^{-9} & M_w^2 & 0 & 1 & \cdots & 0 \\ \vdots & & & & & & & \cdots & \vdots \\ \vdots & & & & & & & \cdots & \vdots \\ \frac{x_0 - X^{n_s}}{\rho_0^{n_s}} & \frac{y_0 - Y^{n_s}}{\rho_0^{n_s}} & \frac{z_0 - Z^{n_s}}{\rho_0^{n}} & c\times 1e^{-9} & M_w^{n_s} & 0 & 0 & \cdots & 0 \\ \frac{x_0 - X^{n_s}}{\rho_0^{n_s}} & \frac{y_0 - Y^{n_s}}{\rho_0^{n_s}} & \frac{z_0 - Z^{n_s}}{\rho_0^{n_s}} & c\times 1e^{-9} & M_w^{n_s} & 0 & 0 & \cdots & 1 \end{bmatrix}_{2n_s\times(n_s+5)}$$

Un-Differenced Decoupled Clock PPP Model

Applying the decoupled clock correction to the un-differenced PPP model adds additional unknowns to the vector of the unknown parameters. As indicated in Section 4.5, we have two receiver clock errors. The first clock error exists in the code observation equations while the second clock error exists in the carrier-phase observation equations. In this case

the vector of the unknown parameters includes the station coordinates (x, y, z), code receiver clock error dt^r_{P3}, carrier-phase receiver clock error $dt^r_{\Phi 3}$, wet component of the tropospheric zenith path delay (zpd_w), and non-integer ambiguities $(N^i, i = 1, n_s)$.

$$X = \left[x, y, z, dt^r_{P3}, dt^r_{\Phi 3}, zpd_w, N^1, N^2, \ldots N^{n_s} \right]^T_{1\times(n_s+6)}$$

$$A = \begin{bmatrix} \frac{x_0 - X^1}{\rho_0^1} & \frac{y_0 - Y^1}{\rho_0^1} & \frac{z_0 - Z^1}{\rho_0^1} & c\times 1e^{-9} & 0 & M_w^1 & 0 & 0 & \cdots & 0 \\ \frac{x_0 - X^1}{\rho_0^1} & \frac{y_0 - Y^1}{\rho_0^1} & \frac{z_0 - Z^1}{\rho_0^1} & 0 & c\times 1e^{-9} & M_w^1 & 1 & 0 & \cdots & 0 \\ \frac{x_0 - X^2}{\rho_0^2} & \frac{y_0 - Y^2}{\rho_0^2} & \frac{z_0 - Z^2}{\rho_0^2} & c\times 1e^{-9} & 0 & M_w^2 & 0 & 0 & \cdots & 0 \\ \frac{x_0 - X^2}{\rho_0^2} & \frac{y_0 - Y^2}{\rho_0^2} & \frac{z_0 - Z^2}{\rho_0^2} & 0 & c\times 1e^{-9} & M_w^2 & 0 & 1 & \cdots & 0\times 1e^{-9} \\ \vdots & & & & & & & & \cdots & \vdots \\ \vdots & & & & & & & & \cdots & \vdots \\ \frac{x_0 - X^{n_s}}{\rho_0^{n_s}} & \frac{y_0 - Y^{n_s}}{\rho_0^{n_s}} & \frac{z_0 - Z^{n_s}}{\rho_0^{n_s}} & c\times 1e^{-9} & 0 & M_w^{n_s} & 0 & 0 & \cdots & 0 \\ \frac{x_0 - X^{n_s}}{\rho_0^{n_s}} & \frac{y_0 - Y^{n_s}}{\rho_0^{n_s}} & \frac{z_0 - Z^{n_s}}{\rho_0^{n_s}} & 0 & c\times 1e^{-9} & M_w^{n_s} & 0 & 0 & \cdots & 1 \end{bmatrix}_{2n_s\times(n_s+6)}$$

Between-Satellite Single-Difference (BSSD) Models

Differencing observations between satellites cancels out the receiver clock error. The vector of the unknown parameters includes the station coordinates (x, y, z), wet component of the tropospheric zenith path delay (zpd_w), and non-integer ambiguities

differences between the reference satellite and other satellites in view $\left(N^{ij}, i = \text{the number of the reference satellite}, j = 1, n_s - 1, i \neq j\right)$.

$$X = \left[x, y, z, zpd_w, N^{1,2}, N^{1,3}, \ldots N^{1,n_s-1}\right]^T_{1\times(n_s+3)}$$

$$A = \begin{bmatrix} A_{11} & A_{12} & A_{13} & A_{14} & 0 & 0 & \cdots & 0 \\ A_{21} & A_{22} & A_{23} & A_{24} & 1 & 0 & \cdots & 0 \\ A_{31} & A_{32} & A_{33} & A_{34} & 0 & 0 & \cdots & 0 \\ A_{41} & A_{42} & A_{43} & A_{44} & 0 & 1 & \cdots & 0 \\ \vdots & & & & & & \cdots & \vdots \\ \vdots & & & & & & \cdots & \vdots \\ A_{(2n_s-3),1} & A_{(2n_s-3),2} & A_{(2n_s-3),3} & A_{(2n_s-3),4} & 0 & 0 & \cdots & 0 \\ A_{(2n_s-2),1} & A_{(2n_s-2),2} & A_{(2n_s-2),3} & A_{(2n_s-2),4} & 0 & 0 & \cdots & 1 \end{bmatrix}_{(2n_s-2)\times(n_s+3)}$$

where,

$$A_{11} = A_{21} = \frac{x_0 - X^1}{\rho_0^1} - \frac{x_0 - X^2}{\rho_0^2}, A_{12} = A_{22} = \frac{y_0 - Y^1}{\rho_0^1} - \frac{y_0 - Y^2}{\rho_0^2},$$

$$A_{13} = A_{23} = \frac{z_0 - Z^1}{\rho_0^1} - \frac{z_0 - Z^2}{\rho_0^2}, A_{14} = A_{24} = M_w^1 - M_w^2,$$

$$A_{31} = A_{41} = \frac{x_0 - X^1}{\rho_0^1} - \frac{x_0 - X^3}{\rho_0^3}, A_{32} = A_{42} = \frac{y_0 - Y^1}{\rho_0^1} - \frac{y_0 - Y^3}{\rho_0^3},$$

$$A_{33} = A_{43} = \frac{z_0 - Z^1}{\rho_0^1} - \frac{z_0 - Z^3}{\rho_0^3}, A_{34} = A_{44} = M_w^1 - M_w^3,$$

$$A_{(2n_s-3),1} = A_{(2n_s-2),1} = \frac{x_0 - X^1}{\rho_0^1} - \frac{x_0 - X^{n_s-1}}{\rho_0^{n_s-1}}, A_{(2n_s-3),2} = A_{(2n_s-2),2} = \frac{y_0 - Y^1}{\rho_0^1} - \frac{y_0 - Y^{n_s-1}}{\rho_0^{n_s-1}},$$

$$A_{(2n_s-3),3} = A_{(2n_s-2),3} = \frac{z_0 - Z^1}{\rho_0^1} - \frac{z_0 - Z^{n_s-1}}{\rho_0^{n_s-1}}, A_{(2n_s-3),4} = A_{(2n_s-2),4} = M_w^1 - M_w^{n_s-1}$$

The least-squares solution with a-priori weighted parameter constraints $\left(P_{X^0}\right)$ for the vector δ is given by:

$$\delta = -(P_{X^0} + A^T P_\ell A)^{-1} A^T P_\ell W \tag{4.24}$$

where P_ℓ is the observations weight matrix (Section 4.7).

The estimated parameters and the corresponding a-priori variance-covariance matrix can be written as:

$$X = X^0 + \delta$$

$$C_{\hat{X}} = P_{\hat{X}}^{-1} = \left(P_{X^0} + A^T P_\ell A\right)^{-1} \tag{4.25}$$

The residuals obtained from Equation (4.23) and the parameters correction vector (Equation 4.24) can be used to estimate the weighted square sum of residuals as follows:

$$V^T PV = \delta^T P_{X^0} \delta + V^T P_\ell V = V^T P_\ell W \tag{4.26}$$

The a-posteriori variance-covariance matrix of the estimated parameters can be written as:

$$\Sigma_{\hat{X}} = \hat{\sigma}_0^2 \left(P_{X^0} + A^T P_\ell A\right)^{-1} \tag{4.27}$$

$$\hat{\sigma}_0^2 = \frac{V^T PV}{(n-u)} \tag{4.28}$$

where *n*, *u* are the number of observations and the number of unknowns, respectively.

Generally, two equivalent methods can be used to solve for the unknown parameters, batch and sequential solutions. The sequential solution is used in this thesis. The a-priori coordinates are obtained from the header of the observation files or obtained by processing the code measurements from the first epoch. The estimated parameters from the current epoch are used as a-priori values for the subsequent epoch.

$$X_i^0 = \hat{X}_{i-1}$$

The propagated covariance matrix from the epoch (*i-1*) to epoch *i* during an interval Δt is given as:

$$C_{\hat{X}_i} = C_{\hat{X}_{i-1}} + C\varepsilon_{\Delta t}$$

where $C\varepsilon_{\Delta t}$ represents the process noise covariance matrix which will vary depending on the used PPP model as follows:

Un-Differenced Model

$$C\varepsilon_{\Delta t} = \begin{bmatrix} C\varepsilon(x)_{\Delta t} & 0 & 0 & 0 & 0 & 0 \\ 0 & C\varepsilon(y)_{\Delta t} & 0 & 0 & 0 & 0 \\ 0 & 0 & C\varepsilon(z)_{\Delta t} & 0 & 0 & 0 \\ 0 & 0 & 0 & C\varepsilon(dt^r)_{\Delta t} & 0 & 0 \\ 0 & 0 & 0 & 0 & C\varepsilon(zpd_w)_{\Delta t} & 0 \\ 0 & 0 & 0 & 0 & 0 & C\varepsilon(N^j_{(j=1,nsat)})_{\Delta t} \end{bmatrix}$$

Un-Differenced Decoupled Clock Model

$$C\varepsilon_{\Delta t} = \begin{bmatrix} C\varepsilon(x)_{\Delta t} & 0 & 0 & 0 & 0 & 0 & 0 \\ 0 & C\varepsilon(y)_{\Delta t} & 0 & 0 & 0 & 0 & 0 \\ 0 & 0 & C\varepsilon(z)_{\Delta t} & 0 & 0 & 0 & 0 \\ 0 & 0 & 0 & C\varepsilon(dt^{r}_{P3})_{\Delta t} & 0 & 0 & 0 \\ 0 & 0 & 0 & 0 & C\varepsilon(dt^{r}_{\Phi 3})_{\Delta t} & 0 & 0 \\ 0 & 0 & 0 & 0 & 0 & C\varepsilon(zpd_{w})_{\Delta t} & 0 \\ 0 & 0 & 0 & 0 & 0 & 0 & C\varepsilon(N^{j}_{(j=1,nsat)})_{\Delta t} \end{bmatrix}$$

Between-Satellite Single-Difference (BSSD) Models

$$C\varepsilon_{\Delta t} = \begin{bmatrix} C\varepsilon(x)_{\Delta t} & 0 & 0 & 0 & 0 \\ 0 & C\varepsilon(y)_{\Delta t} & 0 & 0 & 0 \\ 0 & 0 & C\varepsilon(z)_{\Delta t} & 0 & 0 \\ 0 & 0 & 0 & C\varepsilon(zpd_{w})_{\Delta t} & 0 \\ 0 & 0 & 0 & 0 & C\varepsilon(N^{j}_{(j=1,nsat)})_{\Delta t} \end{bmatrix}$$

Since the ambiguities are constant over time, $C\varepsilon(N^{j}_{(j=1,nsat)})_{\Delta t} = 0$. Also, the coordinates are constants in static mode and as a consequence $C\varepsilon(x)_{\Delta t} = C\varepsilon(y)_{\Delta t} = C\varepsilon(z)_{\Delta t} = 0$. The receiver clock process noise can vary depending on the frequency stability but is usually set to white noise with a large value $C\varepsilon(dt^{r})_{\Delta t}$ to accommodate the unpredictable occurrence of clock resets. Since the zenith path delay parameter changes in the order of a few centimetres per hour, a random walk process of 2, 3, 4 or 5 mm / hour can be used to the wet zenith path delay $C\varepsilon(zpd_{w})_{\Delta t}$ (Kouba, 2009).

5. RESULTS AND DISCUSSIONS

This chapter presents the results of the developed models for improving the PPP solution accuracy and convergence time of the estimated parameters. Section 5.1 introduces the results of the developed stochastic models for the GPS observables, including the modernized L2C signal. Section 5.2 introduces the effect of second-order ionospheric delay on GPS satellite orbit, satellite clock correction, GIMs, and PPP solution. Section 5.3 presents the impact of using the decoupled clock corrections with the un-differenced PPP model. Section 5.4 deals with between-satellite single-difference (BSSD) model. Section 5.5 studies the effect of applying the decoupled clock corrections to the BSSD model. Finally, a comparison between the four models is summarized in terms of the precision of the estimated coordinates and the corresponding convergence time.

5.1 Stochastic Properties of GPS Observables

To examine the stochastic properties of the L2C signal, a short baseline of about 1.5 m long was carried out on the rooftop of the Jorgenson Hall building, Ryerson University campus. Two Trimble R7 GNSS receivers of the same firmware were used for the test. Data at a rate of five Hz were collected for two consecutive days, DOY 336 and DOY 337, 2008. A new observable is formed by differencing the code and carrier-phase measurements (Equation 4.18). As the noise level on carrier-phase measurements is approximately 1% of that of the code measurements, carrier-phase noise, and multipath are assumed to be negligible in comparison with those of code measurements.

The between-receiver single-difference is then formed using the observable obtained from Equation (4.26) which cancels out the ionospheric delay sufficiently. The new BRSD observable is differenced over two consecutive days to essentially cancel out the multipath effect. The hardware delay terms, the ambiguity parameter, and the initial phase bias are removed from the series by differencing with respect to the first value of the series. With these operations, only the differenced system noise remains.

The differenced measurements are divided into 9 bins depending on the satellite elevation angle, starting from 0° to 90° with an increment of 10°. The corresponding mean and standard deviation of each bin are computed as shown in Figures 5.1, 5.2, and 5.3. Under the assumption that each bin is represented by its mean and standard deviation, we used the least-squares method to determine the best-fit model that relates the standard deviation (STD) and satellite elevation angle. The analysis showed that the best-fit model is an exponential decay function.

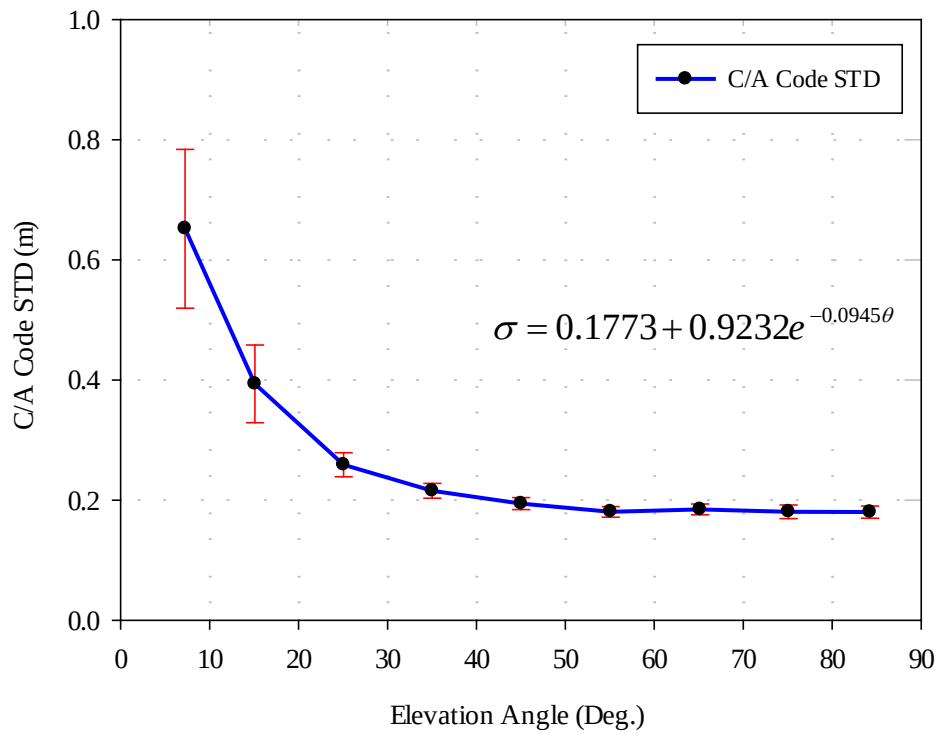

Figure 5.1 C/A Code Standard Deviation with Elevation Angle

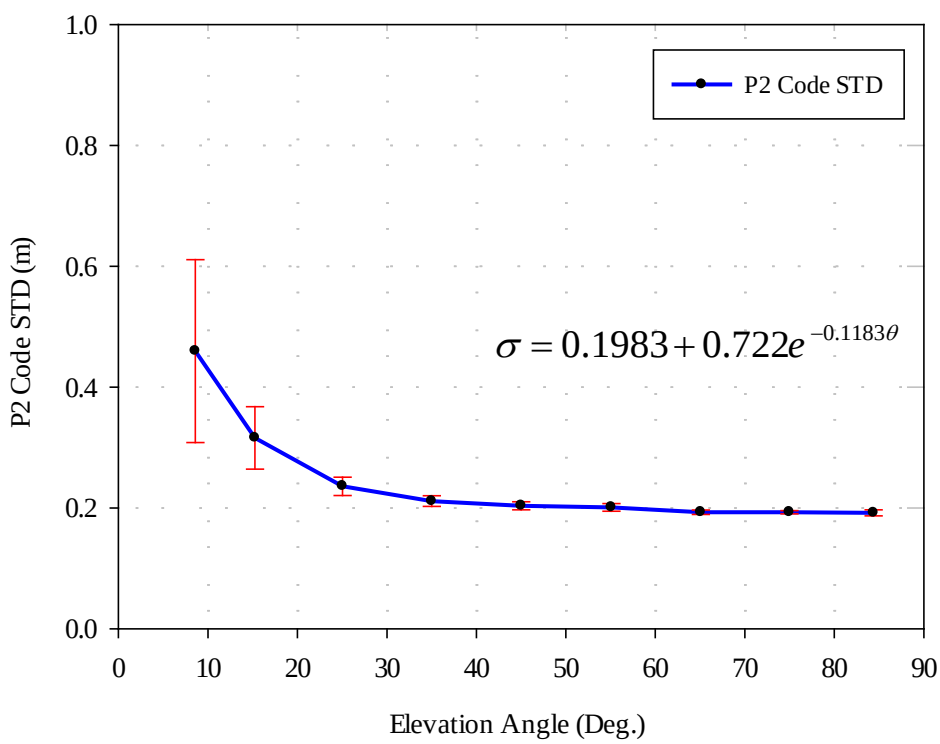

Figure 5.2 P2 Code Standard Deviation with Elevation Angle

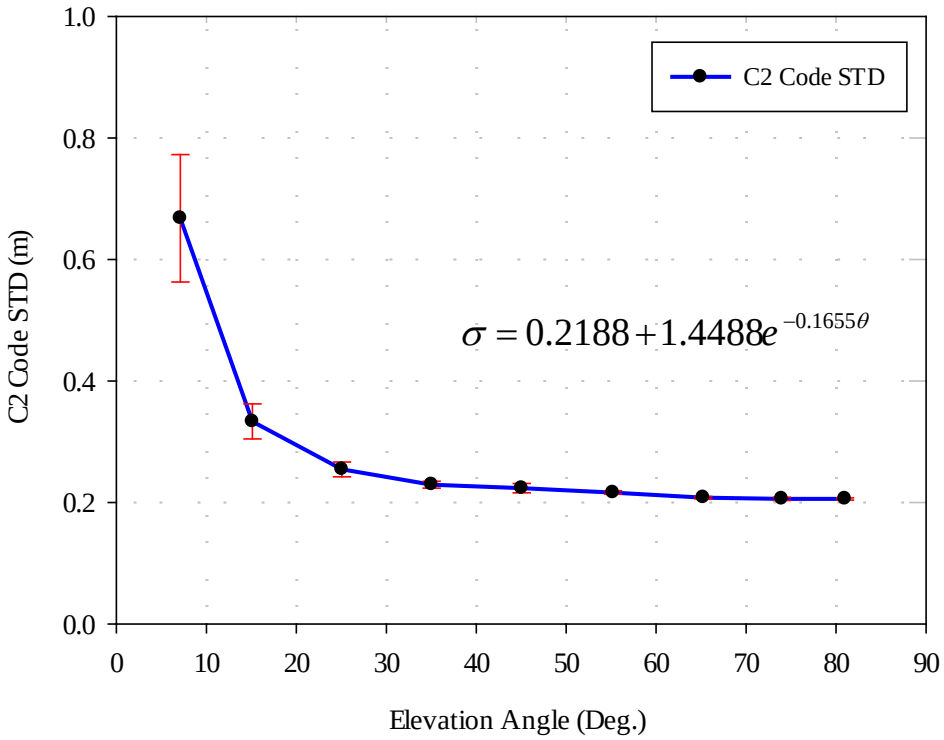

Figure 5.3 C2 Code Standard Deviation with Elevation Angle

From Figures 5.1 through 5.3, we notice that the standard deviation of C/A, P2, and C2 codes are almost constants above an elevation angle of 40°. To validate the developed models in Figures 5.1, 5.2, and 5.3, the same receiver is used to collect several sessions of GPS measurements in DOY 344, DOY 345, and DOY 346, i.e., one week after the last test day. GPSPace PPP software of Natural Resources Canada (NRCan) was modified to accept the newly developed stochastic models shown above. Ionosphere-free linear combination of code and carrier-phase measurements were used to estimate the station coordinates. The error propagation is implemented in GPSPace to compute the ionosphere-free linear combination code weights from C/A and P2 models shown in Figures 5.1 and 5.2. IGS precise ephemeris and satellite clock corrections are used, and

NOAA tropospheric model (Gutman *et al.*, 2003; Ibrahim and El-Rabbany, 2008) along with Vienna mapping function 1 (Boehm et al., 2006a, 2006b) are applied. Figures 5.4 through 5.6 show the results from one session while the results from other sessions are shown in Appendix A. As shown, implementation of the developed stochastic model improved the convergence time by about 40% for all station position components (Latitude, Longitude, and Height), compared with sine function for weighting. It should be pointed out that the convergence time improvement is computed using the second norm as follows:

$$t_1 = \frac{\sum_{i=1}^{n} r_{1i}^2}{n}$$

$$t_2 = \frac{\sum_{i=1}^{n} r_{2i}^2}{n}$$

$$\%improvement = \left(\frac{(t_1 - t_2)}{t_1} \right) * 100 \qquad (5.1)$$

where,

r_1	the difference between the correct coordinates and the corresponding estimated values from the first model
r_2	the difference between the correct coordinates and the corresponding estimated values from the second model
n	the total number of epochs
$\%improvement$	the percentage improvement in the second model over the first model

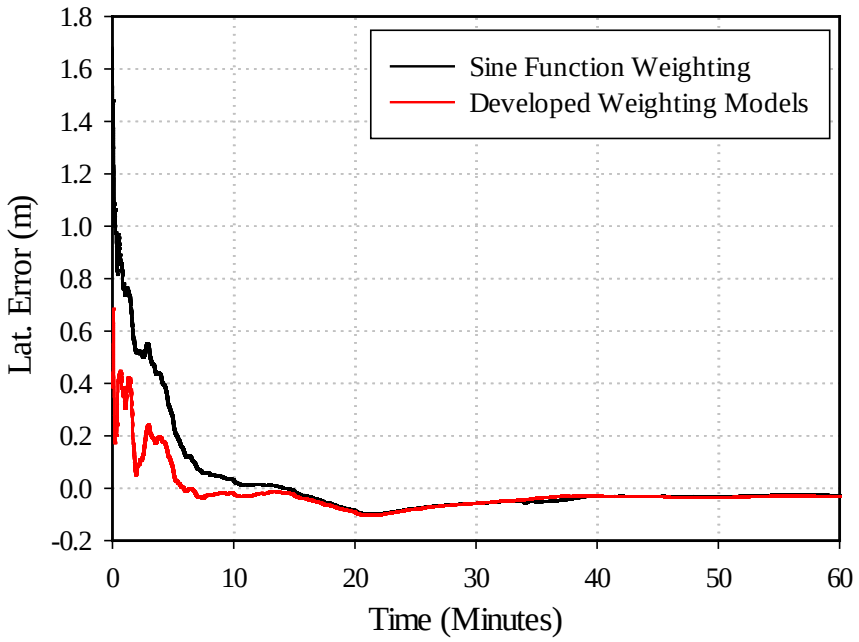

Figure 5.4 Latitude Improvement Using the New Developed Weighting Models

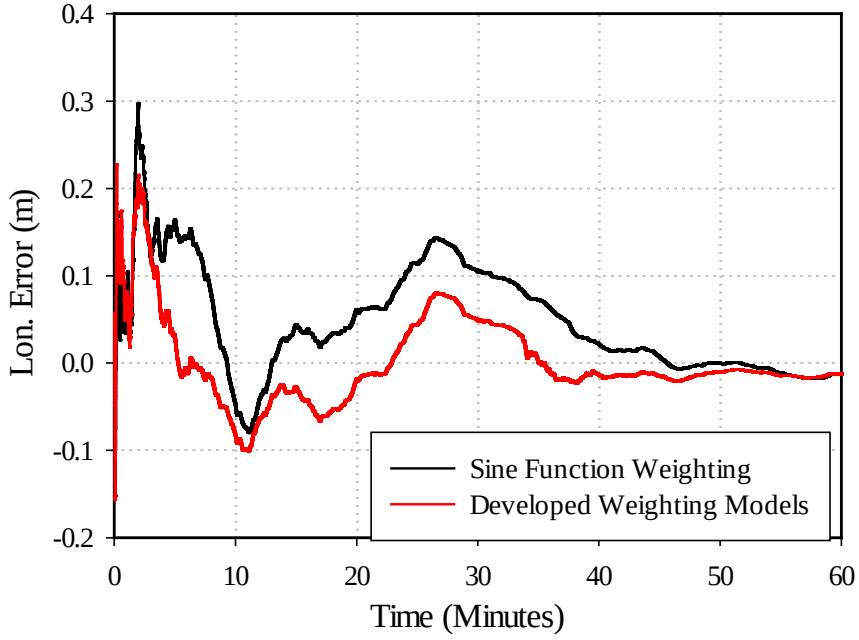

Figure 5.5 Longitude Improvement Using the New Developed Weighting Models

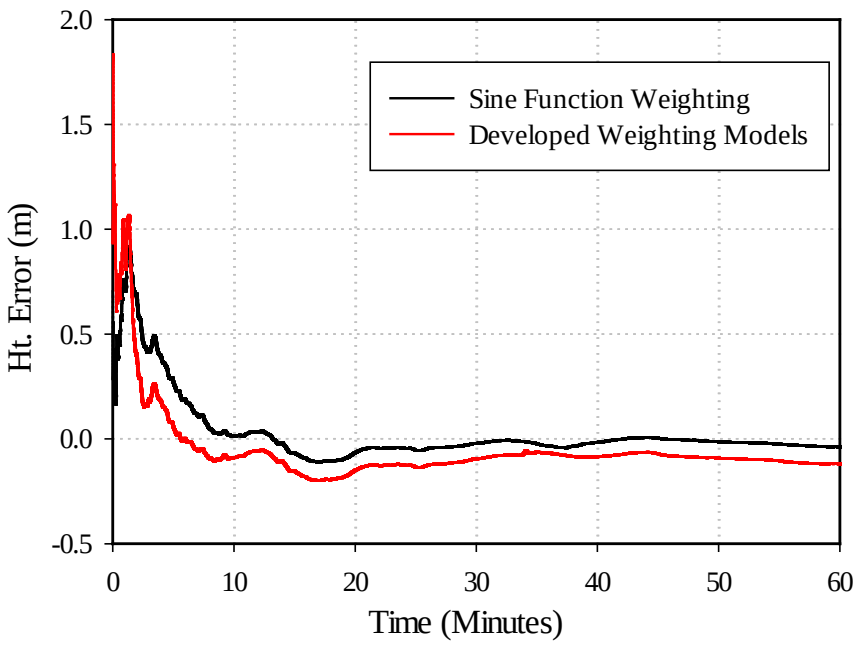

Figure 5.6 Ellipsoidal Height Improvement Using the New Developed Weighting Models

5.1.1 Estimation of P2-C2 Differential Code Bias (DCB_{P2-C2})

To utilize the new modernized L2C signal along with the existing GPS signals, the corresponding satellite hardware delay must be accurately determined. As satellite hardware delay is different for each observable, its absolute value cannot be determined directly. However, the difference between the hardware delays of two observables of the same frequency, i.e., inter-frequency differential delay, can be determined, which is known as differential code bias, DCB. Typically, the geometry-free linear combination of the P_1 and P_2 codes is used to estimate the ionospheric delay, while DCBs is obtained as a byproduct of the estimation process.

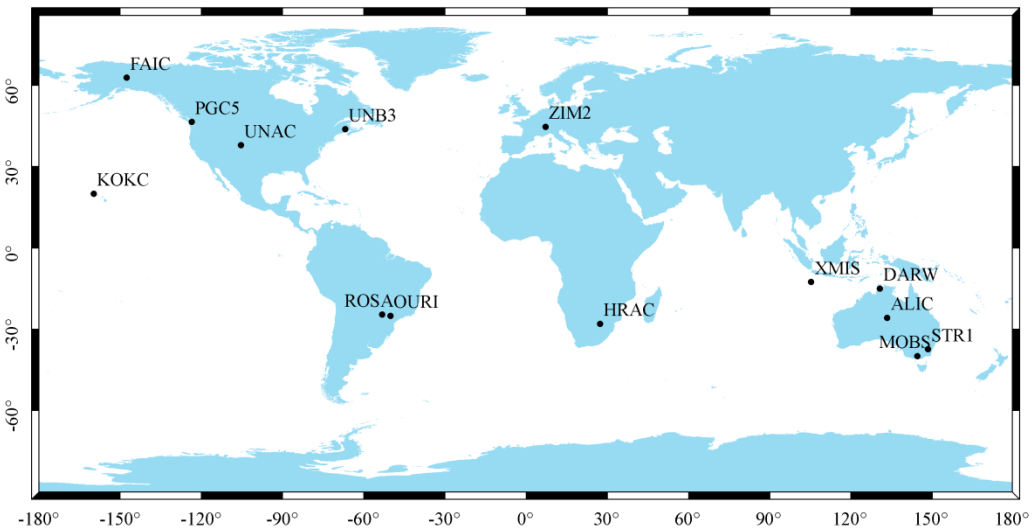

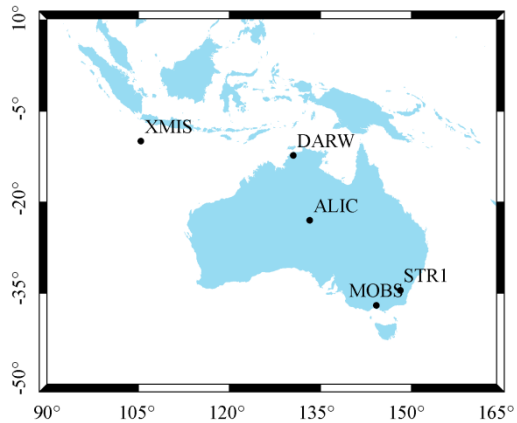

Figure 5.7 IGS L2C Tracking Network Stations as at December 2008 (Top) and the Network used to Estimate P2-C2 DCBs (Bottom)

A cluster consists of 5 IGS L2C tracking network stations were used to estimate DCB_{P2-C2} using Bernese GPS software (see Figure 5.7). The input was the geometry-free linear combination P_4 and C_4 as in Equations (5.2) and (5.3), respectively. However, the C/A code was used instead of P_1 code, and the corresponding DCB_{P1-C1} was applied.

Furthermore, C_4 was corrected for both $DCB_{P1\text{-}C1}$ and $DCB_{P1\text{-}P2}$ using IGS published values. The only unknowns were $DCB_{P2\text{-}C2}$ along with the receiver differential code bias and the ionospheric delay term. Estimates of $DCB_{P2\text{-}C2}$ showed that they are consistently within ±1 ns. Table 5.1 summarizes the estimated values and their corresponding root mean square.

$$P_4 = P_1 - P_2 = \xi I_1 + cDCB^r_{P1-P2} + cDCB^s_{P1-P2} \tag{5.2}$$

$$C_4 = C_1 - C_2 = \xi I_1 + cDCB^r_{C1-C2} - cDCB^s_{P1-C1} + cDCB^s_{P1-P2} + cDCB^s_{P2-C2} \tag{5.3}$$

where,

P_1, C_1, P_2, C_2	pseudorange measurements on both frequencies L1 and L2
I_1	first-order ionospheric delay for L1 observables
f_1, f_2	L1 and L2 frequencies, respectively, ($L_1 : f_1 = 1.57542\ GHz\ ; L_2 : f_2 = 1.22760\ GHz$)
ξ	$-\left(f_1^{\ 2} - f_2^{\ 2}\right) / f_2^{\ 2}$
c	the speed of light in a vacuum
$DCB^r_{P1-P2}, DCB^s_{P1-P2}$	receiver and satellite differential code bias between P1 and P2 observables, respectively
DCB^r_{C1-C2}	receiver differential code bias between C1 and C2 observables
DCB^s_{P1-C1}	satellite differential code bias between P1 and C1 observables
DCB^s_{P2-C2}	satellite differential code bias between P2 and C2 observables

Table 5.1: Estimates of DCB_{P2-C2} for December 2008

Satellite	DCB_{P2-C2} (ns)	RMS (ns)
PRN07	0.718	0.015
PRN12	0.047	0.015
PRN15	0.578	0.019
PRN17	0.437	0.017
PRN29	-0.253	0.015
PRN31	0.385	0.018

The GPSPace software was further modified to read and process the new modernized GPS L2C signal and to accept our newly determined DCB values. Four stations at different locations were selected from the IGS L2C tracking network to examine the developed models. Those stations are occupied by GPS receivers capable of simultaneously tracking both P2 and C2 codes, namely OURI, ROSA, UNB3, and ZIM2 as shown in Figure 5.7. The RINEX files were downloaded from the IGS ftp site for DOY 337, 2008. Firstly, the first-order ionosphere-free code (C/A and P2) and carrier-phase (L1 and L2) measurements were processed. Secondly, the first-order ionosphere-free code (C/A and C2) and carrier-phase measurements were then processed with the corresponding differential code bias and other corrections applied. The results showed promising behavior of the modernized L2C signal especially with the progress in the modernization program. Figures 5.8 through 5.10 show the results for station ROSA as an example.

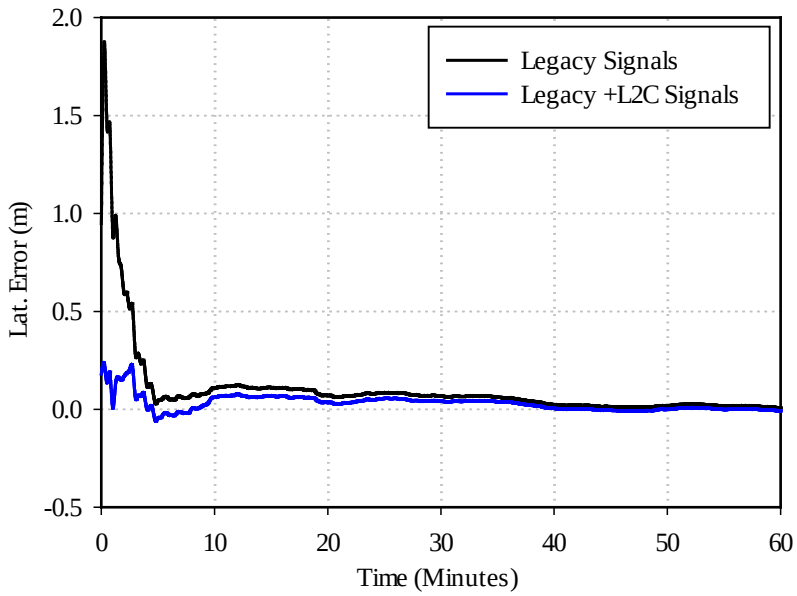

Figure 5.8 Latitude Improvement Using the Modernized L2C Signal at ROSA IGS Station

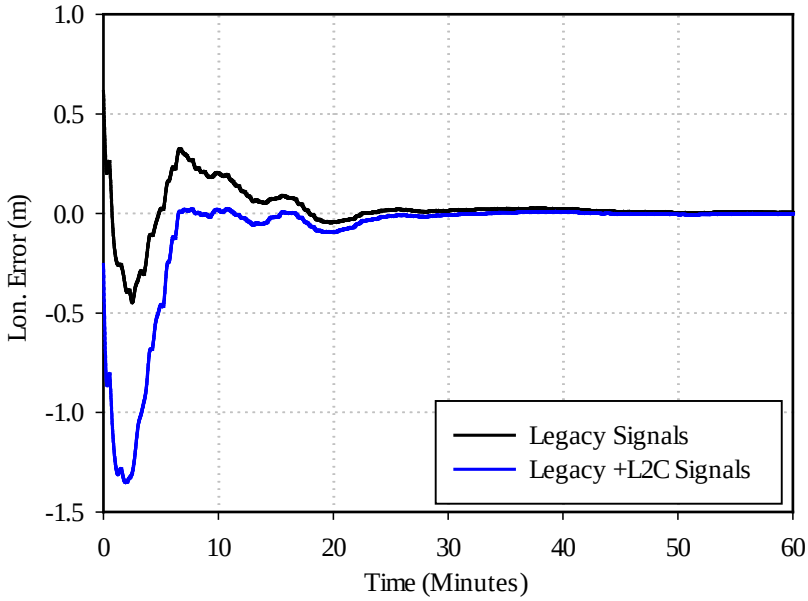

Figure 5.9 Longitude Improvement Using the Modernized L2C Signal at ROSA IGS Station

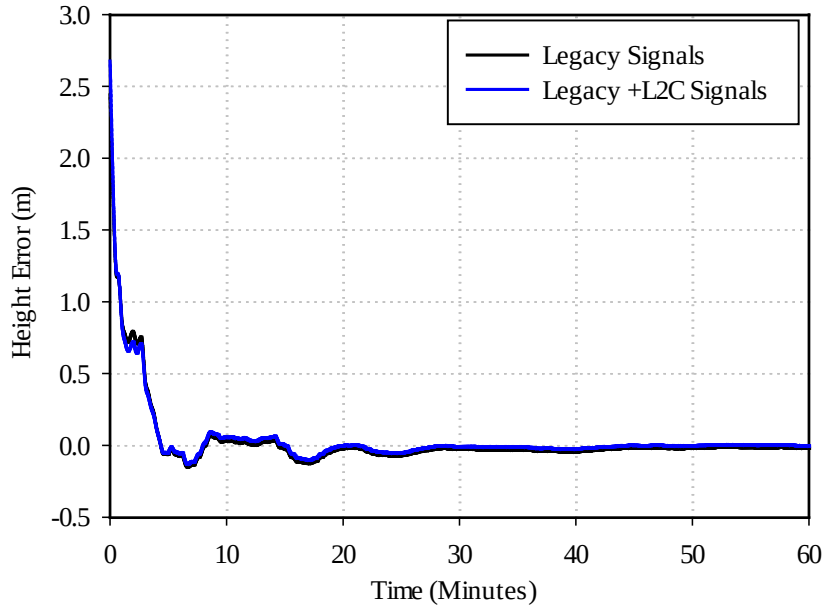

Figure 5.10 Ellipsoidal Height Improvement Using the Modernized L2C Signal at ROSA IGS Station

5.2 Effect of Second-Order Ionospheric Delay

5.2.1 Effect of Second-Order Ionospheric Delay on GPS Satellite Precise Orbit and Clock Corrections

To investigate the effect of second-order ionospheric delay on the determination of GPS satellite precise orbit and clock corrections, Bernese GPS software was used. A global cluster of 284 IGS reference stations (Figure 5.11) was formed based on a priori information about the behaviour of each receiver's clock and the total number of carrier-phase ambiguities in the corresponding observation files. GPS measurements collected at the 284 IGS stations were downloaded from the IGS website for May 05, 2010

(DOY125). The raw data were first corrected for the effect of second-order ionospheric delay using Equation 4.15. Equation 4.16 was used to compute the STEC values, and the IGS published DCBs were applied (Dach *et al.*, 2007). The corrected data along with the broadcast ephemeris were used as input to the Bernese GPS software to estimate the satellite orbit and clock corrections (see Appendix C and Appendix D). Our results showed that the effect of second-order ionospheric delay on the GPS satellite orbit ranges from 1.5 to 24.7 mm in radial, 2.7 to 18.6 mm in the along-track, and 3.2 to 15.9 mm in cross-track directions, respectively (Figure 5.12).

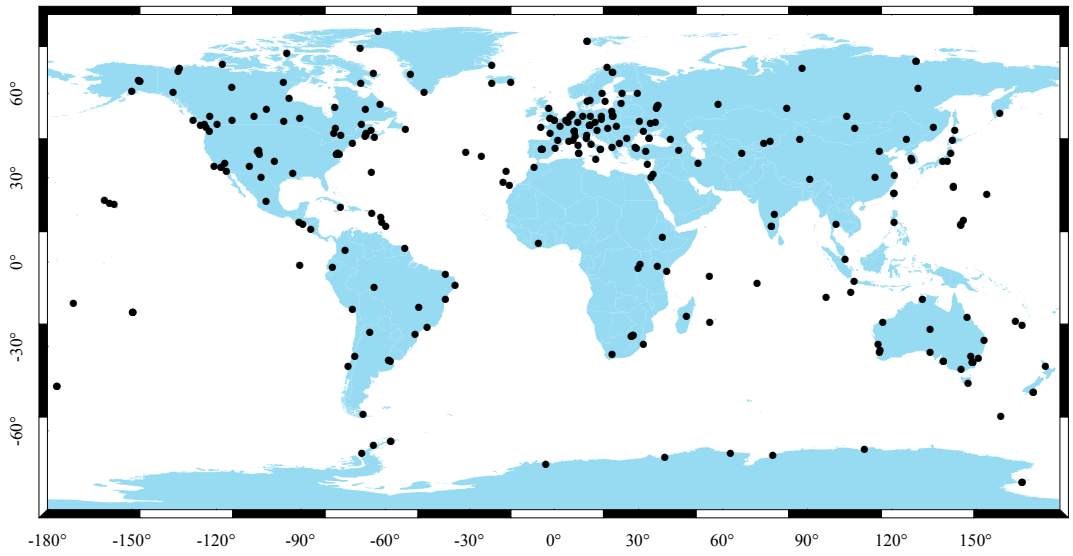

Figure 5.11 Global Cluster of IGS Stations Used in Estimation of GPS Satellite Orbit, Satellite Clock Corrections, and GIMs

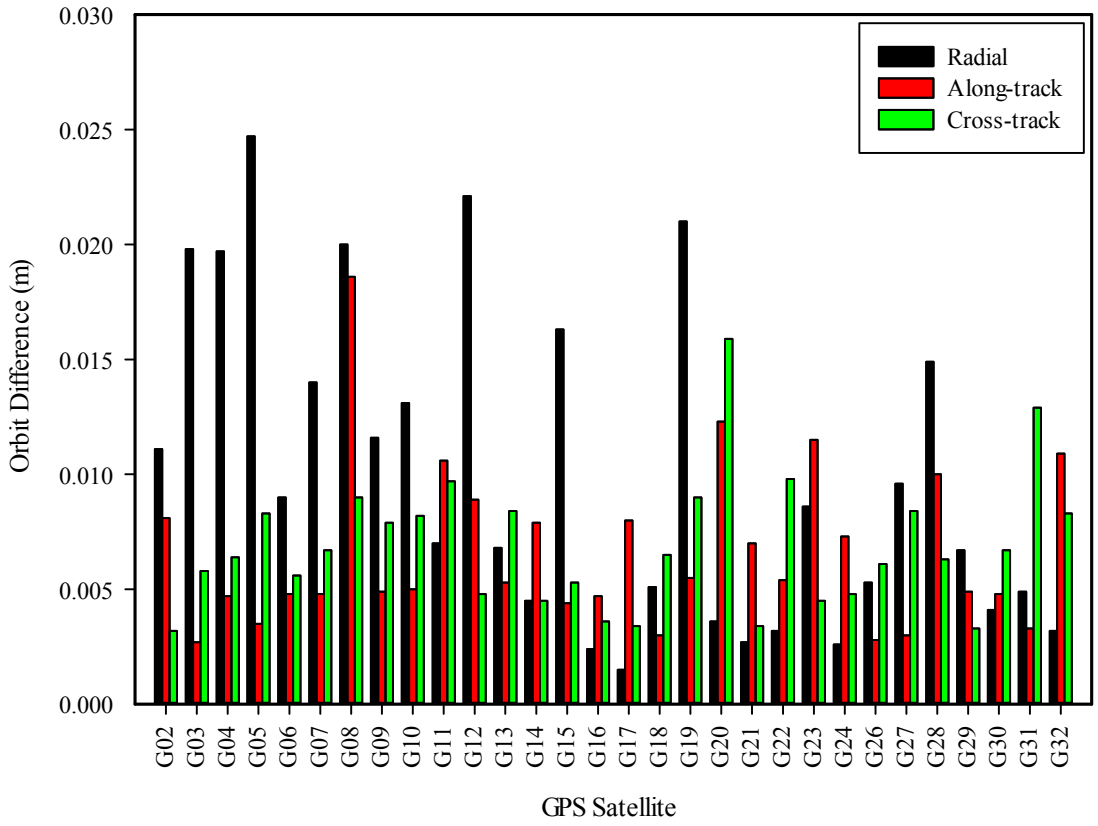

Figure 5.12 Effect of Second-Order Ionospheric Delay on GPS Satellite Orbit

In addition, our study showed that the effect of second-order ionospheric delay on the estimated satellite clock solution differences were within 0.067 ns (2 cm). Figure 5.13 shows the RMS (in picoseconds) of the estimated satellite clock corrections compared with the corresponding values of the IGS final satellite clock corrections.

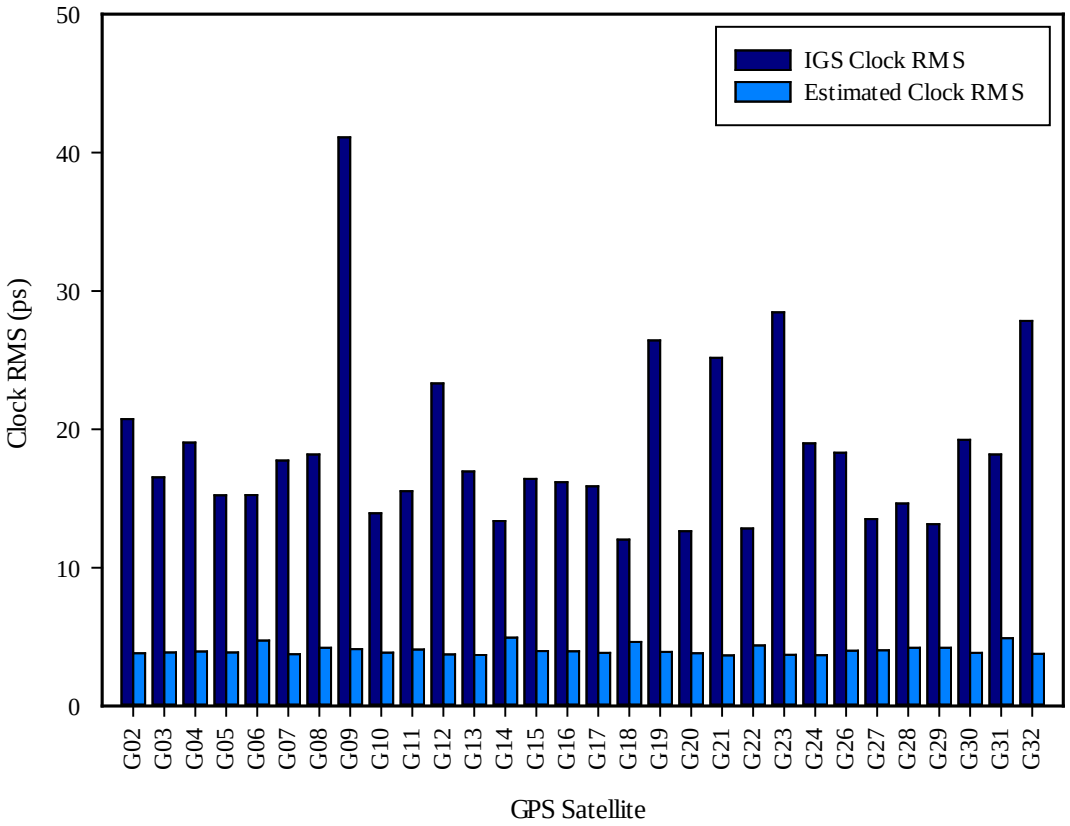

Figure 5.13 Effect of Second-Order Ionospheric Delay on GPS Satellite Clock Corrections

5.2.2 Effect of Second-Order ionospheric Delay on Global ionospheric Maps (GIMs)

GIMs were estimated from the previously described global cluster (Figure 5.12) using the Bernese GPS software. Our results indicate that neglecting second-order ionospheric delay can cause an error of up to 4.28 TECU, in the absolute sense, in the estimated GIM values. Also, accounting for the second-order ionospheric delay improves the RMS of the estimated GIMs by 11%. Figure 5.14 shows the estimated GIM at time 00h (GMT) on May 5, 2010. Figure 5.15, on the other hand, shows the effect of second-order

ionospheric delay on GIM estimation at the same time. It can be seen that most of the effect is concentrated according to the Sun-Earth relative position. This behaviour is expected as the second-order ionospheric delay is dependent on the TEC and magnetic-field conditions.

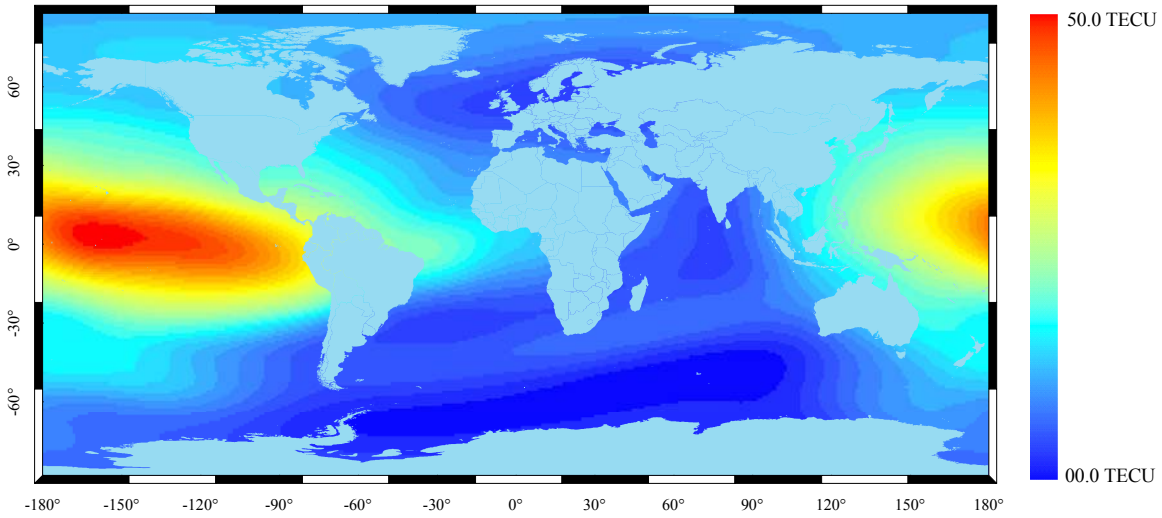

Figure 5.14 Estimated GIM at 00h (GMT Time) DOY125, 2010

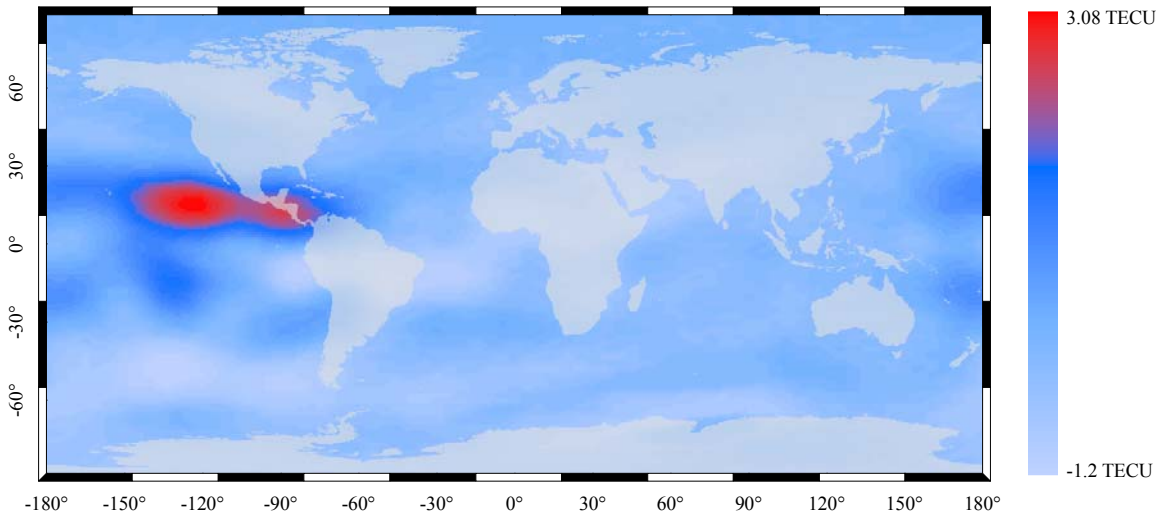

Figure 5.15 Effect of Second-Order Ionospheric Delay on GIM at 00h (GMT Time) DOY125, 2010

5.2.3 Effect of Second-Order ionospheric Delay on PPP Solution

To examine the effect of second-order ionospheric delay on the PPP solution, the GPSPace PPP processing software was modified to accept the second-order ionospheric correction. GPS data from 12 IGS stations (Figure 5.16) were processed using the modified GPSPace. The stations are chosen randomly and were not included in the estimation of satellite orbit and clock corrections. The data used were the un-differenced ionosphere-free (with both first- and second-order corrections included) linear combination of pseudorange and carrier-phase measurements. The estimated precise satellite orbit and clock corrections (Section 5.2.1) were used in the data processing. The results show that improvements are attained in all three components of the station coordinates. Figures 5.17 through 5.22 show the 3D solutions obtained with and without the second-order ionospheric corrections included, for stations TAH1 and DRAG, as examples. As can be seen, the amplitude variation of the estimated coordinates during the first 15 minutes is reduced when considering the second-order ionospheric delay. In addition, the convergence time for the estimated parameters is reduced by about 15% (Equation 5.1). The standard deviation of the estimated coordinates is also improved by about 25% as seen in Figures 5.23 through 5.25. It should be pointed out that the solution improvement is much higher at low latitudes where the second-order ionospheric effect is much higher (see Figure 5.15). Appendix E shows the results of other IGS stations.

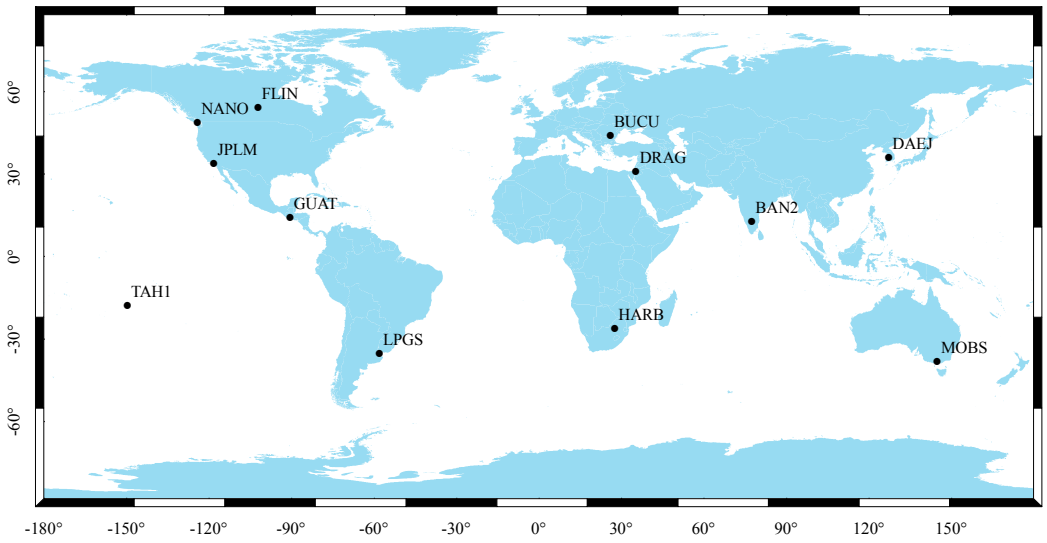

Figure 5.16 IGS Stations Used in Examining the Effect of Second-Order Ionospheric Delay on PPP Solution

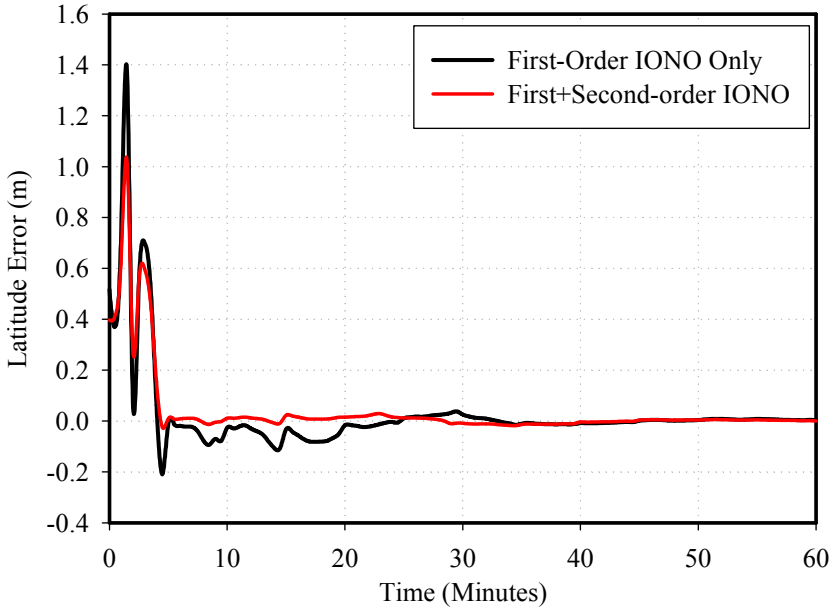

Figure 5.17 Latitude Improvement Due to Accounting for Second-Order Ionospheric Delay at DRAG Station, DOY125, 2010

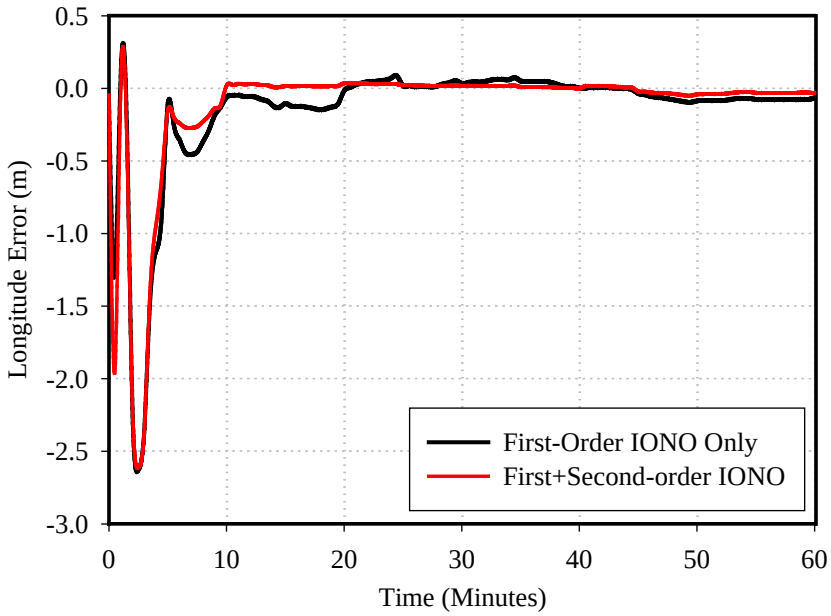

Figure 5.18 Longitude Improvement Due to Accounting for Second-Order Ionospheric Delay at DRAG Station, DOY125, 2010

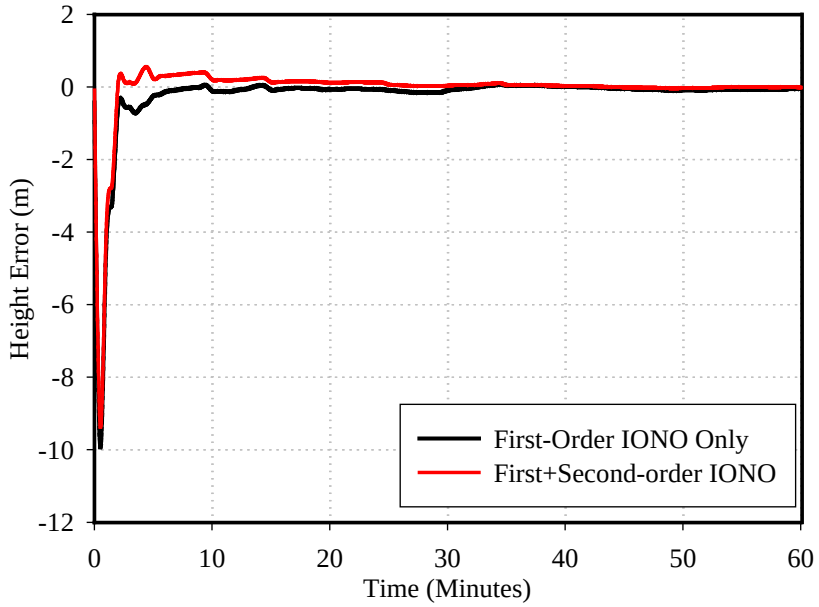

Figure 5.19 Ellipsoidal Height Improvement Due to Accounting for Second-Order Ionospheric Delay at DRAG Station, DOY125, 2010

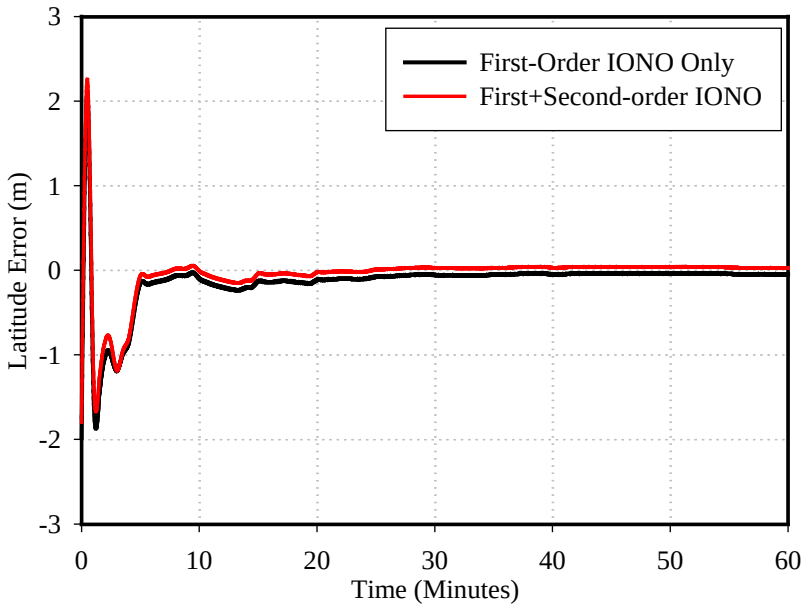

Figure 5.20 Latitude Improvement Due to Accounting for Second-Order Ionospheric Delay at THA1 Station, DOY125, 2010

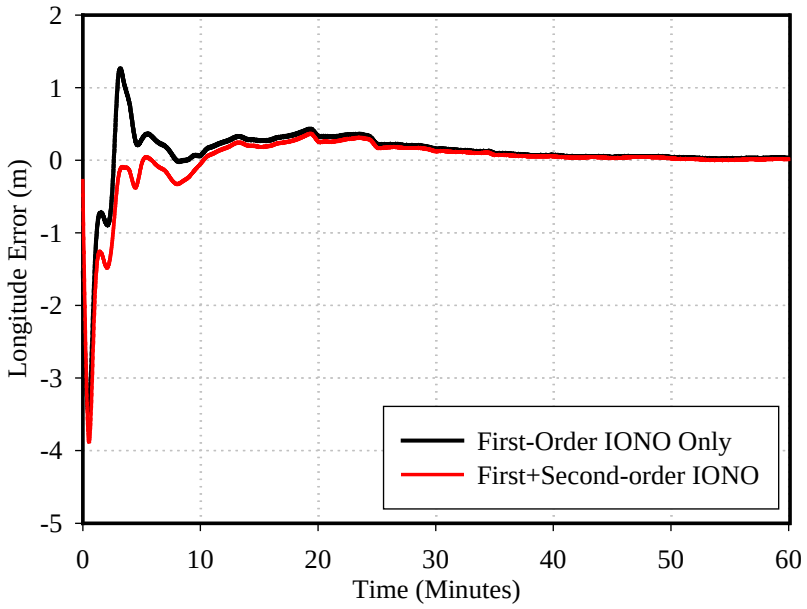

Figure 5.21 Longitude Improvement Due to Accounting for Second-Order Ionospheric Delay at THA1 Station, DOY125, 2010

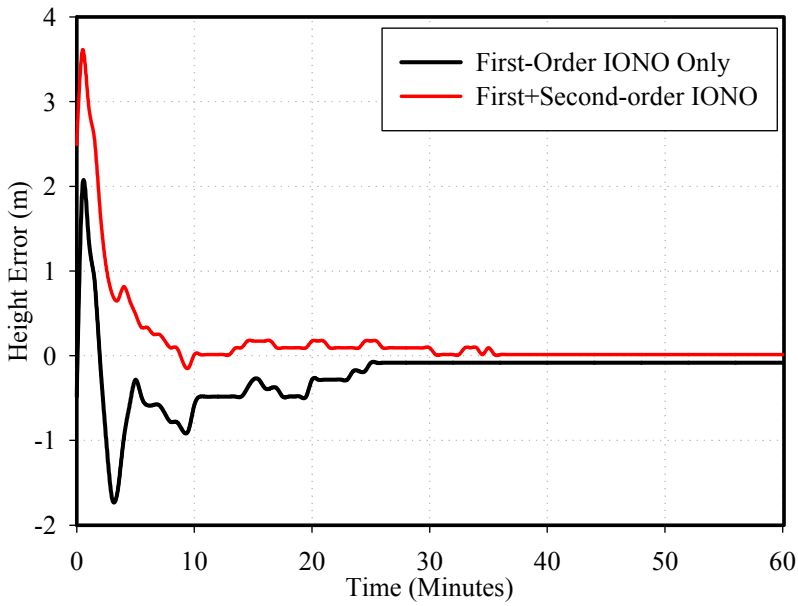

Figure 5.22 Height Improvement Due to Accounting for Second-Order Ionospheric Delay at THA1 Station, DOY125, 2010

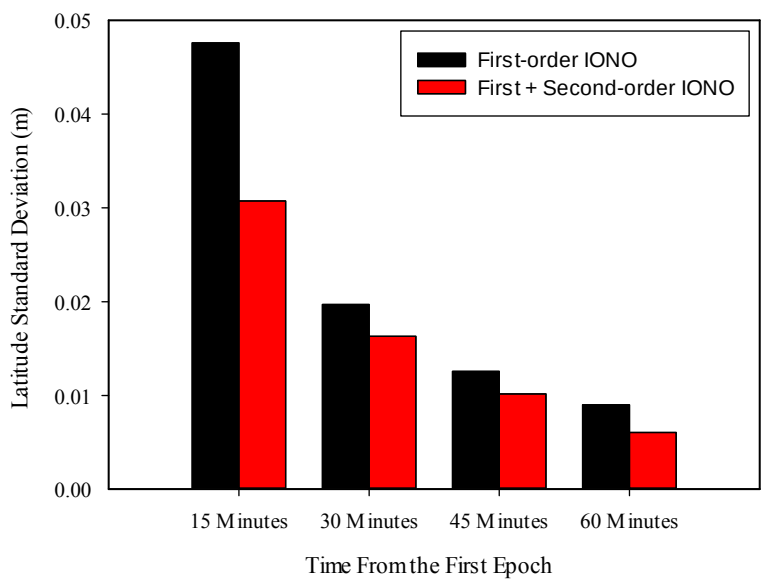

Figure 5.23 Latitude Improvement Due to Accounting for Second-Order Ionospheric Delay, DOY125, 2010

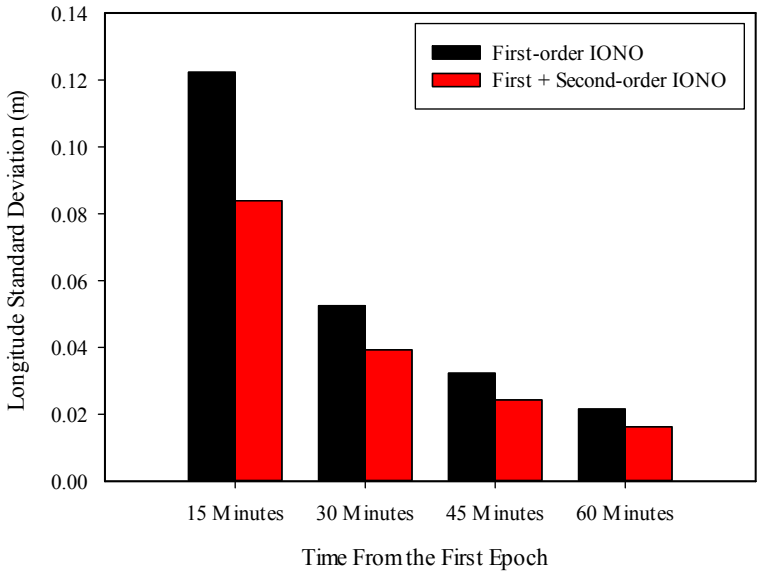

Figure 5.24 Longitude Improvement Due to Accounting for Second-Order Ionospheric Delay, DOY125, 2010

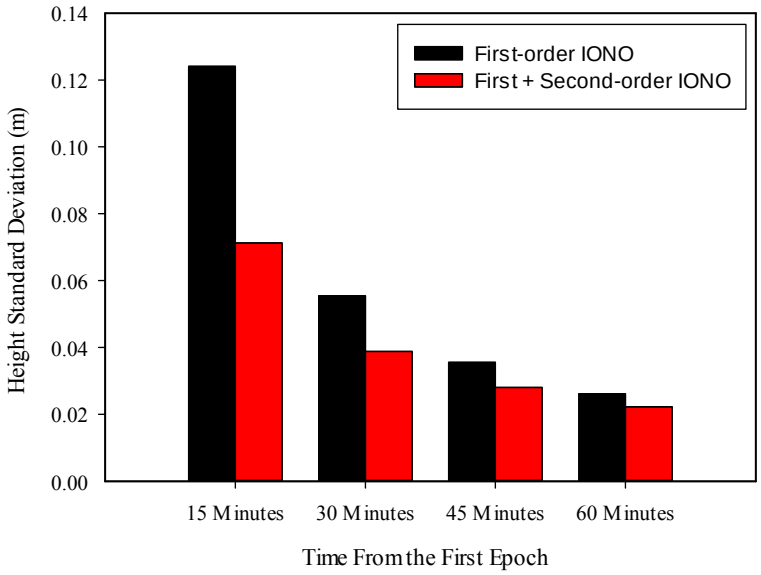

Figure 5.25 Height Improvement Due to Accounting for Second-Order Ionospheric Delay, DOY125, 2010

5.3 Un-Difference Decoupled Clock (Un-Differenced-DC) Model

As seen in the previous analysis, the convergence time of the un-differenced PPP model could likely be improved further. The first step to improve the PPP model is to use the decoupled clock model to correct for the satellite (code and carrier-phase) clock errors. The decoupled clock corrections include the satellite hardware delays and satellite initial phase bias. Receiver hardware delays and receiver initial phase bias, on the other hand, are assumed to be lumped to the receiver clock errors. Unlike the satellite hardware delays, however, the receiver hardware delays are not stable overtime. In addition, the receiver clock is very cheap and unstable compared with the satellite clock (see Sections 3.1 and 3.3). Our results showed that the estimated receiver clock errors are not stable overtime (Figure 5.26). These results indicate that both the receiver hardware delays and the receiver clock error are not stable overtime.

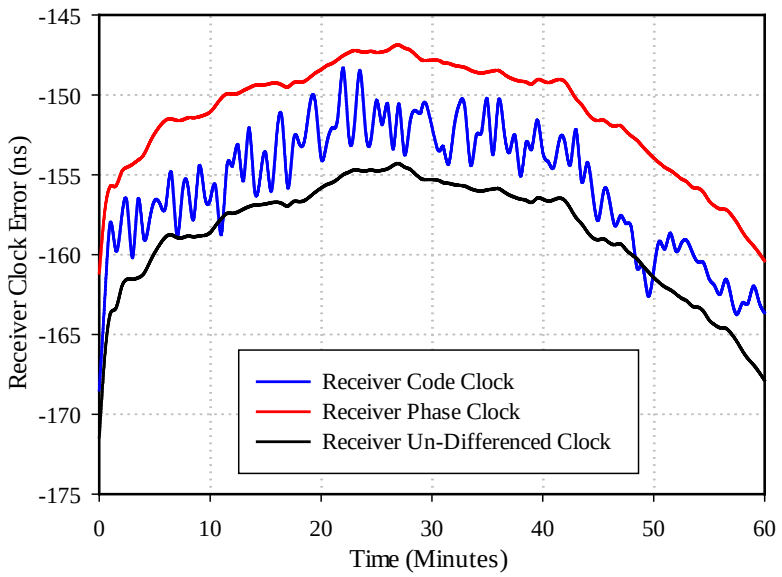

Figure 5.26 Behaviour of Receiver Clock Error Over Time using Un-Differenced and Un-Differenced-DC Models (AJAC IGS Station)

5.4 Between-Satellite Single-Difference (BSSD) Model

Between-satellite single-difference has the advantages that it cancels out most receiver related errors. These include the receiver initial phase bias, receiver hardware delay, and receiver clock error. However, differencing observations between satellites causes mathematical correlation, which, unless modelled properly, is expected to affect the PPP convergence time as described in Section 4.8.1. Figures 5.27 through 5.29 show the effect of neglecting BSSD mathematical correlation on PPP convergence time.

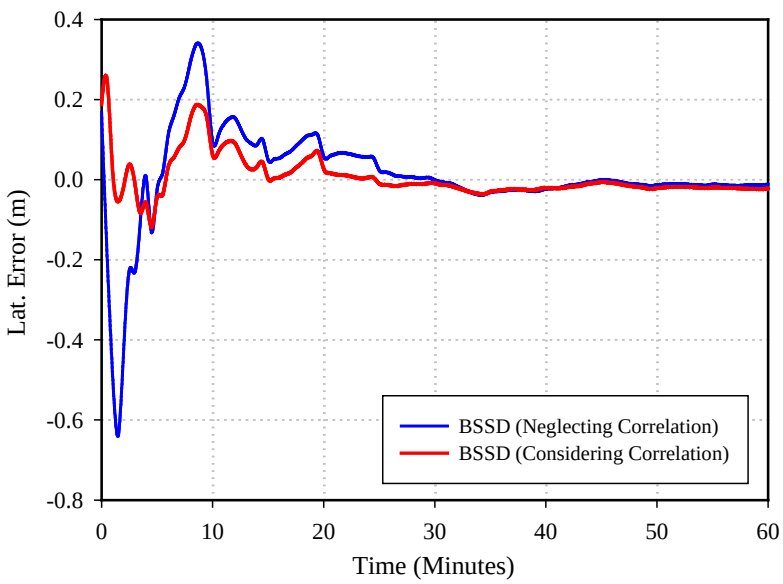

Figure 5.27 Effect of Neglecting BSSD Mathematical Correlation on Latitude Solution

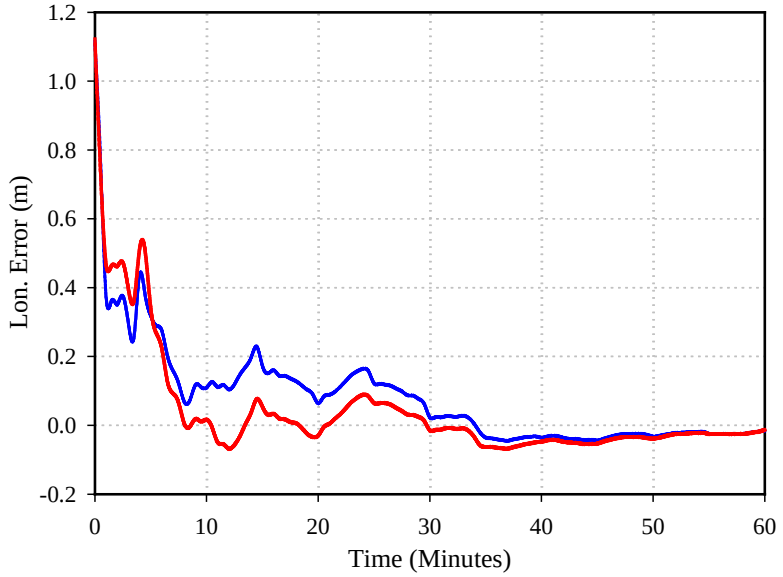

Figure 5.28 Effect of Neglecting BSSD Mathematical Correlation on Longitude Solution

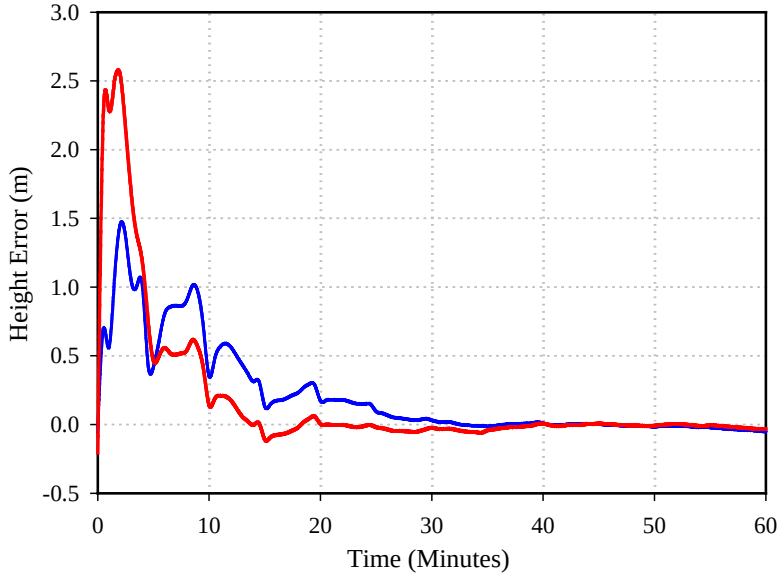

Figure 5.29 Effect of Neglecting BSSD Mathematical Correlation on Height Solution

5.5 Between-Satellite Single-Difference Decoupled Clock Model (BSSD-DC)

To further improve the PPP model, we applied the decoupled clock correction to the BSSD model. At this stage we have four PPP models; Un-Differenced, Un-Differenced-DC, BSSD, BSSD-DC models. To test the developed models, GPS data from 26 randomly selected IGS stations were processed including four stations tracking the modernized L2C signal, Figure 5.30. The input data are the first-order ionosphere-free linear combination of code and carrier phase. IGS precise orbit is used for satellite coordinates. IGS precise clock corrections are applied to the un-differenced and BSSD models. However, decoupled clock corrections, obtained from NRCan, were applied to the Un-differenced-DC and BSSD-DC models to correct for code and carrier-phase satellite clock error. Tropospheric corrections are accounted for using the global numerical weather model developed by the European Centre for Medium-Range Weather Forecasts ECMWF. ECMWF Vienna mapping function 1 is used for mapping the zenith tropospheric delays (wet and dry) to each satellite specific elevation angle (Boehm et al., 2006a, 2006b). All remaining errors, including carrier-phase windup, relativity, sagnac, Earth tides, and ocean loading are accounted for with sufficient accuracy using existing models. Figures 5.31 through 5.36 show the results for AJAC and JPLM IGS stations as examples. The results for all stations are summarized in Appendix F.

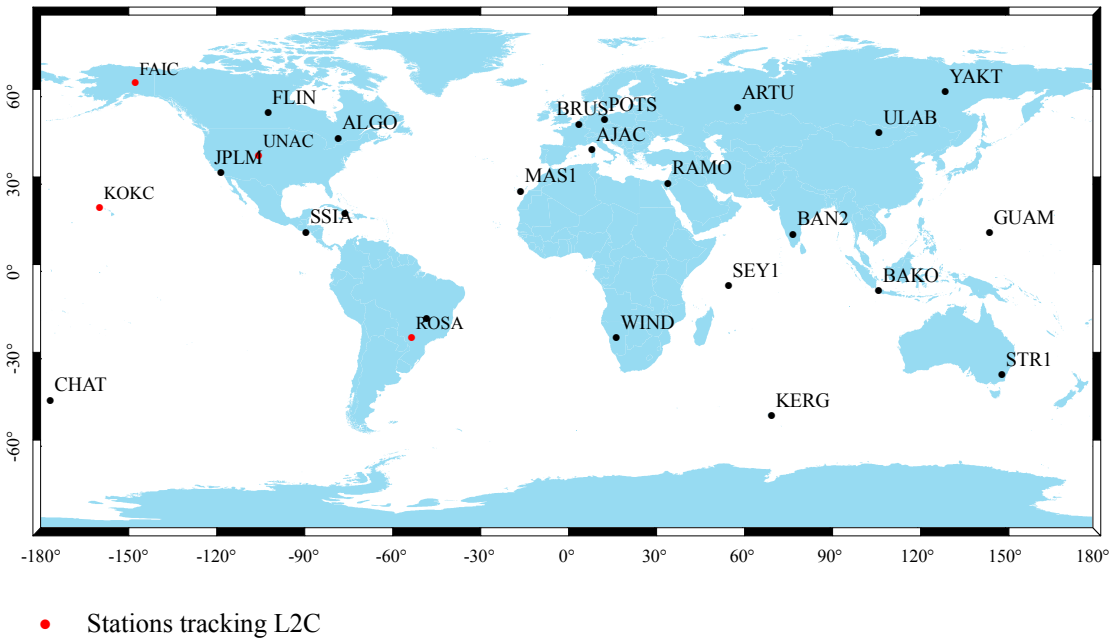

Figure 5.30 IGS Network Used to Test the Developed Models

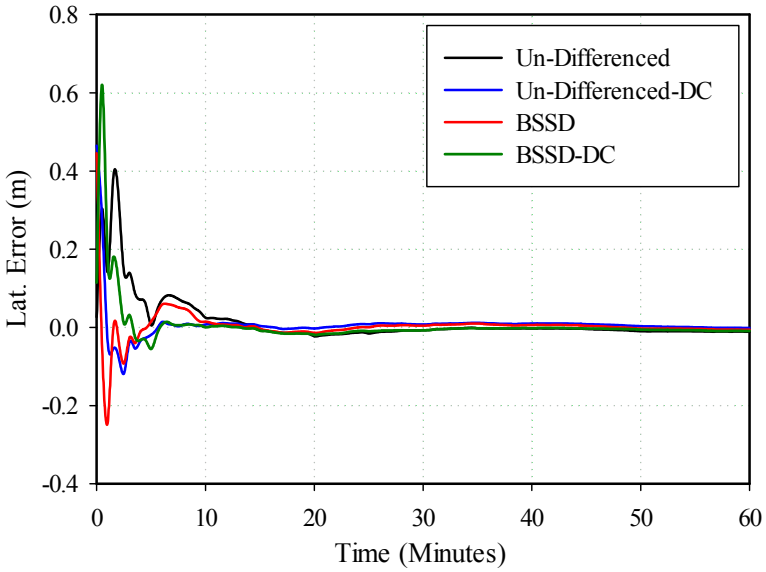

Figure 5.31 Latitude Improvement at AJAC IGS Station Using the Developed Models

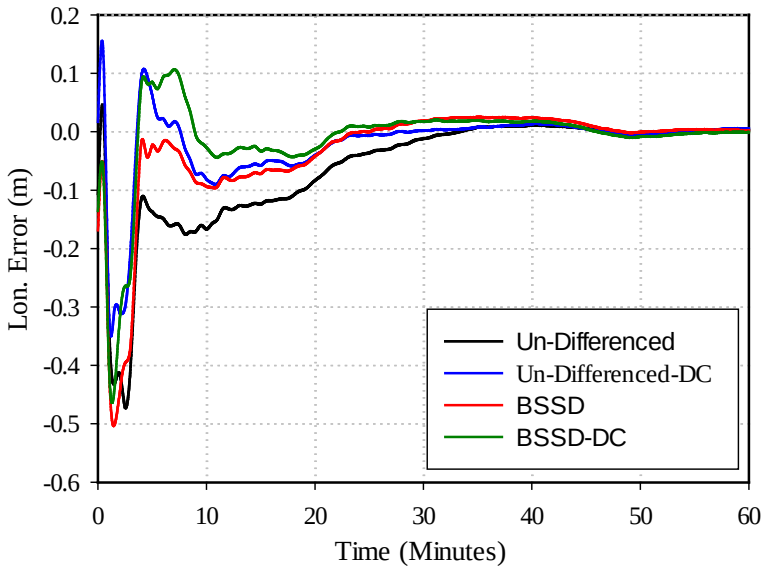

Figure 5.32 Longitude Improvement at AJAC IGS Station Using the Developed Models

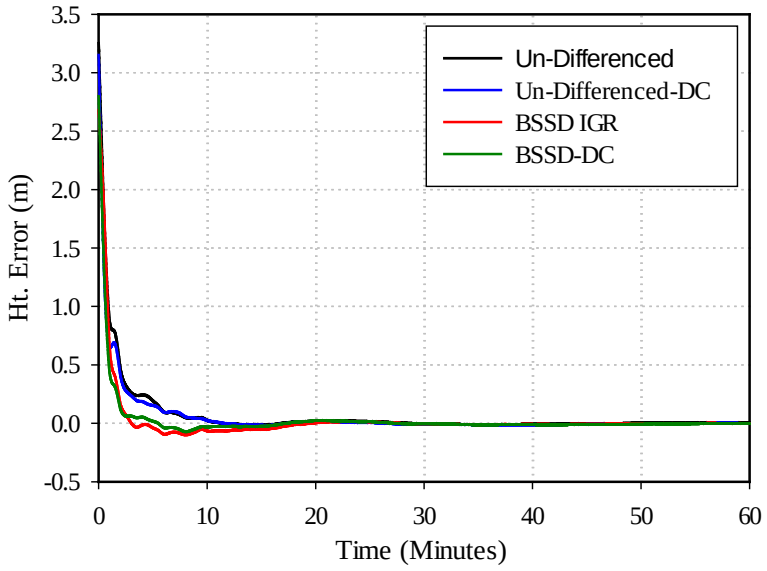

Figure 5.33 Height Improvement at AJAC IGS Station Using the Developed Models

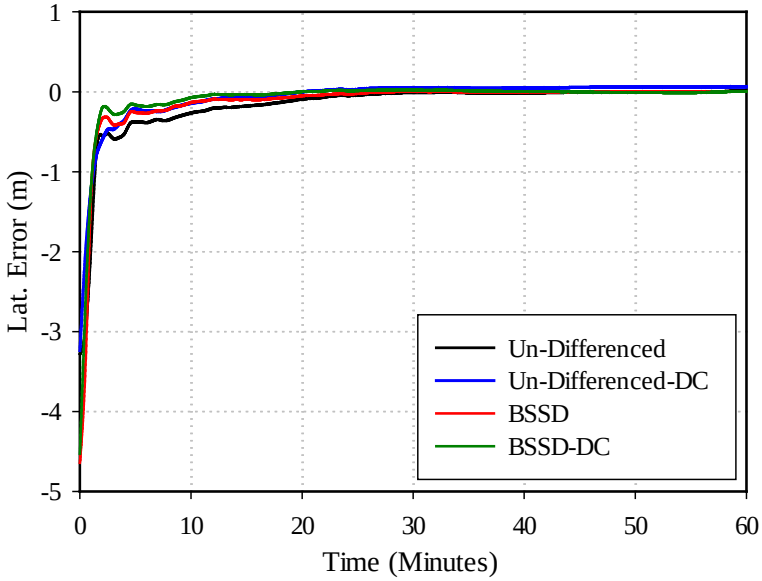

Figure 5.34 Latitude Improvement at JPLM IGS Station Using the Developed Models

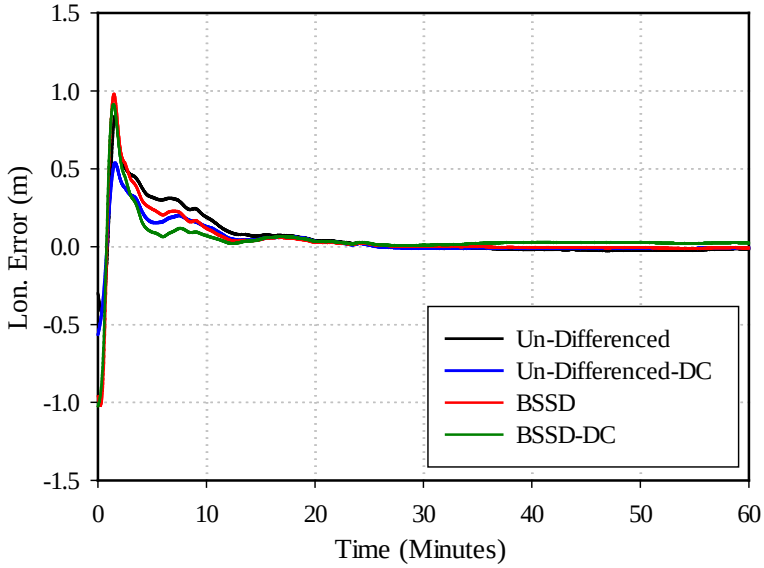

Figure 5.35 Longitude Improvement at JPLM IGS Station Using the Developed Models

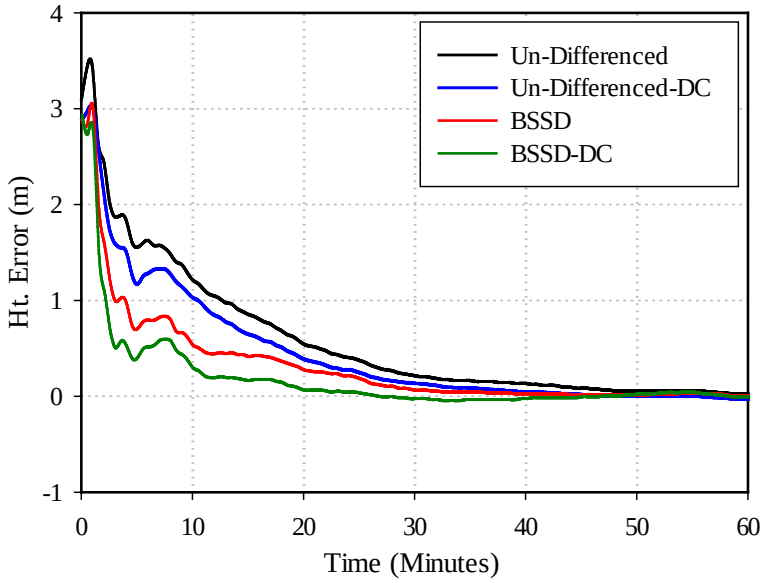

Figure 5.36 Height Improvement at JPLM IGS Station Using the Developed Models

Our results showed that between-satellite single-difference decoupled clock model is the best model among the four developed models. The improvement obtained from applying the decoupled clock correction in the BSSD model is only about 10%, which reflects the stability of the satellite hardware delays in comparison with that of the receiver hardware delays. The same conclusion can be drawn when comparing the un-differenced model with the BSSD model. Figures 5.37 through 5.39 show the standard deviation for the three positioning components, latitude, longitude, and height from the four PPP models. It is clear that between-satellite single-difference using the decoupled clock corrections improves the standard deviation of the estimated coordinates by more than 60% (Figures 5.37 through 5.39) and improves the convergence time of the estimated coordinates by about 50% (using Equation 5.1).

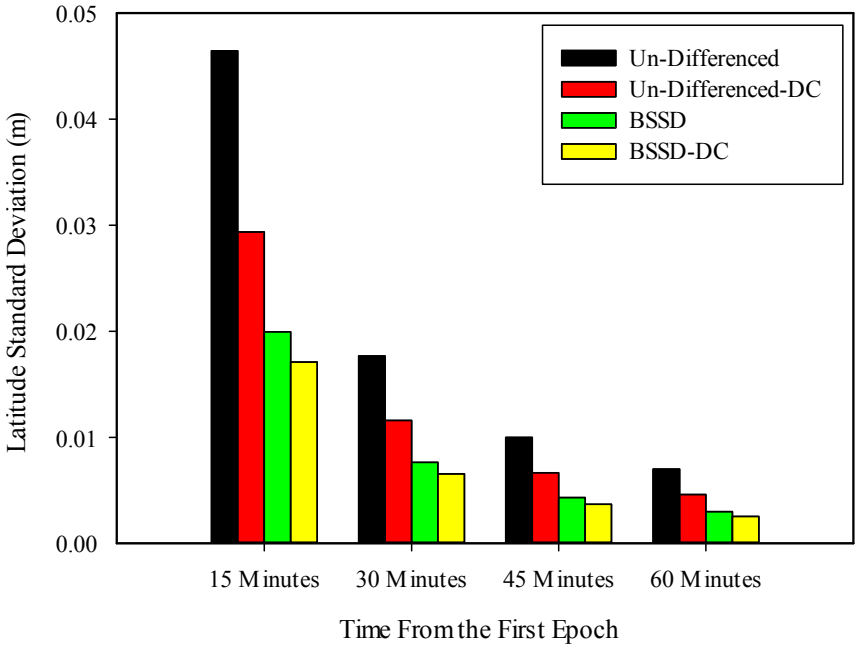

Figure 5.37 Latitude Standard Deviation Using the Developed Models

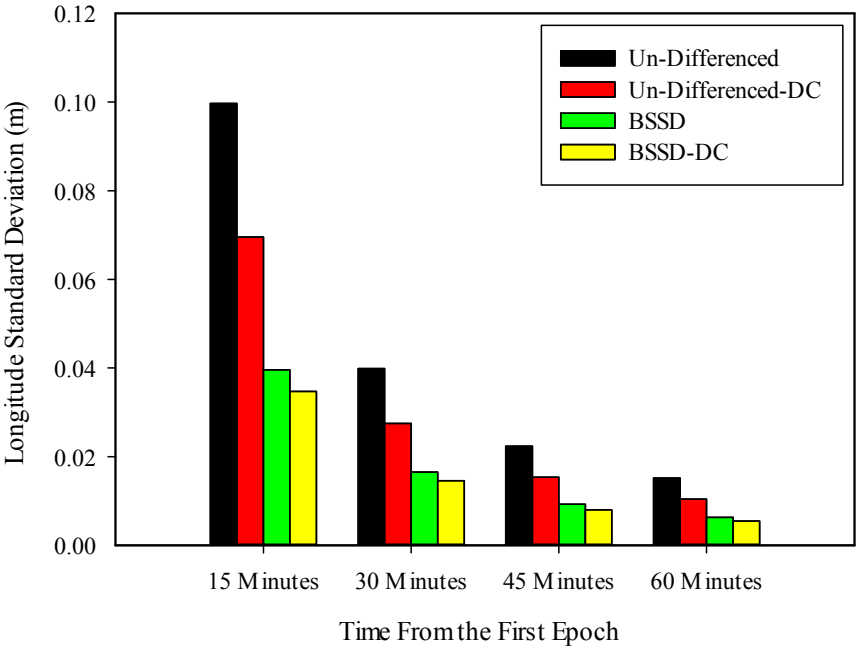

Figure 5.38 Longitude Standard Deviation Using the Developed Models

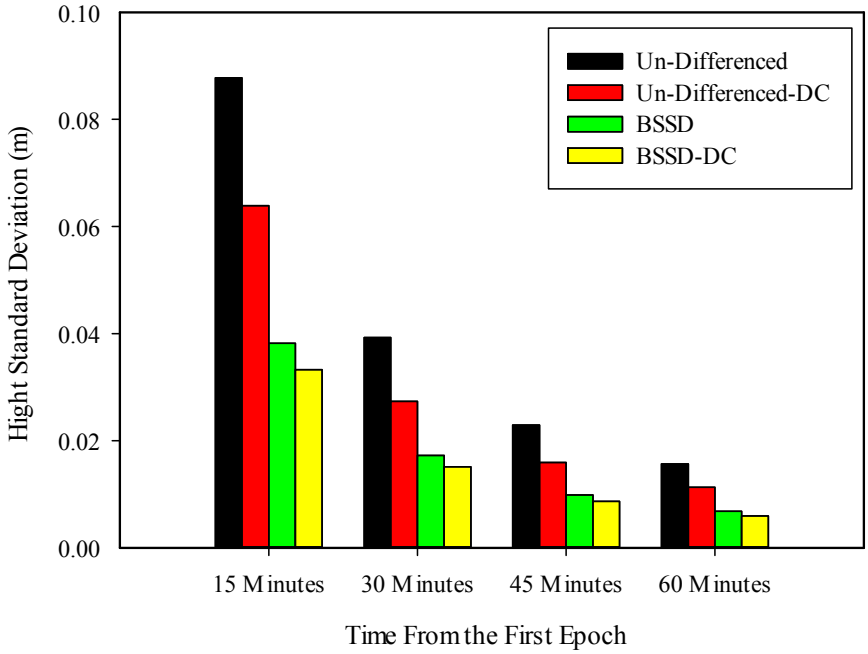

Figure 5.39 Height Standard Deviation Using the Developed Models

6. SUMMARY, CONCLUSIONS AND RECOMMENDATIONS

6.1 Summary

The main goal of this research was to develop rigorous models for near real-time precise point positioning using both un-differenced and between-satellite single-difference GPS observations. To achieve this goal, the stochastic properties of the modernized GPS L2C signal were investigated. A complete mathematical and stochastic model for the L2C signal was introduced and tested, and a complete model of the second-order ionospheric delay was developed. The impact of the second-order ionospheric delay on GPS satellite orbit and satellite clock corrections was also investigated. Between-satellite single-difference algorithms were developed to cancel out the receiver clock error, receiver initial phase bias, and receiver hardware delay. The decoupled clock corrections, provided by NRCan, were also applied to account for code and carrier-phase clock corrections. The decoupled clock correction absorbs the satellite hardware delay and satellite initial phase bias. GPS data from several IGS stations were processed using an un-differenced model, an un-differenced model featuring satellite decoupled clock corrections (un-differenced-DC), a between-satellite single-difference (BSSD) model, and a between-satellite single-difference model using the decoupled clock (BSSD-DC). BSSD and BSSD-DC solutions were compared using the un-differenced solution in terms of positioning solution accuracy and convergence time. Several conclusions from this investigation and recommendations for future research were provided in the following sections.

6.2 Conclusions

Proper modeling of the stochastic characteristics of the GPS observables can improve the convergence time of the estimated coordinates by up to 40%, especially for horizontal components. To fully explore the modernized L2C signal, the differential code bias $DCB_{P2\text{-}C2}$ was estimated using Bernese GPS software. The results showed that the values of $DCB_{P2\text{-}C2}$ were consistent in the range of ±1 ns. The implementation of the modernized GPS L2C signal with proper error modeling yielded promising results of the L2C code effect in terms of the solution stability and convergence time.

A complete modeling for the second-order ionospheric delay was also developed, and its effect on the GPS satellite orbit and clock corrections was also investigated. Neglecting the second-order ionospheric delay caused an orbital error ranging from 1.5 to 24.7 mm in radial, 2.7 to 18.6 mm along-track, and 3.2 to 15.9 mm in cross-track directions, respectively; failure to account for the delay also resulted in a satellite clock error of up to 0.067 ns (i.e., equivalent to a ranging error of 2 cm). Moreover, neglecting the second-order ionospheric delay caused an absolute error of up to 4.28 TECU (i.e., equivalent to a ranging error of 0.70 m on L1 frequency observations) in GIM values. Furthermore, the results demonstrated an improvement in the precision of the estimated coordinates up to 25% with consideration of the second-order ionospheric delay, as well as reduction of the convergence time of the estimated parameters by about 15%, depending on the geographic location and ionospheric and geomagnetic conditions.

Between-satellite single-difference (BSSD) algorithms, which cancel out the receiver clock error, receiver initial phase bias, and receiver hardware delay, were developed. The decoupled clock corrections, provided by NRCan, were applied to account for code and carrier-phase satellite clock corrections. The decoupled clock corrections were used with the un-differenced and BSSD models (un-differenced-DC and BSSD-DC, respectively). The results from the three models (un-differenced-DC, BSSD and BSSD-DC) were compared with the traditional (un-differenced) solution. The proposed BSSD model significantly improved the PPP convergence time by 50% and improved the solution precision more than 60% compared with the traditional PPP model.

6.3 Recommendations

To further improve the findings of this dissertation, further research is needed in the following areas:

- The developed BSSD-DC model is the key to ambiguity resolution in precise point positioning. More studies are required to implement and test ambiguity resolution techniques along with the developed models.
- More studies are required to take into account the temporal correlation of GPS observables.
- More studies are required to investigate and implement the new signals in Block IIF and Block III. This should have a significant impact on the GPS positioning accuracy and convergence time.

APPENDIX A: RESULTS FROM THE DEVELOPED STOCHASTIC MODELS

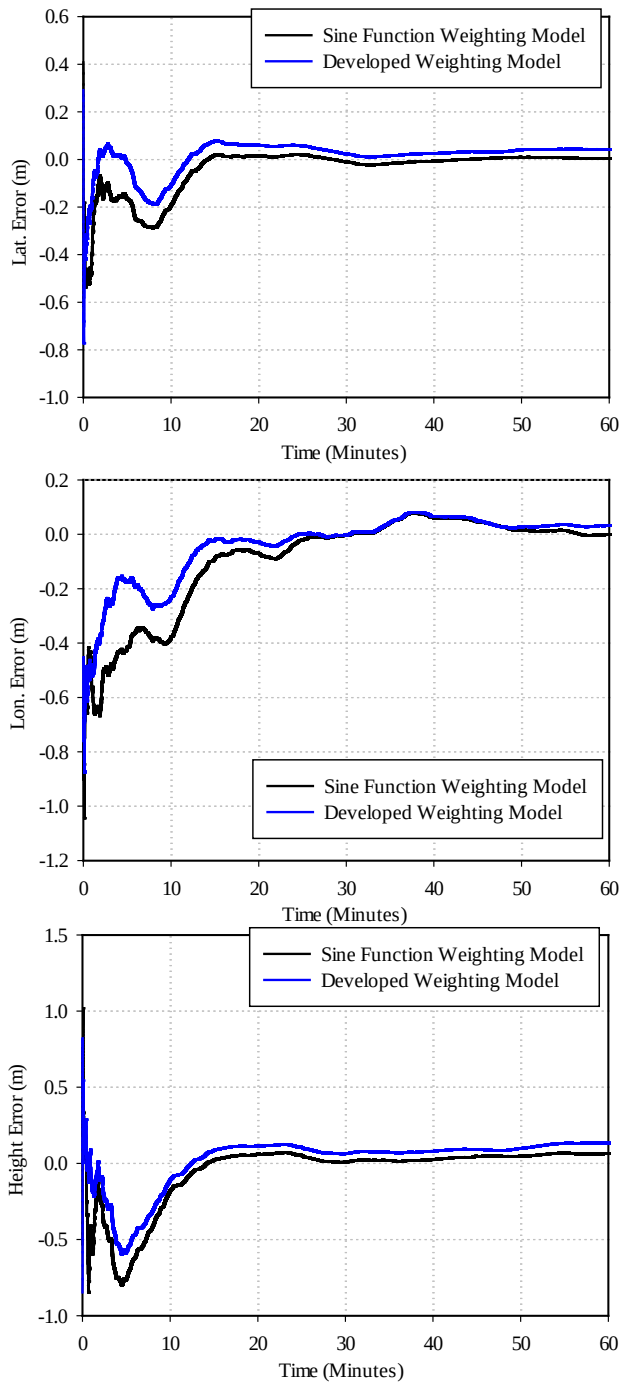

Figure A.1 Position Improvement Using the New Developed

Weighting Models (Session 01)

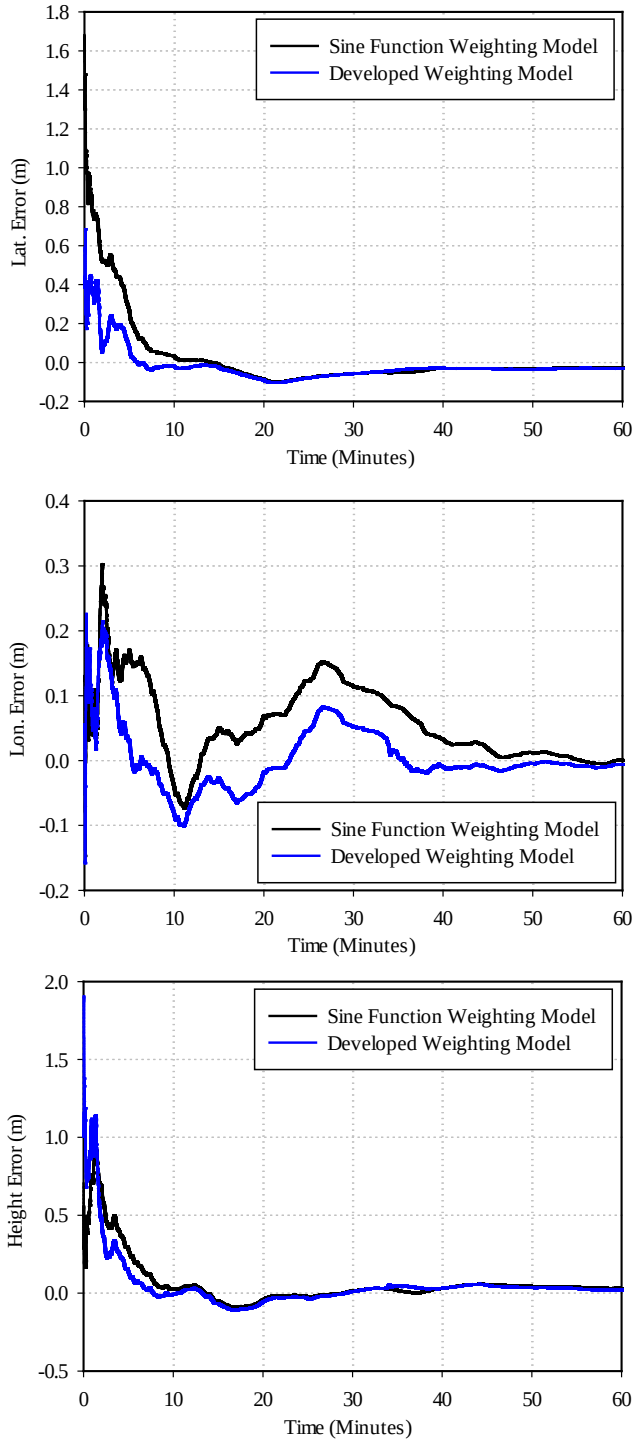

Figure A.2 Position Improvement Using the New Developed Weighting Models (Session 02)

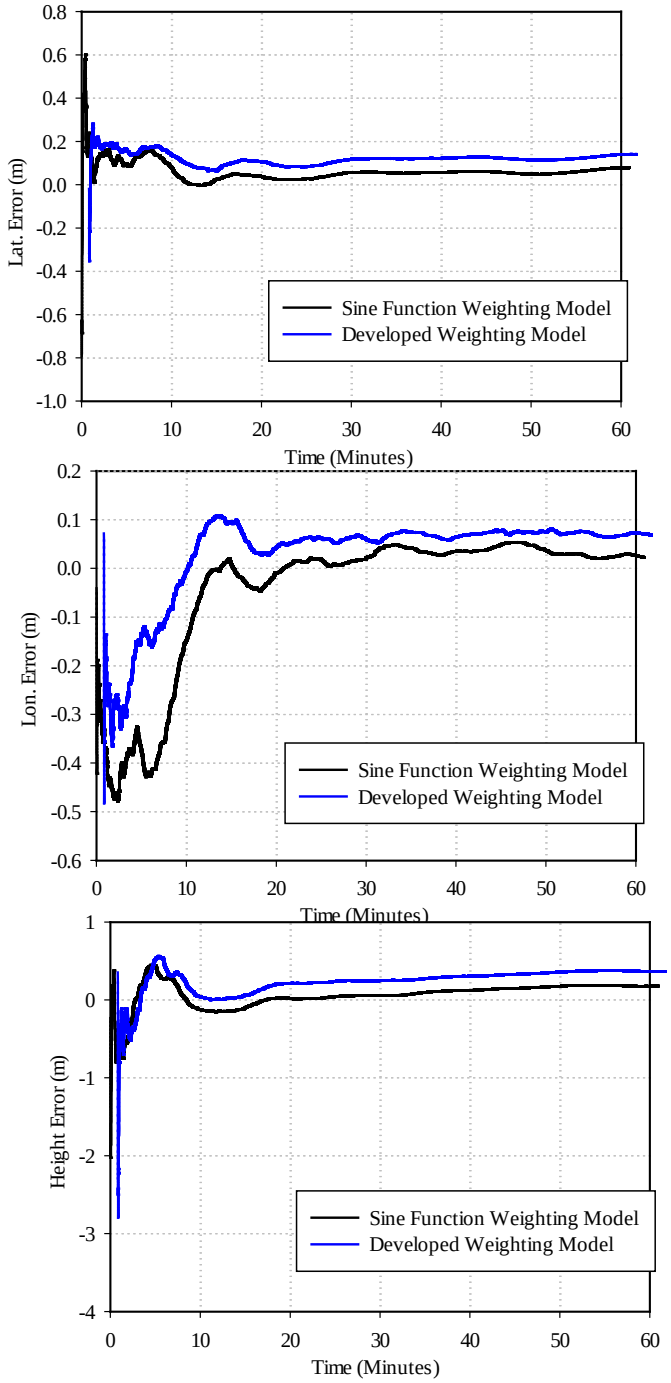

Figure A.3 Position Improvement Using the New Developed Weighting Models (Session 03)

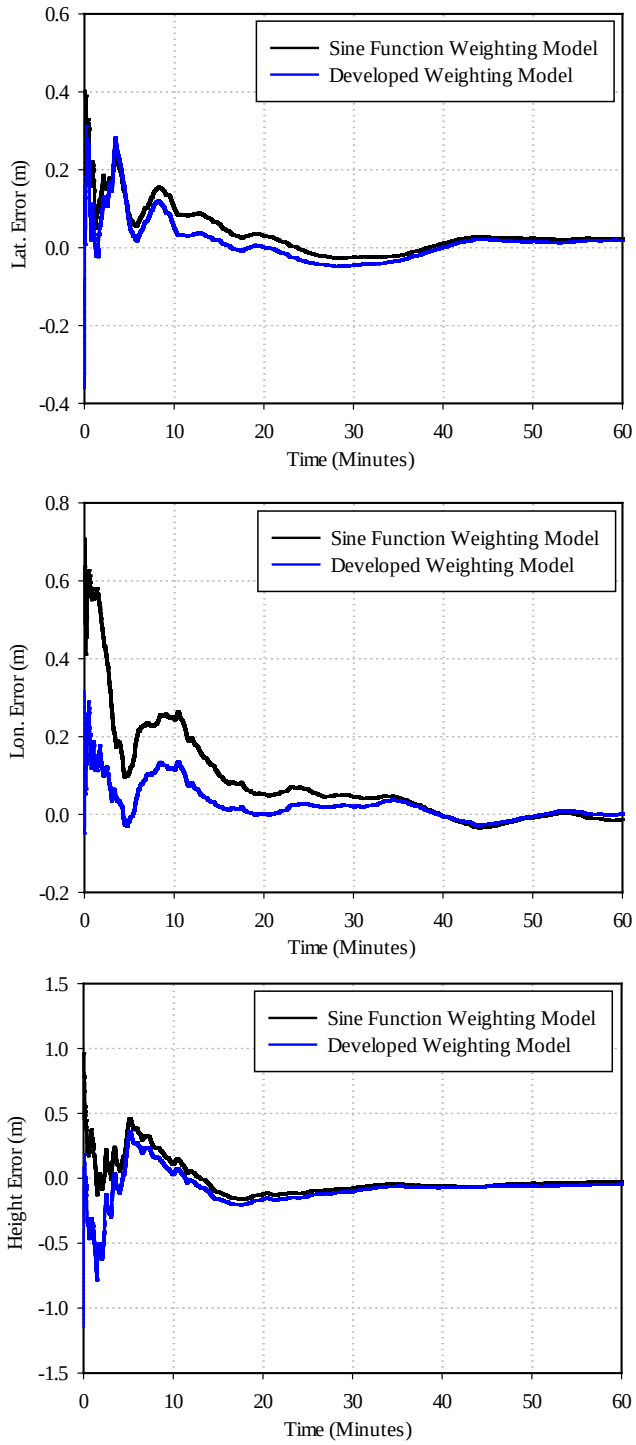

Figure A.4 Position Improvement Using the New Developed Weighting Models (Session 04)

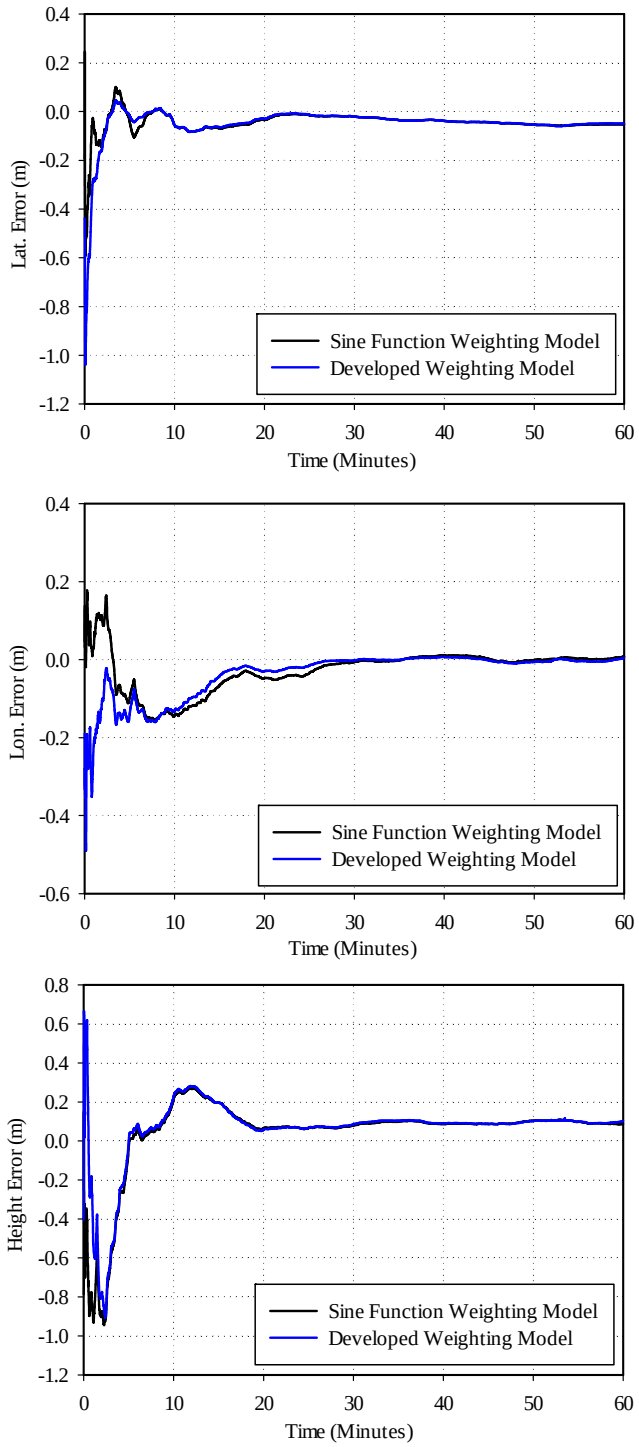

Figure A.5 Position Improvement Using the New Developed Weighting Models (Session 05)

APPENDIX B: EFFECT OF L2C ON PPP SOLUTION

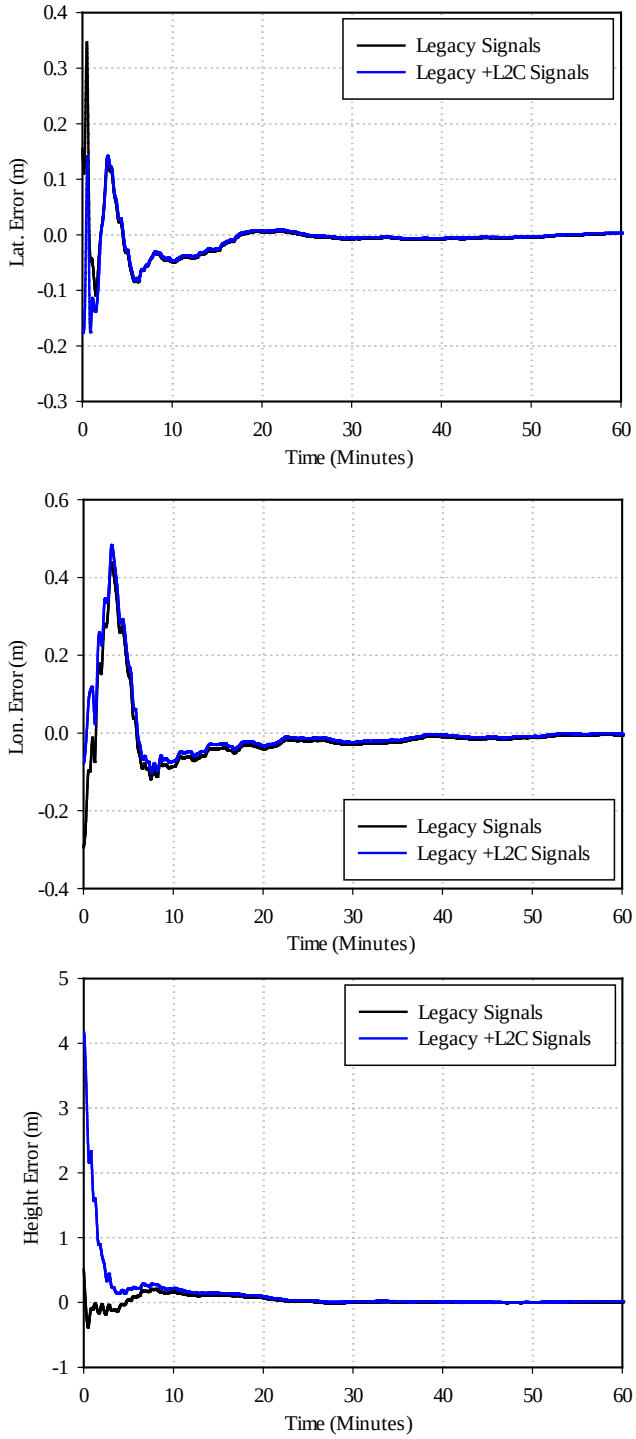

Figure B.1 Position Improvement Using the Modernized L2C Signal

OURI IGS Station (Session 01)

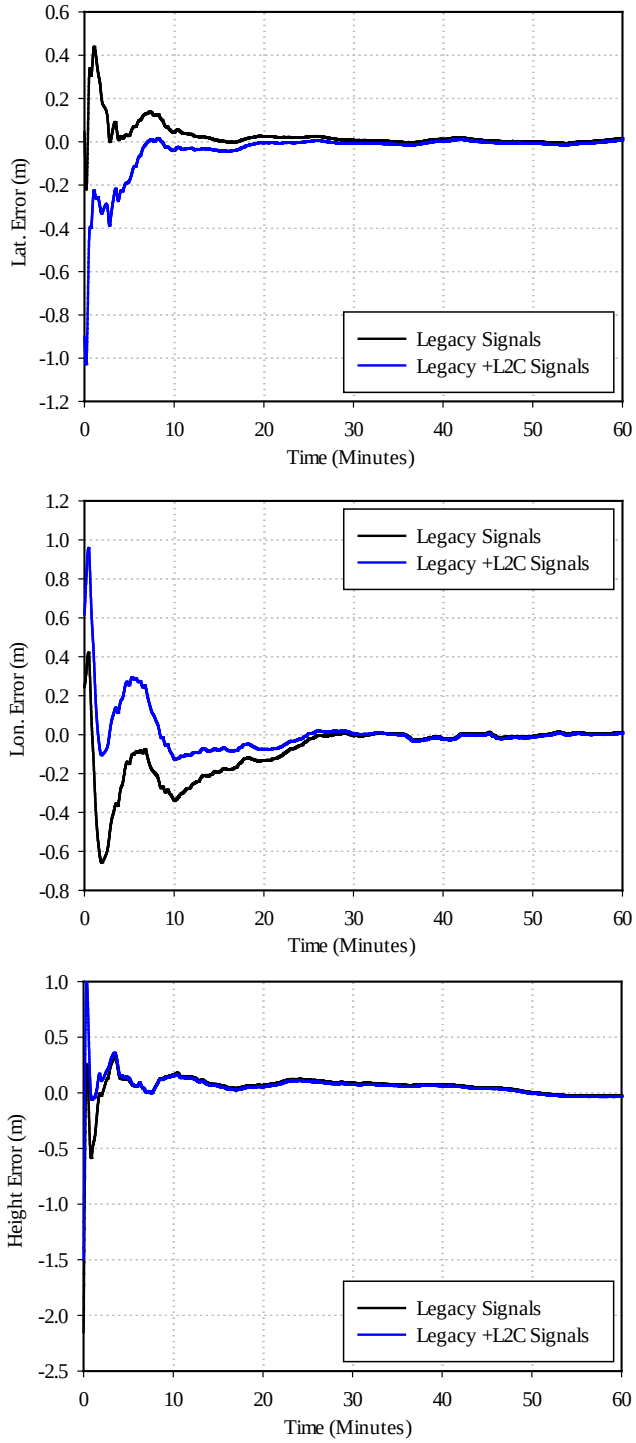

Figure B.2 Position Improvement Using the Modernized L2C Signal

OURI IGS Station (Session 02)

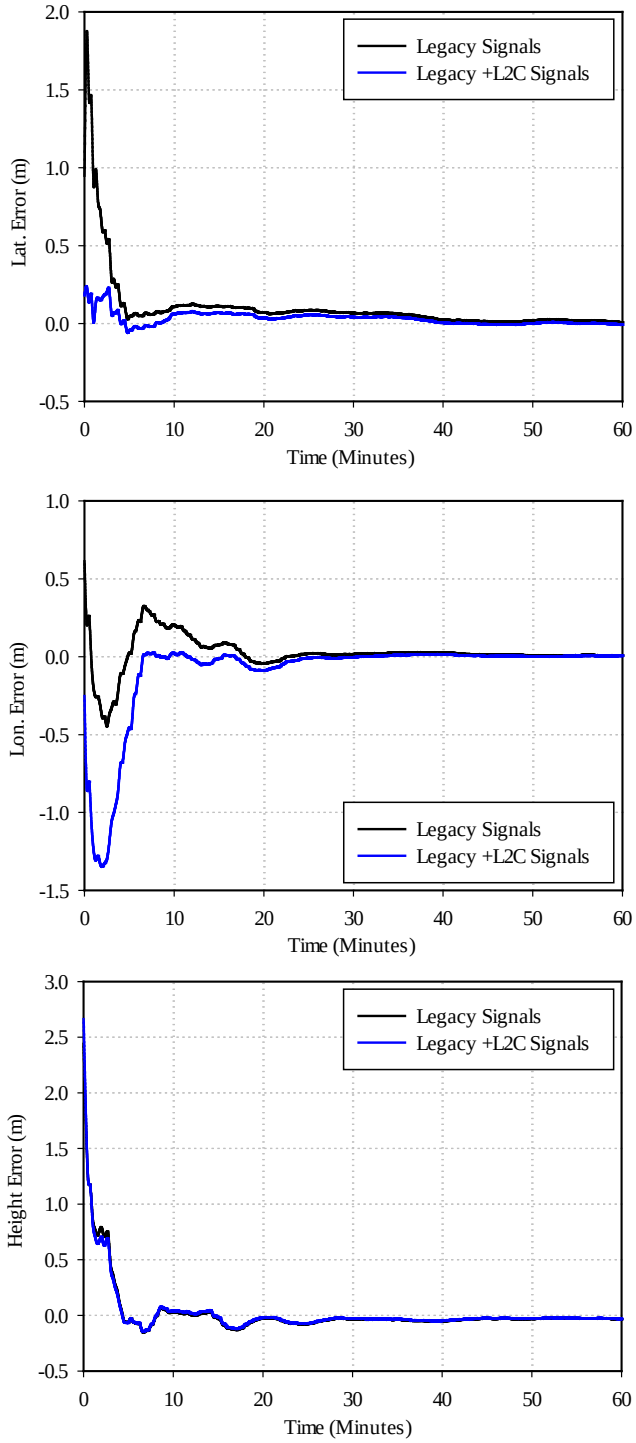

Figure B.3 Latitude Improvement Using the Modernized L2C Signal

ROSA IGS Station (Session 01)

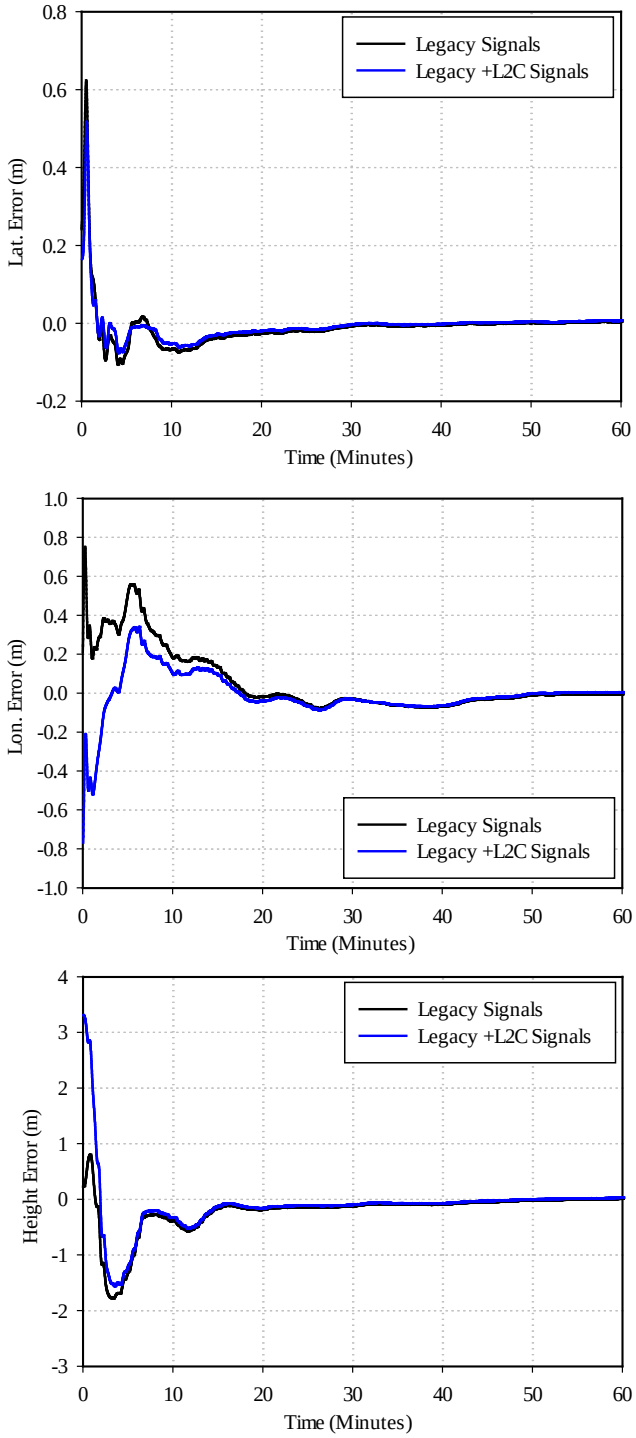

Figure B.4 Position Improvement Using the Modernized L2C Signal

ROSA IGS Station (Session 02)

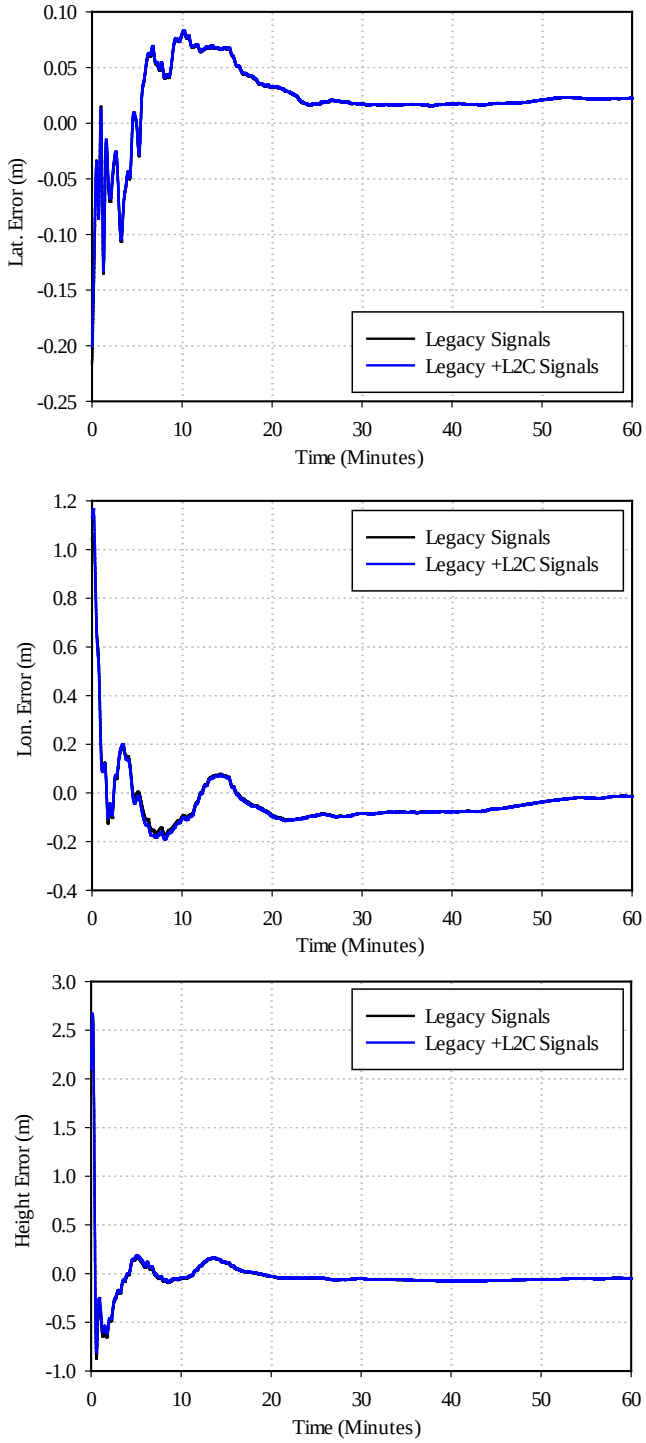

Figure B.5 Position Improvement Using the Modernized L2C Signal

ROSA IGS Station (Session 03)

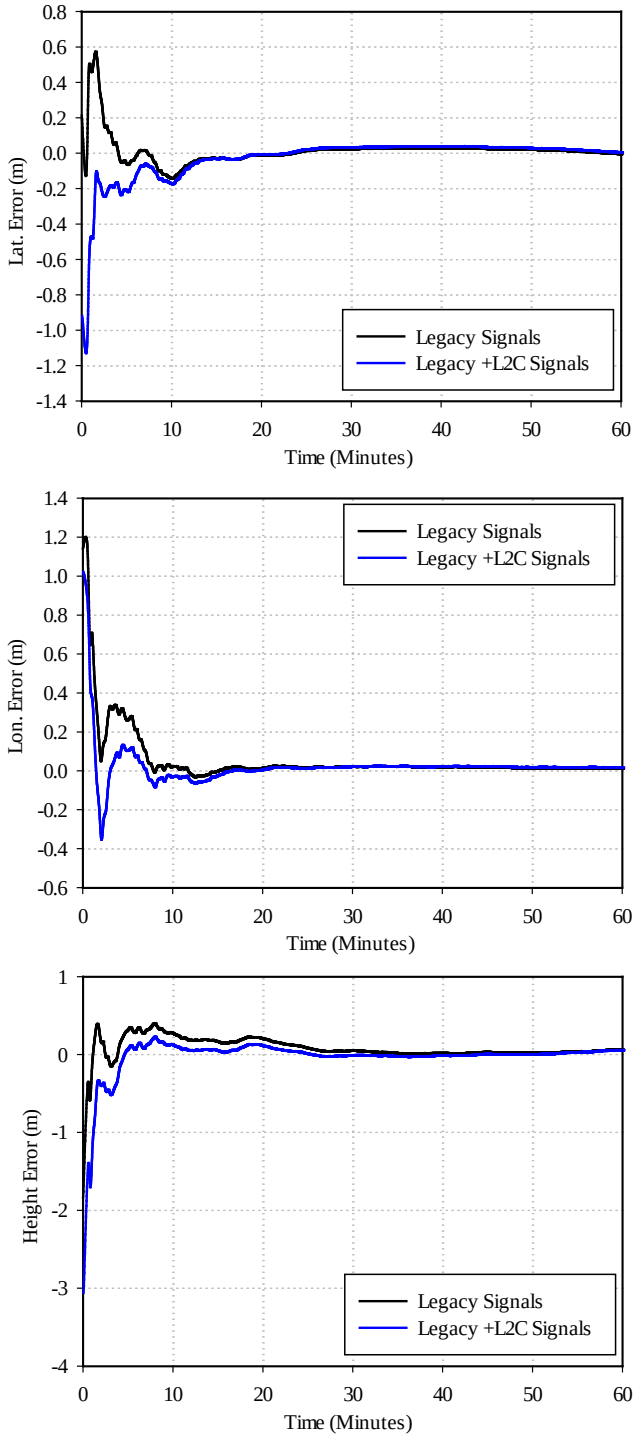

Figure B.6 Position Improvement Using the Modernized L2C Signal

UNB3 IGS Station (Session 01)

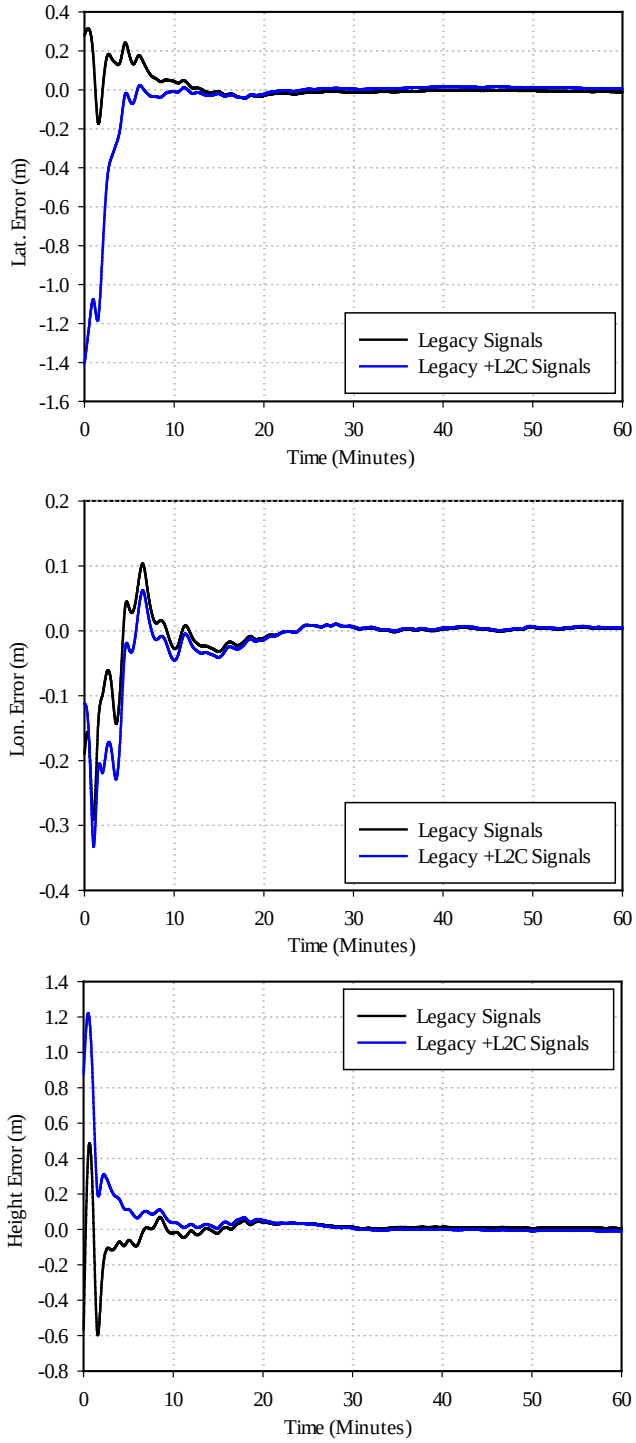

Figure B.7 Position Improvement Using the Modernized L2C Signal

UNB3 IGS Station (Session 02)

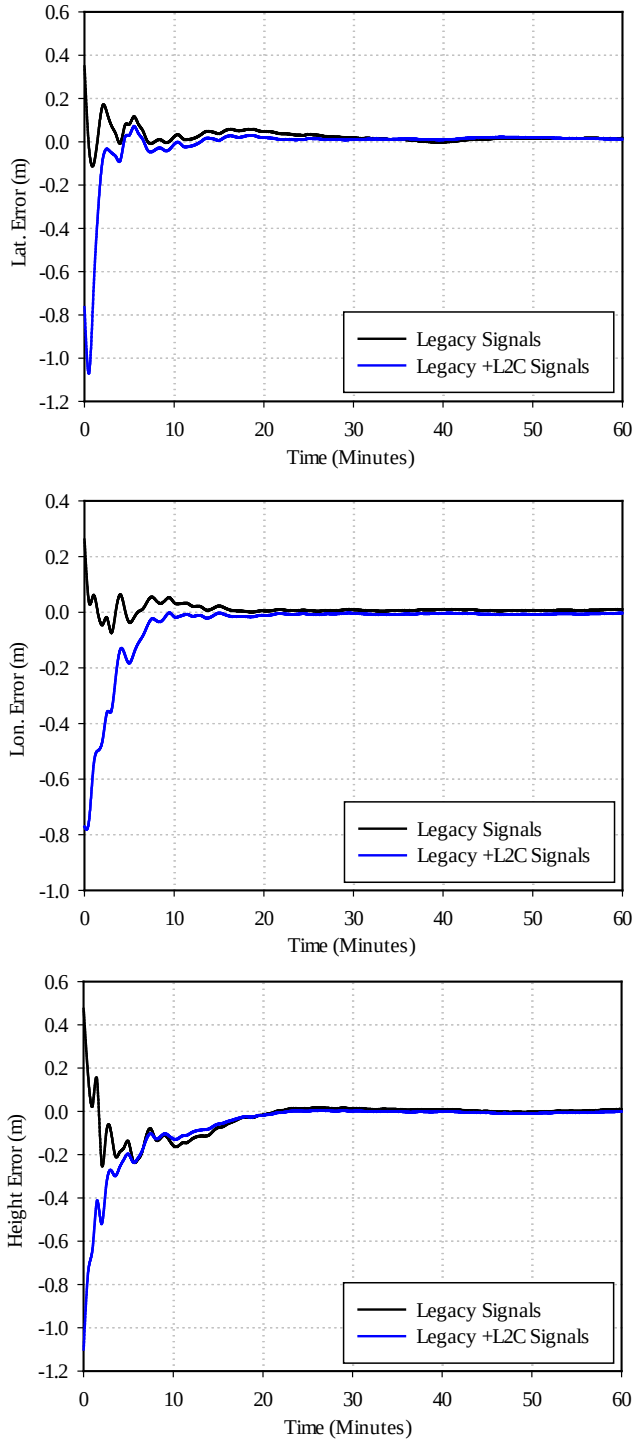

Figure B.8 Position Improvement Using the Modernized L2C Signal

ZIM2 IGS Station (Session 01)

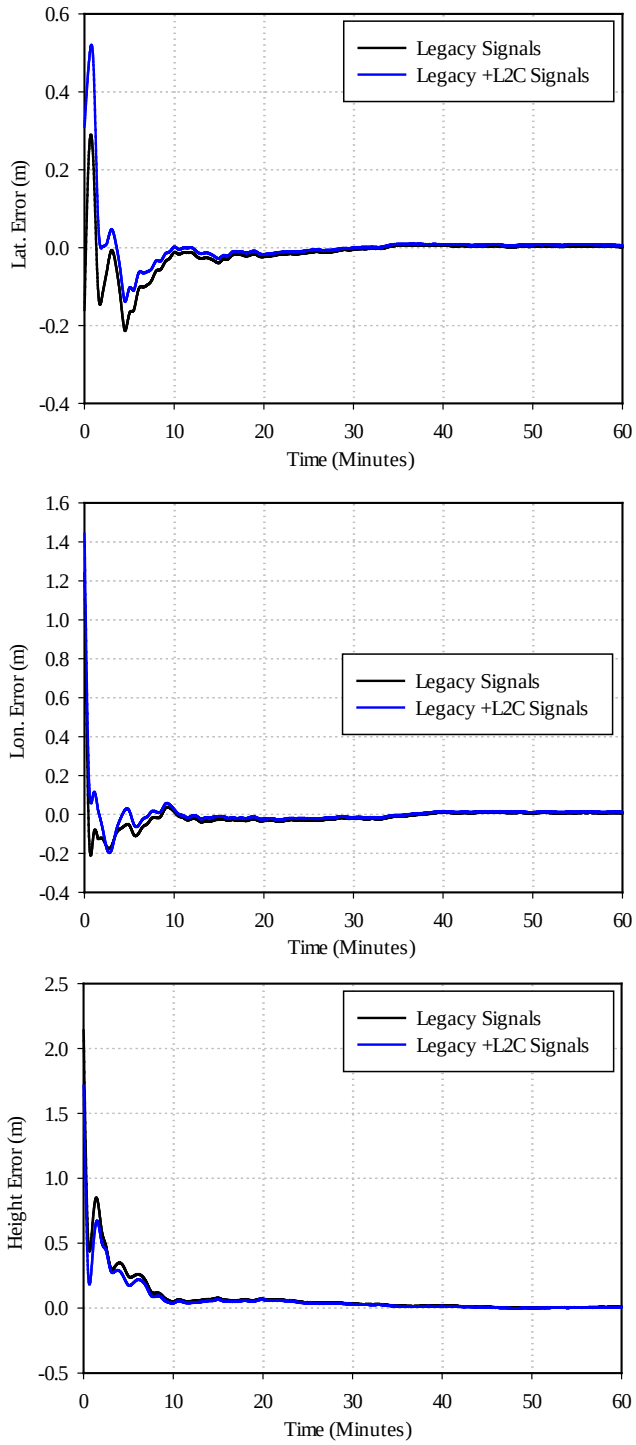

Figure B.9 Position Improvement Using the Modernized L2C Signal

ZIM2 IGS Station (Session 02)

APPENDIX C: PRECISE SATELLITE ORBIT DETERMINATION USING BERNESE GPS SOFTWARE

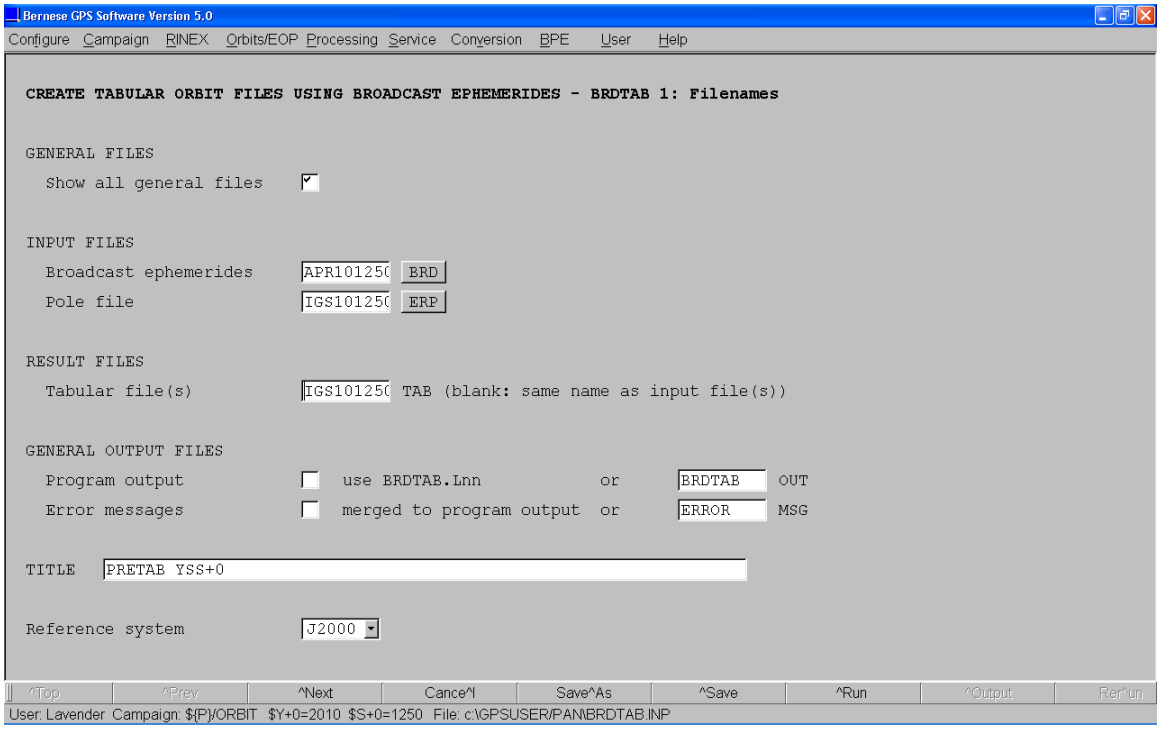

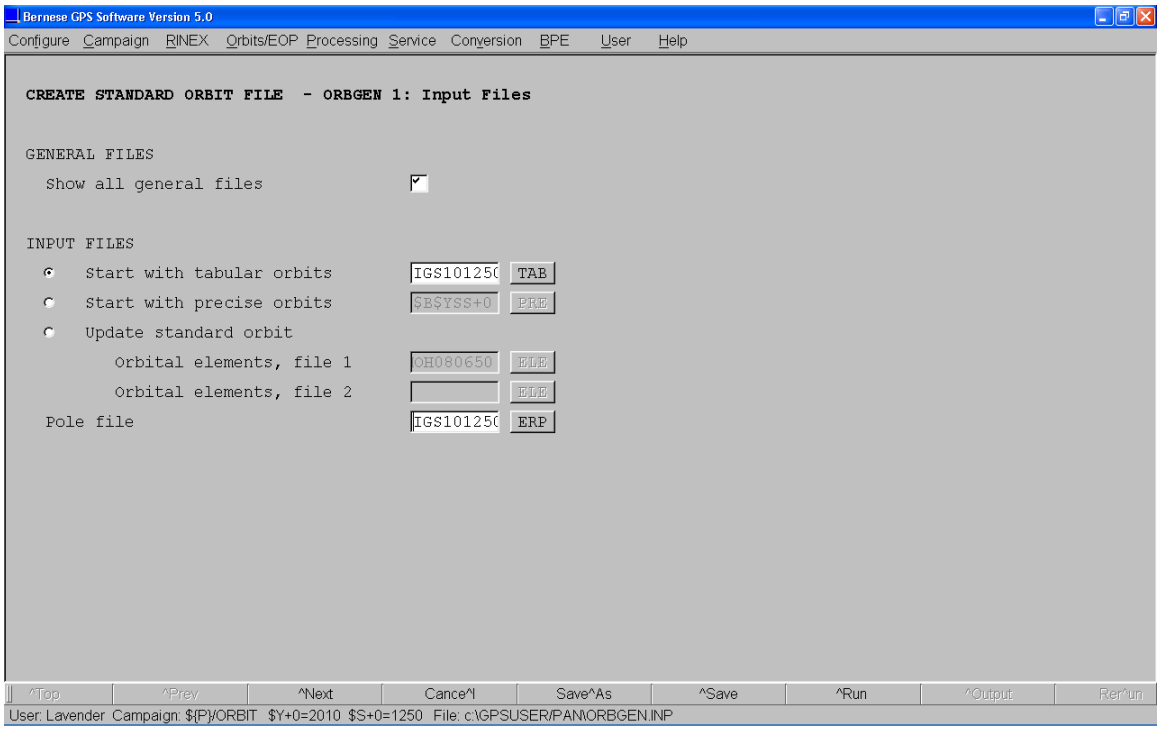

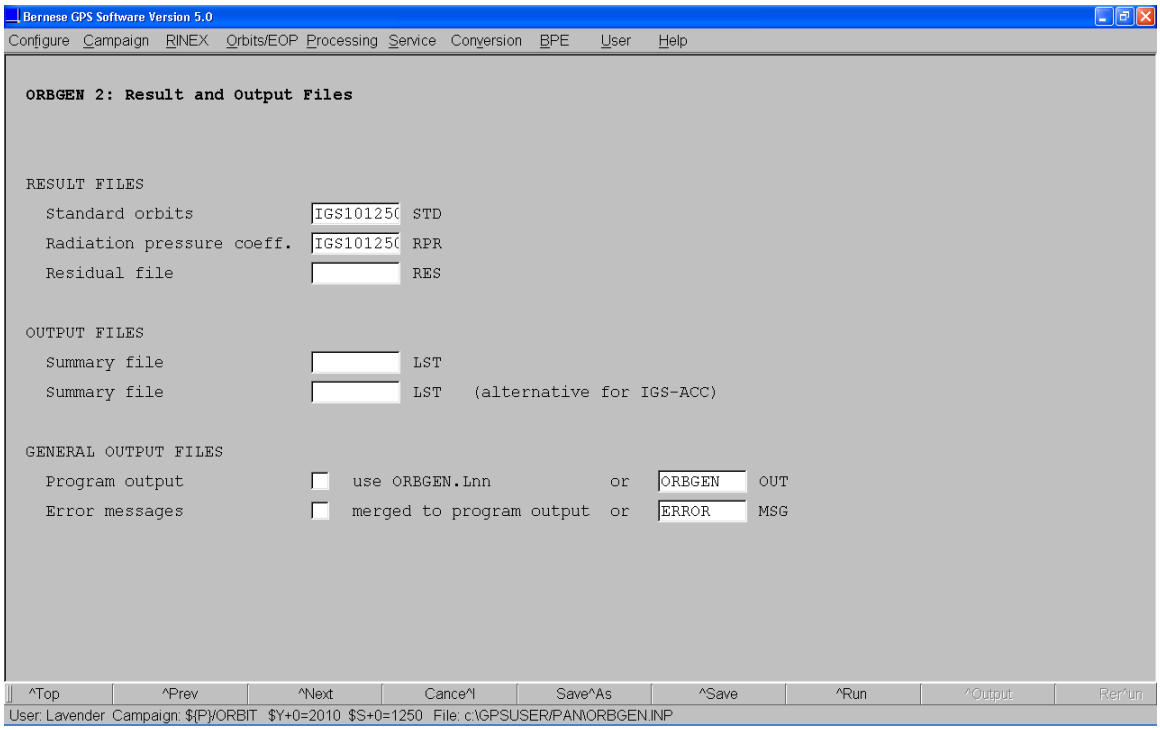
Bernese GPS Software Version 5.0
Configure Campaign RINEX Orbits/EOP Processing Service Conversion BPE User Help
ORBGEN 2: Result and Output Files
RESULT FILES
Standard orbits IGS101250 STD
Radiation pressure coeff. IGS101250 RPR
Residual file RES
OUTPUT FILES
Summary file LST
Summary file LST (alternative for IGS-ACC)
GENERAL OUTPUT FILES
Program output use ORBGEN.Lnn or ORBGEN OUT
Error messages merged to program output or ERROR MSG
^Top ^Prev ^Next Cance^l Save^As ^Save ^Run ^Output Re^un
User: Lavender Campaign: ${P}/ORBIT $Y+0=2010 $S+0=1250 File: c:\GPSUSER/PAN\ORBGEN.INP

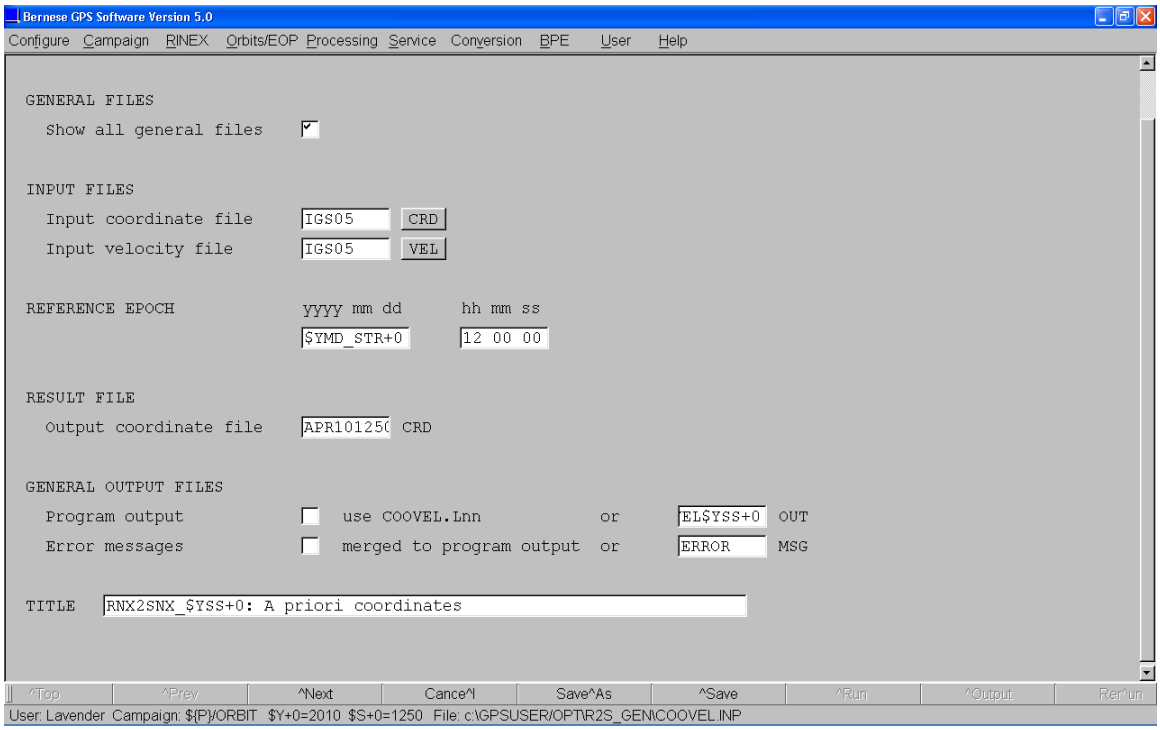
Bernese GPS Software Version 5.0
Configure Campaign RINEX Orbits/EOP Processing Service Conversion BPE User Help
GENERAL FILES
Show all general files
INPUT FILES
Input coordinate file IGS05 CRD
Input velocity file IGS05 VEL
REFERENCE EPOCH yyyy mm dd hh mm ss
$YMD_STR+0 12 00 00
RESULT FILE
Output coordinate file APR101250 CRD
GENERAL OUTPUT FILES
Program output use COOVEL.Lnn or EL$YSS+0 OUT
Error messages merged to program output or ERROR MSG
TITLE RNX2SNX_$YSS+0: A priori coordinates
^Top ^Prev ^Next Cance^l Save^As ^Save ^Run ^Output Re^un
User: Lavender Campaign: ${P}/ORBIT $Y+0=2010 $S+0=1250 File: c:\GPSUSER/OPT\R2S_GEN\COOVEL.INP

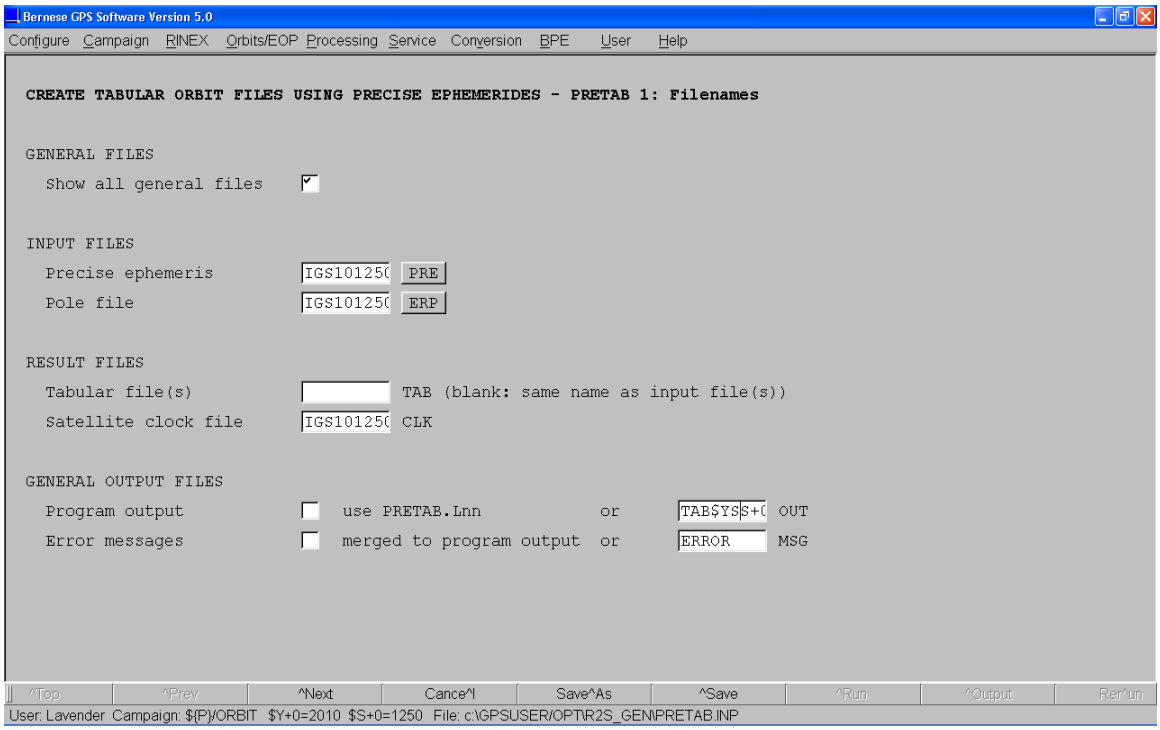
Bernese GPS Software Version 5.0
Configure Campaign RINEX Orbits/EOP Processing Service Conversion BPE User Help
CREATE TABULAR ORBIT FILES USING PRECISE EPHEMERIDES - PRETAB 1: Filenames
GENERAL FILES
Show all general files
INPUT FILES
Precise ephemeris IGS101250 PRE
Pole file IGS101250 ERP
RESULT FILES
Tabular file(s) TAB (blank: same name as input file(s))
Satellite clock file IGS101250 CLK
GENERAL OUTPUT FILES
Program output use PRETAB.Lnn or TABYSS+0 OUT
Error messages merged to program output or ERROR MSG
^Top ^Prev ^Next Cance^l Save^As ^Save ^Run ^Output Re^un
User: Lavender Campaign: ${P}/ORBIT $Y+0=2010 $S+0=1250 File: c:\GPSUSER/OPT\R2S_GEN\PRETAB.INP

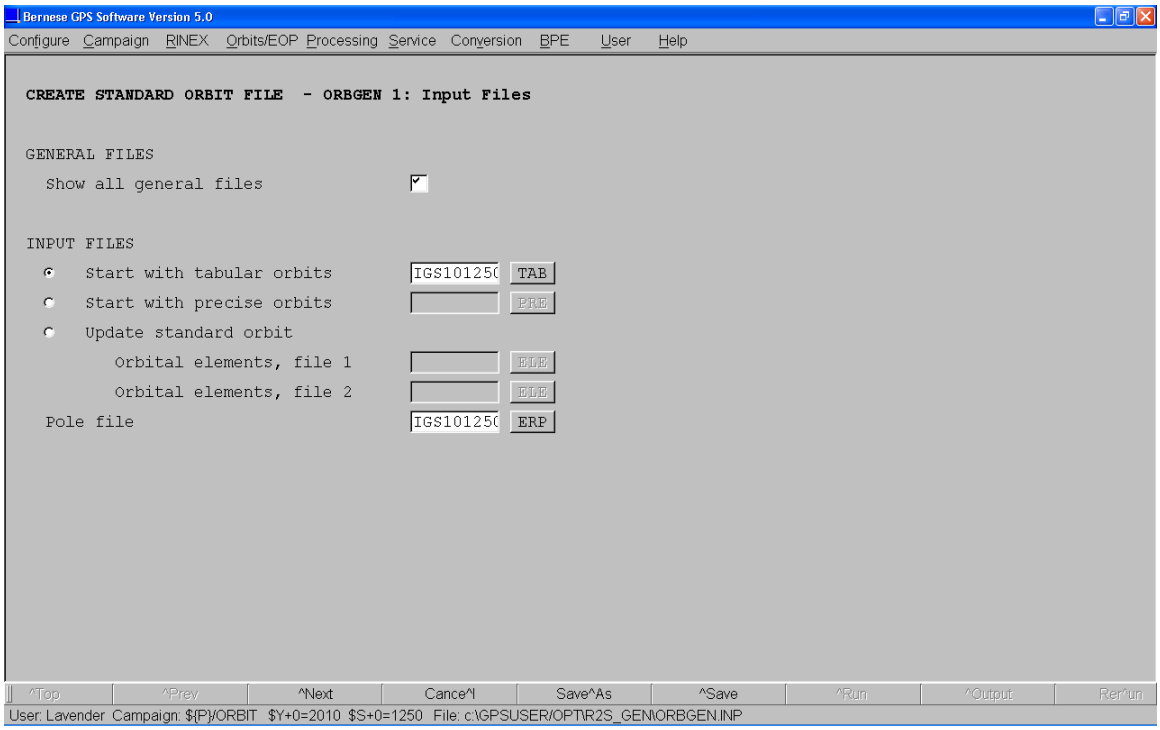
Bernese GPS Software Version 5.0
Configure Campaign RINEX Orbits/EOP Processing Service Conversion BPE User Help
CREATE STANDARD ORBIT FILE - ORBGEN 1: Input Files
GENERAL FILES
Show all general files
INPUT FILES
Start with tabular orbits IGS101250 TAB
Start with precise orbits PRE
Update standard orbit
Orbital elements, file 1 ELE
Orbital elements, file 2 ELE
Pole file IGS101250 ERP
^Top ^Prev ^Next Cance^l Save^As ^Save ^Run ^Output Re^un
User: Lavender Campaign: ${P}/ORBIT $Y+0=2010 $S+0=1250 File: c:\GPSUSER/OPT\R2S_GEN\ORBGEN.INP

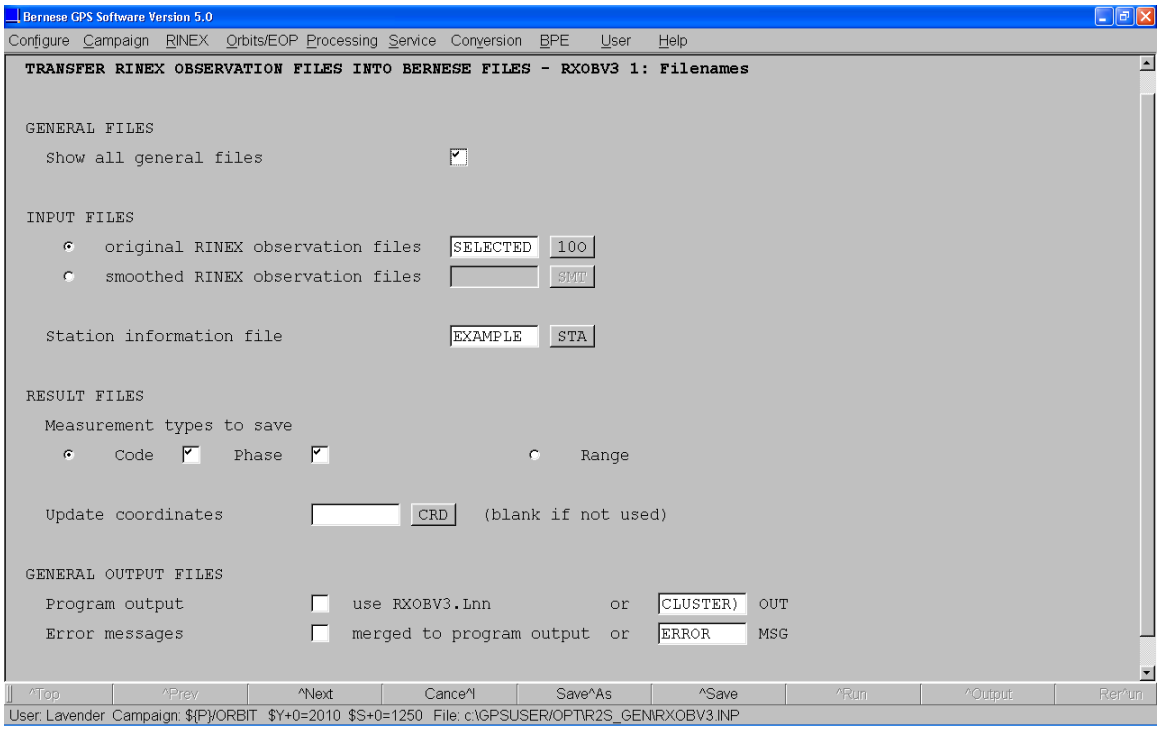
Bernese GPS Software Version 5.0
Configure Campaign RINEX Orbits/EOP Processing Service Conversion BPE User Help
TRANSFER RINEX OBSERVATION FILES INTO BERNESE FILES - RXOBV3 1: Filenames
GENERAL FILES
Show all general files
INPUT FILES
original RINEX observation files
SELECTED
100
smoothed RINEX observation files
SMT
Station information file
EXAMPLE
STA
RESULT FILES
Measurement types to save
Code
Phase
Range
Update coordinates
CRD
(blank if not used)
GENERAL OUTPUT FILES
Program output
use RXOBV3.Lnn
or
CLUSTER)
OUT
Error messages
merged to program output
or
ERROR
MSG
^Top
^Prev
^Next
Cance^l
Save^As
^Save
^Run
^Output
Re^un
User: Lavender Campaign: ${P}/ORBIT $Y+0=2010 $S+0=1250 File: c:\GPSUSER/OPT\R2S_GEN\RXOBV3.INP

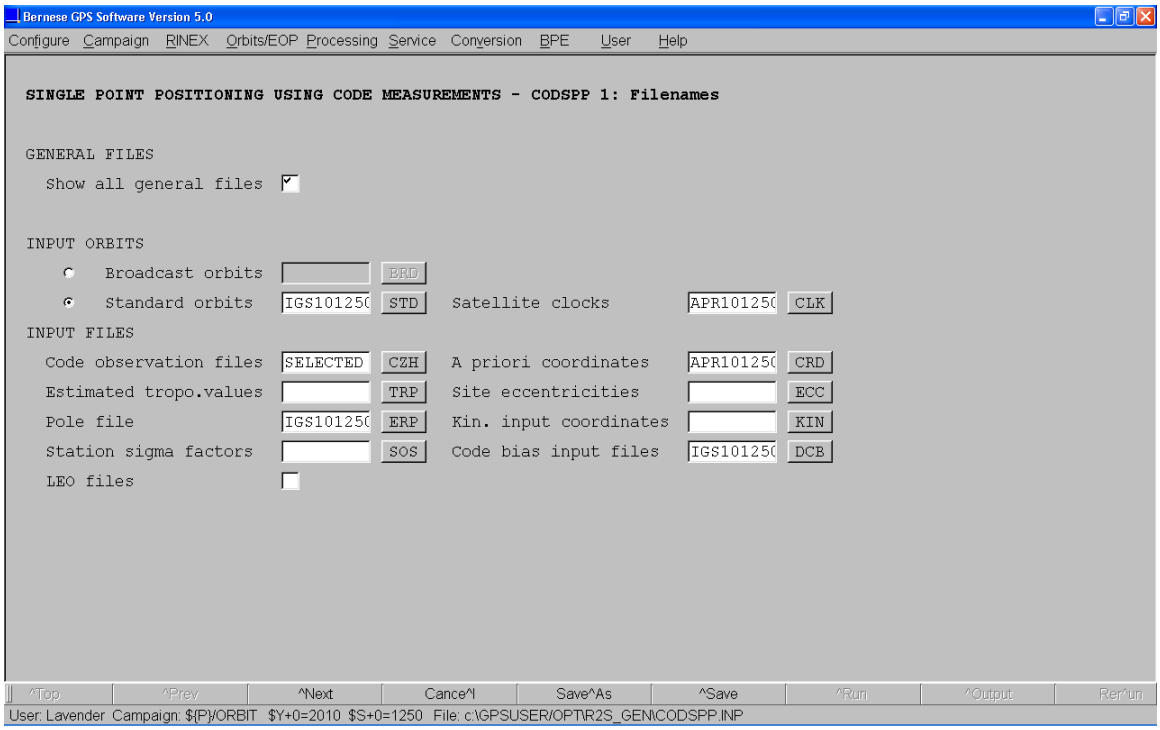
Bernese GPS Software Version 5.0
Configure Campaign RINEX Orbits/EOP Processing Service Conversion BPE User Help
SINGLE POINT POSITIONING USING CODE MEASUREMENTS - CODSPP 1: Filenames
GENERAL FILES
Show all general files
INPUT ORBITS
Broadcast orbits
BRD
Standard orbits
IGS10125(
STD
Satellite clocks
APR10125(
CLK
INPUT FILES
Code observation files
SELECTED
CZH
A priori coordinates
APR10125(
CRD
Estimated tropo.values
TRP
Site eccentricities
ECC
Pole file
IGS10125(
ERP
Kin. input coordinates
KIN
Station sigma factors
SOS
Code bias input files
IGS10125(
DCB
LEO files
^Top
^Prev
^Next
Cance^l
Save^As
^Save
^Run
^Output
Re^un
User: Lavender Campaign: ${P}/ORBIT $Y+0=2010 $S+0=1250 File: c:\GPSUSER/OPT\R2S_GEN\CODSPP.INP

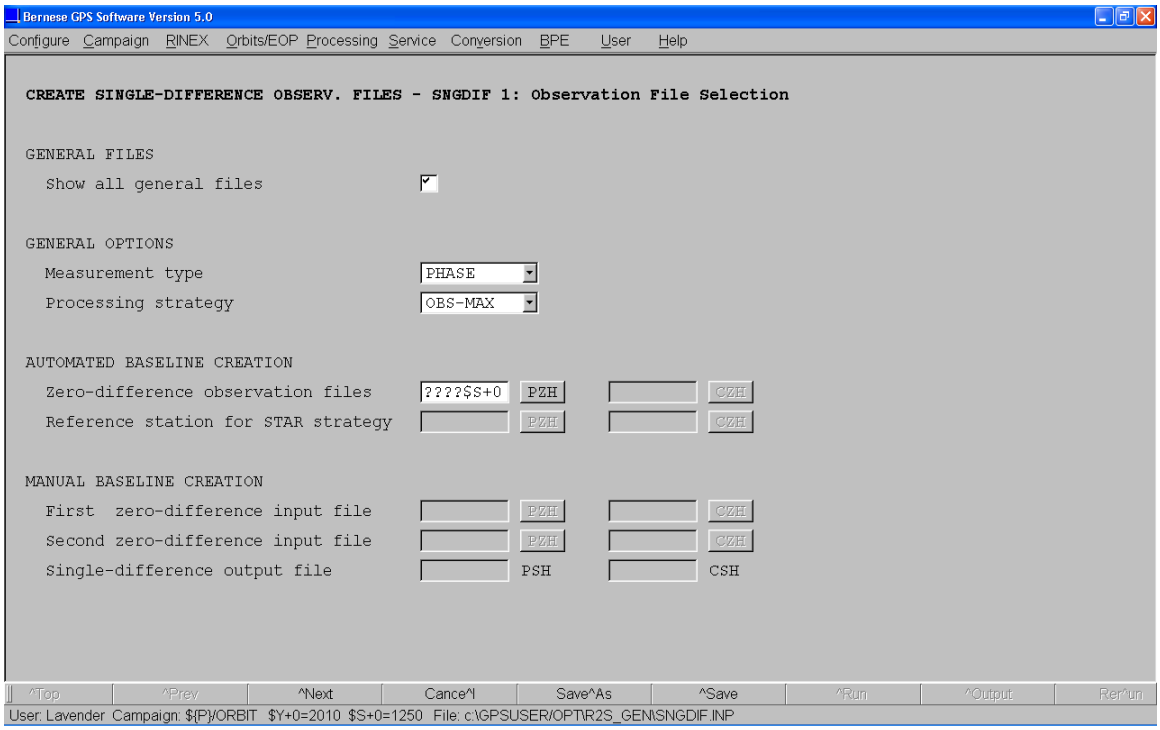
Bernese GPS Software Version 5.0
Configure Campaign RINEX Orbits/EOP Processing Service Conversion BPE User Help
CREATE SINGLE-DIFFERENCE OBSERV. FILES - SNGDIF 1: Observation File Selection
GENERAL FILES
Show all general files
GENERAL OPTIONS
Measurement type
PHASE
Processing strategy
OBS-MAX
AUTOMATED BASELINE CREATION
Zero-difference observation files
????$S+0
PZH
CZH
Reference station for STAR strategy
PZH
CZH
MANUAL BASELINE CREATION
First zero-difference input file
PZH
CZH
Second zero-difference input file
PZH
CZH
Single-difference output file
PSH
CSH
^Top
^Prev
^Next
Cance^l
Save^As
^Save
^Run
^Output
Re^un
User: Lavender Campaign: ${P}/ORBIT $Y+0=2010 $S+0=1250 File: c:\GPSUSER/OPT\R2S_GEN\SNGDIF.INP

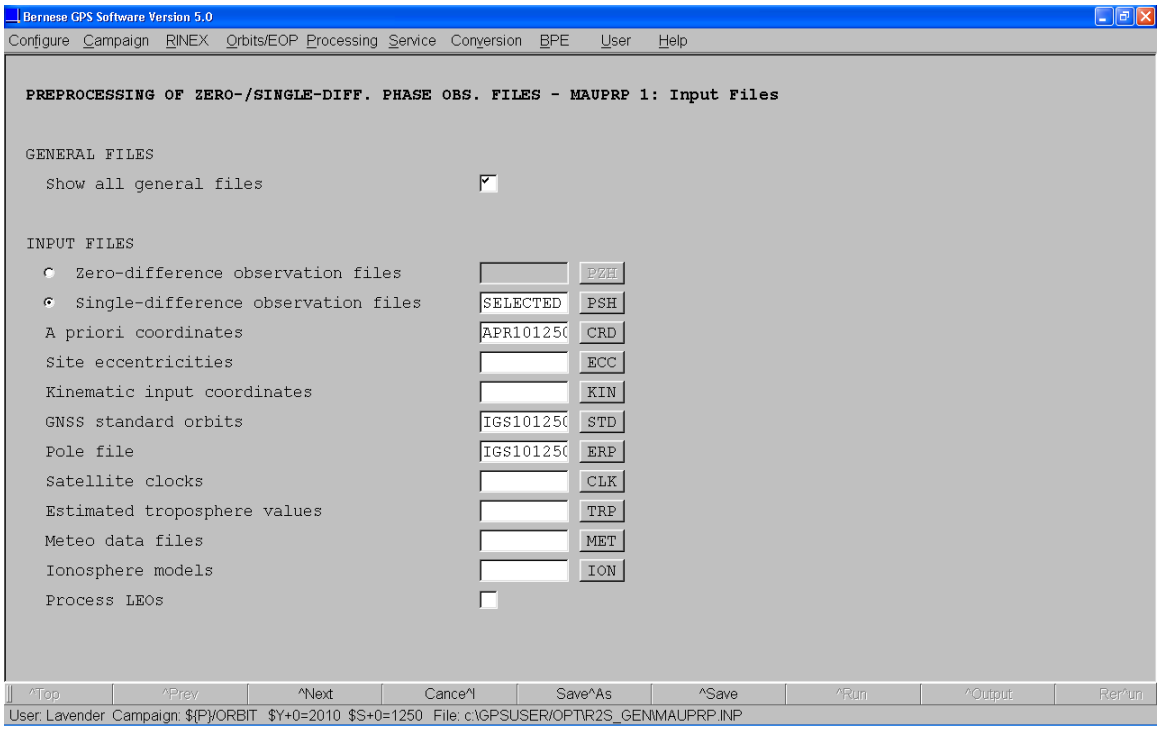
Bernese GPS Software Version 5.0
Configure Campaign RINEX Orbits/EOP Processing Service Conversion BPE User Help
PREPROCESSING OF ZERO-/SINGLE-DIFF. PHASE OBS. FILES - MAUPRP 1: Input Files
GENERAL FILES
Show all general files
INPUT FILES
Zero-difference observation files
PZH
Single-difference observation files
SELECTED
PSH
A priori coordinates
APR10125(
CRD
Site eccentricities
ECC
Kinematic input coordinates
KIN
GNSS standard orbits
IGS10125(
STD
Pole file
IGS10125(
ERP
Satellite clocks
CLK
Estimated troposphere values
TRP
Meteo data files
MET
Ionosphere models
ION
Process LEOs
^Top
^Prev
^Next
Cance^l
Save^As
^Save
^Run
^Output
Re^un
User: Lavender Campaign: ${P}/ORBIT $Y+0=2010 $S+0=1250 File: c:\GPSUSER/OPT\R2S_GEN\MAUPRP.INP

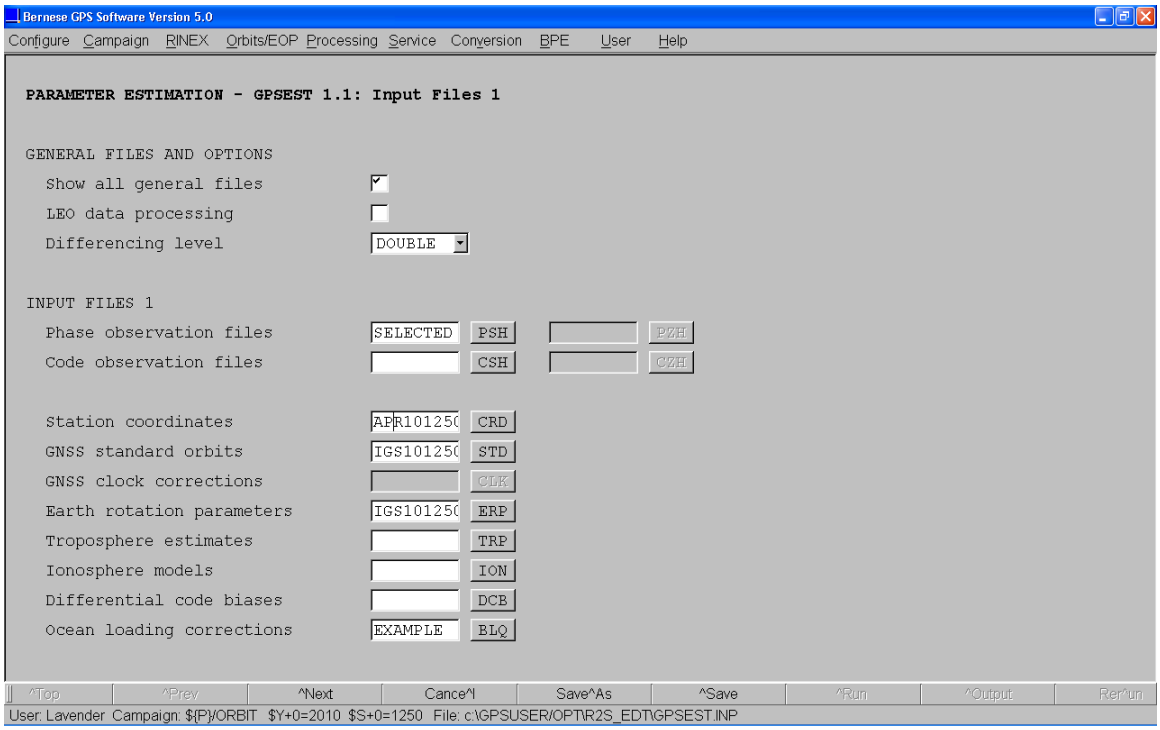
Bernese GPS Software Version 5.0
Configure Campaign RINEX Orbits/EOP Processing Service Conversion BPE User Help
PARAMETER ESTIMATION - GPSEST 1.1: Input Files 1
GENERAL FILES AND OPTIONS
Show all general files
LEO data processing
Differencing level
DOUBLE
INPUT FILES 1
Phase observation files
SELECTED
PSH
P2H
Code observation files
CSH
C2H
Station coordinates
APR101250
CRD
GNSS standard orbits
IGS101250
STD
GNSS clock corrections
CLK
Earth rotation parameters
IGS101250
ERP
Troposphere estimates
TRP
Ionosphere models
ION
Differential code biases
DCB
Ocean loading corrections
EXAMPLE
BLQ
^Top
^Prev
^Next
Cance^l
Save^As
^Save
^Run
^Output
Re^un
User: Lavender Campaign: ${P}/ORBIT $Y+0=2010 $S+0=1250 File: c:\GPSUSER/OPT\R2S_EDT\GPSEST.INP

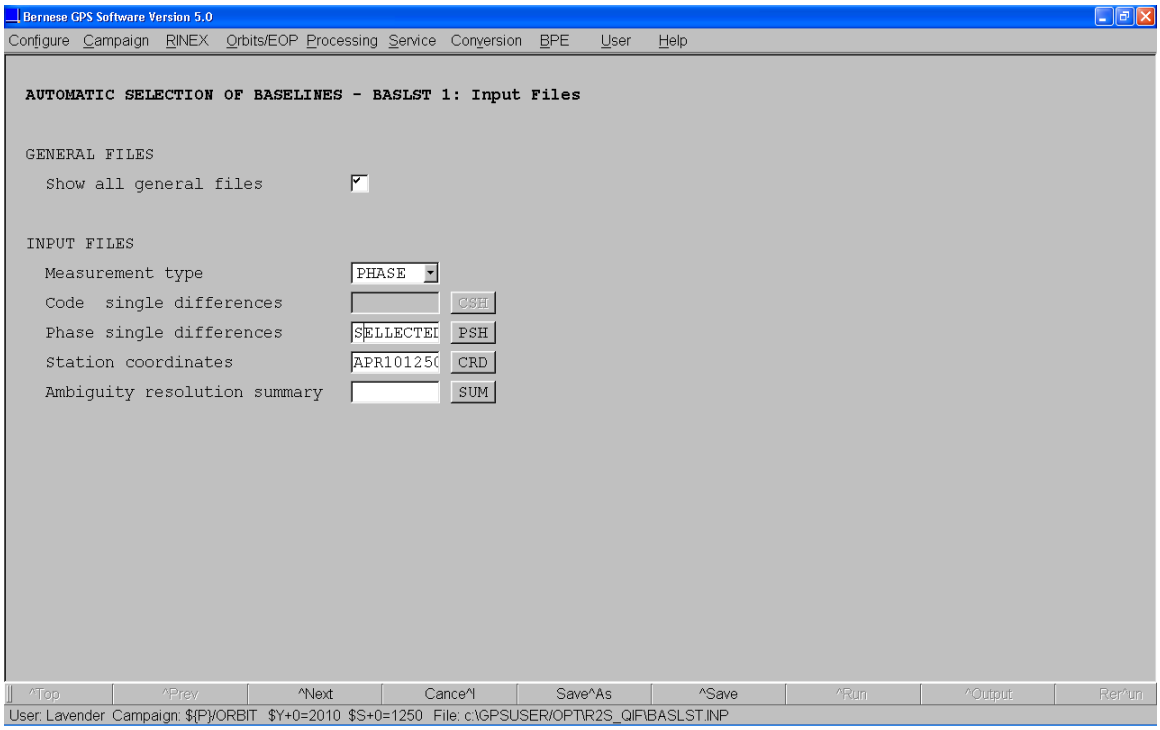
Bernese GPS Software Version 5.0
Configure Campaign RINEX Orbits/EOP Processing Service Conversion BPE User Help
AUTOMATIC SELECTION OF BASELINES - BASLST 1: Input Files
GENERAL FILES
Show all general files
INPUT FILES
Measurement type
PHASE
Code single differences
CSH
Phase single differences
SELLECTED
PSH
Station coordinates
APR101250
CRD
Ambiguity resolution summary
SUM
^Top
^Prev
^Next
Cance^l
Save^As
^Save
^Run
^Output
Re^un
User: Lavender Campaign: ${P}/ORBIT $Y+0=2010 $S+0=1250 File: c:\GPSUSER/OPT\R2S_QIF\BASLST.INP

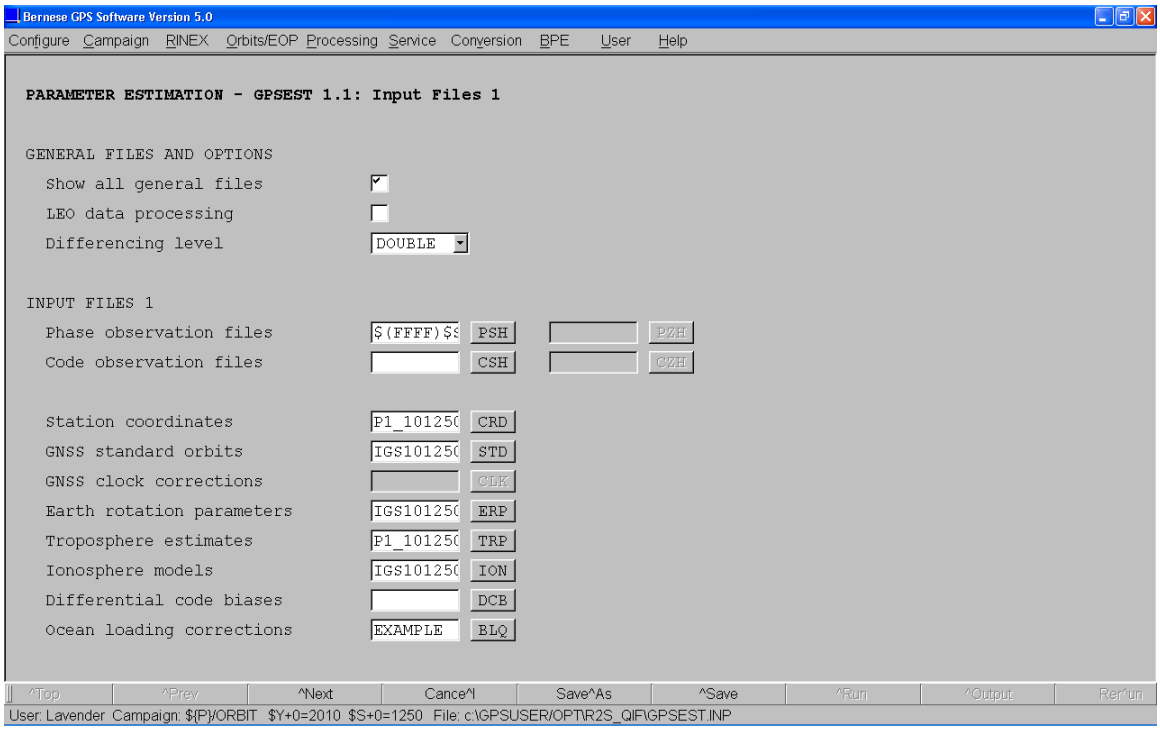
Bernese GPS Software Version 5.0
Configure Campaign RINEX Orbits/EOP Processing Service Conversion BPE User Help
PARAMETER ESTIMATION - GPSEST 1.1: Input Files 1
GENERAL FILES AND OPTIONS
Show all general files
LEO data processing
Differencing level
DOUBLE
INPUT FILES 1
Phase observation files
$(FFFF)$S
PSH
P2H
Code observation files
CSH
C2H
Station coordinates
P1_10125(
CRD
GNSS standard orbits
IGS10125(
STD
GNSS clock corrections
CLK
Earth rotation parameters
IGS10125(
ERP
Troposphere estimates
P1_10125(
TRP
Ionosphere models
IGS10125(
ION
Differential code biases
DCB
Ocean loading corrections
EXAMPLE
BLQ
^Top
^Prev
^Next
Cance^l
Save^As
^Save
^Run
^Output
Re^un
User: Lavender Campaign: ${P}/ORBIT $Y+0=2010 $S+0=1250 File: c:\GPSUSER/OPT\R2S_QIF\GPSEST.INP

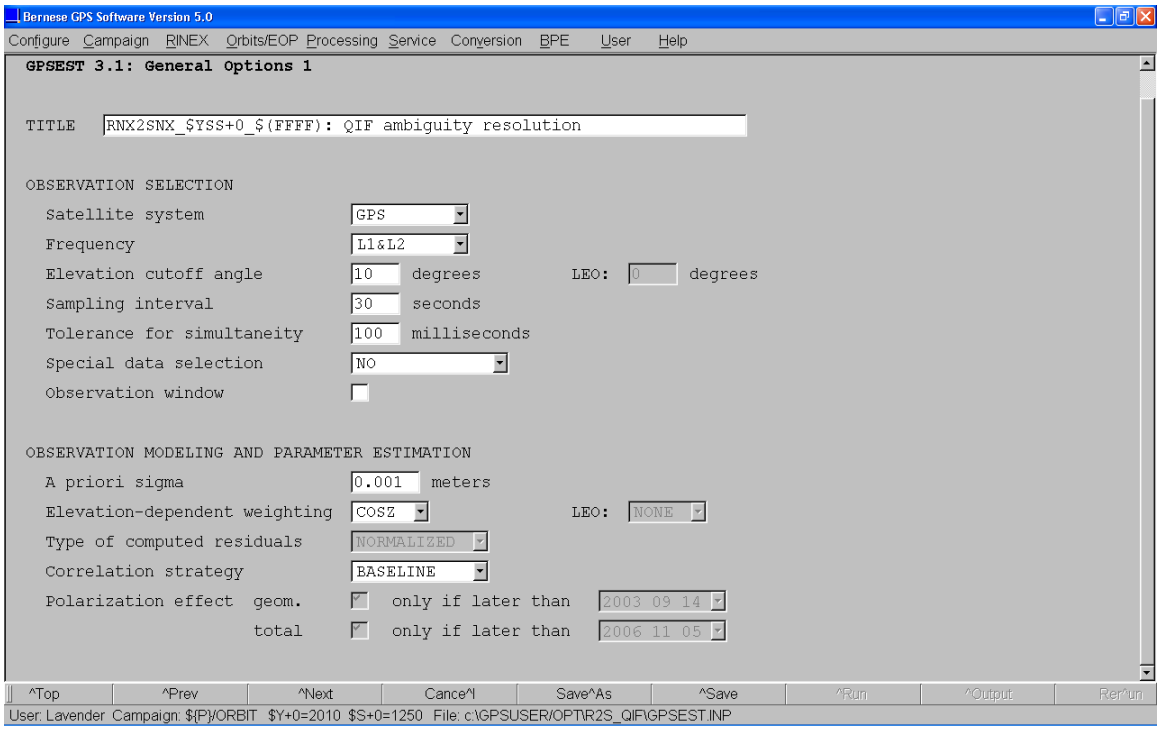
Bernese GPS Software Version 5.0
Configure Campaign RINEX Orbits/EOP Processing Service Conversion BPE User Help
GPSEST 3.1: General Options 1
TITLE
RNX2SNX_$YSS+0_$(FFFF): QIF ambiguity resolution
OBSERVATION SELECTION
Satellite system
GPS
Frequency
L1&L2
Elevation cutoff angle
10
degrees
LEO:
0
degrees
Sampling interval
30
seconds
Tolerance for simultaneity
100
milliseconds
Special data selection
NO
Observation window
OBSERVATION MODELING AND PARAMETER ESTIMATION
A priori sigma
0.001
meters
Elevation-dependent weighting
COSZ
LEO:
NONE
Type of computed residuals
NORMALIZED
Correlation strategy
BASELINE
Polarization effect geom.
only if later than
2003 09 14
total
only if later than
2006 11 05
^Top
^Prev
^Next
Cance^l
Save^As
^Save
^Run
^Output
Re^un
User: Lavender Campaign: ${P}/ORBIT $Y+0=2010 $S+0=1250 File: c:\GPSUSER/OPT\R2S_QIF\GPSEST.INP

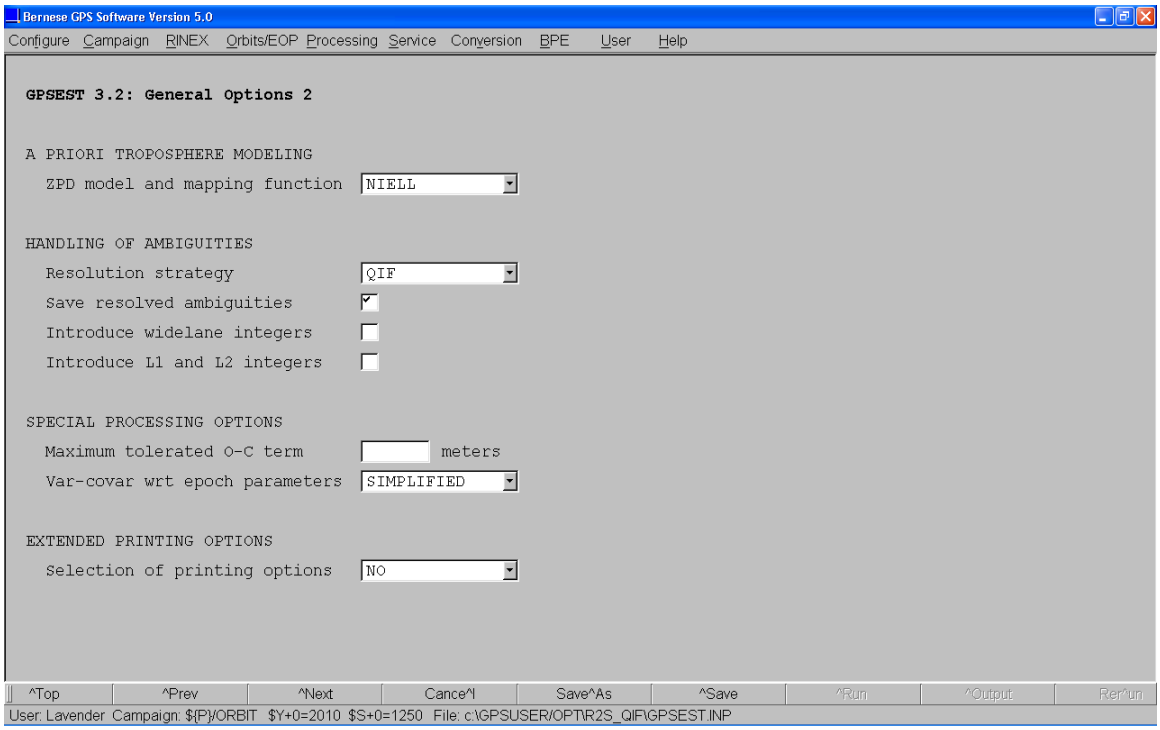
Bernese GPS Software Version 5.0
Configure Campaign RINEX Orbits/EOP Processing Service Conversion BPE User Help
GPSEST 3.2: General Options 2
A PRIORI TROPOSPHERE MODELING
ZPD model and mapping function NIELL
HANDLING OF AMBIGUITIES
Resolution strategy QIF
Save resolved ambiguities
Introduce widelane integers
Introduce L1 and L2 integers
SPECIAL PROCESSING OPTIONS
Maximum tolerated O-C term meters
Var-covar wrt epoch parameters SIMPLIFIED
EXTENDED PRINTING OPTIONS
Selection of printing options NO
^Top ^Prev ^Next Cance^l Save^As ^Save ^Run ^Output Re^un
User: Lavender Campaign: ${P}/ORBIT $Y+0=2010 $S+0=1250 File: c:\GPSUSER/OPT\R2S_QIF\GPSEST.INP

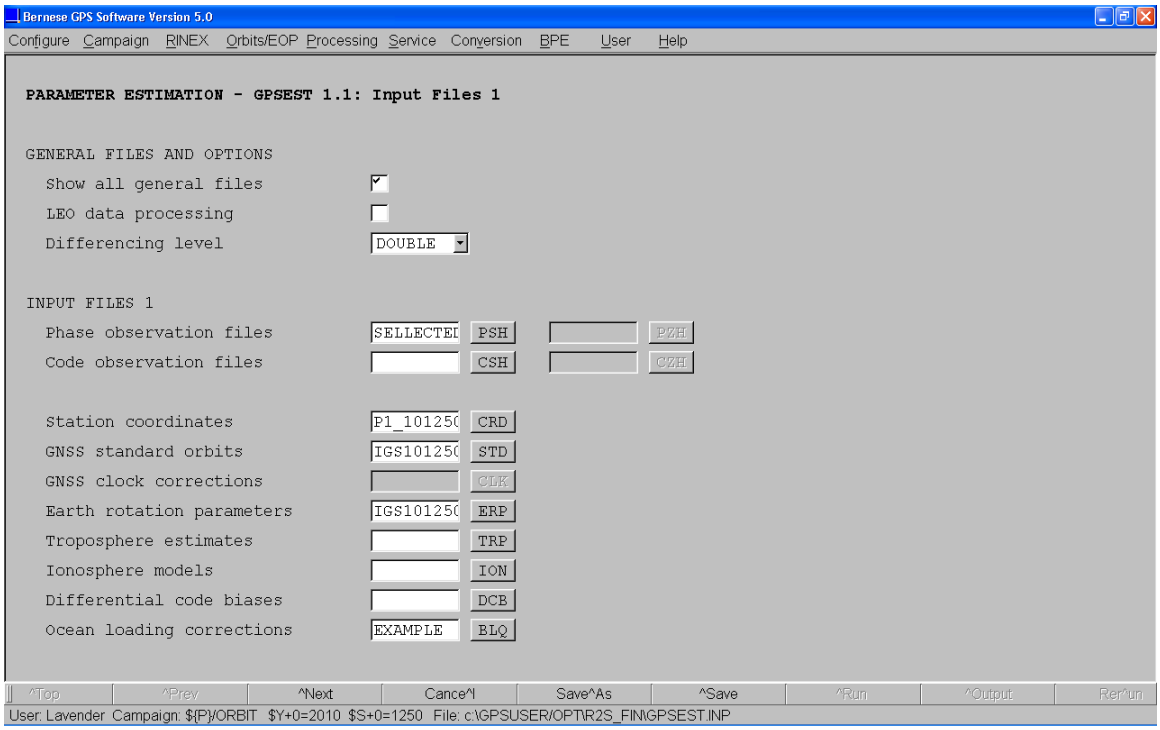
Bernese GPS Software Version 5.0
Configure Campaign RINEX Orbits/EOP Processing Service Conversion BPE User Help
PARAMETER ESTIMATION - GPSEST 1.1: Input Files 1
GENERAL FILES AND OPTIONS
Show all general files
LEO data processing
Differencing level DOUBLE
INPUT FILES 1
Phase observation files SELLECTED PSH PZH
Code observation files CSH CZH
Station coordinates P1_101250 CRD
GNSS standard orbits IGS101250 STD
GNSS clock corrections CLK
Earth rotation parameters IGS101250 ERP
Troposphere estimates TRP
Ionosphere models ION
Differential code biases DCB
Ocean loading corrections EXAMPLE BLQ
^Top ^Prev ^Next Cance^l Save^As ^Save ^Run ^Output Re^un
User: Lavender Campaign: ${P}/ORBIT $Y+0=2010 $S+0=1250 File: c:\GPSUSER/OPT\R2S_FIN\GPSEST.INP

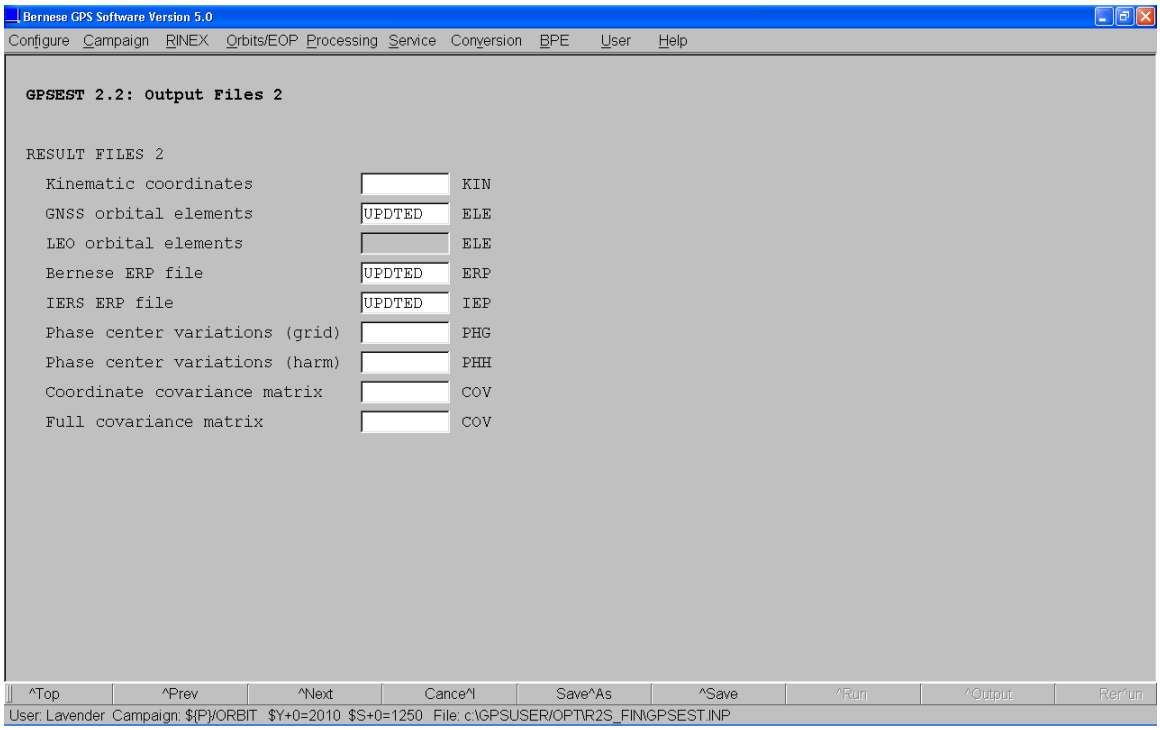
Bernese GPS Software Version 5.0
Configure Campaign RINEX Orbits/EOP Processing Service Conversion BPE User Help
GPSEST 2.2: Output Files 2
RESULT FILES 2
Kinematic coordinates KIN
GNSS orbital elements UPDTED ELE
LEO orbital elements ELE
Bernese ERP file UPDTED ERP
IERS ERP file UPDTED IEP
Phase center variations (grid) PHG
Phase center variations (harm) PHH
Coordinate covariance matrix COV
Full covariance matrix COV
^Top ^Prev ^Next Cance^l Save^As ^Save ^Run ^Output Re^un
User: Lavender Campaign: ${P}/ORBIT $Y+0=2010 $S+0=1250 File: c:\GPSUSER/OPT\R2S_FIN\GPSEST.INP

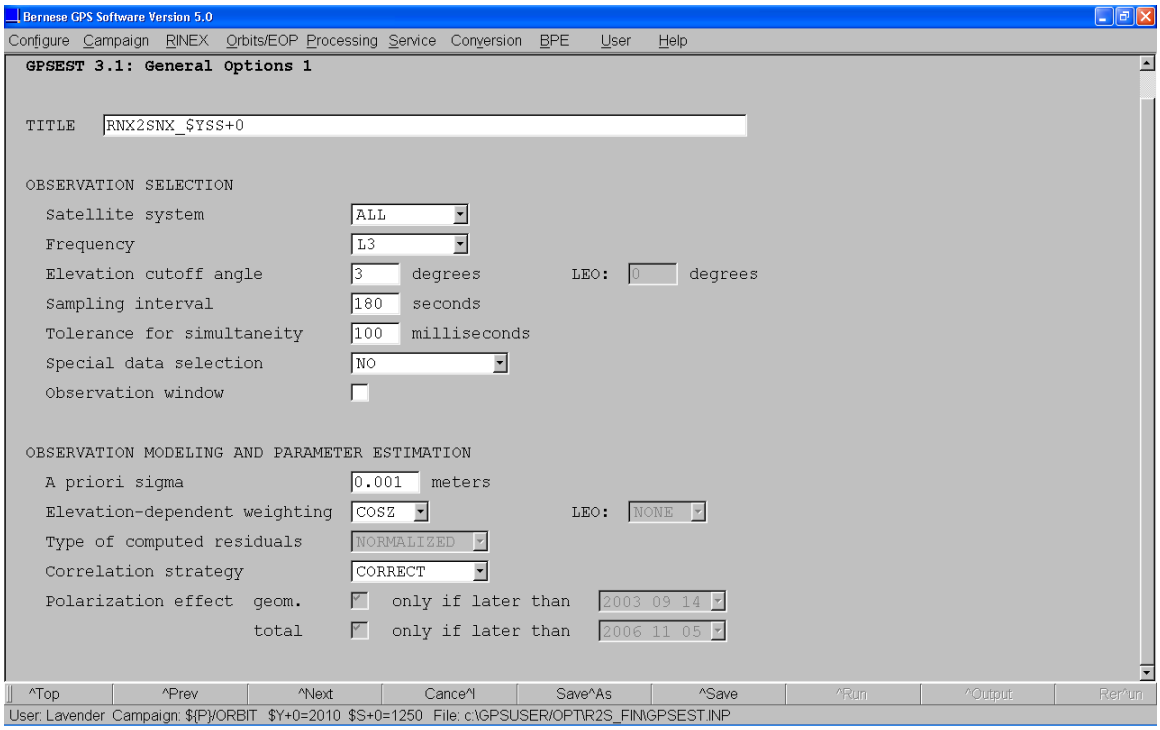
Bernese GPS Software Version 5.0
Configure Campaign RINEX Orbits/EOP Processing Service Conversion BPE User Help
GPSEST 3.1: General Options 1
TITLE RNX2SNX_$YSS+0
OBSERVATION SELECTION
Satellite system ALL
Frequency L3
Elevation cutoff angle 3 degrees LEO: 0 degrees
Sampling interval 180 seconds
Tolerance for simultaneity 100 milliseconds
Special data selection NO
Observation window
OBSERVATION MODELING AND PARAMETER ESTIMATION
A priori sigma 0.001 meters
Elevation-dependent weighting COSZ LEO: NONE
Type of computed residuals NORMALIZED
Correlation strategy CORRECT
Polarization effect geom. only if later than 2003 09 14
total only if later than 2006 11 05
^Top ^Prev ^Next Cance^l Save^As ^Save ^Run ^Output Re^un
User: Lavender Campaign: ${P}/ORBIT $Y+0=2010 $S+0=1250 File: c:\GPSUSER/OPT\R2S_FIN\GPSEST.INP

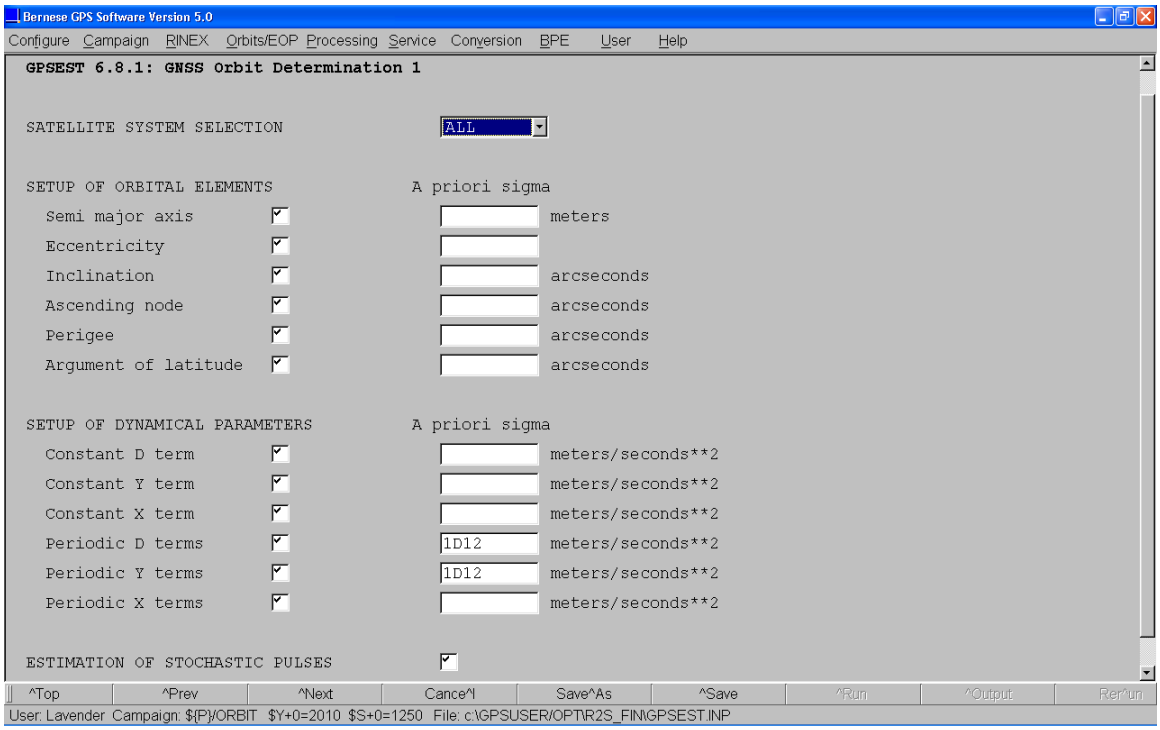
Bernese GPS Software Version 5.0
Configure Campaign RINEX Orbits/EOP Processing Service Conversion BPE User Help
GPSEST 6.8.1: GNSS Orbit Determination 1
SATELLITE SYSTEM SELECTION
ALL
SETUP OF ORBITAL ELEMENTS
A priori sigma
Semi major axis
meters
Eccentricity
Inclination
arcseconds
Ascending node
arcseconds
Perigee
arcseconds
Argument of latitude
arcseconds
SETUP OF DYNAMICAL PARAMETERS
A priori sigma
Constant D term
meters/seconds**2
Constant Y term
meters/seconds**2
Constant X term
meters/seconds**2
Periodic D terms
1D12
meters/seconds**2
Periodic Y terms
1D12
meters/seconds**2
Periodic X terms
meters/seconds**2
ESTIMATION OF STOCHASTIC PULSES
^Top ^Prev ^Next Cance^l Save^As ^Save ^Run ^Output Re^un
User: Lavender Campaign: ${P}/ORBIT $Y+0=2010 $S+0=1250 File: c:\GPSUSER/OPT\R2S_FIN\GPSEST.INP

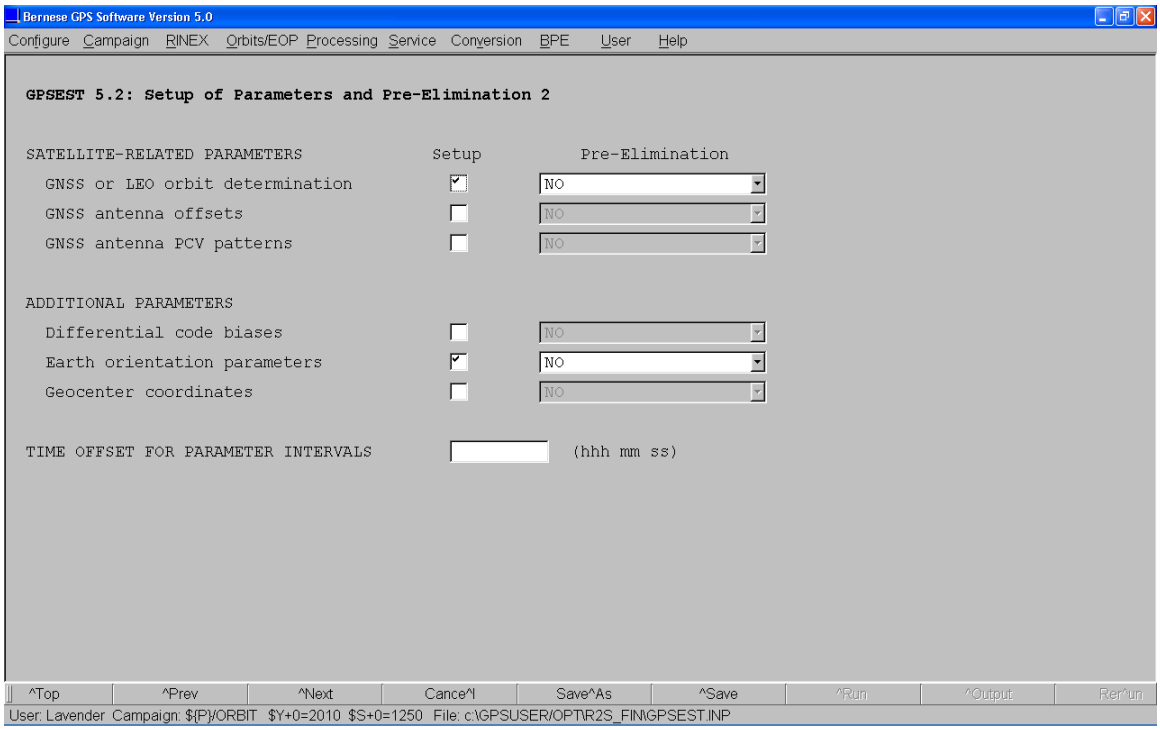
Bernese GPS Software Version 5.0
Configure Campaign RINEX Orbits/EOP Processing Service Conversion BPE User Help
GPSEST 5.2: Setup of Parameters and Pre-Elimination 2
SATELLITE-RELATED PARAMETERS
Setup
Pre-Elimination
GNSS or LEO orbit determination
NO
GNSS antenna offsets
NO
GNSS antenna PCV patterns
NO
ADDITIONAL PARAMETERS
Differential code biases
NO
Earth orientation parameters
NO
Geocenter coordinates
NO
TIME OFFSET FOR PARAMETER INTERVALS
(hhh mm ss)
^Top ^Prev ^Next Cance^l Save^As ^Save ^Run ^Output Re^un
User: Lavender Campaign: ${P}/ORBIT $Y+0=2010 $S+0=1250 File: c:\GPSUSER/OPT\R2S_FIN\GPSEST.INP

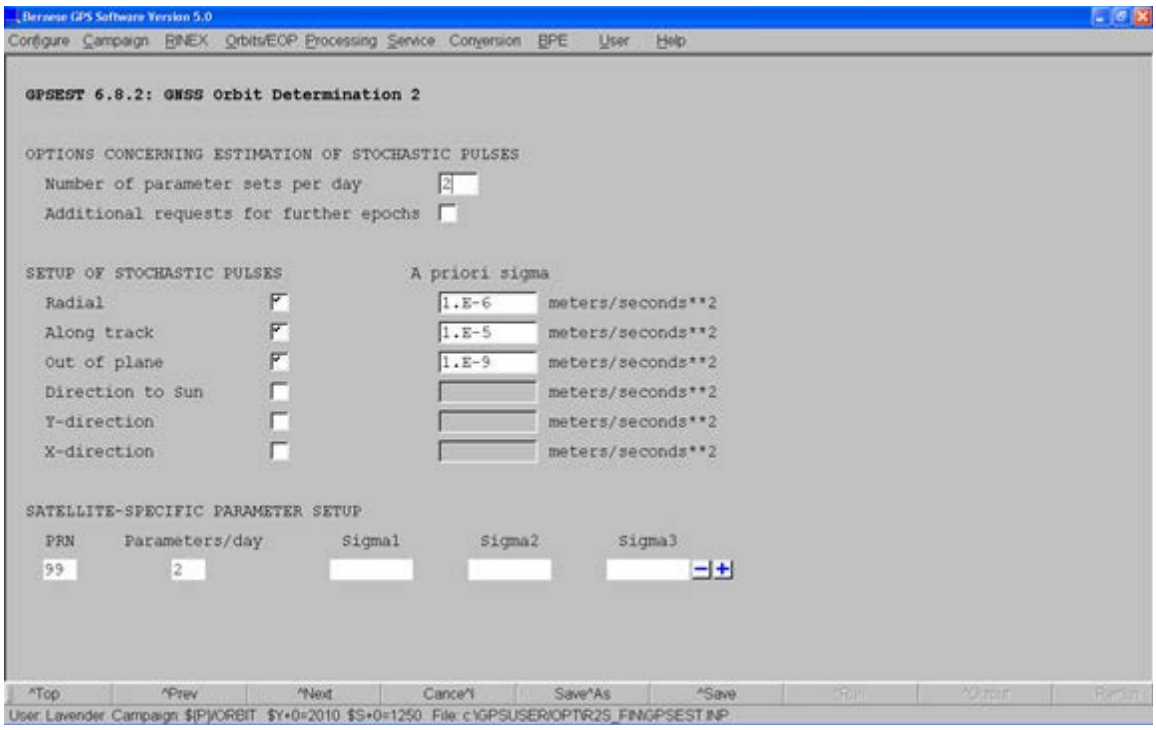
Bernese GPS Software Version 5.0
Configure Campaign RINEX Orbits/EOP Processing Service Conversion BPE User Help
GPSEST 6.8.2: GNSS Orbit Determination 2
OPTIONS CONCERNING ESTIMATION OF STOCHASTIC PULSES
Number of parameter sets per day 2
Additional requests for further epochs
SETUP OF STOCHASTIC PULSES
A priori sigma
Radial 1.E-6 meters/seconds**2
Along track 1.E-5 meters/seconds**2
Out of plane 1.E-9 meters/seconds**2
Direction to Sun meters/seconds**2
Y-direction meters/seconds**2
X-direction meters/seconds**2
SATELLITE-SPECIFIC PARAMETER SETUP
PRN Parameters/day Sigma1 Sigma2 Sigma3
99 2
^Top ^Prev ^Next Cance^l Save^As ^Save
User: Lavender Campaign: $(P)/ORBIT $Y+0=2010 $S+0=1250 File: c:\GPSUSER/OPT\R2S_FIN\GPSEST.INP

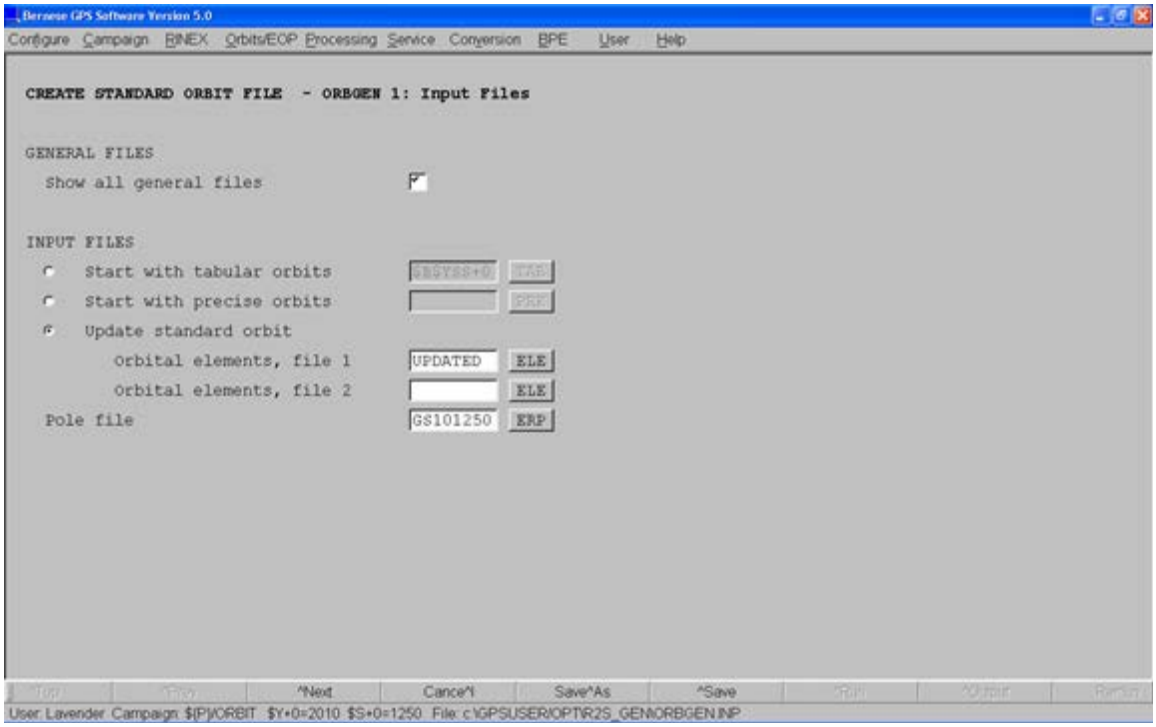
Bernese GPS Software Version 5.0
Configure Campaign RINEX Orbits/EOP Processing Service Conversion BPE User Help
CREATE STANDARD ORBIT FILE - ORBGEN 1: Input Files
GENERAL FILES
Show all general files
INPUT FILES
Start with tabular orbits
Start with precise orbits
Update standard orbit
Orbital elements, file 1 UPDATED ELE
Orbital elements, file 2 ELE
Pole file GS101250 ERP
^Next Cance^l Save^As ^Save
User: Lavender Campaign: $(P)/ORBIT $Y+0=2010 $S+0=1250 File: c:\GPSUSER/OPT\R2S_GEN\ORBGEN.INP

APPENDIX D: PRECISE SATELLITE CLOCK CORRECTIONS DETERMINATION USING BERNESE GPS SOFTWARE

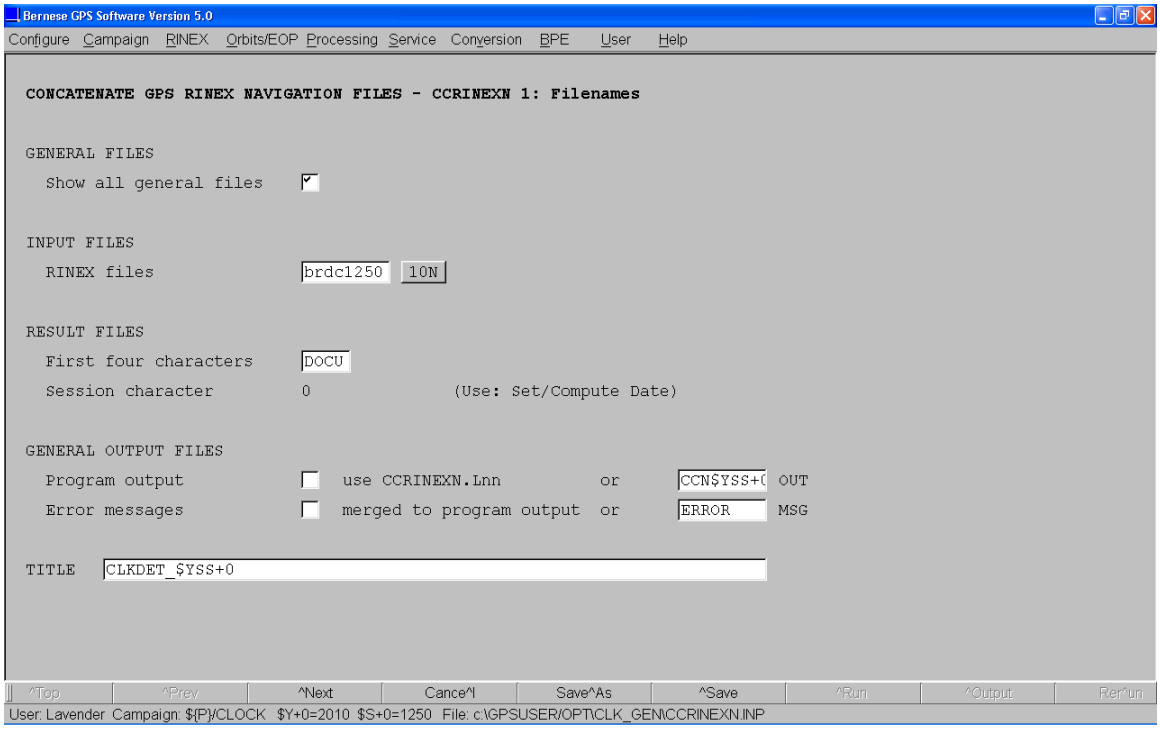

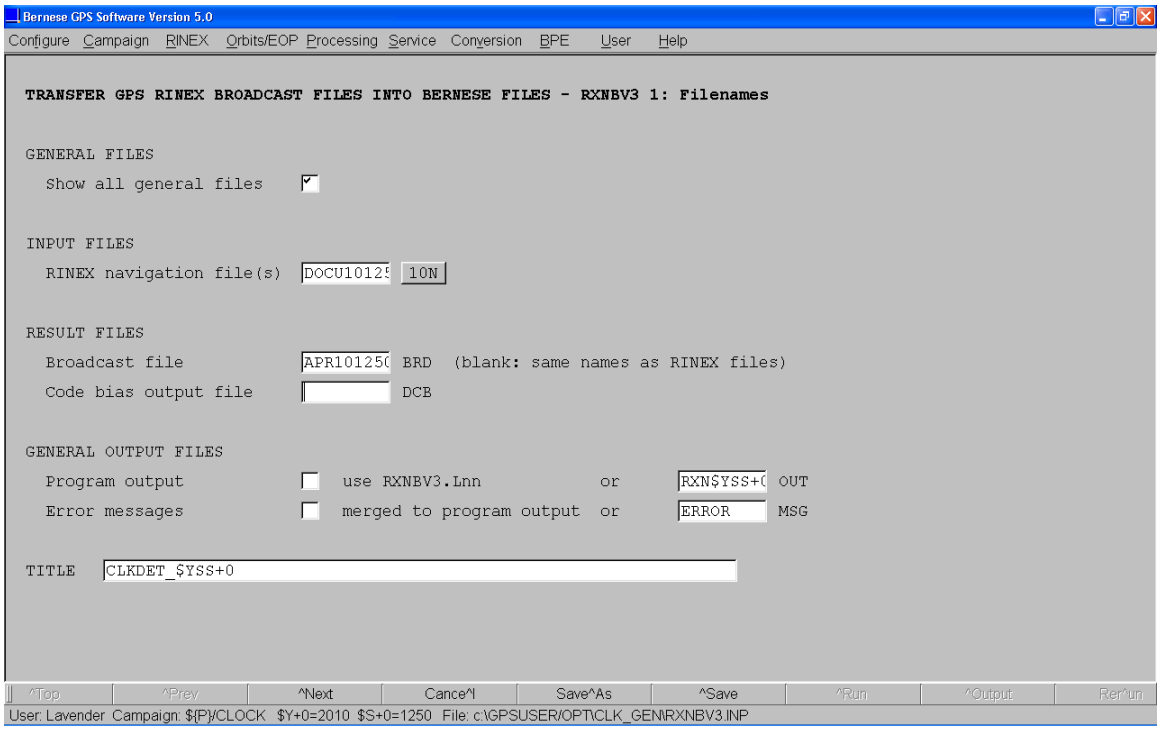

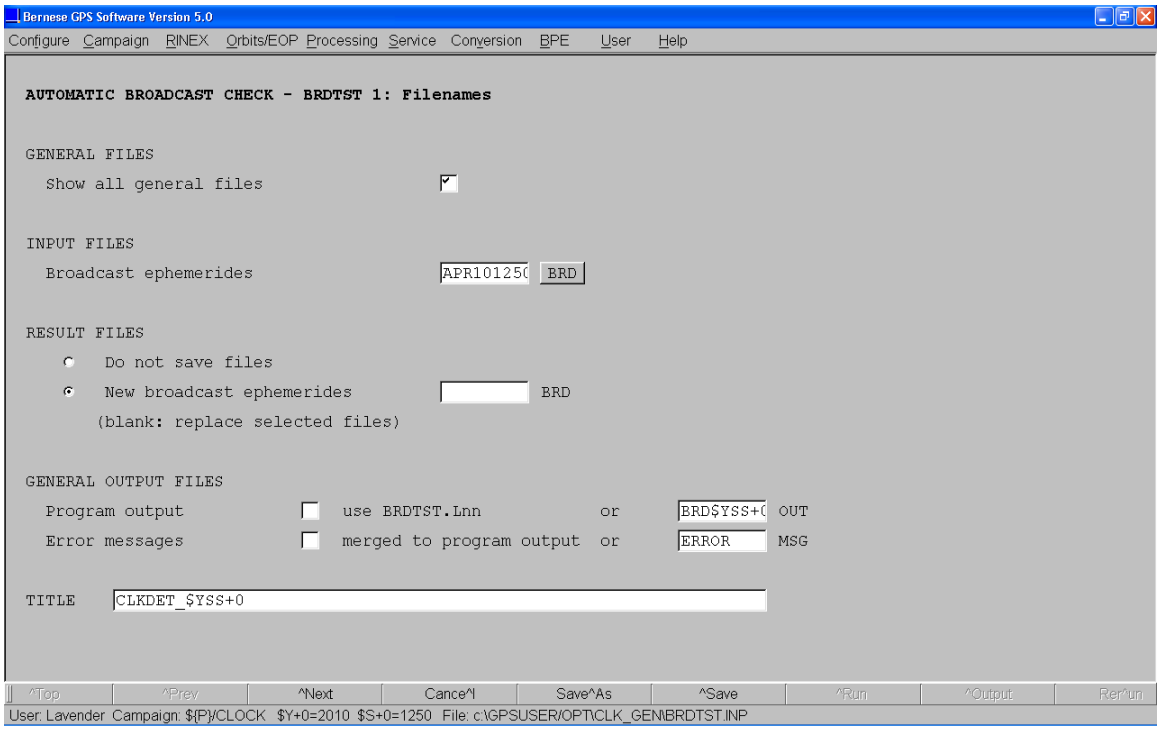
Bernese GPS Software Version 5.0
Configure Campaign RINEX Orbits/EOP Processing Service Conversion BPE User Help
AUTOMATIC BROADCAST CHECK - BRDTST 1: Filenames
GENERAL FILES
Show all general files
INPUT FILES
Broadcast ephemerides
APR10125(
BRD
RESULT FILES
Do not save files
New broadcast ephemerides
BRD
(blank: replace selected files)
GENERAL OUTPUT FILES
Program output
use BRDTST.Lnn
or
BRD$YSS+(
OUT
Error messages
merged to program output
or
ERROR
MSG
TITLE
CLKDET_$YSS+0
^Top
^Prev
^Next
Cance^l
Save^As
^Save
^Run
^Output
Re^un
User: Lavender Campaign: ${P}/CLOCK $Y+0=2010 $S+0=1250 File: c:\GPSUSER/OPT\CLK_GEN\BRDTST.INP

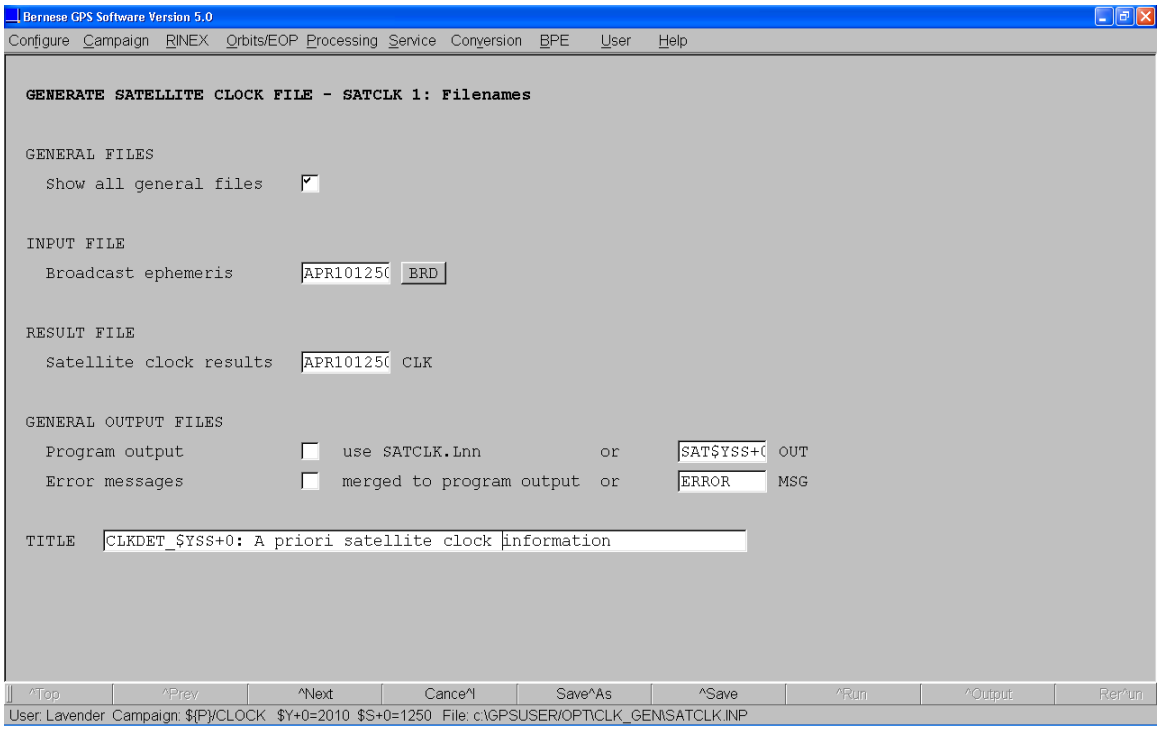
Bernese GPS Software Version 5.0
Configure Campaign RINEX Orbits/EOP Processing Service Conversion BPE User Help
GENERATE SATELLITE CLOCK FILE - SATCLK 1: Filenames
GENERAL FILES
Show all general files
INPUT FILE
Broadcast ephemeris
APR10125(
BRD
RESULT FILE
Satellite clock results
APR10125(
CLK
GENERAL OUTPUT FILES
Program output
use SATCLK.Lnn
or
SAT$YSS+(
OUT
Error messages
merged to program output
or
ERROR
MSG
TITLE
CLKDET_$YSS+0: A priori satellite clock information
^Top
^Prev
^Next
Cance^l
Save^As
^Save
^Run
^Output
Re^un
User: Lavender Campaign: ${P}/CLOCK $Y+0=2010 $S+0=1250 File: c:\GPSUSER/OPT\CLK_GEN\SATCLK.INP

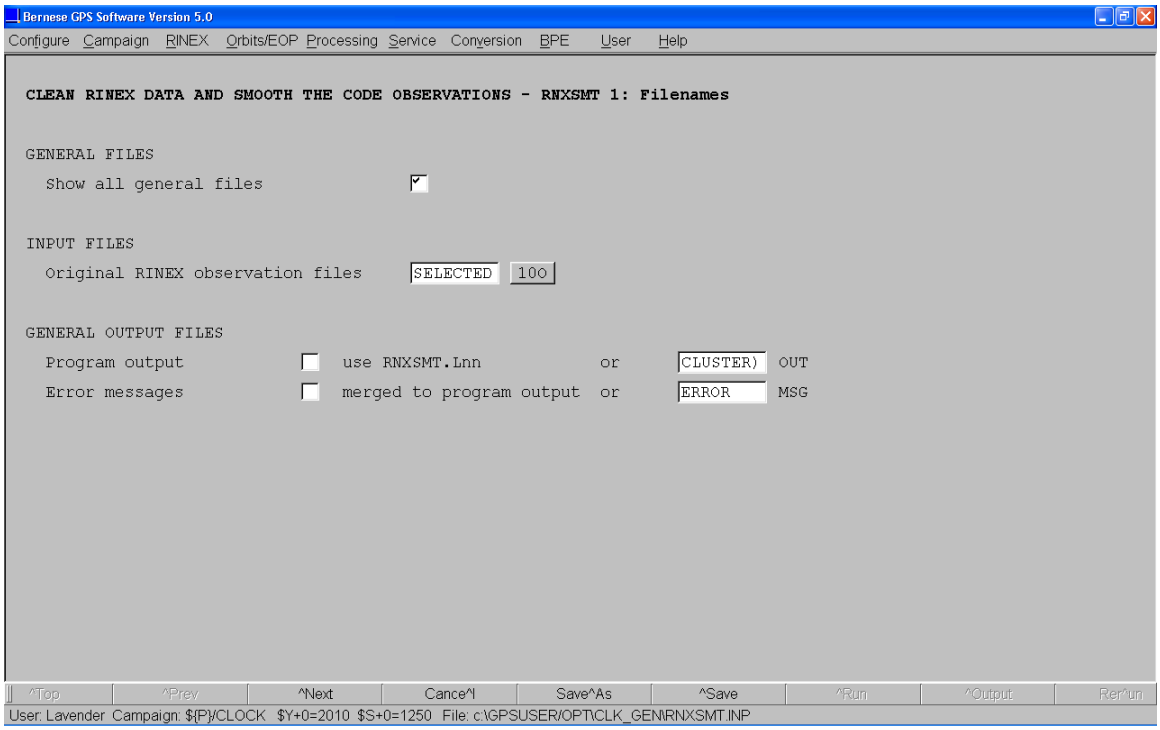
Bernese GPS Software Version 5.0
Configure Campaign RINEX Orbits/EOP Processing Service Conversion BPE User Help
CLEAN RINEX DATA AND SMOOTH THE CODE OBSERVATIONS - RNXSMT 1: Filenames
GENERAL FILES
Show all general files
INPUT FILES
Original RINEX observation files SELECTED 100
GENERAL OUTPUT FILES
Program output use RNXSMT.Lnn or CLUSTER) OUT
Error messages merged to program output or ERROR MSG
^Top ^Prev ^Next Cance^l Save^As ^Save ^Run ^Output Re^un
User: Lavender Campaign: ${P}/CLOCK $Y+0=2010 $S+0=1250 File: c:\GPSUSER/OPT\CLK_GEN\RNXSMT.INP

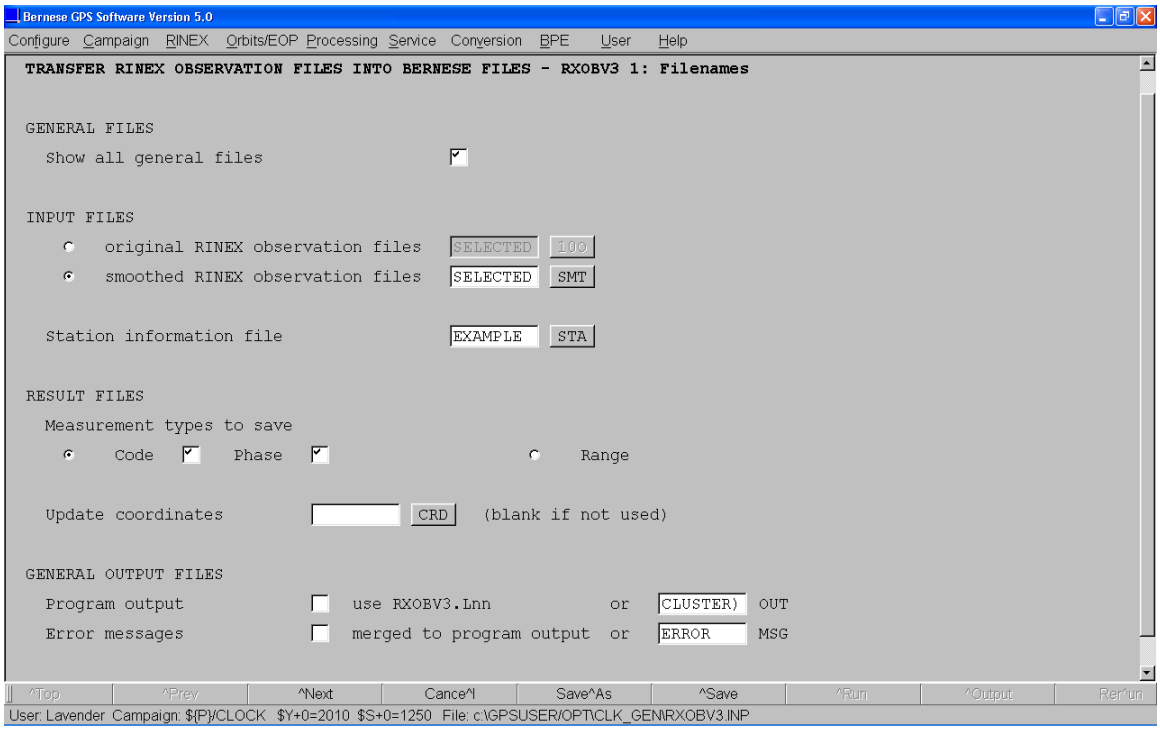
Bernese GPS Software Version 5.0
Configure Campaign RINEX Orbits/EOP Processing Service Conversion BPE User Help
TRANSFER RINEX OBSERVATION FILES INTO BERNESE FILES - RXOBV3 1: Filenames
GENERAL FILES
Show all general files
INPUT FILES
original RINEX observation files SELECTED 100
smoothed RINEX observation files SELECTED SMT
Station information file EXAMPLE STA
RESULT FILES
Measurement types to save
Code Phase Range
Update coordinates CRD (blank if not used)
GENERAL OUTPUT FILES
Program output use RXOBV3.Lnn or CLUSTER) OUT
Error messages merged to program output or ERROR MSG
^Top ^Prev ^Next Cance^l Save^As ^Save ^Run ^Output Re^un
User: Lavender Campaign: ${P}/CLOCK $Y+0=2010 $S+0=1250 File: c:\GPSUSER/OPT\CLK_GEN\RXOBV3.INP

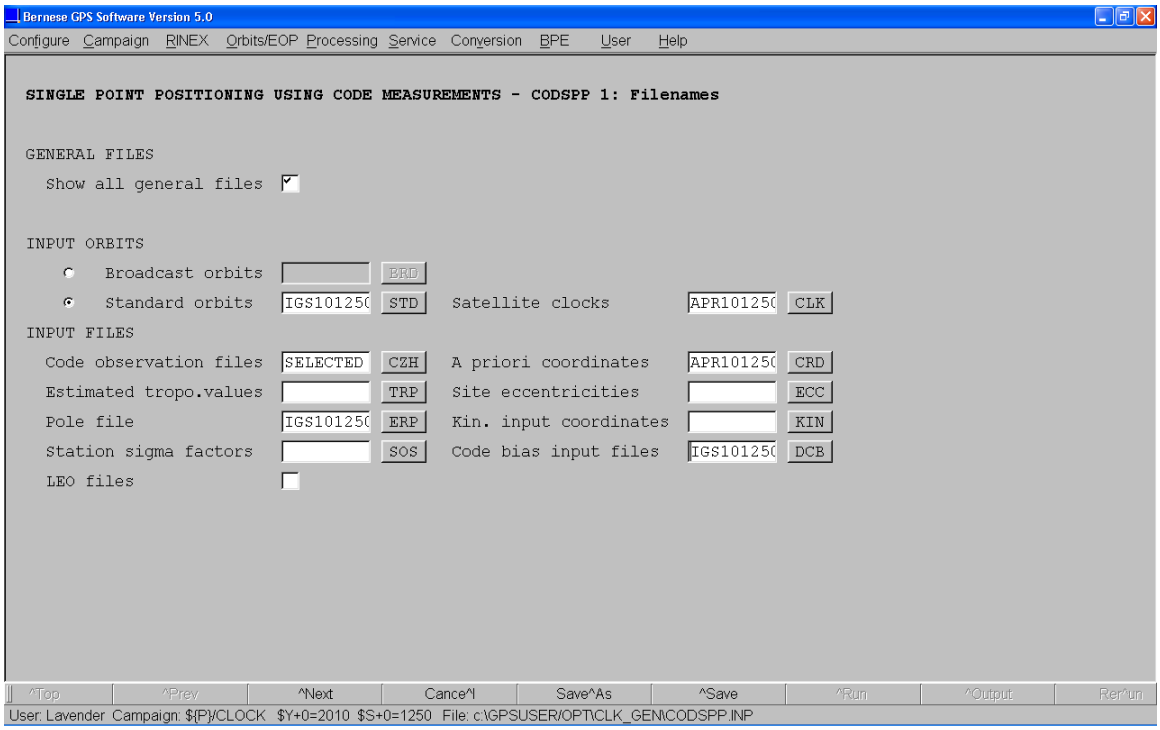
Bernese GPS Software Version 5.0
Configure Campaign RINEX Orbits/EOP Processing Service Conversion BPE User Help
SINGLE POINT POSITIONING USING CODE MEASUREMENTS - CODSPP 1: Filenames
GENERAL FILES
Show all general files
INPUT ORBITS
Broadcast orbits BRD
Standard orbits IGS10125(STD
Satellite clocks APR10125(CLK
INPUT FILES
Code observation files SELECTED CZH
A priori coordinates APR10125(CRD
Estimated tropo.values TRP
Site eccentricities ECC
Pole file IGS10125(ERP
Kin. input coordinates KIN
Station sigma factors SOS
Code bias input files IGS10125(DCB
LEO files
^Top ^Prev ^Next Cance^l Save^As ^Save ^Run ^Output Re^un
User: Lavender Campaign: ${P}/CLOCK $Y+0=2010 $S+0=1250 File: c:\GPSUSER/OPT\CLK_GEN\CODSPP.INP

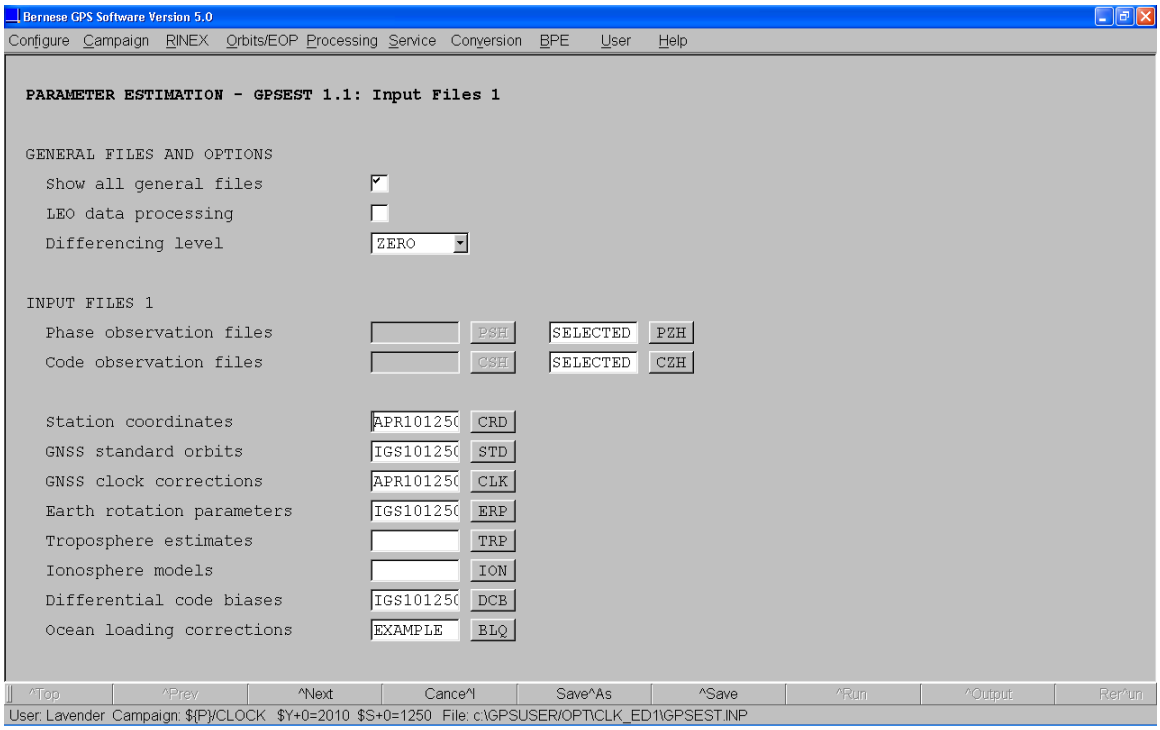
Bernese GPS Software Version 5.0
Configure Campaign RINEX Orbits/EOP Processing Service Conversion BPE User Help
PARAMETER ESTIMATION - GPSEST 1.1: Input Files 1
GENERAL FILES AND OPTIONS
Show all general files
LEO data processing
Differencing level ZERO
INPUT FILES 1
Phase observation files PSH SELECTED PZH
Code observation files CSH SELECTED CZH
Station coordinates APR10125(CRD
GNSS standard orbits IGS10125(STD
GNSS clock corrections APR10125(CLK
Earth rotation parameters IGS10125(ERP
Troposphere estimates TRP
Ionosphere models ION
Differential code biases IGS10125(DCB
Ocean loading corrections EXAMPLE BLQ
^Top ^Prev ^Next Cance^l Save^As ^Save ^Run ^Output Re^un
User: Lavender Campaign: ${P}/CLOCK $Y+0=2010 $S+0=1250 File: c:\GPSUSER/OPT\CLK_ED1\GPSEST.INP

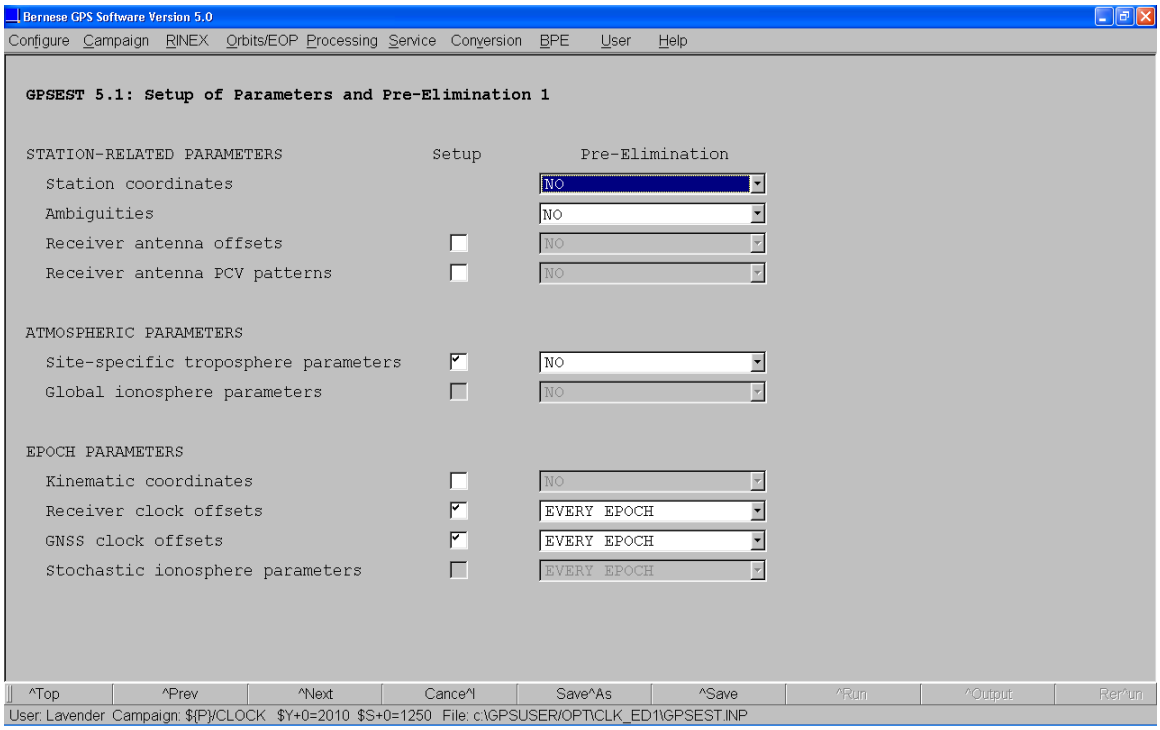
Bernese GPS Software Version 5.0
Configure Campaign RINEX Orbits/EOP Processing Service Conversion BPE User Help
GPSEST 5.1: Setup of Parameters and Pre-Elimination 1
STATION-RELATED PARAMETERS
Setup
Pre-Elimination
Station coordinates
NO
Ambiguities
NO
Receiver antenna offsets
NO
Receiver antenna PCV patterns
NO
ATMOSPHERIC PARAMETERS
Site-specific troposphere parameters
NO
Global ionosphere parameters
NO
EPOCH PARAMETERS
Kinematic coordinates
NO
Receiver clock offsets
EVERY EPOCH
GNSS clock offsets
EVERY EPOCH
Stochastic ionosphere parameters
EVERY EPOCH
^Top
^Prev
^Next
Cance^l
Save^As
^Save
^Run
^Output
Re^un
User: Lavender Campaign: ${P}/CLOCK $Y+0=2010 $S+0=1250 File: c:\GPSUSER/OPT\CLK_ED1\GPSEST.INP

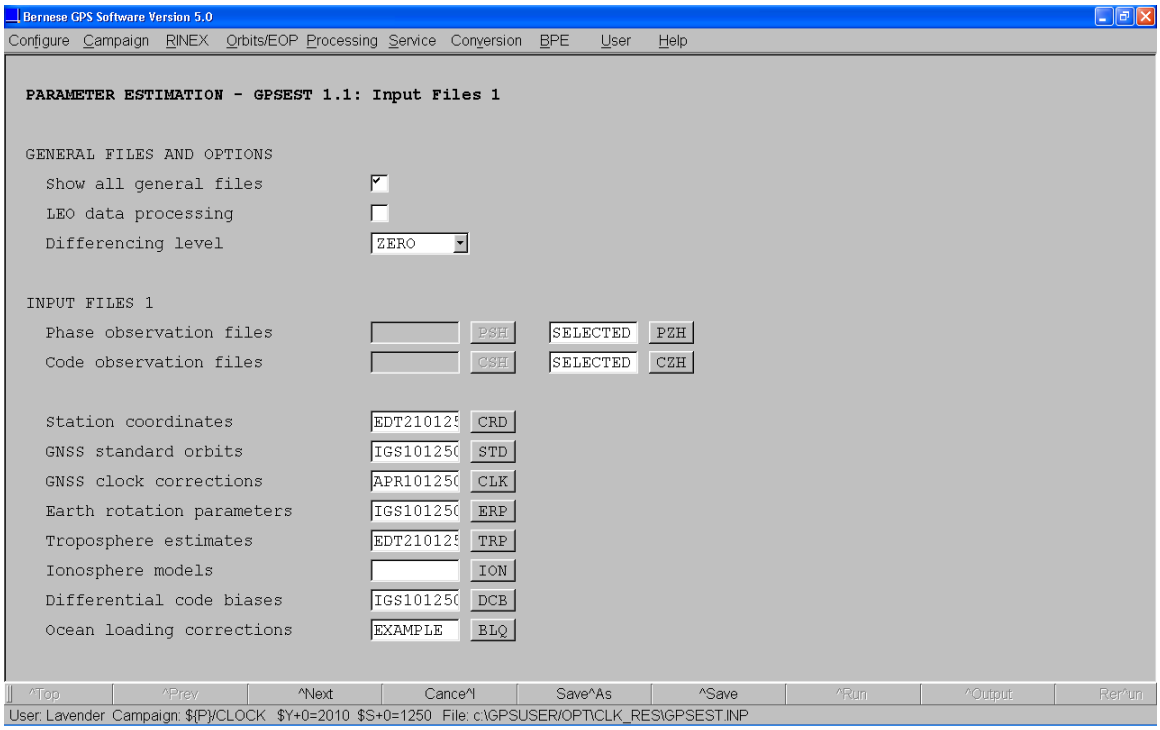
Bernese GPS Software Version 5.0
Configure Campaign RINEX Orbits/EOP Processing Service Conversion BPE User Help
PARAMETER ESTIMATION - GPSEST 1.1: Input Files 1
GENERAL FILES AND OPTIONS
Show all general files
LEO data processing
Differencing level
ZERO
INPUT FILES 1
Phase observation files
PSH
SELECTED
PZH
Code observation files
CSH
SELECTED
CZH
Station coordinates
EDT210125
CRD
GNSS standard orbits
IGS101250
STD
GNSS clock corrections
APR101250
CLK
Earth rotation parameters
IGS101250
ERP
Troposphere estimates
EDT210125
TRP
Ionosphere models
ION
Differential code biases
IGS101250
DCB
Ocean loading corrections
EXAMPLE
BLQ
^Top
^Prev
^Next
Cance^l
Save^As
^Save
^Run
^Output
Re^un
User: Lavender Campaign: ${P}/CLOCK $Y+0=2010 $S+0=1250 File: c:\GPSUSER/OPT\CLK_RES\GPSEST.INP

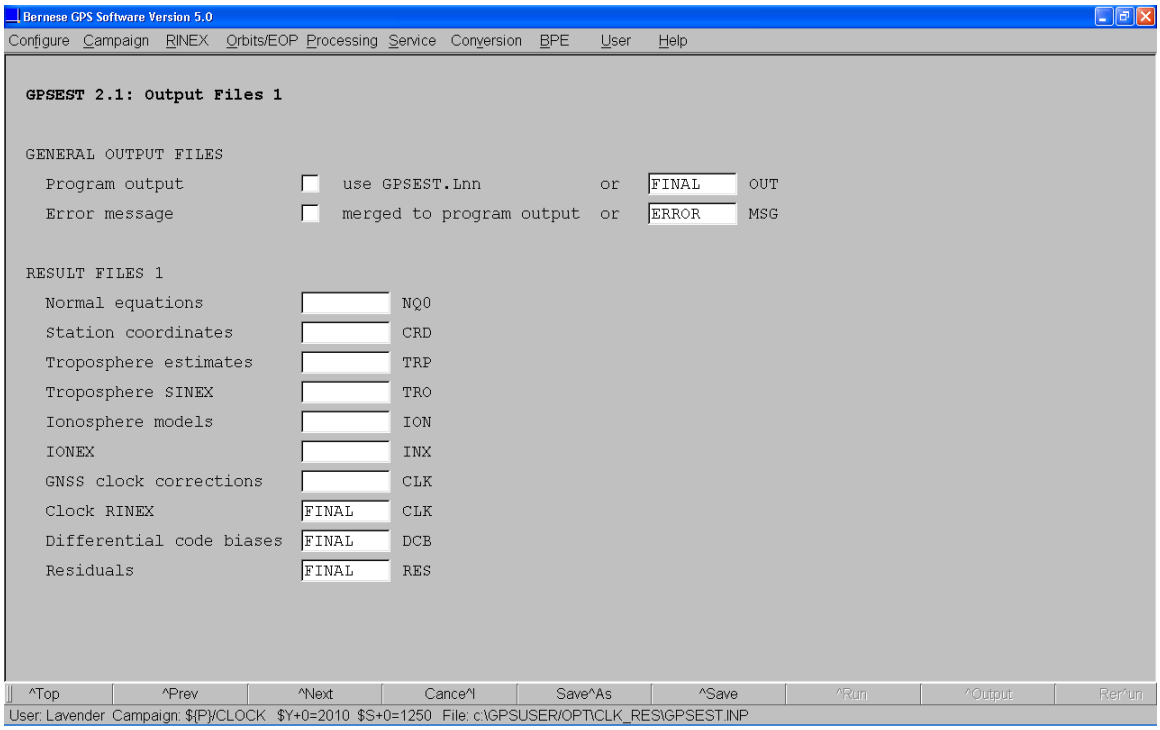
Bernese GPS Software Version 5.0
Configure Campaign RINEX Orbits/EOP Processing Service Conversion BPE User Help
GPSEST 2.1: Output Files 1
GENERAL OUTPUT FILES
Program output
use GPSEST.Lnn
or
FINAL
OUT
Error message
merged to program output
or
ERROR
MSG
RESULT FILES 1
Normal equations
NQ0
Station coordinates
CRD
Troposphere estimates
TRP
Troposphere SINEX
TRO
Ionosphere models
ION
IONEX
INX
GNSS clock corrections
CLK
Clock RINEX
FINAL
CLK
Differential code biases
FINAL
DCB
Residuals
FINAL
RES
^Top
^Prev
^Next
Cance^l
Save^As
^Save
^Run
^Output
Re^un
User: Lavender Campaign: ${P}/CLOCK $Y+0=2010 $S+0=1250 File: c:\GPSUSER/OPT\CLK_RES\GPSEST.INP

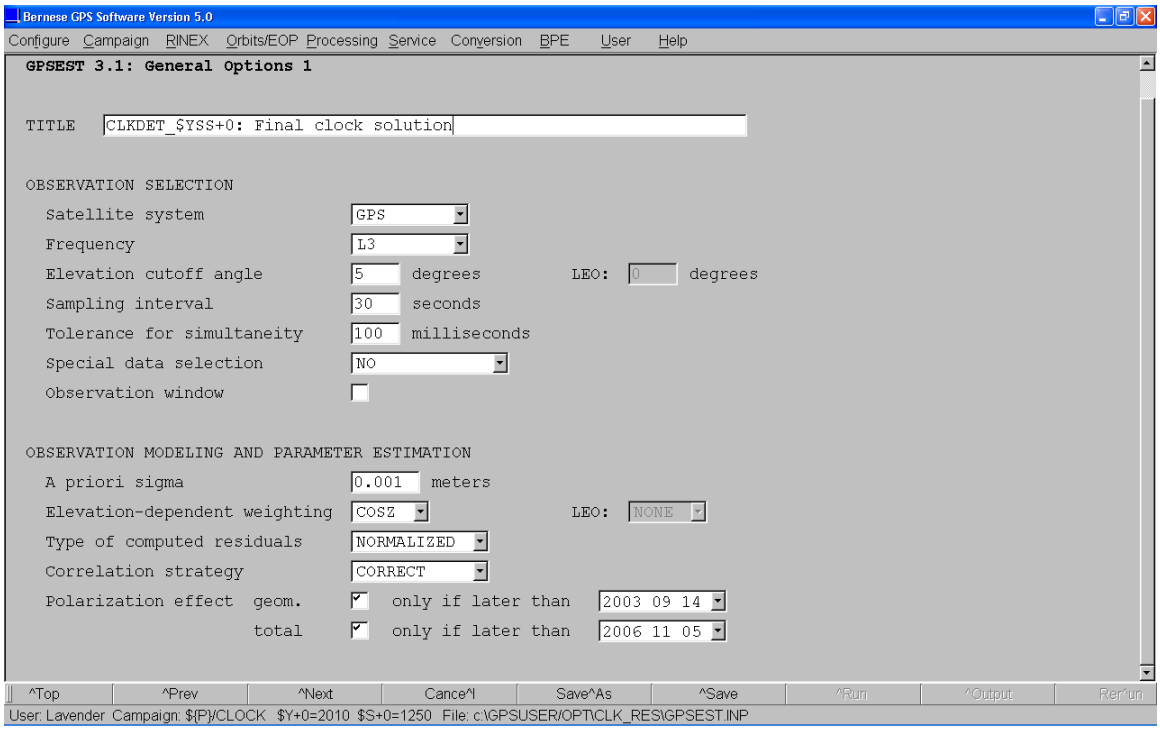
Bernese GPS Software Version 5.0
Configure Campaign RINEX Orbits/EOP Processing Service Conversion BPE User Help
GPSEST 3.1: General Options 1
TITLE
CLKDET_$YSS+0: Final clock solution
OBSERVATION SELECTION
Satellite system
GPS
Frequency
L3
Elevation cutoff angle
5
degrees
LEO:
0
degrees
Sampling interval
30
seconds
Tolerance for simultaneity
100
milliseconds
Special data selection
NO
Observation window
OBSERVATION MODELING AND PARAMETER ESTIMATION
A priori sigma
0.001
meters
Elevation-dependent weighting
COSZ
LEO:
NONE
Type of computed residuals
NORMALIZED
Correlation strategy
CORRECT
Polarization effect geom.
only if later than
2003 09 14
total
only if later than
2006 11 05
^Top
^Prev
^Next
Cance^l
Save^As
^Save
^Run
^Output
Re^un
User: Lavender Campaign: ${P}/CLOCK $Y+0=2010 $S+0=1250 File: c:\GPSUSER/OPT\CLK_RES\GPSEST.INP

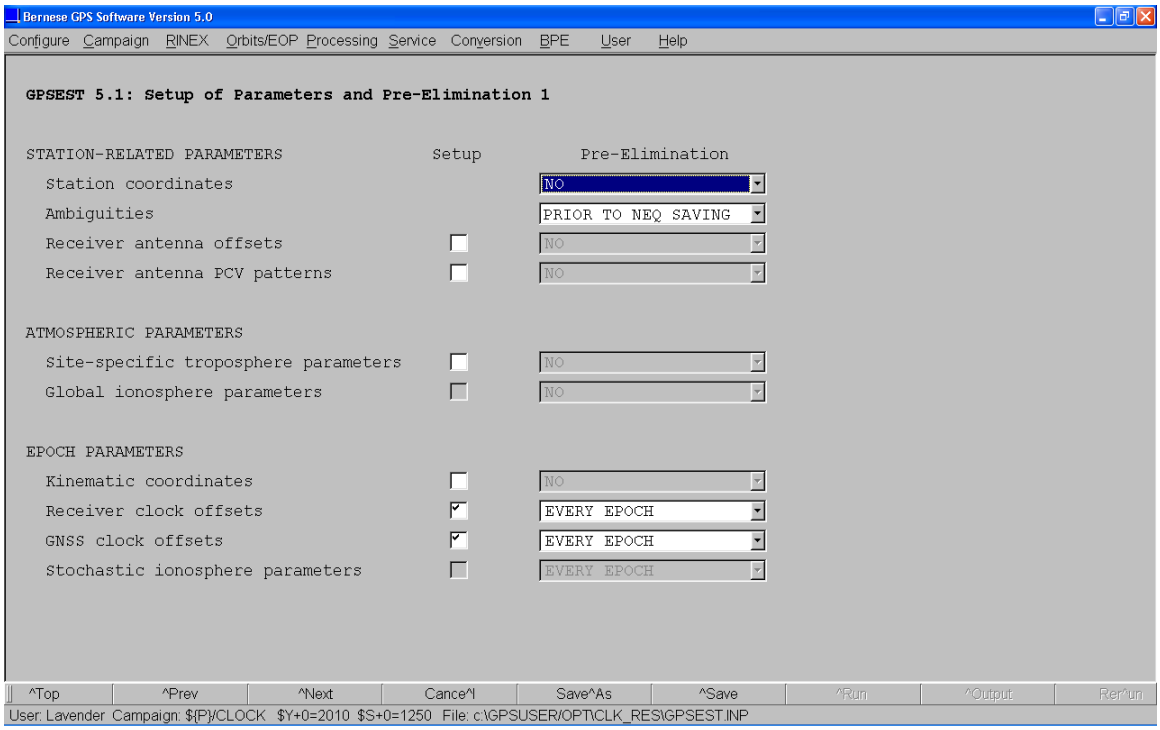
Bernese GPS Software Version 5.0
Configure Campaign RINEX Orbits/EOP Processing Service Conversion BPE User Help
GPSEST 5.1: Setup of Parameters and Pre-Elimination 1
STATION-RELATED PARAMETERS
Setup
Pre-Elimination
Station coordinates
NO
Ambiguities
PRIOR TO NEQ SAVING
Receiver antenna offsets
NO
Receiver antenna PCV patterns
NO
ATMOSPHERIC PARAMETERS
Site-specific troposphere parameters
NO
Global ionosphere parameters
NO
EPOCH PARAMETERS
Kinematic coordinates
NO
Receiver clock offsets
EVERY EPOCH
GNSS clock offsets
EVERY EPOCH
Stochastic ionosphere parameters
EVERY EPOCH
^Top
^Prev
^Next
Cance^l
Save^As
^Save
^Run
^Output
Re^un
User: Lavender Campaign: ${P}/CLOCK $Y+0=2010 $S+0=1250 File: c:\GPSUSER/OPT\CLK_RES\GPSEST.INP

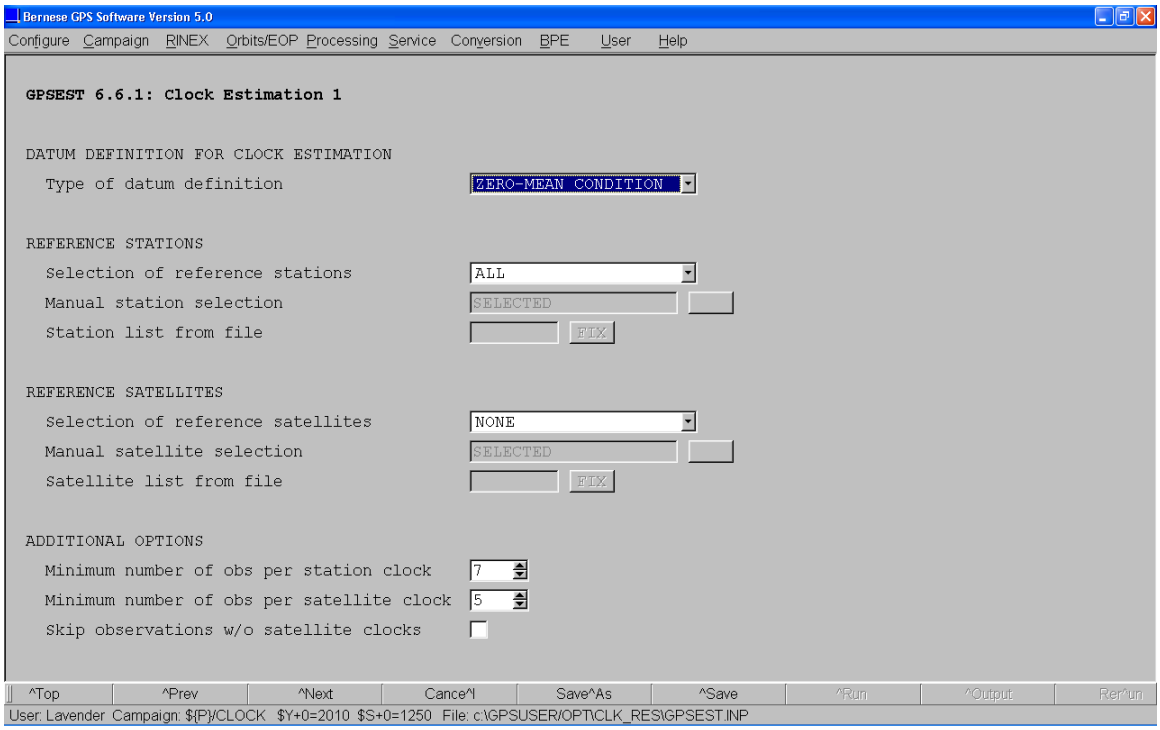
Bernese GPS Software Version 5.0
Configure Campaign RINEX Orbits/EOP Processing Service Conversion BPE User Help
GPSEST 6.6.1: Clock Estimation 1
DATUM DEFINITION FOR CLOCK ESTIMATION
Type of datum definition
ZERO-MEAN CONDITION
REFERENCE STATIONS
Selection of reference stations
ALL
Manual station selection
SELECTED
Station list from file
FIX
REFERENCE SATELLITES
Selection of reference satellites
NONE
Manual satellite selection
SELECTED
Satellite list from file
FIX
ADDITIONAL OPTIONS
Minimum number of obs per station clock
7
Minimum number of obs per satellite clock
5
Skip observations w/o satellite clocks
^Top
^Prev
^Next
Cance^l
Save^As
^Save
^Run
^Output
Re^un
User: Lavender Campaign: ${P}/CLOCK $Y+0=2010 $S+0=1250 File: c:\GPSUSER/OPT\CLK_RES\GPSEST.INP

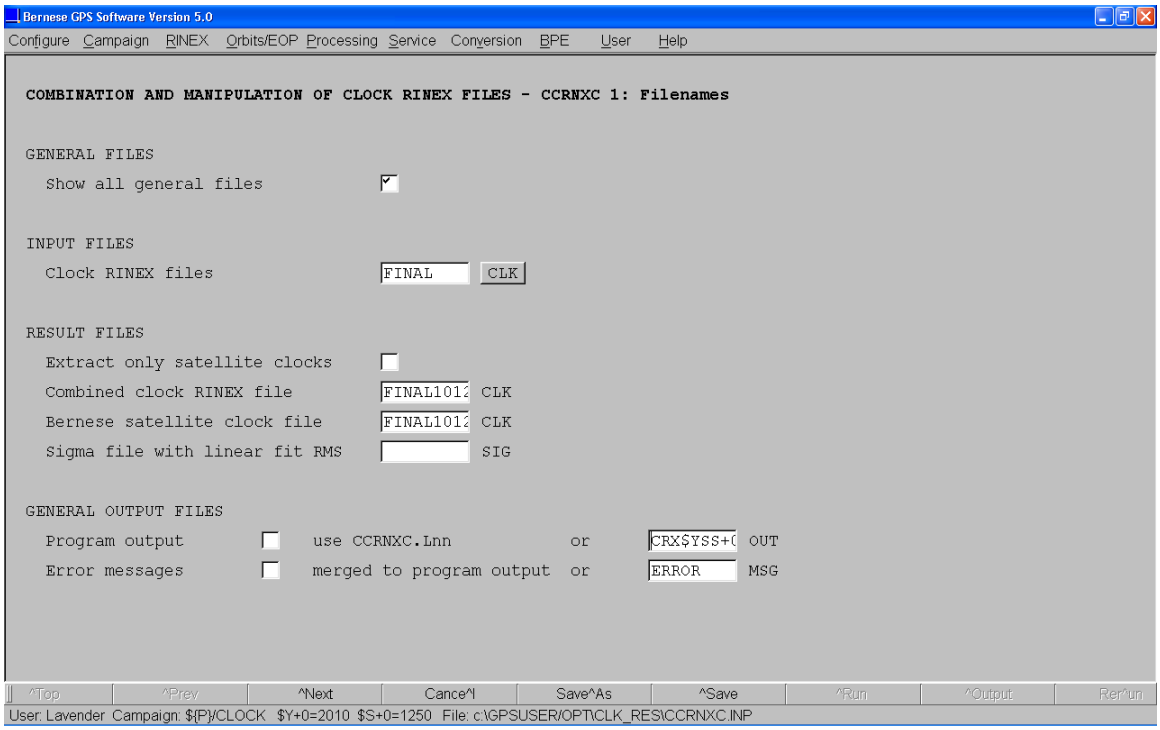
Bernese GPS Software Version 5.0
Configure Campaign RINEX Orbits/EOP Processing Service Conversion BPE User Help
COMBINATION AND MANIPULATION OF CLOCK RINEX FILES - CCRNXC 1: Filenames
GENERAL FILES
Show all general files
INPUT FILES
Clock RINEX files
FINAL
CLK
RESULT FILES
Extract only satellite clocks
Combined clock RINEX file
FINAL1012
CLK
Bernese satellite clock file
FINAL1012
CLK
Sigma file with linear fit RMS
SIG
GENERAL OUTPUT FILES
Program output
use CCRNXC.Lnn
or
CRX$YSS+0
OUT
Error messages
merged to program output
or
ERROR
MSG
^Top
^Prev
^Next
Cance^l
Save^As
^Save
^Run
^Output
Re^un
User: Lavender Campaign: ${P}/CLOCK $Y+0=2010 $S+0=1250 File: c:\GPSUSER/OPT\CLK_RES\CCRNXC.INP

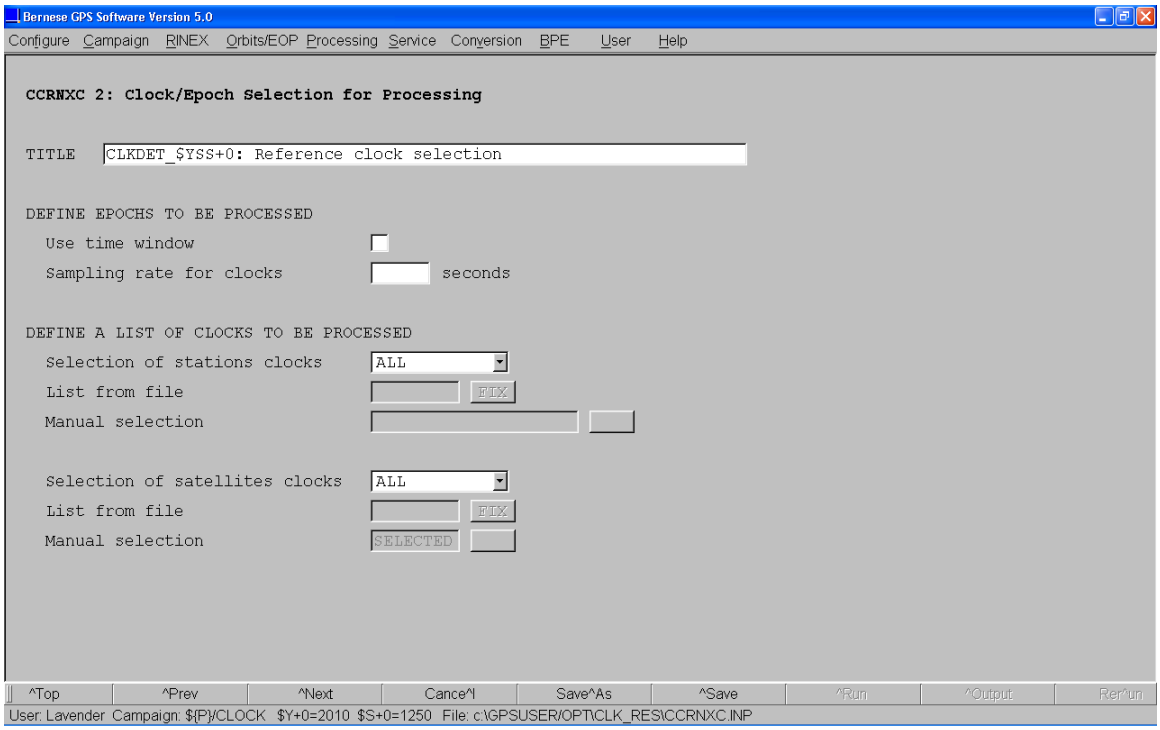
Bernese GPS Software Version 5.0
Configure Campaign RINEX Orbits/EOP Processing Service Conversion BPE User Help
CCRNXC 2: Clock/Epoch Selection for Processing
TITLE
CLKDET_$YSS+0: Reference clock selection
DEFINE EPOCHS TO BE PROCESSED
Use time window
Sampling rate for clocks
seconds
DEFINE A LIST OF CLOCKS TO BE PROCESSED
Selection of stations clocks
ALL
List from file
FIX
Manual selection
Selection of satellites clocks
ALL
List from file
FIX
Manual selection
SELECTED
^Top
^Prev
^Next
Cance^l
Save^As
^Save
^Run
^Output
Re^un
User: Lavender Campaign: ${P}/CLOCK $Y+0=2010 $S+0=1250 File: c:\GPSUSER/OPT\CLK_RES\CCRNXC.INP

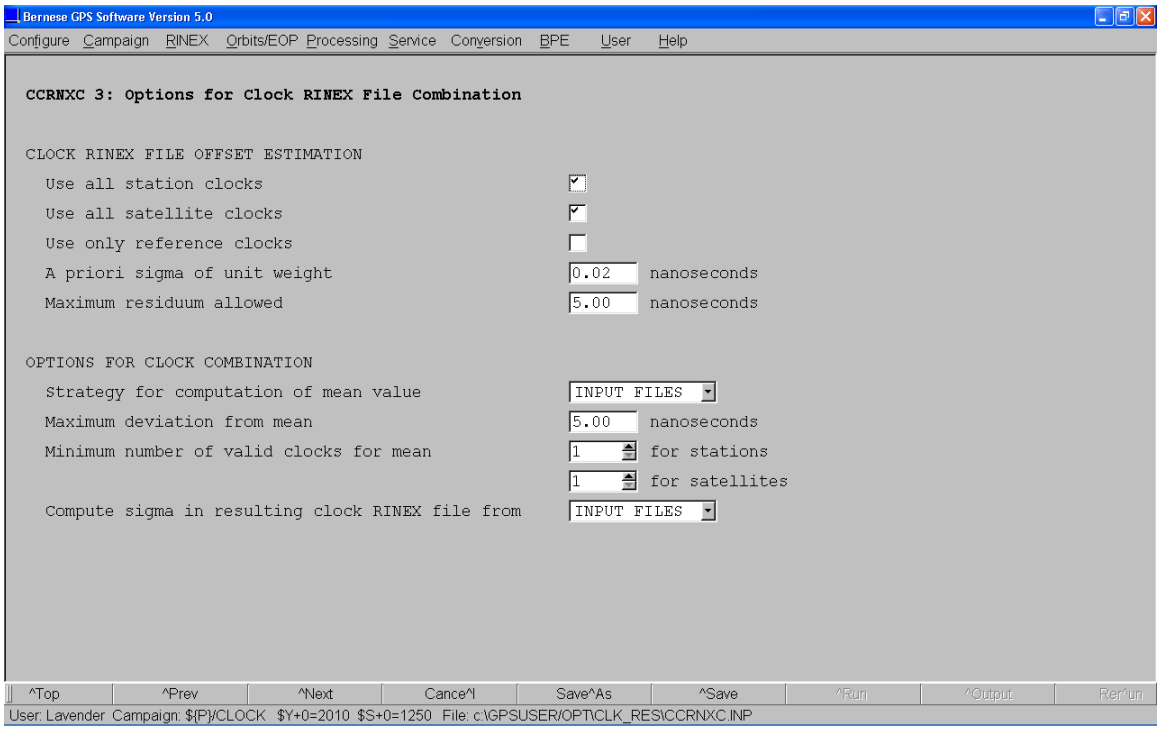
Bernese GPS Software Version 5.0
Configure Campaign RINEX Orbits/EOP Processing Service Conversion BPE User Help
CCRNXC 3: Options for Clock RINEX File Combination
CLOCK RINEX FILE OFFSET ESTIMATION
Use all station clocks
Use all satellite clocks
Use only reference clocks
A priori sigma of unit weight
0.02
nanoseconds
Maximum residuum allowed
5.00
nanoseconds
OPTIONS FOR CLOCK COMBINATION
Strategy for computation of mean value
INPUT FILES
Maximum deviation from mean
5.00
nanoseconds
Minimum number of valid clocks for mean
1
for stations
1
for satellites
Compute sigma in resulting clock RINEX file from
INPUT FILES
^Top
^Prev
^Next
Cance^l
Save^As
^Save
^Run
^Output
Re^un
User: Lavender Campaign: ${P}/CLOCK $Y+0=2010 $S+0=1250 File: c:\GPSUSER/OPT\CLK_RES\CCRNXC.INP

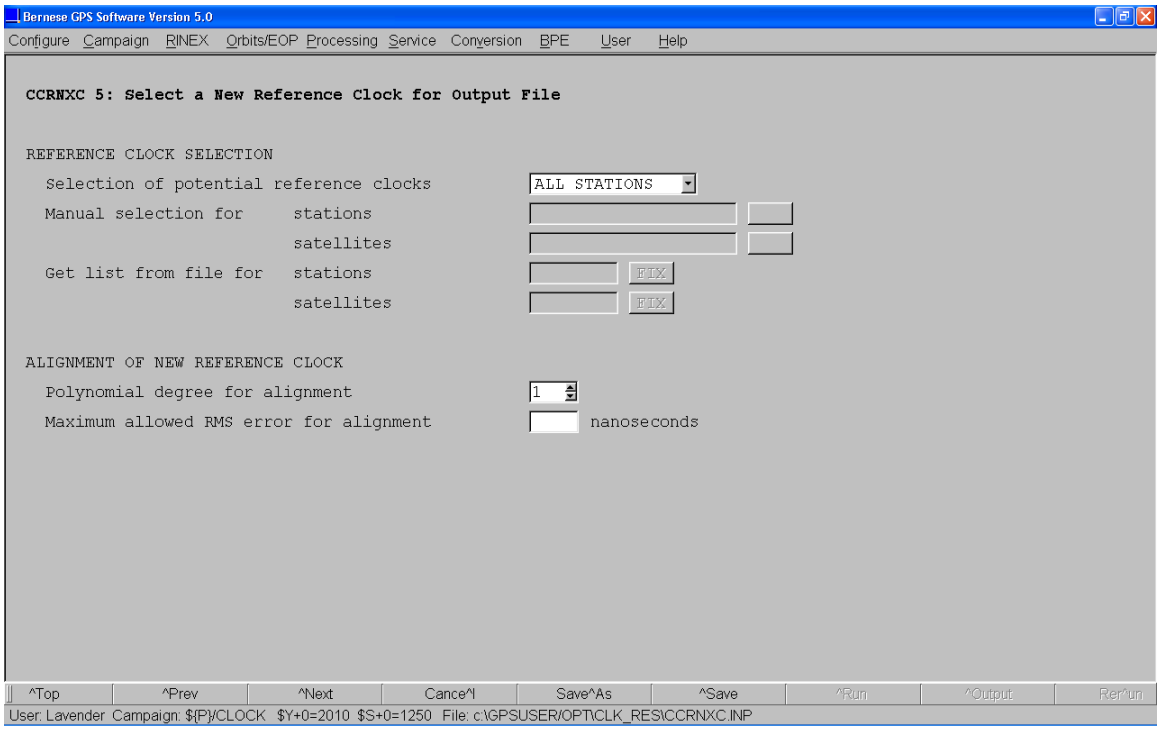
Bernese GPS Software Version 5.0
Configure Campaign RINEX Orbits/EOP Processing Service Conversion BPE User Help
CCRNXC 5: Select a New Reference Clock for Output File
REFERENCE CLOCK SELECTION
Selection of potential reference clocks
ALL STATIONS
Manual selection for stations
satellites
Get list from file for stations
FIX
satellites
FIX
ALIGNMENT OF NEW REFERENCE CLOCK
Polynomial degree for alignment
1
Maximum allowed RMS error for alignment
nanoseconds
^Top
^Prev
^Next
Cance^l
Save^As
^Save
^Run
^Output
Re^un
User: Lavender Campaign: ${P}/CLOCK $Y+0=2010 $S+0=1250 File: c:\GPSUSER/OPT\CLK_RES\CCRNXC.INP

APPENDIX E: EFFECT OF SECOND-ORDER IONOSPHERIC DELAY ON PPP

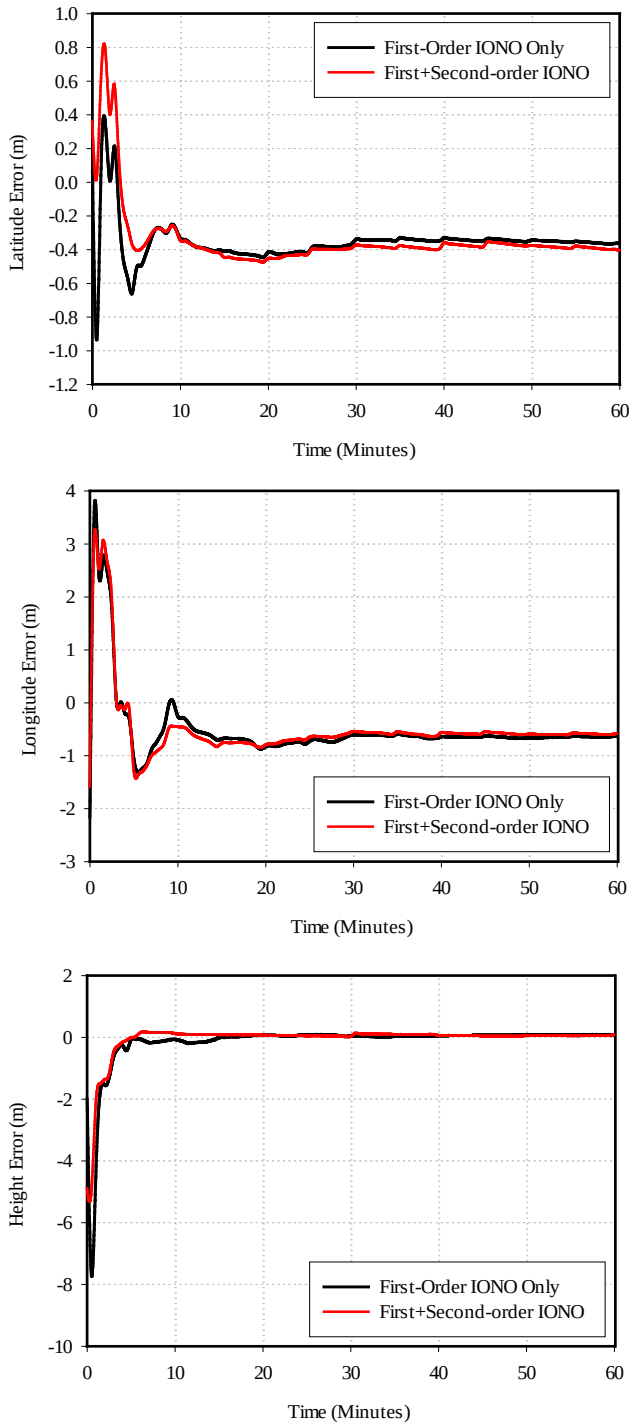

Figure E.1 Position Improvement Due to Accounting for Second-Order

Ionospheric Delay at BAN2 IGS Station

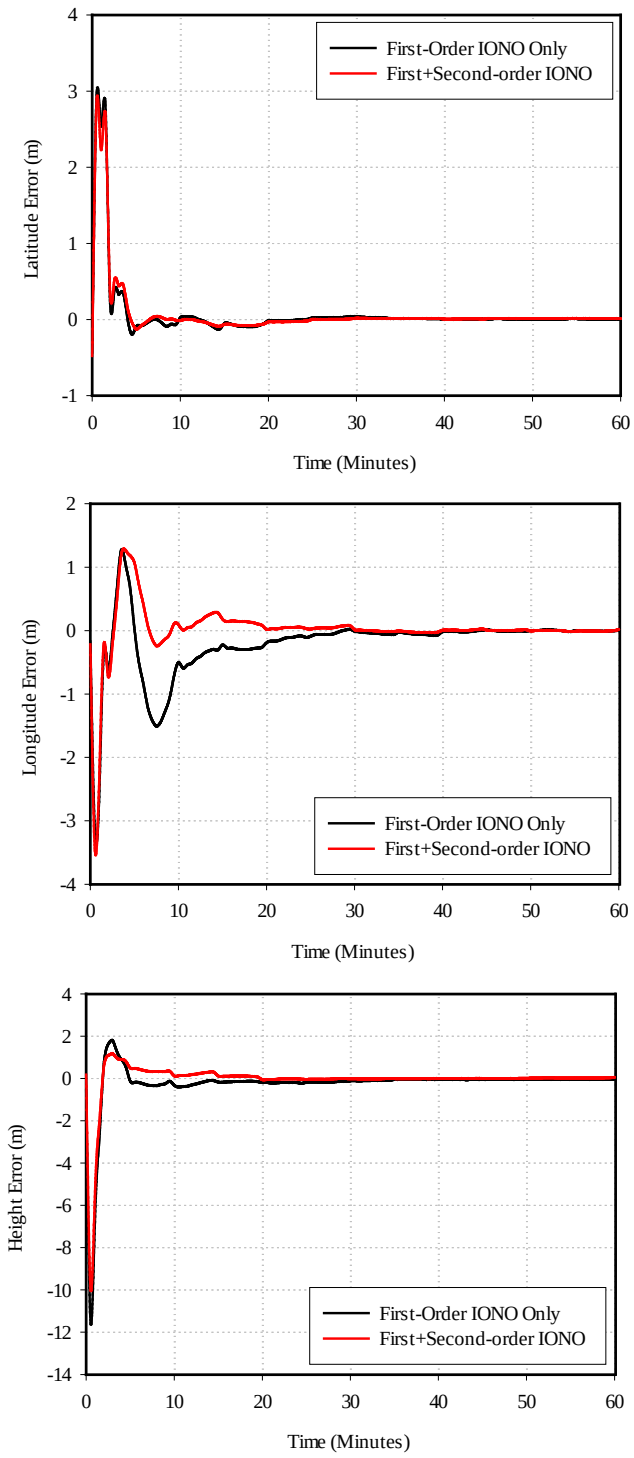

Figure E.2 Position Improvement Due to Accounting for Second-Order Ionospheric Delay at BUCU IGS Station

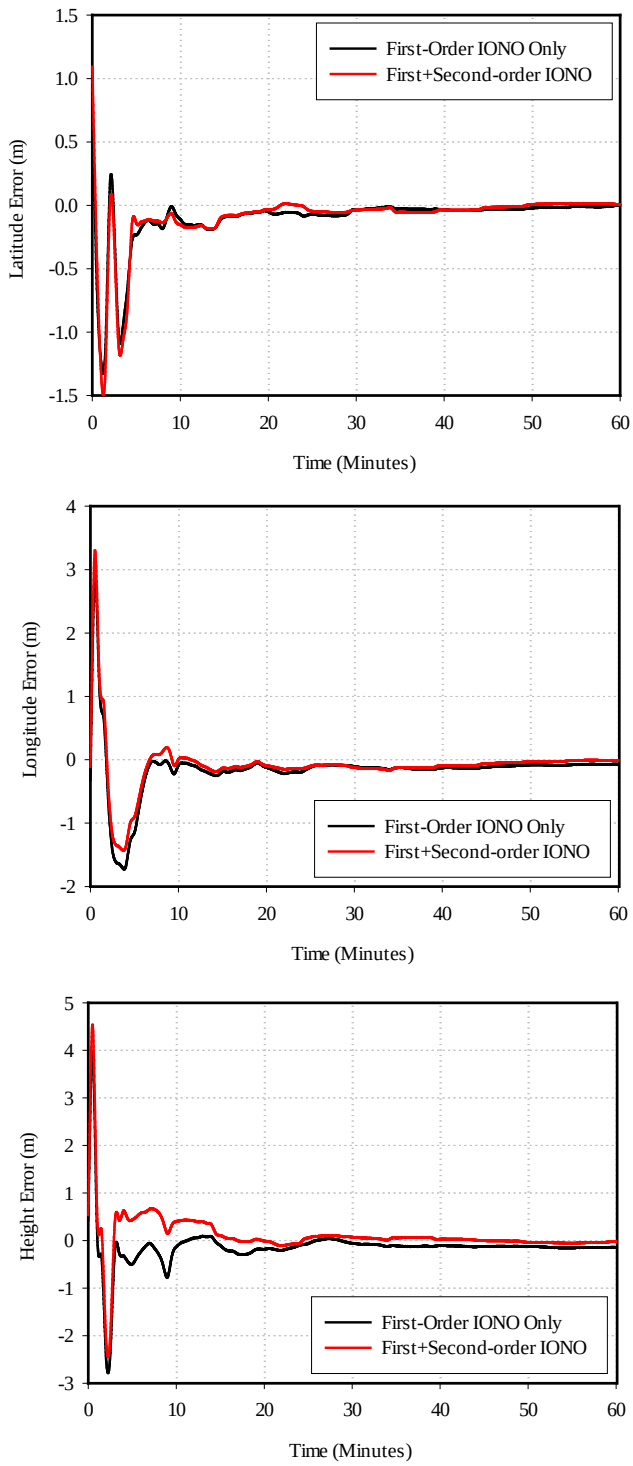

Figure E.3 Position Improvement Due to Accounting for Second-Order Ionospheric Delay at DAEJ IGS Station

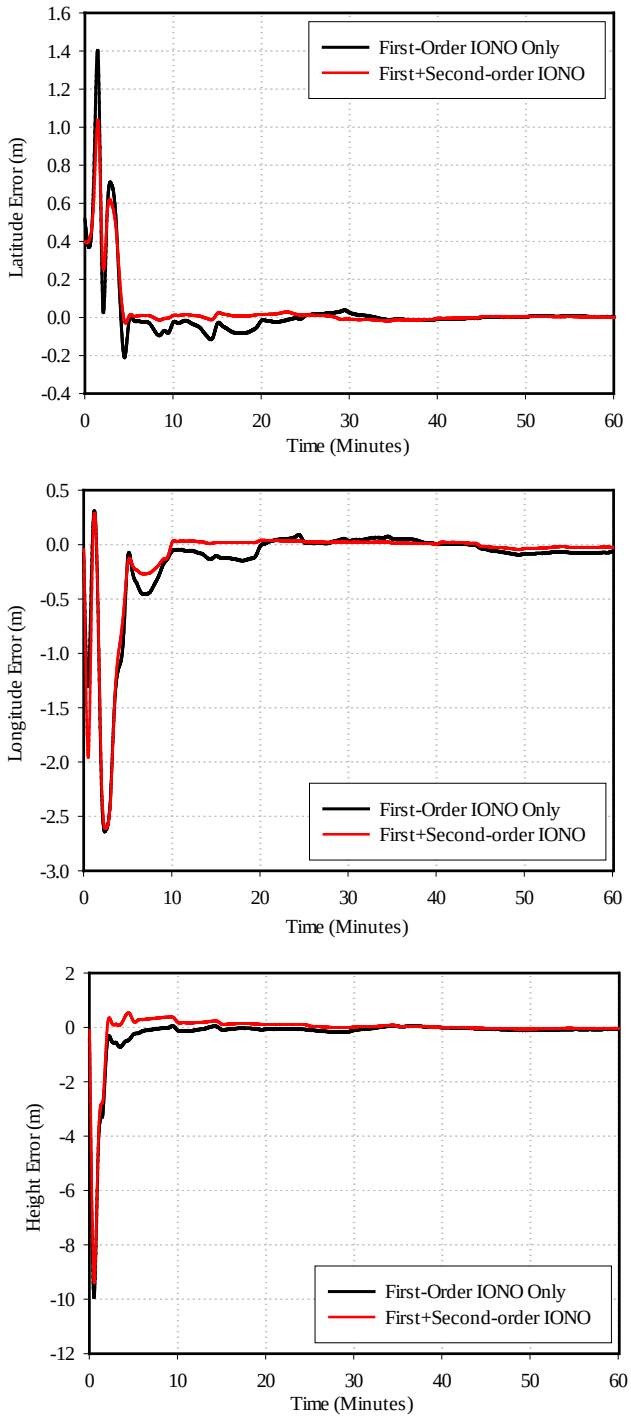

Figure E.4 Position Improvement Due to Accounting for Second-Order Ionospheric Delay at DRAG IGS Station

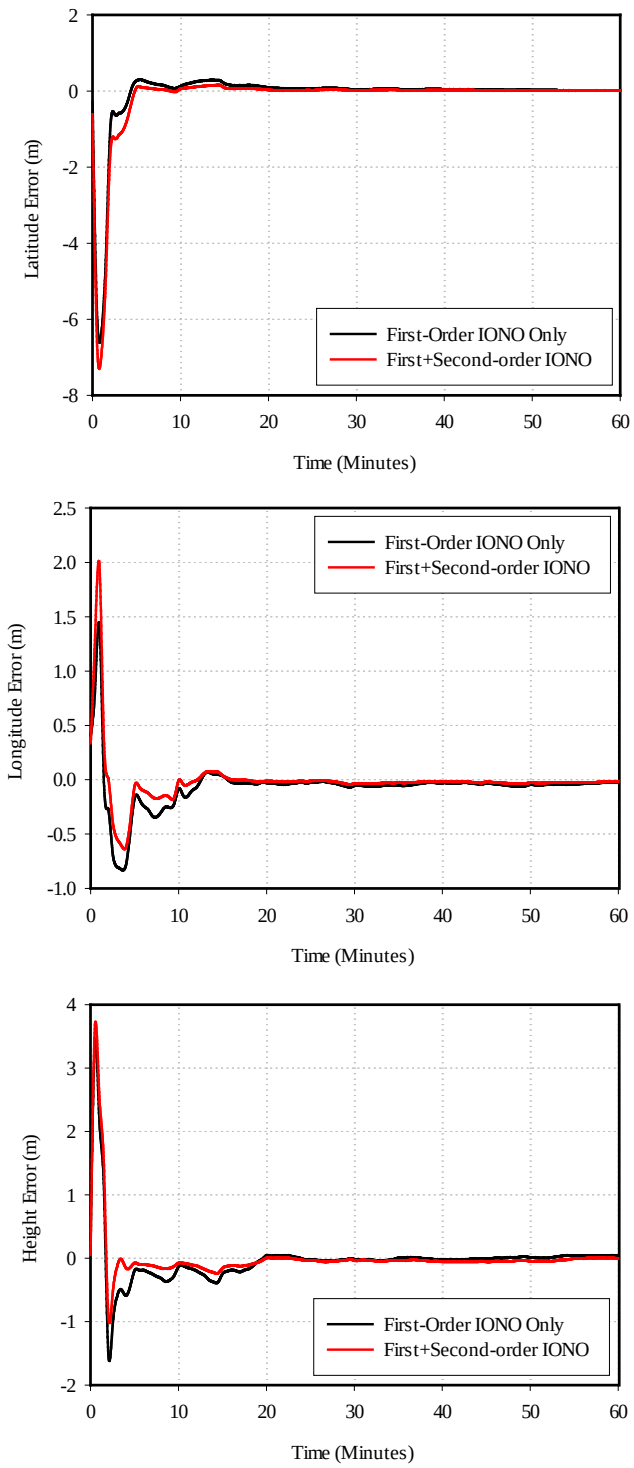

Figure E.5 Position Improvement Due to Accounting for Second-Order Ionospheric Delay at FLIN IGS Station

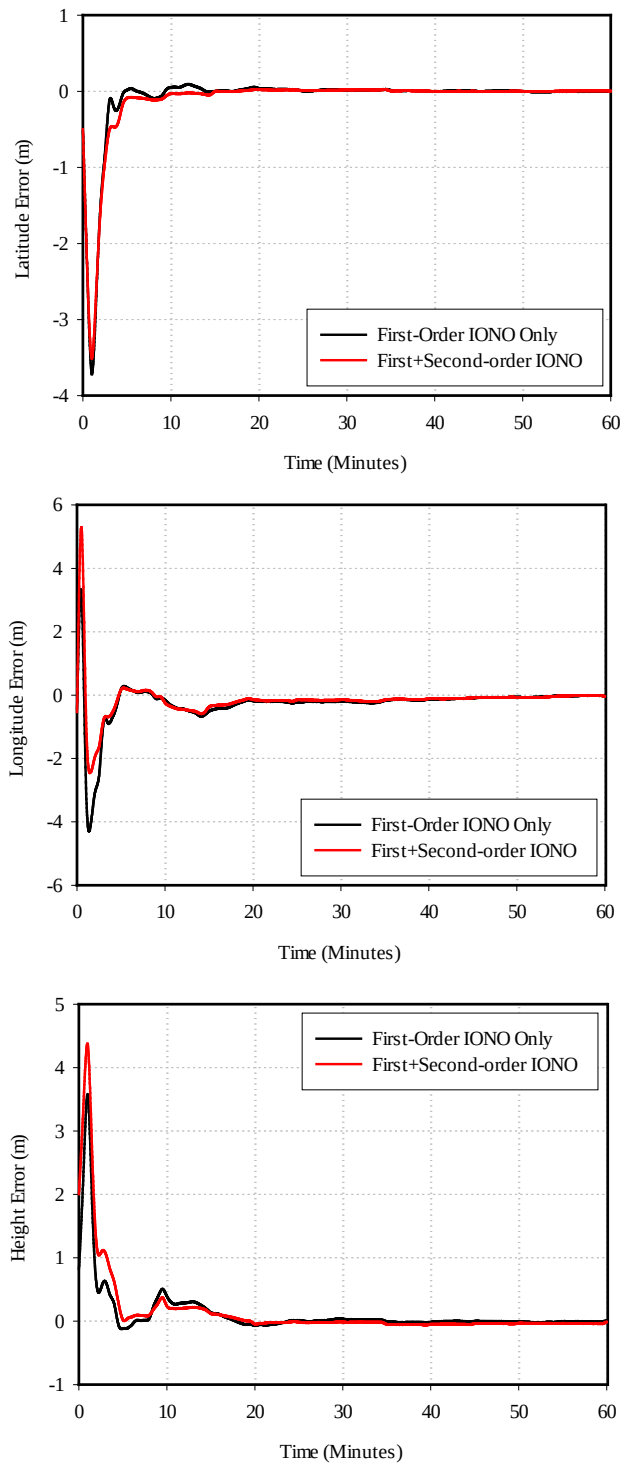

Figure E.6 Position Improvement Due to Accounting for Second-Order Ionospheric Delay at GUAT IGS Station

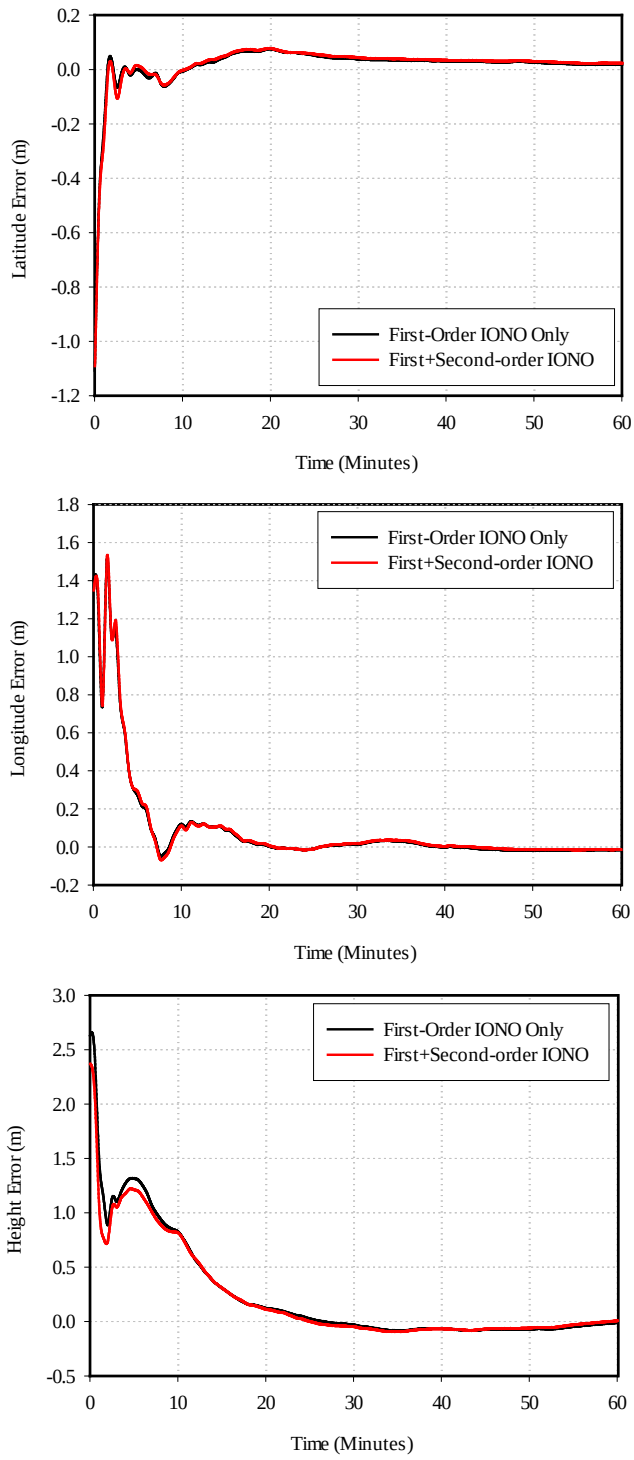

Figure E.7 Position Improvement Due to Accounting for Second-Order Ionospheric Delay at HARB IGS Station

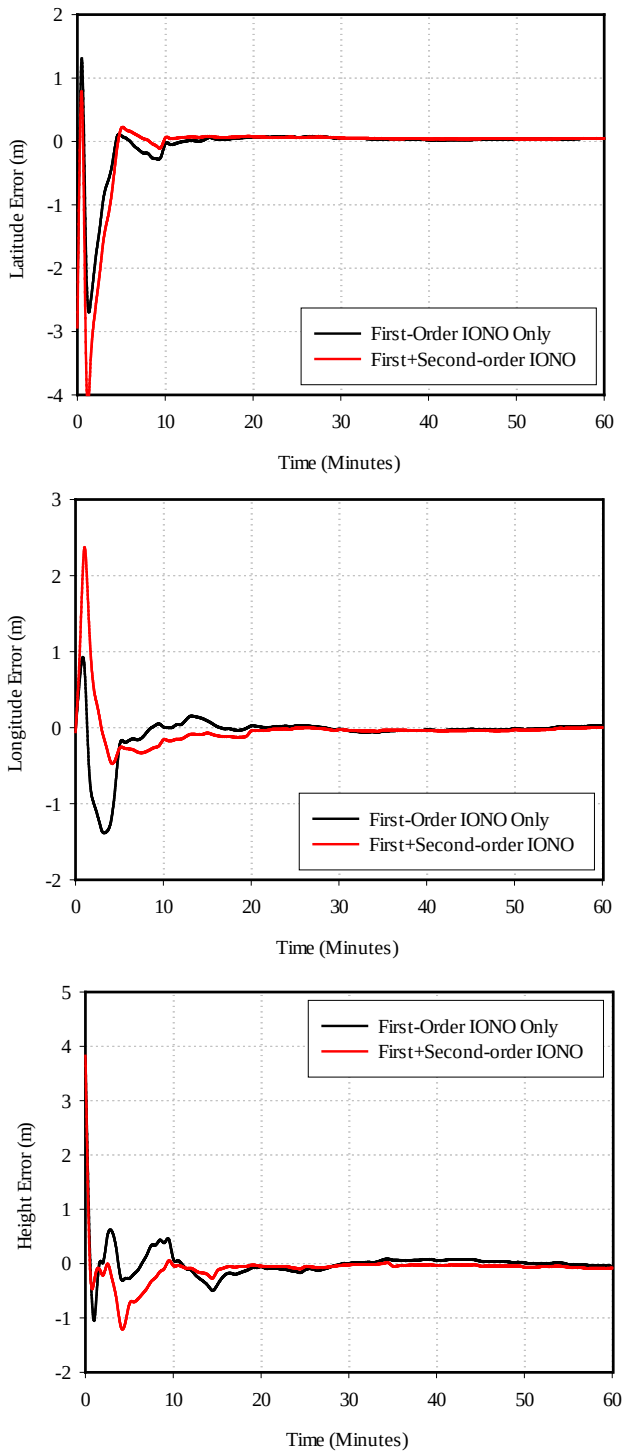

Figure E.8 Position Improvement Due to Accounting for Second-Order Ionospheric Delay at JPLM IGS Station

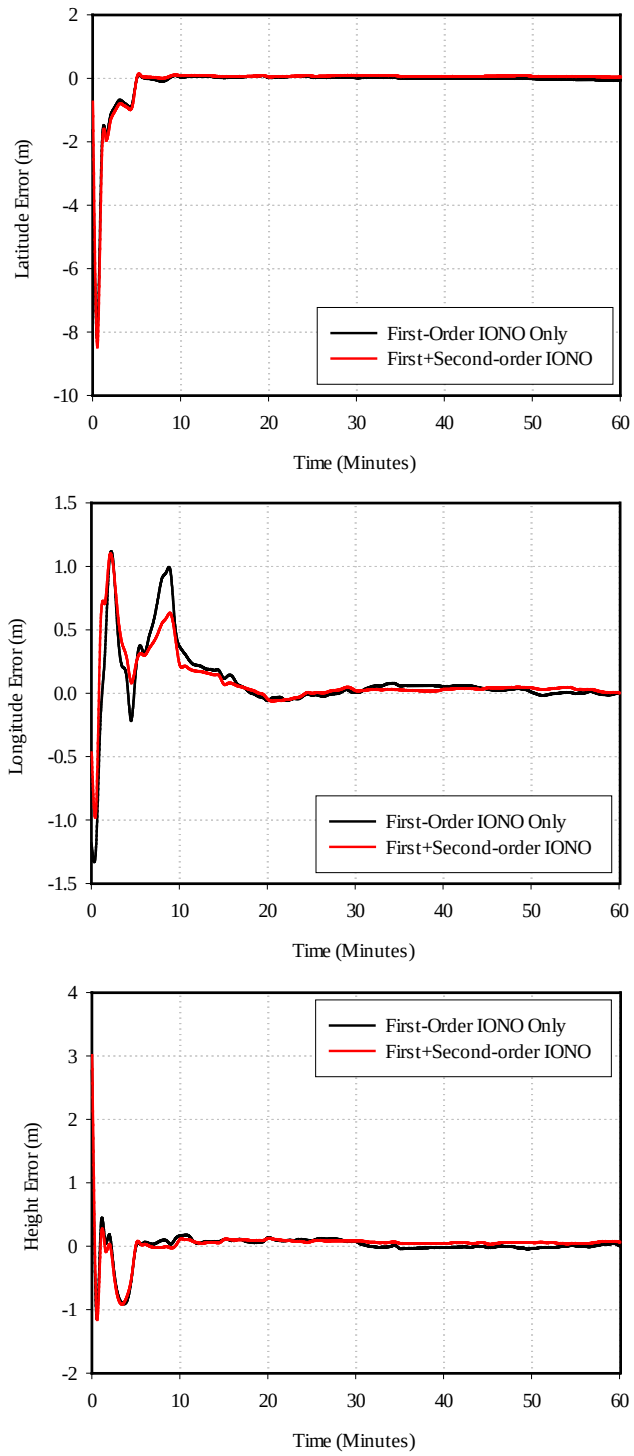

Figure E.9 Position Improvement Due to Accounting for Second-Order Ionospheric Delay at LPGS IGS Station

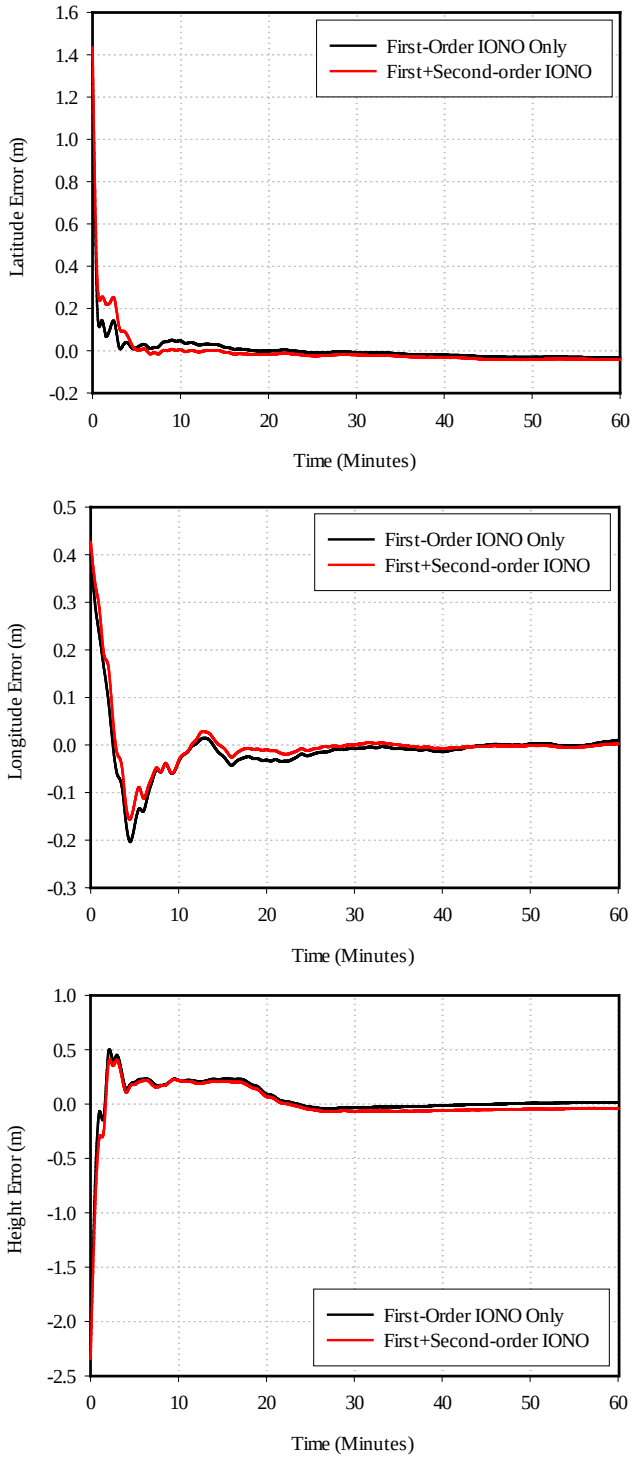

Figure E.10 Position Improvement Due to Accounting for Second-Order Ionospheric Delay at MOBS IGS Station

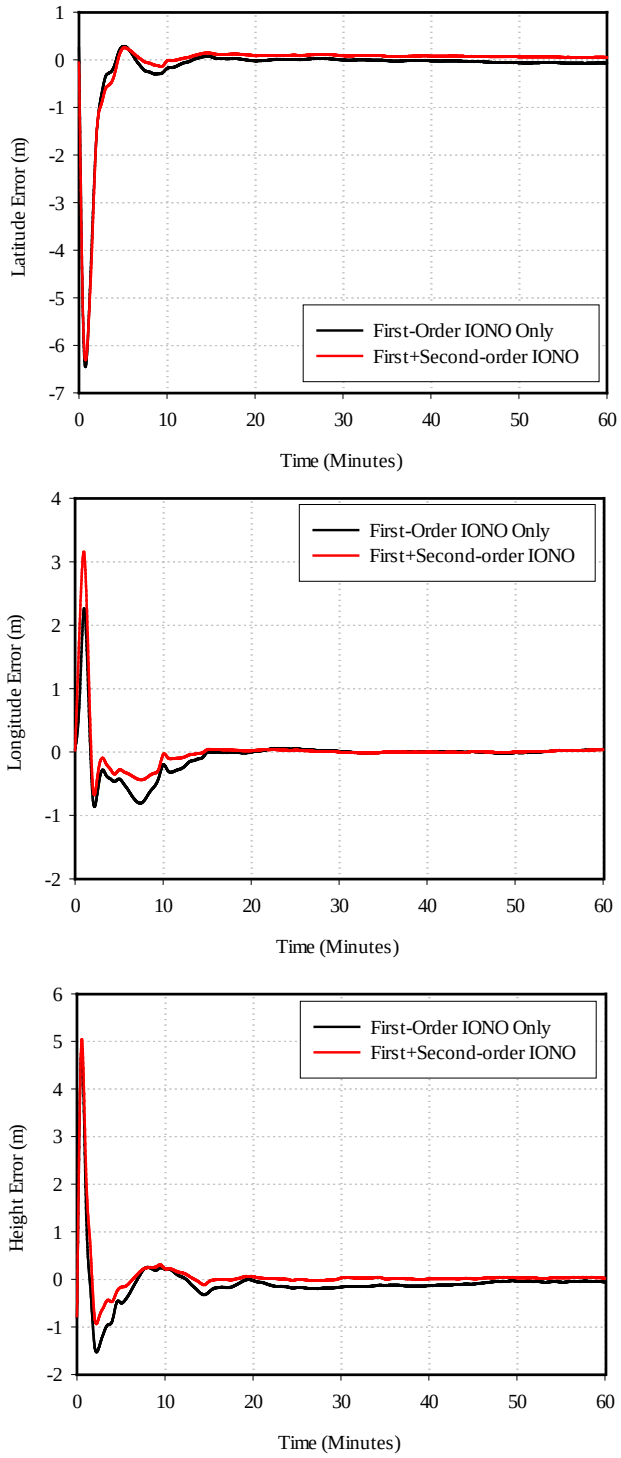

Figure E.11 Position Improvement Due to Accounting for Second-Order Ionospheric Delay at NANO IGS Station

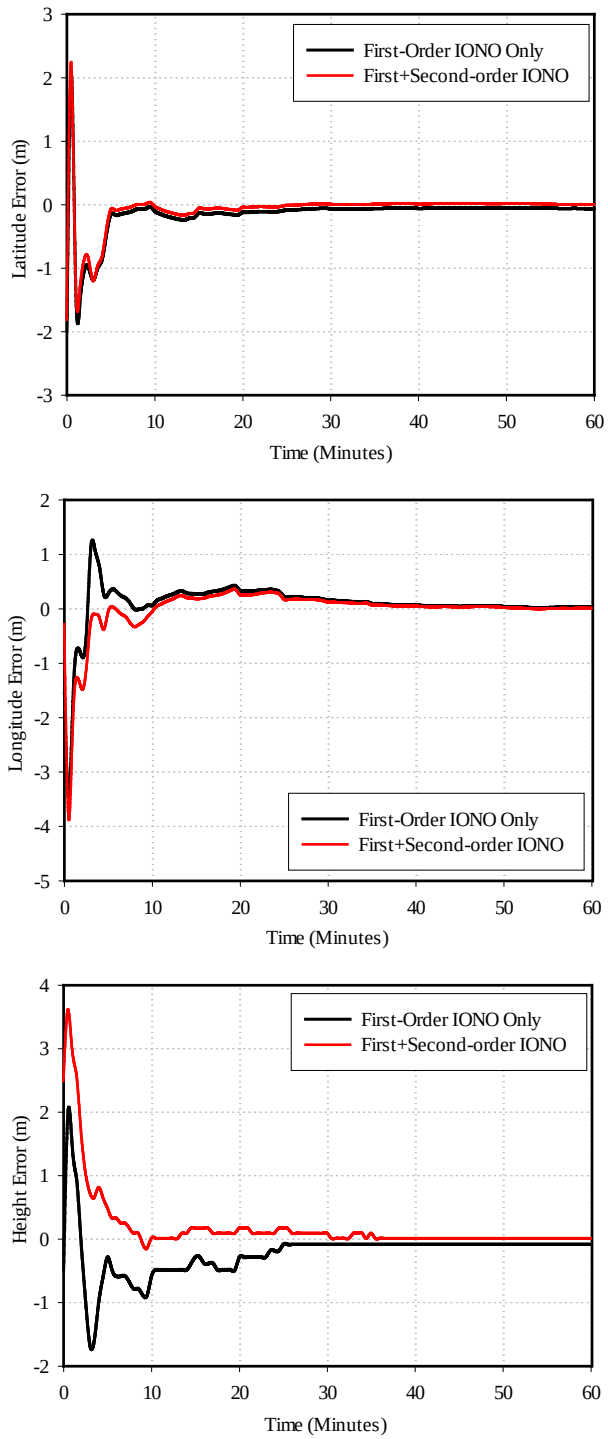

Figure E.12 Position Improvement Due to Accounting for Second-Order Ionospheric Delay at TAH1 IGS Station

APPENDIX F: VERIFICATION OF THE DEVELOPED PPP MODELS

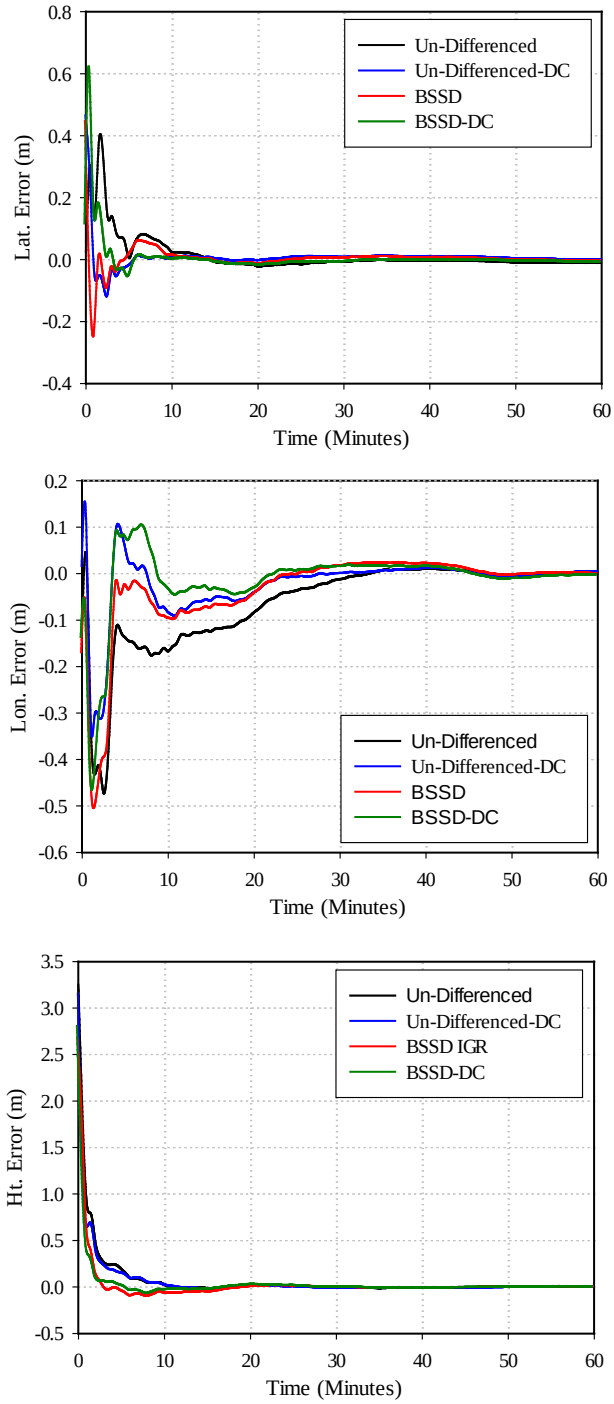

Figure F.1 Position Solution Using the Developed PPP Models for AJAC IGS Station

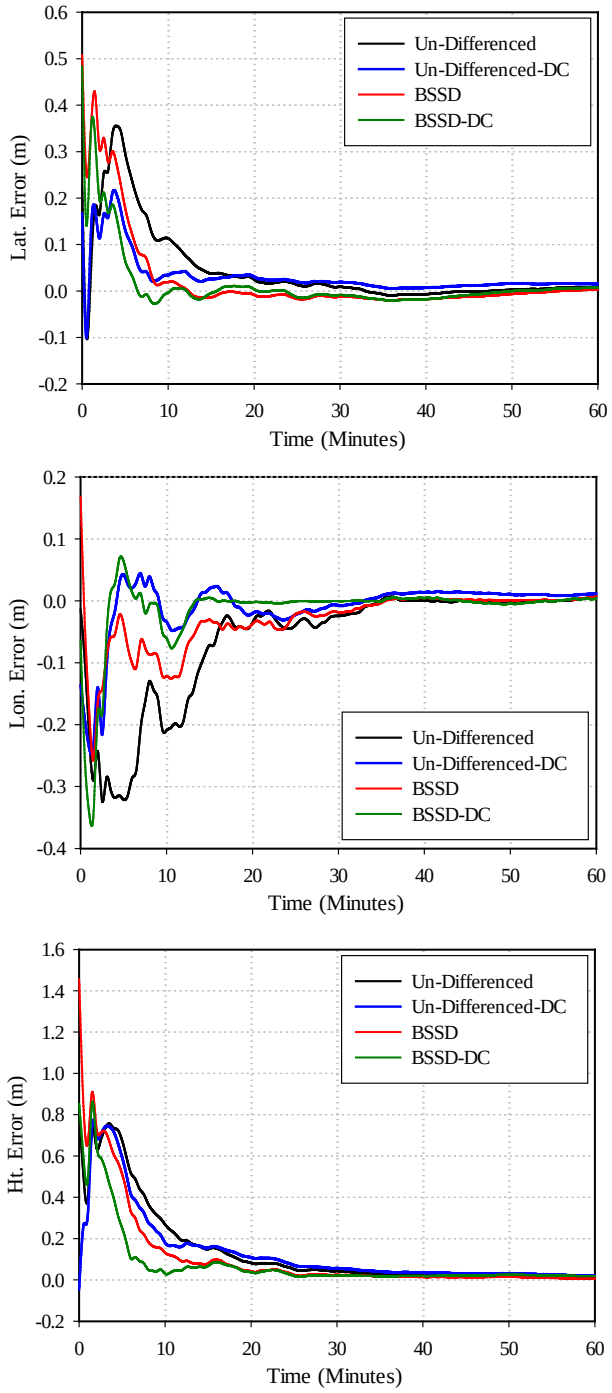

Figure F.2 Position Solution Using the Developed PPP Models for ALGO IGS Station

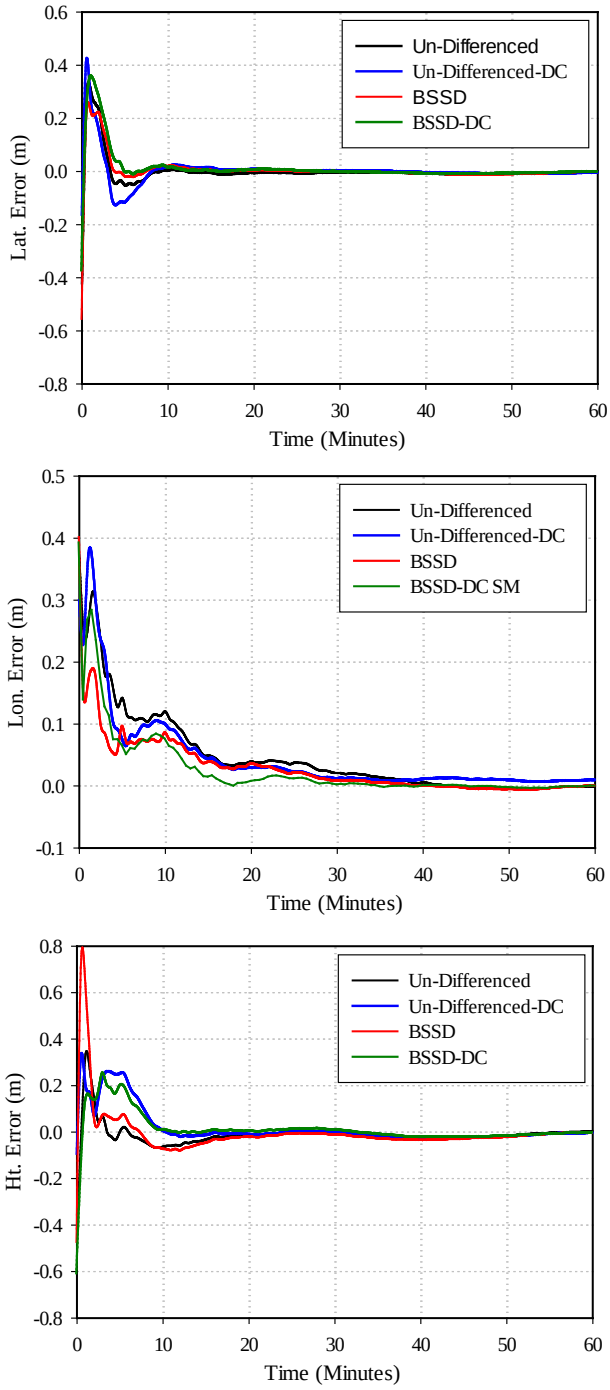

Figure F.3 Position Solution Using the Developed PPP Models for ARTU IGS Station

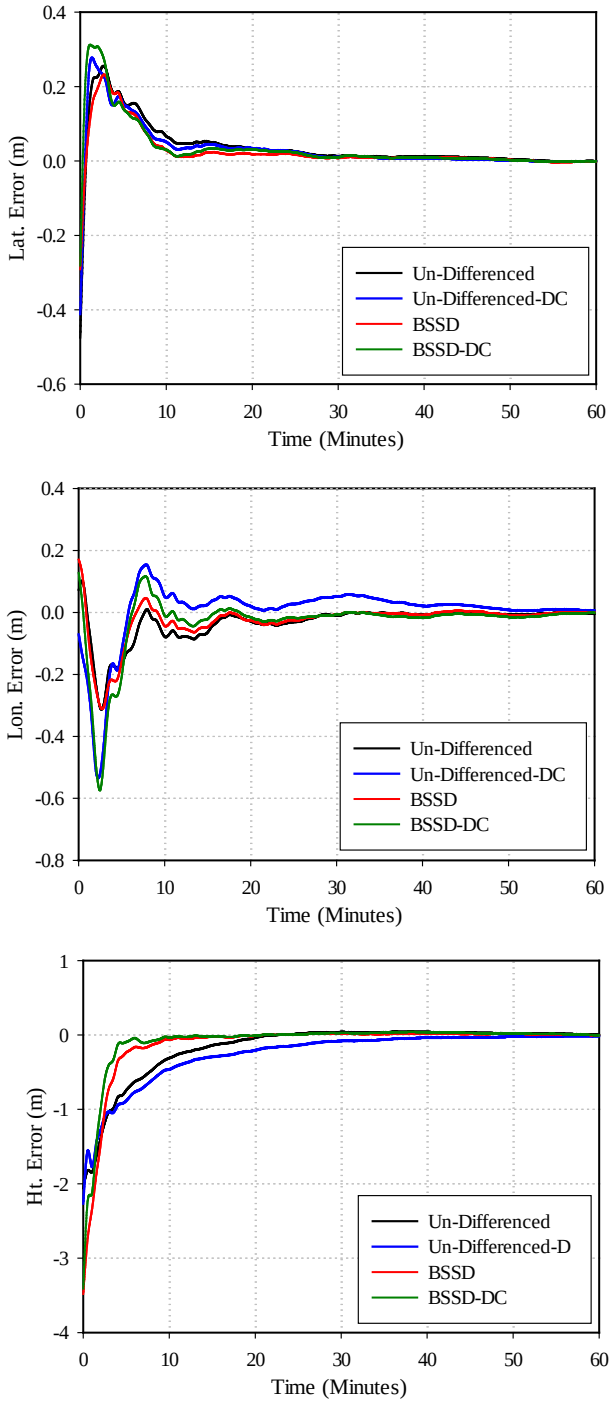

Figure F.4 Position Solution Using the Developed PPP Models for BAKO IGS Station

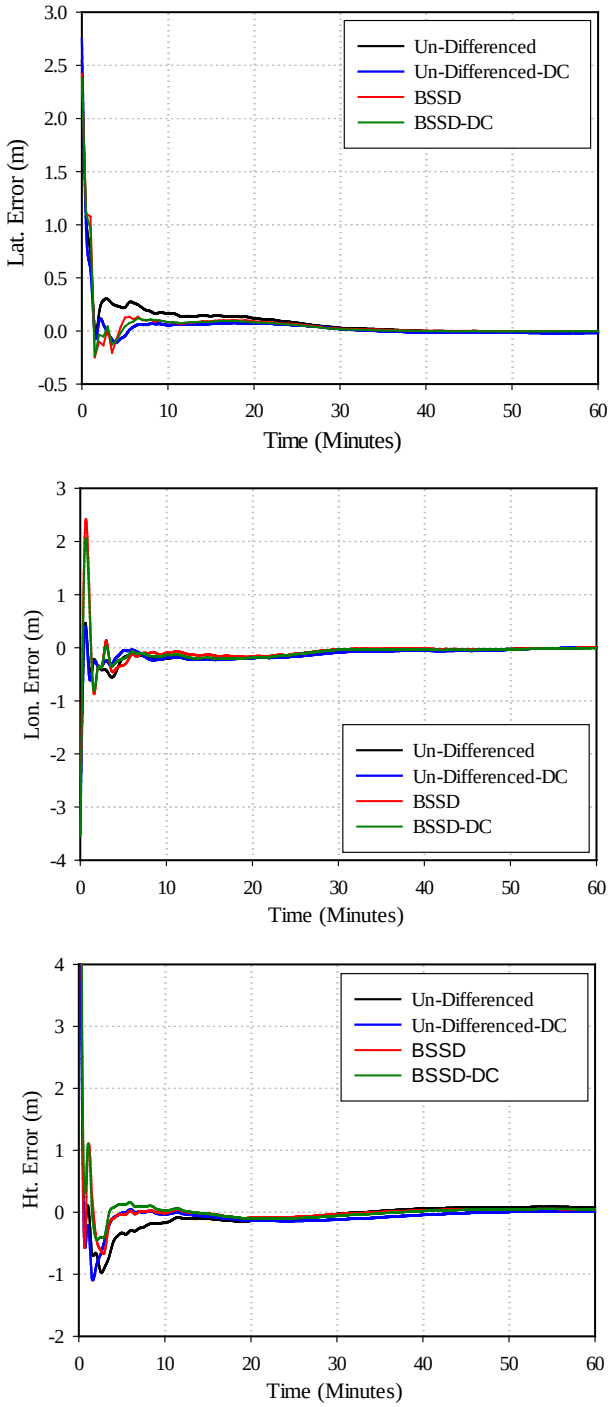

Figure F.5 Position Solution Using the Developed PPP Models for BAN2 IGS Station

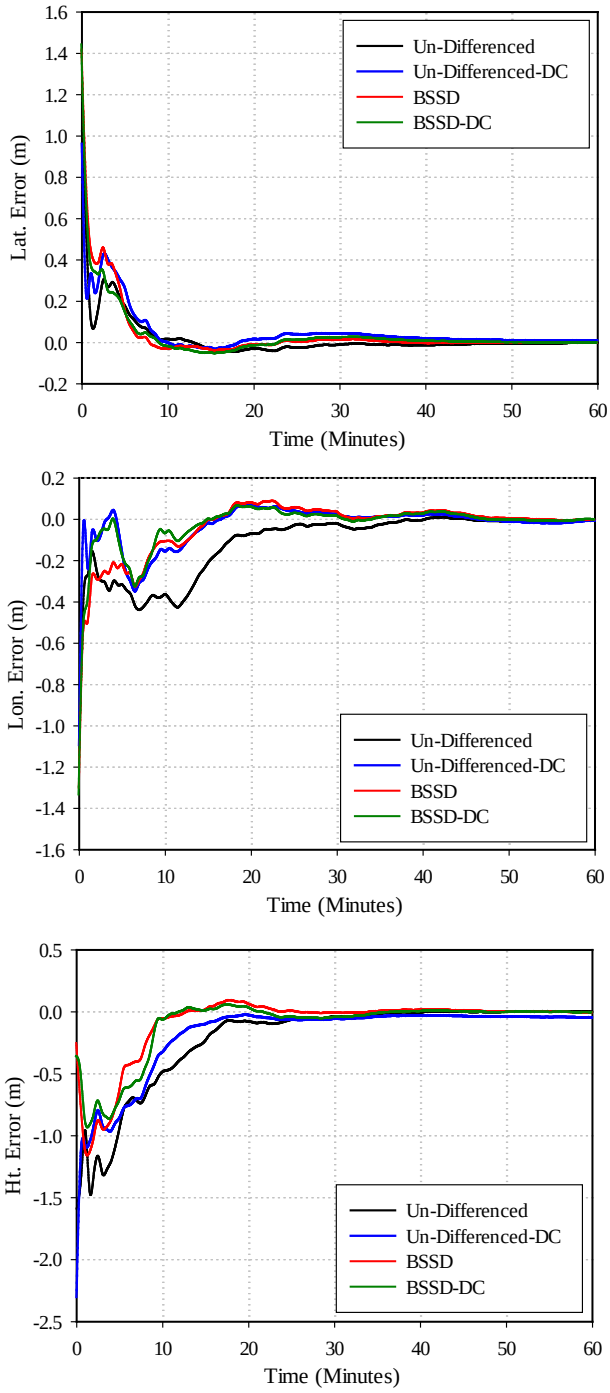

Figure F.6 Position Solution Using the Developed PPP Models for BRAZ IGS Station

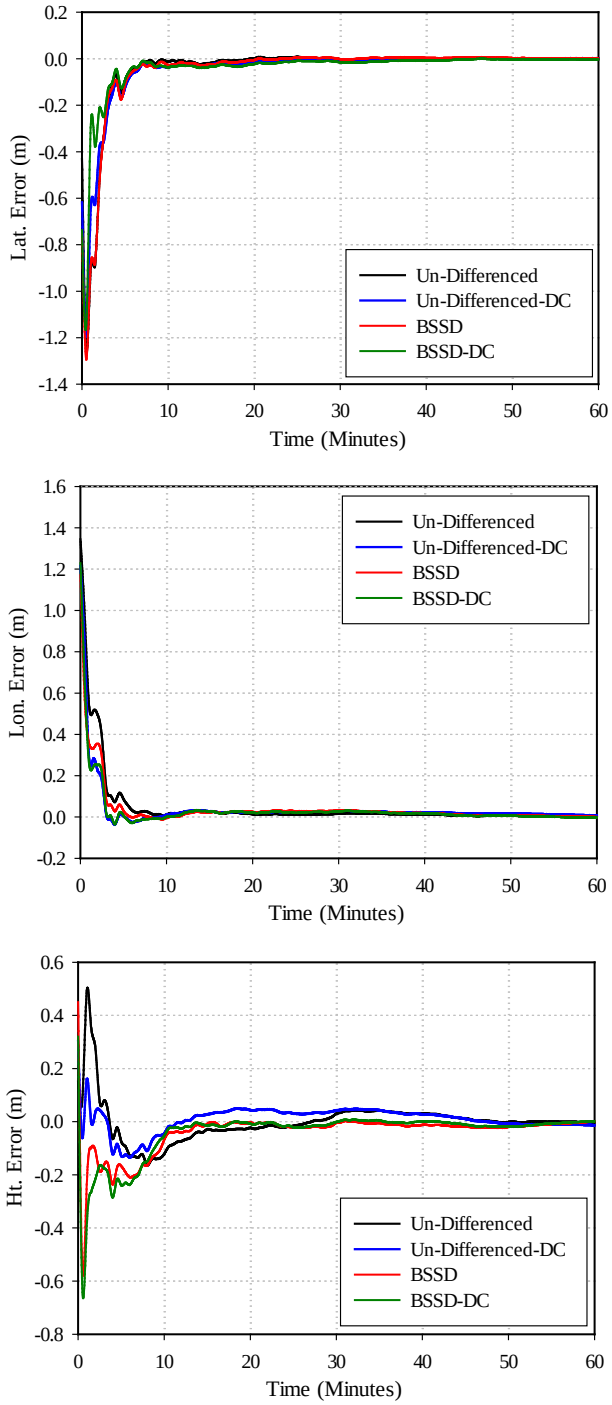

Figure F.7 Position Solution Using the Developed PPP Models for BRUS IGS Station

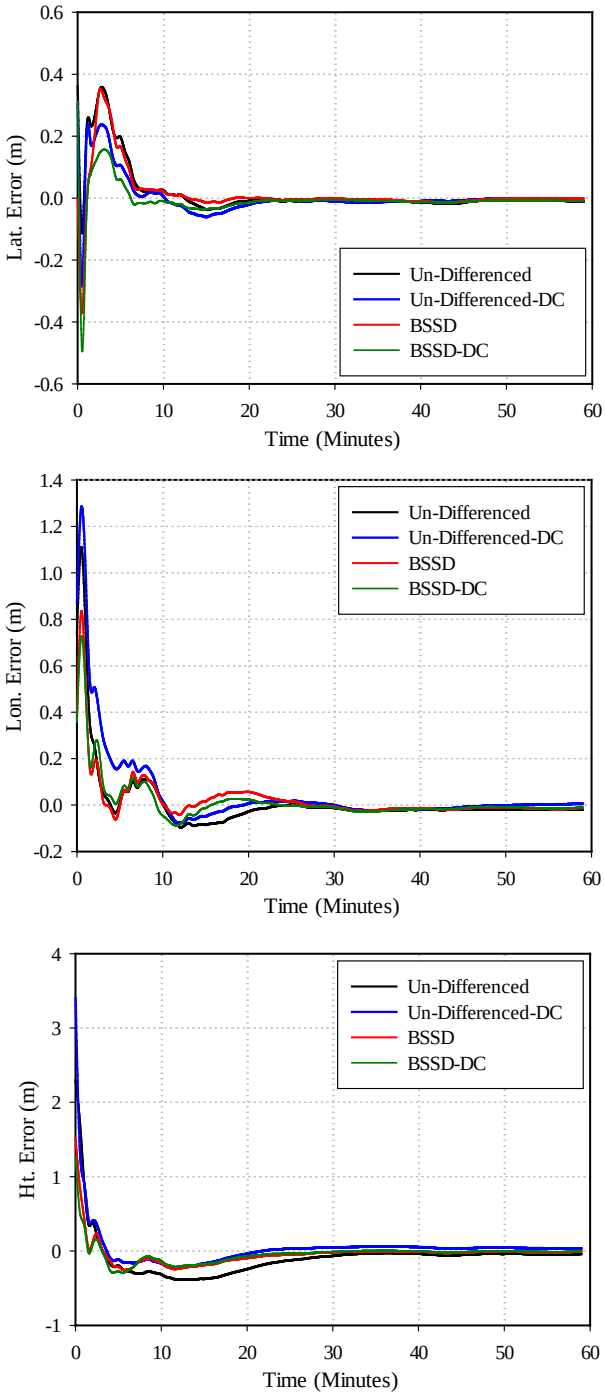

Figure F.8 Position Solution Using the Developed PPP Models **for** CHAT IGS Station

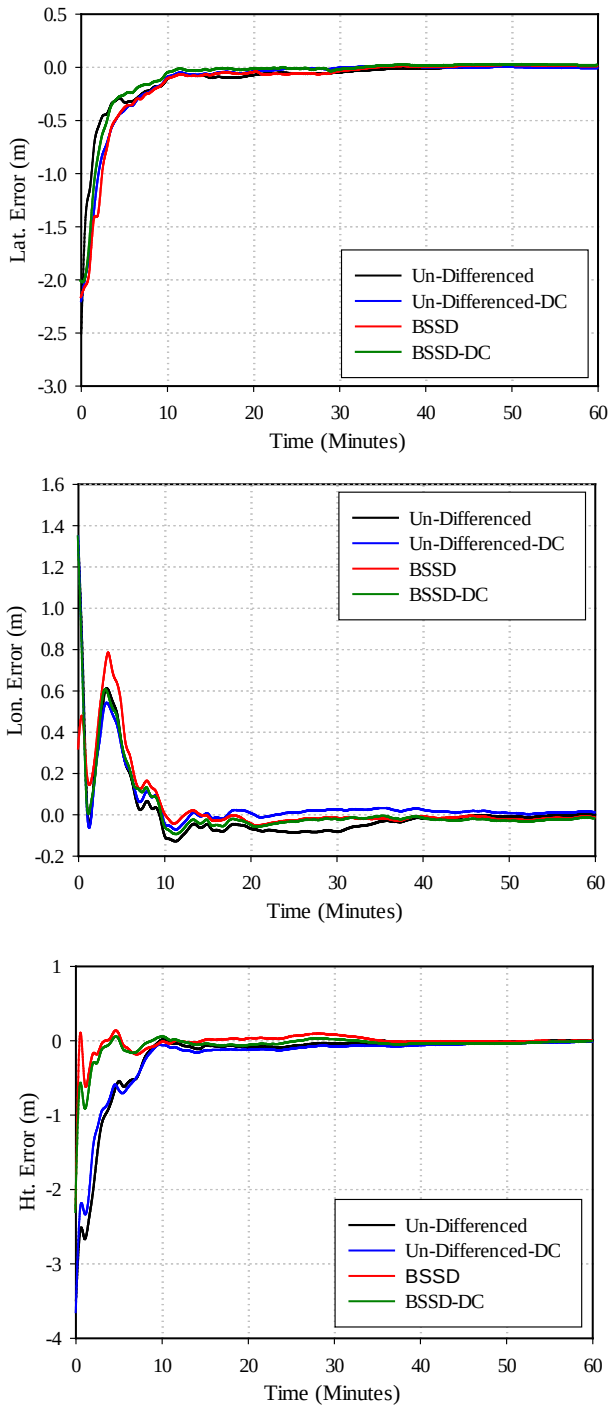

Figure F.9 Position Solution Using the Developed PPP Models for FAIC IGS Station

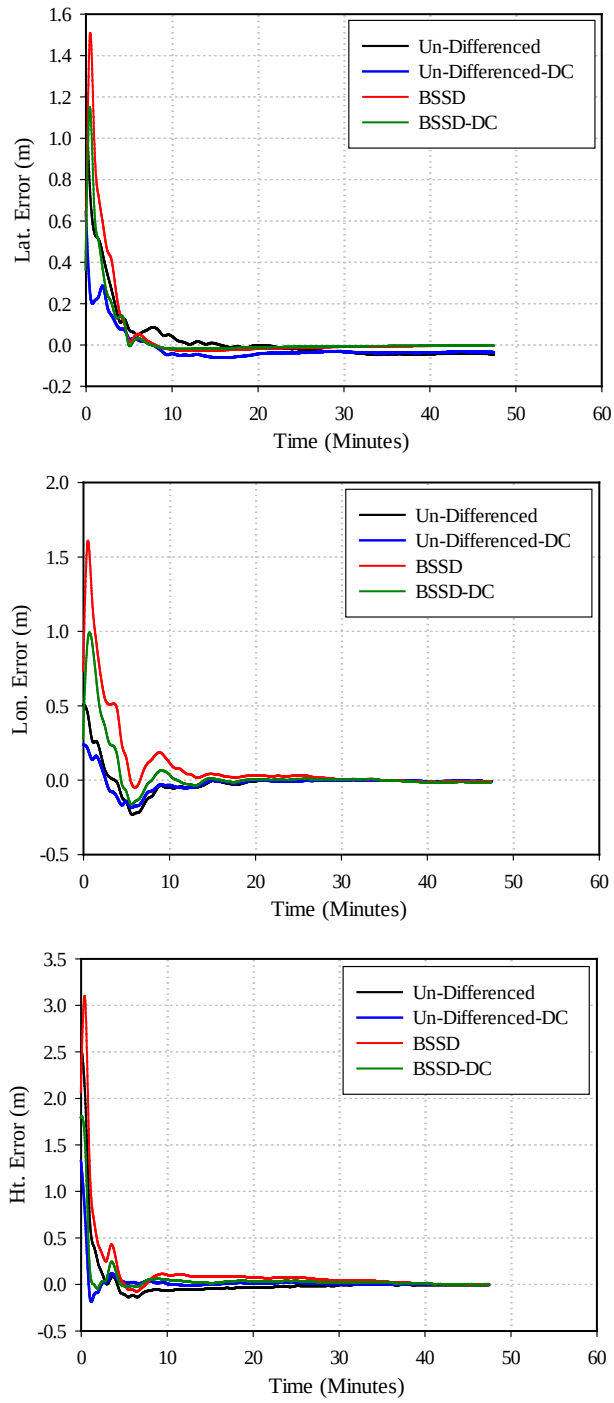

Figure F.10 Position Solution Using the Developed PPP Models for FLIN IGS Station

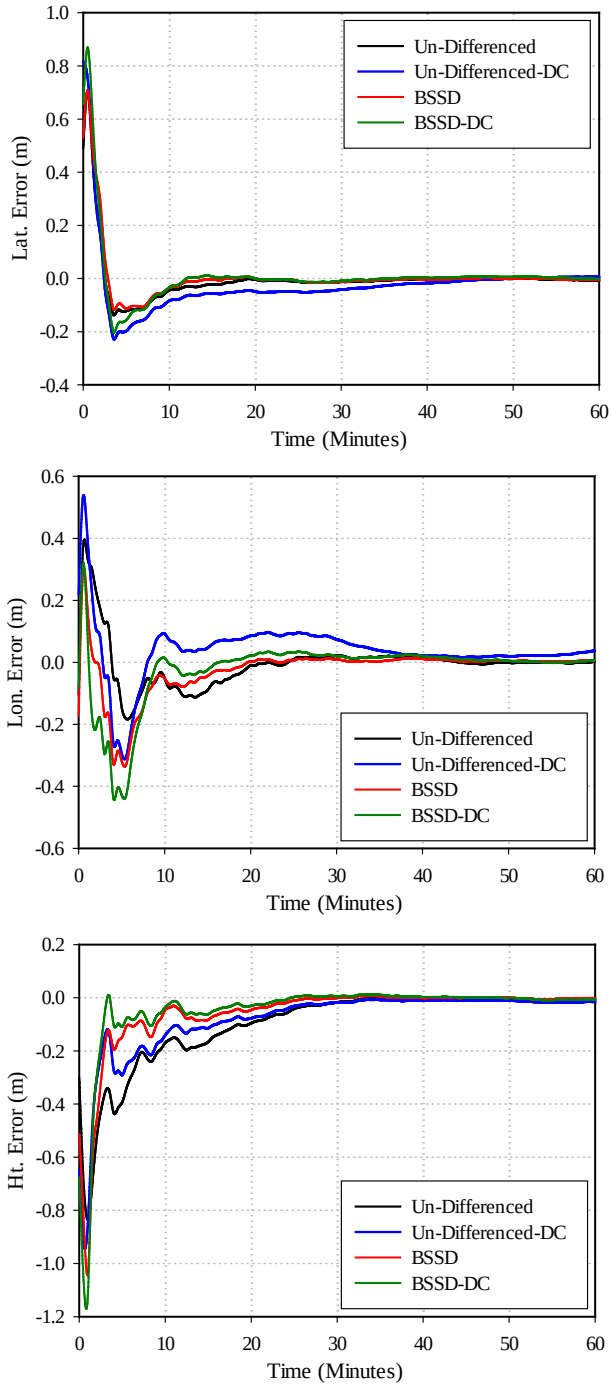

Figure F.11 Position Solution Using the Developed PPP Models for GUAM IGS Station

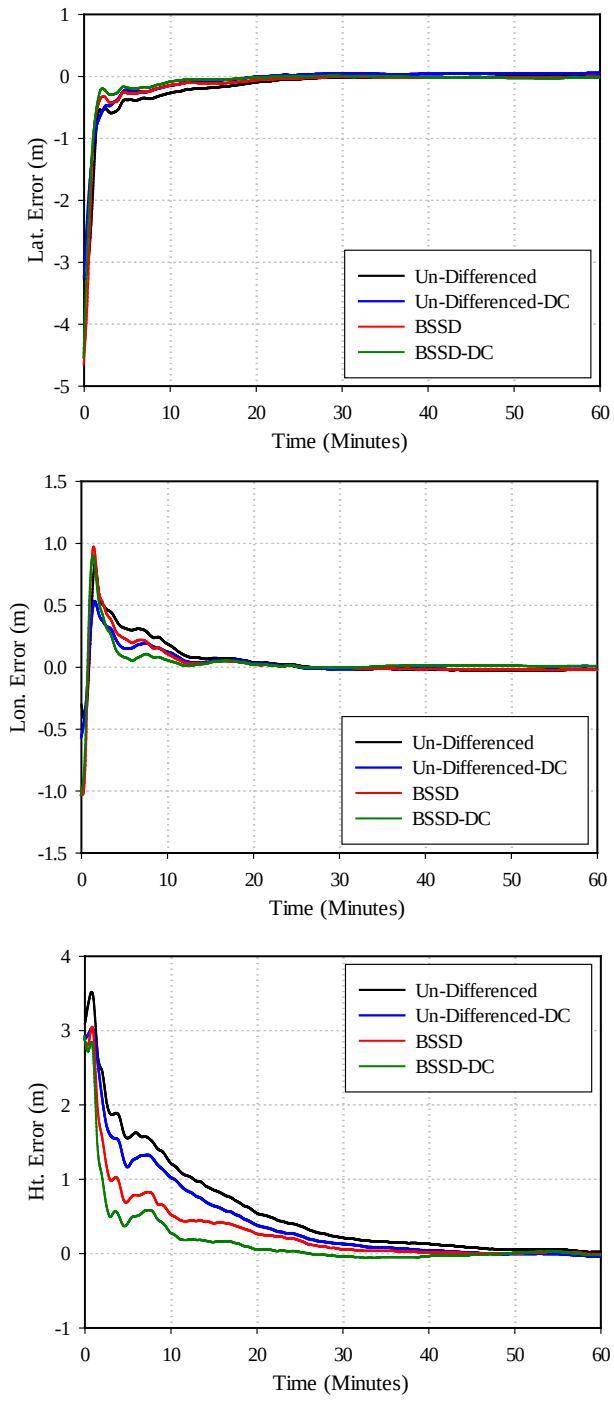

Figure F.12 Position Solution Using the Developed PPP Models for JPLM IGS Station

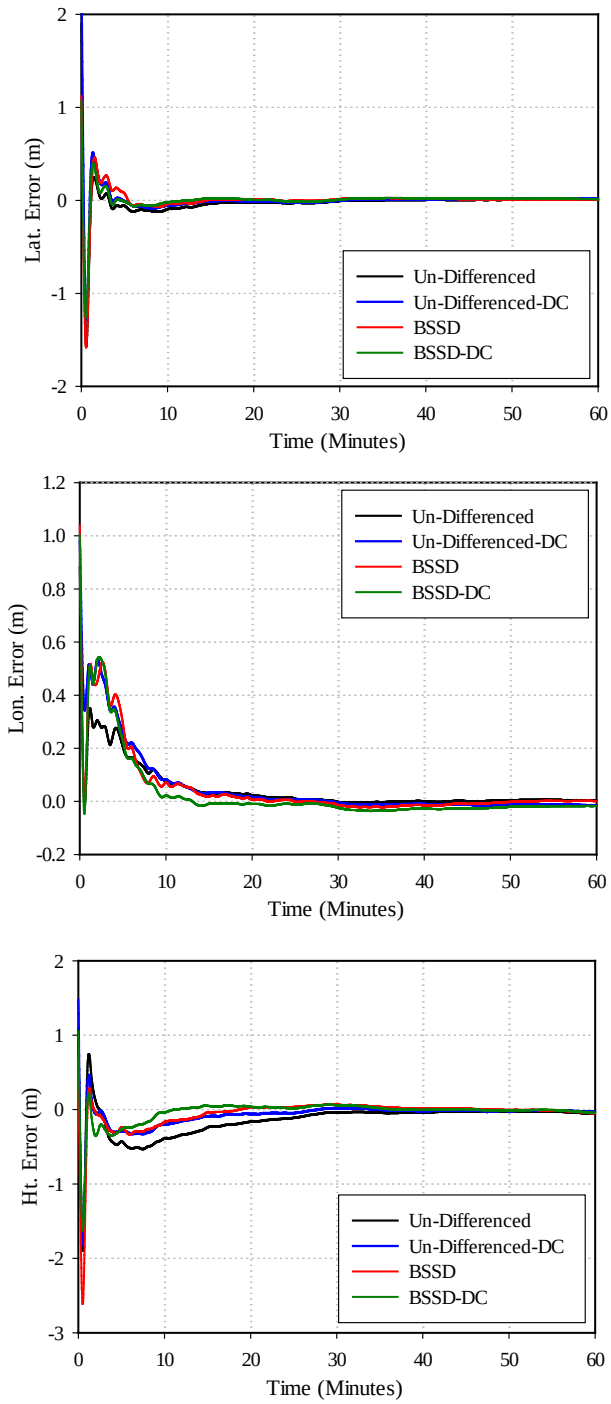

Figure F.13 Position Solution Using the Developed PPP Models for KERG IGS Station

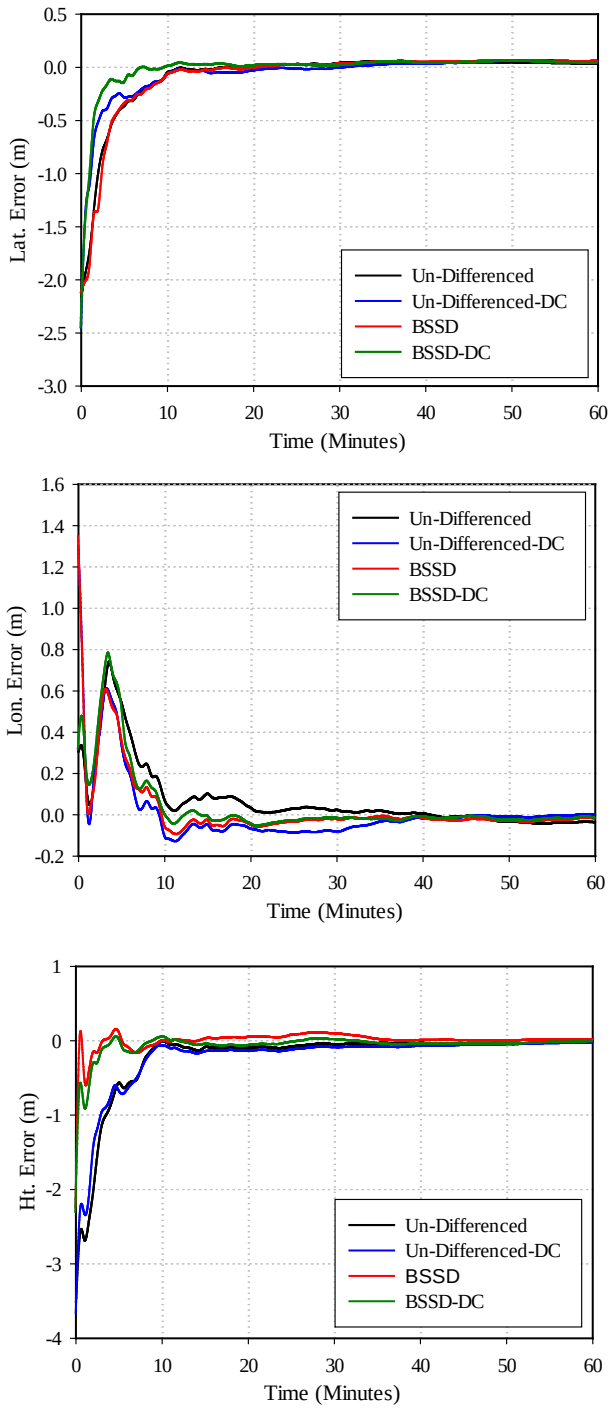

Figure F.14 Position Solution Using the Developed PPP Models for KOKC IGS Station

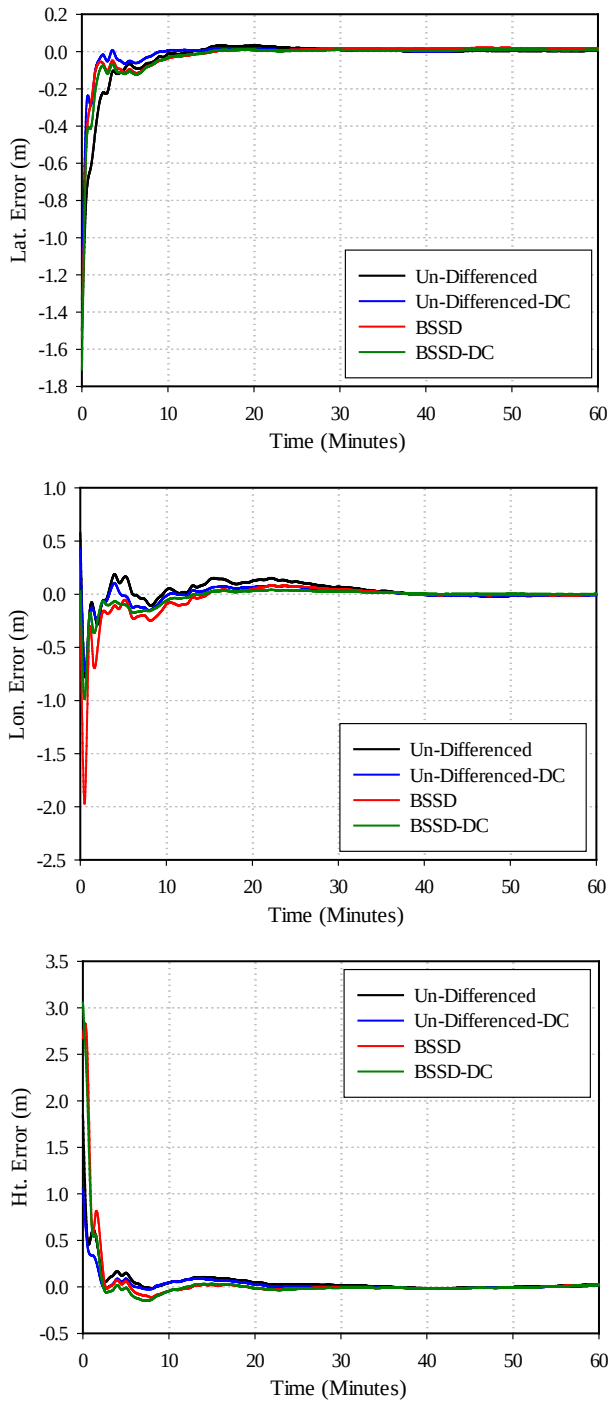

Figure F.15 Position Solution Using the Developed PPP Models for MAS1 IGS Station

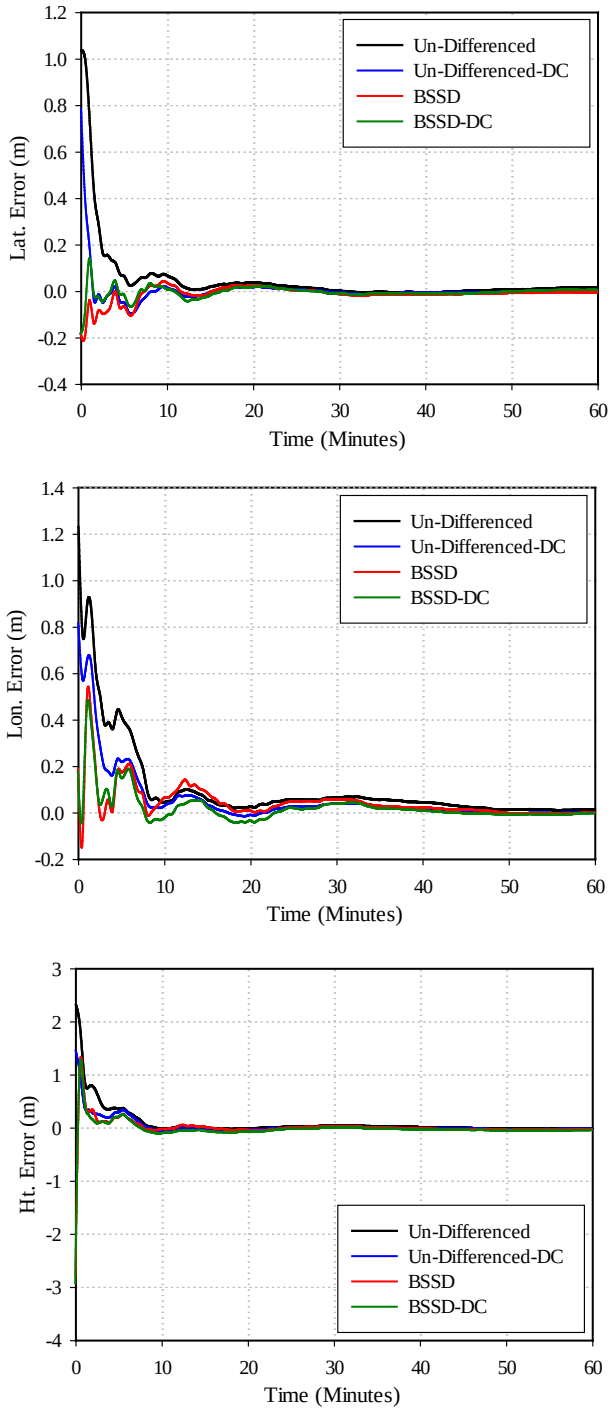

Figure F.16 Position Solution Using the Developed PPP Models for POTS IGS Station

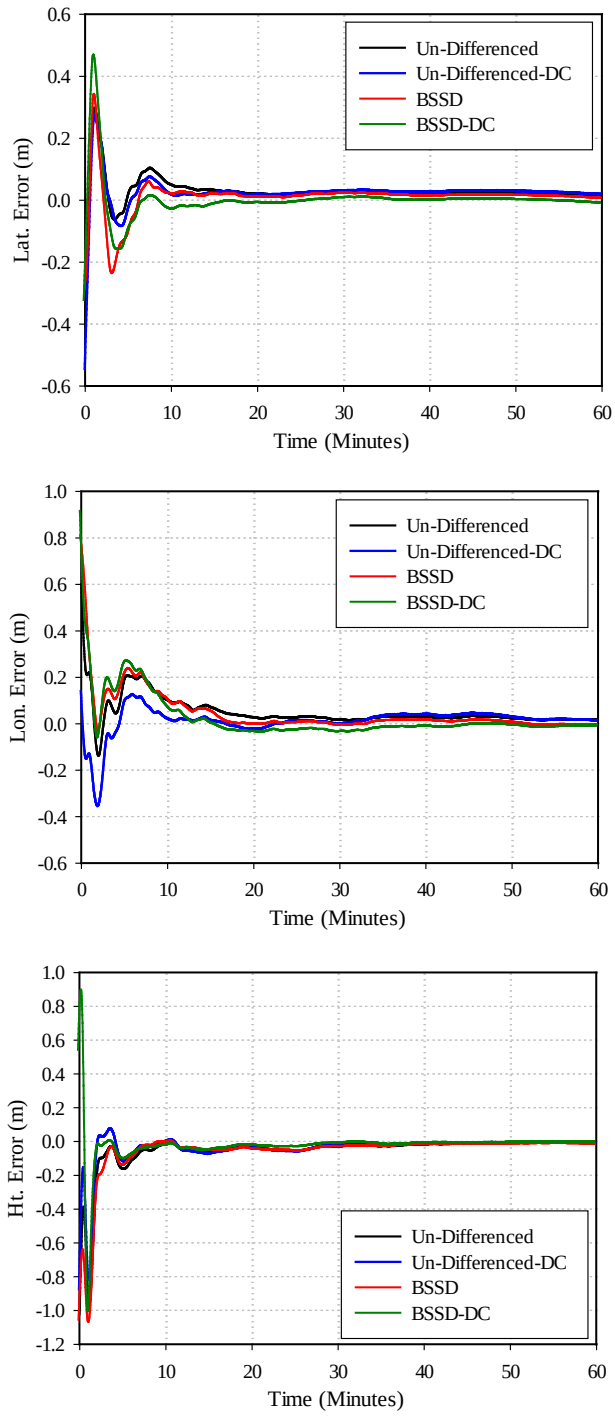

Figure F.17 Position Solution Using the Developed PPP Models for RAMO IGS Station

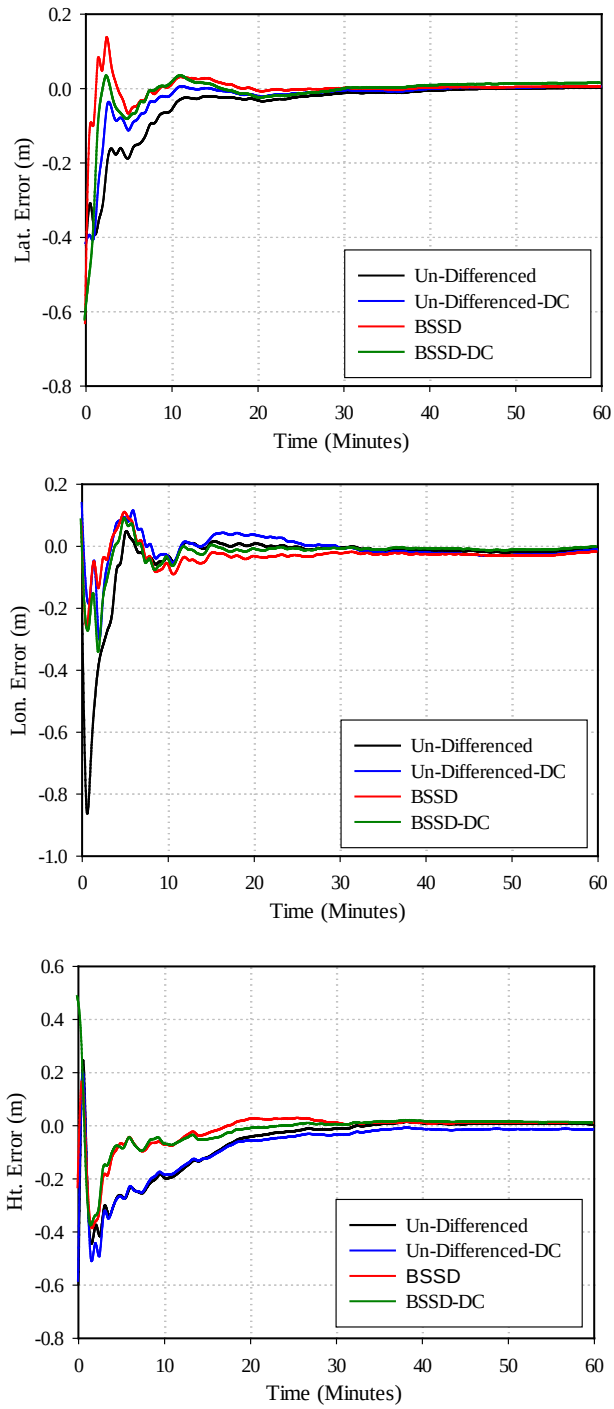

Figure F.18 Position Solution Using the Developed PPP Models for ROSA IGS Station

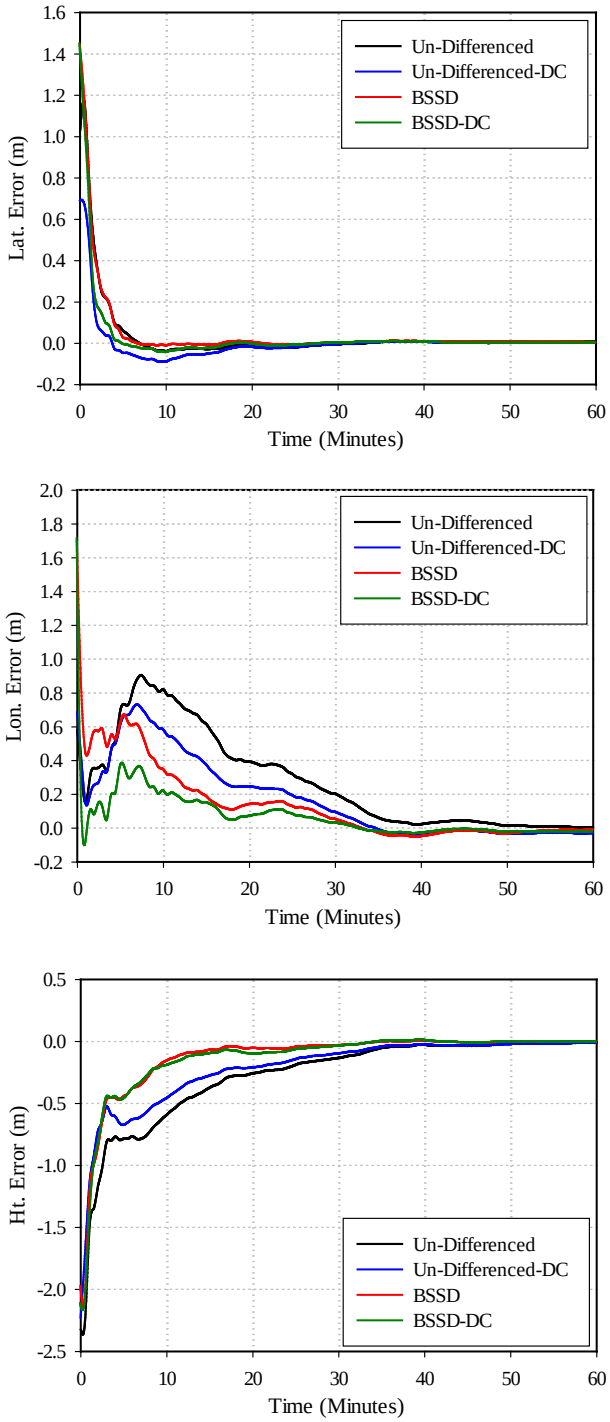

Figure F.19 Position Solution Using the Developed PPP Models for SCUB IGS Station

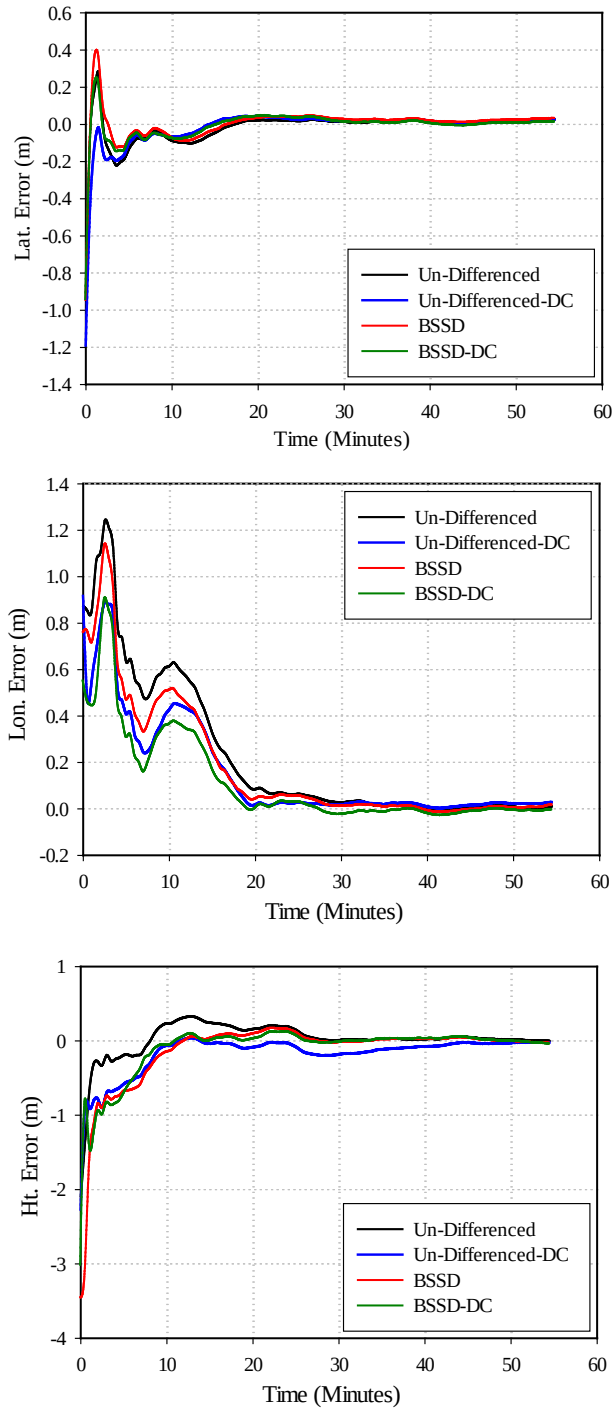

Figure F.20 Position Solution Using the Developed PPP Models for SEY1 IGS Station

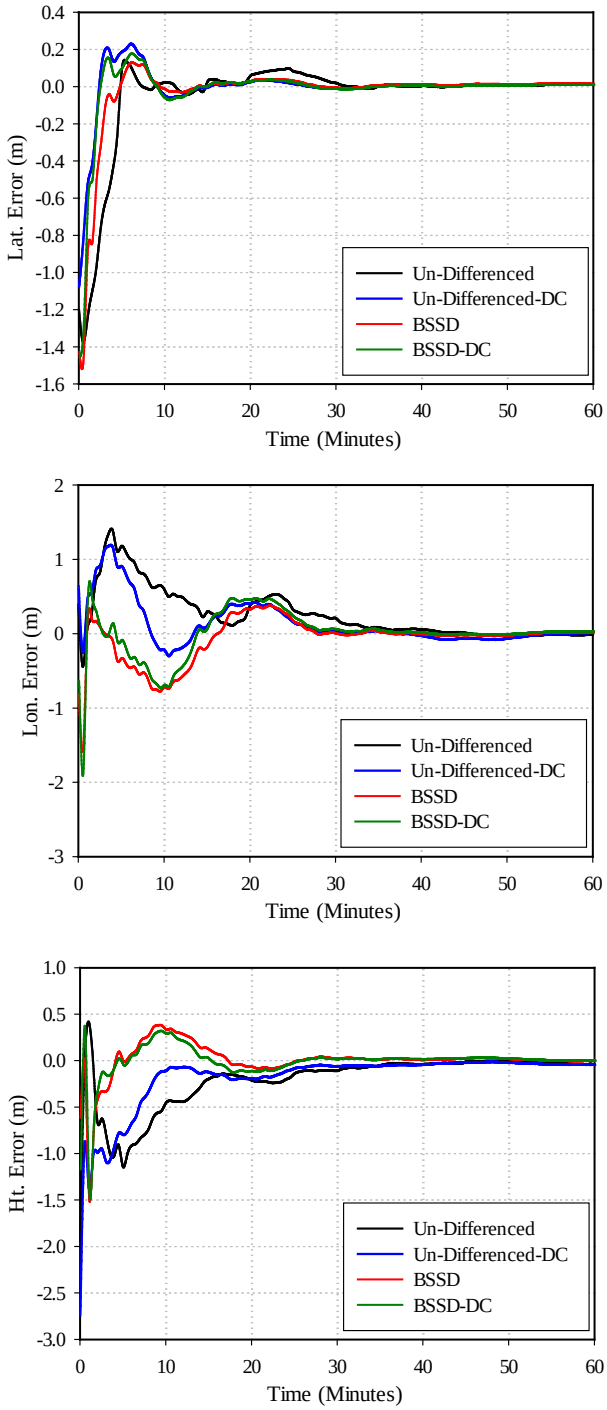

Figure F.21 Position Solution Using the Developed PPP Models for SSIA IGS Station

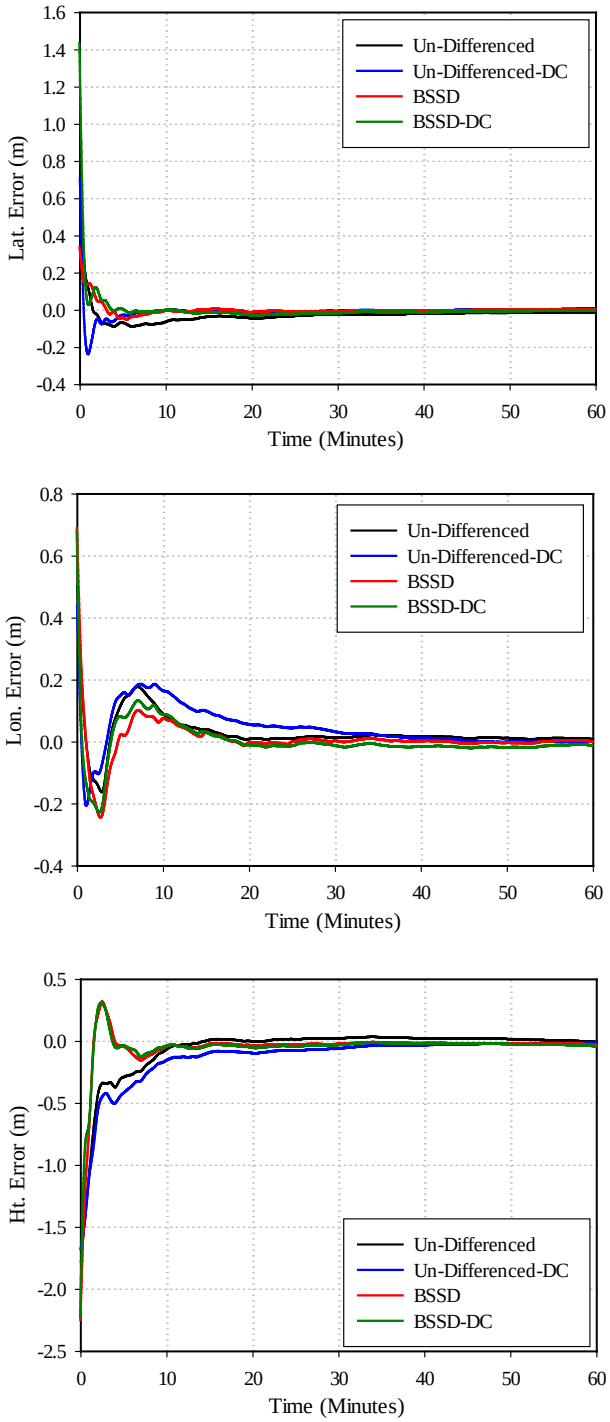

Figure F.22 Position Solution Using the Developed PPP Models for STR1 IGS Station

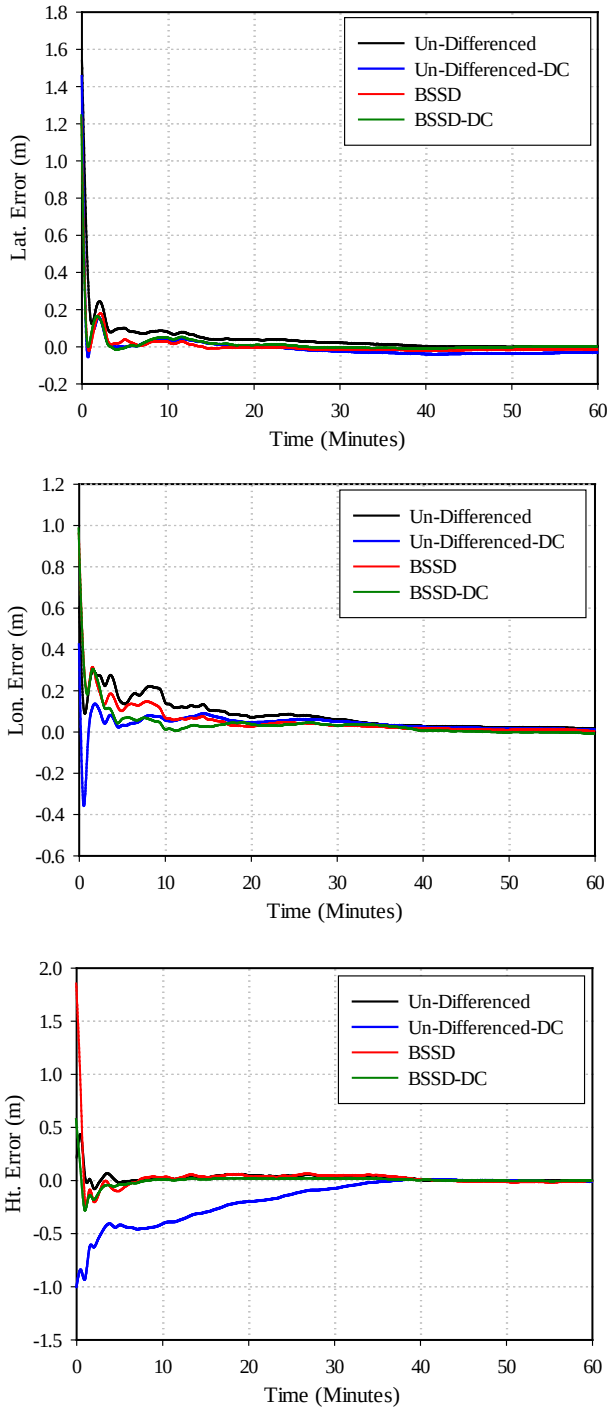

Figure F.23 Position Solution Using the Developed PPP Models for ULAB IGS Station

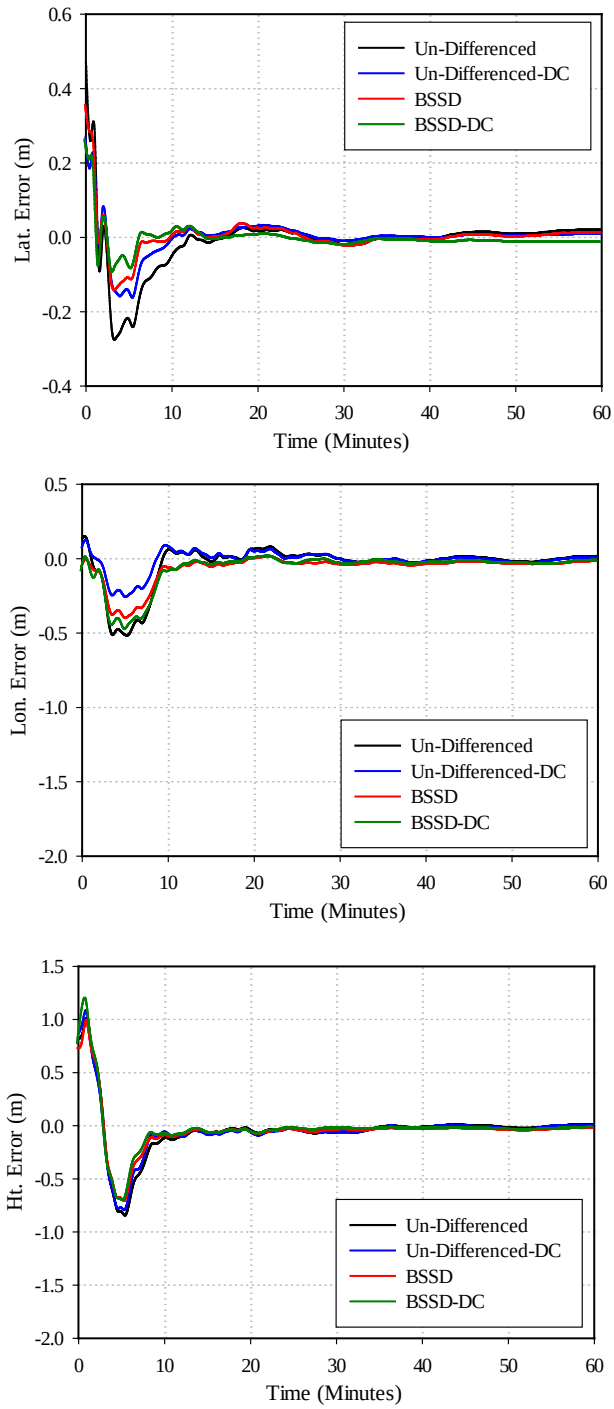

Figure F.24 Position Solution Using the Developed PPP Models for UNAC IGS Station

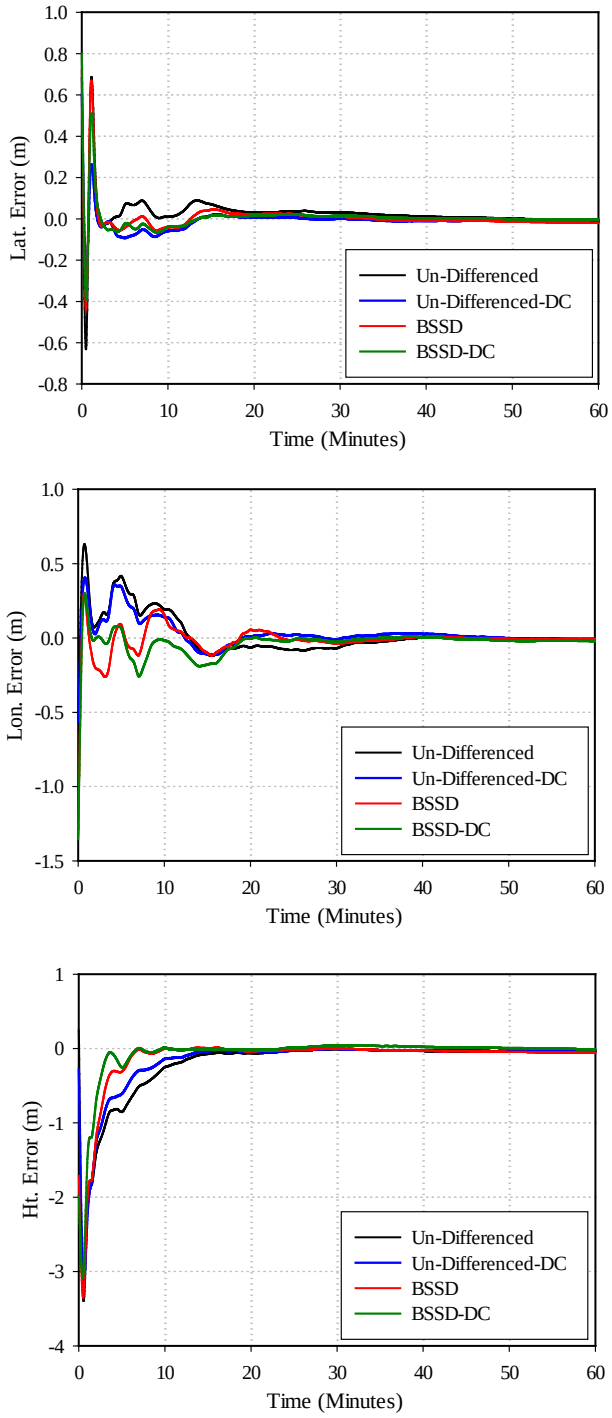

Figure F.25 Position Solution Using the Developed PPP Models for WIND IGS Station

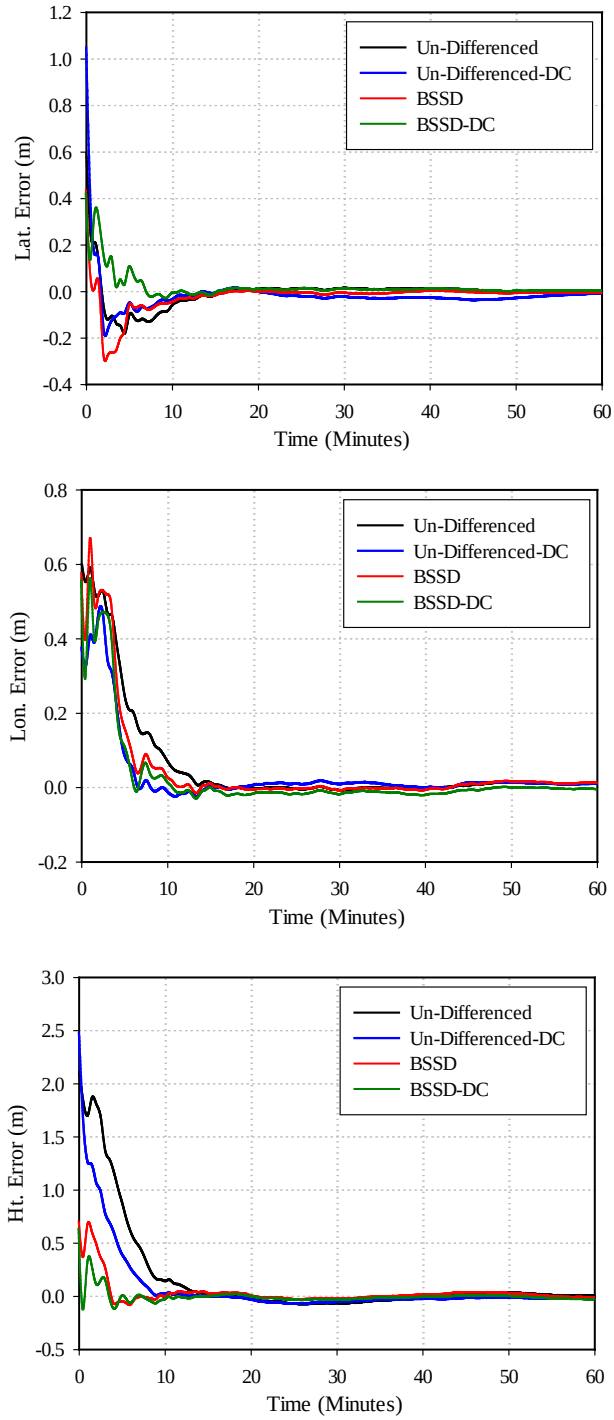

Figure F.26 Position Solution Using the Developed PPP Models for YAKT IGS Station

REFERENCES

Ahn, Y., G. Lachapelle, S. Skone, S. Gutman, and S. Sahm (2006). Analysis of GPS RTK Performance Using external NOAA Tropospheric Corrections Integrated with a Multiple Reference Station Approach. GPS Solutions Vol. 10, No. 3, pp. 171-186.

ARINC Engineering Services (2010). NAVSTAR GPS Space Segment / Navigation User Interfaces. Interface specification, IS-GPS-200, revision E. Available at www.arinc.com/gps.

Barclay, L. W. (2002). Propagation of Radiowaves, 2nd Edition (Electromagnetic Waves) The Institute of Engineering and Technology, London, United Kingdom.

Bassiri, S., and G. Hajj (1993). High-order ionospheric effects on the global positioning system observables and means of modeling them. Manuscr. Geod. Vol. 18. pp 280-289.

Boehm, J., and H. Schuh (2004). Vienna mapping functions in VLBI analyses. Geophys. Res. Lett., 31, L01603, doi:10.1029/2003GL018984.

Boehm, J., B. Werl, and H. Schuh (2006a). Troposphere mapping functions for GPS and very long baseline interferometry from European Centre for Medium-Range Weather Forecasts operational analysis data. Geophysical Research 111:B02406. doi:10.1029/2005JB003629.

Boehm, J., A. Niell, P. Tregoning, and H. Schuh (2006b). Global Mapping Function (GMF): a new empirical mapping function based on numerical weather model data. Geophysical Research Lett 33:L07304. doi:10.1029/2005GL025546.

Collins, P., S. Bisnath, F. Lahaye, and P. Heroux (2010). Undifferenced GPS Ambiguity Resolution Using the Decoupled Clock Model and Ambiguity Datum Fixing. Journal of Navigation, Vol. 57, No. 2, pp. 123-135.

Colombo, O.L., A.W. Sutter, and A.G. Evans (2004), "Evaluation of Precise, Kinematic GPS Point Positioning". ION GNSS 17th International Technical Meeting of the Satellite Division, 21-24 Sept. 2004, Long Beach, CA.

Dach, R., U. Hugentobler, P. Fridez, and M. Meindl (2007). Bernese GPS Software Version 5.0. Astronomical Institute, University of Berne, Switzerland.

El-Rabbany, A. (2006). Introduction to GPS: The Global Positioning System. Artech House Inc.

Elsobeiey, M., and A. El-Rabbany (2009). Effect of Second-Order Ionospheric Delay on GPS Orbit and Precise Point Positioning. Proceedings of the 22nd International Technical Meeting of The Satellite Division of the Institute of Navigation (ION GNSS 2009), Savannah, GA, September 2009, pp. 2489-2495.

Elsobeiey, M., and A. El-Rabbany (2010). On Stochastic Modeling of the Modernized Global Positioning System (GPS) L2C Signal. Meas. Sci. Technol. 21 (2010) 055105 (6pp).

Gao, Y. and X. Shen (2001), "Improving Ambiguity Convergence in Carrier Phase-Based Precise Point Point Positioning", ION GPS 2001, Salt Lake City, UT, 11-14 September, pp. 1532-1539.

Gao, Y. and X. Shen (2002), "Ambiguity Pseudo-fixing in Precise Single Point Positioning". ION 58th Annual Meeting/CIGTF 21st Guidance Test Symposium, 24-26 June 2002, Albuquerque, NM, PP 163-168

Ge, M., G. Gendt, M. Rothacher, C. Shi, and J. Liu (2008). Resolution of GPS carrier-phase ambiguities in Precise Point Positioning (PPP) with daily observations. Journal of Geodesy (2008) 82 389-399.

Ghilani, Charles D. (2011). Adjustment Computations, Spatial Data Analysis. Fifth Edition, John Wiley & Sons Inc.

Gutman, S., T. Fuller-Rowell, and D. Robinson (2003). Using NOAA Atmospheric Models to Improve Ionospheric and Tropospheric Corrections. U.S. Coast Guard DGPS Symposium, Portsmouth, VA. 19 June 2003.

Hernández-Pajares, M., J. M. Juan, J. Sanz, and R. Orús (2007). Second-order Ionospheric Term in GPS: Implementation and Impact on Geodetic Estimates. Journal of Geophysical Research. Vol. 112. B08417.

Hofmann-Wellenhof, B., H. Lichtenegger, and E. Walse (2008). GNSS Global Navigation Satellite Systems; GPS, Glonass, Galileo & more, Springer Wien, New York.

Hopfield, H. S. (1969). Two-Quartic Tropospheric Refractivity Profile for Correcting Satellite Data. J. Geophys. Res., 74(18), 4487-4499.

Houghton, J. T., M. J. Rycroft, and A. J. Dessler (1998). Physics of the space environment, Cambridge University Press.

Ibrahim, H. E., and A. El-Rabbany (2008). Regional Stochastic Models for NOAA-Based Residual Tropospheric Delays. The Journal of Navigation. 61. 209-219.

IERS (2010). IERS Concention (2010), IERS Technical Note 36, available at http://www.iers.org/IERS/EN/Publications/TechnicalNotes/tn36.html/.

IGS (2011). International GNSS service (IGS) website, http://igscb.jpl.nasa.gov/components/prods.html (accessed Audust 2011).

Kaplan, E., and H. Christopher (2006). Understanding GPS Principles and Applications, Artech House Inc.

Kelley, M. C. (2009). The earth's ionosphere: plasma physics and electrodynamics, Academic Press, New York.

Klobuchar, J. (1996). Ionospheric Effects on GPS, Global Positioning System: Theory and Applications, Vol. 1, pp 485–515 pp., American Institute of Aeronautics and Astronautics, Washington, D.C

Komjathy, A. (1997). Global Ionospheric Total Electron Content Mapping Using the Global Positioning System. Ph.D. dissertation, Department of Geodesy and Geomatics Engineering. . Technical Report No. 188, University of New Brunswick, Fredericton, New Brunswick, Canada, 248 pp.

Kouba, J. and P. Heroux (2001) "Precise Point Positioning Using IGS Orbit and Clock Products." GPS Solutions, 5(2), PP 12-28.

Kouba, Jan. (2007). Implementation and testing of the gridded Vienna Mapping Function 1 (VMF1). Journal of Geodesy 82, 193-205.

Kouba, Jan. (2009). A guide to Using International GNSS Service (IGS) Products. Available at http://igscb.jpl.nasa.gov/igscb/resource/pubs/GuidetoUsingIGSProducts.pdf.

Leick, A. (2004). GPS Satellite Surveying, 3rd ed., John Wiley & Sons Inc.

Merrill, R. T., and M. W. McElhinny (1983). The Earth's Magnetic Field, its History, Origin and Planetary Perspective. International Geophysics series. Vol. 32. Academic press Inc.

Misra, P., and P. Enge (2006). Global positioning system; signals, measurements, and performance. 2nd edition, Ganga-Jamuna Press.

Niell, A. E. (1996) "Global mapping functions for the atmosphere delay at radio wavelengths." Journal of Geophysical Research, Vol. 101, No. B2, pp. 3227-3246.

NOAA (2010). National Oceanic and Atmospheric Administration (NOAA) website, http://www.ngdc.noaa.gov/IAGA/vmod/igrf.html (accessed April 2010).

Nolan, J., S. Gourevitch, and J. Ladd (1992). Geodetic processing using dual band observables. Proceedings of the ION GPS-92, 5th Int. Technical Meeting, Satellite Div., Institute of Navigation (Albuquerque, NM, 16–18 September 1992) pp 1033–41.

Ozludemir, T. M. (2004). The Stochastic Modeling of GPS Observations. Turkish journal of Engineering and Environmental Sciences. Vol. 28, pp 223-231.

Schunk, R. W., and A. Nagy (2009). Ionospheres: Physics, Plasma Physics, and Chemistry, 2nd ed., Cambridge University Press, Cambridge, UK.

Seeber, G. (2003). Satellite Geodesy. 2nd revised and extended ed edition, Walter de Gruyter, Berlin

Teunissen, P. J. G., and A. Kleusberg (1998). GPS for Geodesy, New York:Springer-Verlag.

Wang, M., and Y. Gao (2007). An Investigation on GPS Receiver Initial Phase Bias and Its Determination. in proceeding of ION NTM 2007, 22-24 January 2007, San Diego, CA.

Witchayangkoon, B. (2000). Elements of GPS Precise Point Positioning. PhD Thesis, the University of Maine.

Wu, J. T., S, C. Wu, G.A. Hajj, W.I. Bertiger, and S. M. Lichten (1993). Effects of Antenna Orientation on GPS Carrier Phase. Man. Geodetica 18, pp. 91-98.

Zhong, P., X. Ding, D. Zheng and W. Chen (2007). "Adaptive wavelet transform based on cross-validation method and its application to GPS multipath mitigation". GPS solution. Springer-Verlag.Vol. 12, No. 2 pp. 109-117.

Zhu, S. Y., F. H. Massmann, Y. Yu, and C. Reigber (2002). Satellite Antenna Phase Center Offset and Scale Errors in GPS Solutions. Journal of Geodesy 76:668-672, Springer-Verlag, September 11-14, 2003.

Zumberge, J.F., M.B. Heflin, D.C. Jefferson, M.M. Watkins and F.H. Webb (1997). "Precise Point Processing for the Efficient and Robust Analysis of GPS Data from Large Networks. Journal of Geophysical Research, Vol. 102, No. B3, pp 5005-5017.